Université de Valenciennes et du Hainaut-Cambrésis

Thèse de doctorat

Pour obtenir le grade de Docteur de l'Université de

VALENCIENNES ET DU HAINAUT-CAMBRESIS

et de l'Université de SFAX (Tunisie)

Discipline, spécialité selon la liste des spécialités pour lesquelles l'Ecole Doctorale est accréditée :
Mécanique

Présentée et soutenue par Rami TOUNSI

Le 11/03/2014, à Valenciennes

Ecole doctorale :
Sciences Pour l'Ingénieur (SPI)

Equipe de recherche, Laboratoire :
Laboratoire d'Automatique, de Mécanique et d'Informatique Industrielles et Humaines (LAMIH)

Comportement des structures en nids d'abeilles sous sollicitations dynamiques mixtes compression/cisaillement et effet de l'orientation des cellules

JURY

Président du jury
- Haddar, Mohamed. Professeur. ENIS, Université de Sfax.

Rapporteurs
- Zhao, Han. Professeur. Université Pierre et Marie Curie.
- Chafra, Moez. Professeur. IPEIEM, Université de Tunis El Manar.

Examinateurs
- Hiermaier, Stefan. Professeur. Fraunhofer-EMI, Freiburg.
- Haugou, Gregory. Maître de conférences. Université de Valenciennes.
- Chaari, Fahmi. Maître de conférences. Université de Valenciennes.

Directeurs de thèse
- Markiewicz, Éric. Professeur. Université de Valenciennes.
- Zouari, Bassem. Maître de conférences. ENIS, Université de Sfax.

République Tunisienne
Ministère de l'Enseignement Supérieur,
de la Recherche Scientifique

Université de Sfax
École Nationale d'Ingénieurs de Sfax

Ecole Doctorale
Sciences et Technologies

Thèse de *DOCTORAT*
Génie MECANIQUE
N° d'ordre : 2014 – 405/14

THESE

Présentée à

L'École Nationale d'Ingénieurs de Sfax

En vue de l'obtention du

DOCTORAT

Dans la discipline *Génie MECANIQUE*

Par

Rami TOUNSI

Comportement des structures en nids d'abeilles sous sollicitations dynamiques mixtes compression/cisaillement et effet de l'orientation des cellules

Soutenu le 11 mars 2014, devant le jury composé de :

M.	**Mohamed HADDAR** (Professeur)	Président
M.	**Moez CHAFRA** (Professeur)	Rapporteur
M.	**Han ZHAO** (Professeur)	Rapporteur
M.	**Stefan HIERMAIER** (Professeur)	Examinateur
M.	**Gregory HAUGOU** (Maître de Conférences)	Examinateur
M.	**Fahmi CHAARI** (Maître de Conférences)	Examinateur
M.	**Bassem ZOUARI** (Maître de Conférences)	Directeur de Thèse
M.	**Eric MARKIEWICZ** (Professeur)	Directeur de Thèse

Acknowledgments

The present work is a collaboration between the *University of Valenciennes and Hainaut Cambresis* (UVHC) and the *National Engineering School of Sfax* (ENIS). I would like to acknowledge my supervisors Professor Eric MARKIEWICZ and Doctor Bassem ZOUARI who followed the first step of my thesis until the end of this thesis. I would like also to express my appreciation for their support and guidance during this thesis and for their trust and confidence in my abilities.

I would like also to thank Professors Han ZHAO and Moez CHAFRA for reviewing this dissection.

I would like also to thank Professors Stefan HIERMAIER and Mohamed HADDAR for examining this thesis.

I also thank all those who have contributed to this PhD work: Fahmi CHAARI, Denis LESUEUR and especially to Gregory HAUGOU for giving me their time and expertise in the experimental works. I would like to acknowledge all the LAMIH, TEMPO and LA2MP laboratory members and all those that I have met through this thesis, Olivier MAYEUR, Romain BALIEU, Florian VANDENBULCKE and many others without forgetting Cedric HUBERT, David MORIN...

Finally, I am very grateful to all my family who have always been present for me and particularly my parents for their continuous support through all my studies.

Contents

List of figures v

List of tables xv

General introduction 1

1 Literature review on honeycomb behaviour 7
- 1.1 Introduction . . . 8
- 1.2 Honeycomb behaviour under uni-axial compression . . . 9
  - 1.2.1 Experimental investigations . . . 9
  - 1.2.2 Numerical investigations . . . 10
- 1.3 Honeycomb behaviour under mixed shear-compression . . . 12
  - 1.3.1 Experimental investigations . . . 12
  - 1.3.2 Numerical investigations . . . 22
- 1.4 Macroscopic yield criterion . . . 27
  - 1.4.1 Description of the macroscopic yield criterion for honeycomb structure . . . 27
  - 1.4.2 Application of the macroscopic yield criterion for honeycomb structure . . . 29
- 1.5 Summary of the literature study and conclusion . . . 32

2 Honeycomb behaviour under quasi-static and dynamic mixed shear-compression loading 35
- 2.1 Introduction . . . 36
- 2.2 Specimens and materials preparation . . . 36
- 2.3 Experimental techniques and methods . . . 39
  - 2.3.1 Mixed shear-compression device . . . 39
  - 2.3.2 FE analysis of the whole testing system . . . 40
  - 2.3.3 Experimental set-up . . . 46
  - 2.3.4 Analysis of beveled bars effects and validation of the whole testing system . . . 47

2.4 Experimental results and analysis . . . 53
2.4.1 Crushing responses . . . 54
2.4.2 Dynamic enhancement . . . 64
2.4.3 Collapse mechanisms analysis . . . 75
2.5 Conclusion . . . 82

3 FE modelling of aluminium honeycomb under mixed shear-compression loading 85
3.1 Introduction . . . 86
3.2 General description of the FE numerical model . . . 87
3.2.1 The FE numerical model and materials . . . 87
3.2.2 FEM: Mesh and boundary conditions . . . 88
3.3 Numerical results and experimental validation . . . 90
3.3.1 The crushing responses under quasi-static loading . . . 90
3.3.2 The crushing responses under dynamic loading . . . 97
3.3.3 The collapse mechanisms . . . 103
3.3.4 Numerical and experimental deforming pattern modes . 109
3.3.5 Numerical and experimental local collapse mechanisms . . . 111
3.4 The normal and shear behaviours . . . 114
3.4.1 The in-plane orientation angle effects on the tangential force component (F_Y) . . . 114
3.4.2 Normal and shear crushing responses . . . 115
3.5 Macroscopic Yield Criterion . . . 118
3.6 Conclusion . . . 122

4 Reduced FE model of honeycomb specimen and its validity range 125
4.1 Introduction . . . 126
4.2 Reduced FE Model . . . 127
4.2.1 Cell model and periodic boundary conditions . . . 128
4.2.2 Validation of the reduced model under uni-axial loading 130
4.2.3 Validation of the reduced model under mixed shear-compression loading . . . 132
4.3 Reduced model validity range . . . 136
4.3.1 Comparison between the reduced and complete models results . . . 136
4.3.2 Pressure-crush curves . . . 137
4.3.3 Collapse mechanisms . . . 142
4.4 Conclusion . . . 145

Conclusions and perspectives 147

Annexes **151**

A The experimental honeycomb behaviour **153**
A.1 Quasi-static crushing responses 153
A.2 Dynamic crushing responses 156

B The numerical honeycomb behaviour **161**
B.1 Quasi-static crushing responses 161
B.2 Dynamic crushing responses 164

Bibliography **169**

List of Figures

1 Different kind of cellular materials 1
2 Honeycomb structures and applications 2
3 Aluminium honeycomb energy absorbers 2
4 Aluminium honeycomb and crash test barriers 3
5 The loading angle and the in-plane orientation angle under mixed loading 4
6 The thesis outline 5

1.1 The numerical model of one "Y" cross-sectional. 11
1.2 The honeycomb specimen, the schematic of the EAA with the butterfly-shaped honeycomb specimen and photography of the test-setup.[Doyo 03] 13
1.3 The honeycomb specimen: the cell parameters. [Mohr 04b] . . 13
1.4 The experimental set-up under quasi-static mixed shear-compression loading for the Nomex honeycombs. [Zhou 12] . . 14
1.5 The aluminium honeycomb specimen.[Hong 06a] 15
1.6 A test set-up for crush tests under quasi-static mixed shear-compression loading. [Hong 06a] 15
1.7 The influence of the in-plane orientation angle on normalized energy absorption rate under quasi-static mixed shear-compression loading. [Hong 06a] 16
1.8 The influence of the shear loads on the collapse mechanisms under quasi-static uni-axial compression (a) and mixed shear-compression loading (b) $\beta = 0°$, (c) $\beta = 30°$ and (d) $\beta = 90°$. [Hong 06a] 17
1.9 Experiment set-up for crush tests under dynamic mixed shear-compression loading (a) whole testing set-up (b) loading device (specimen and load cell). [Hong 08] 18
1.10 The collapse mechanisms under quasi-static and dynamic mixed shear-compression loading. [Hong 08] 19
1.11 The experimental test set-up under quasi-static (a) and dynamic (b) mixed shear-compression loading. [Hou 11a] . . . 20
1.12 The aluminium honeycomb specimen used by Hou.[Hou 11] . 21

1.13 The initial peak and the crush strength under quasi-static and dynamic mixed shear-compression loading in the two stages: (a) Stage I and (b) Stage II. [Hou 11a] 21
1.14 The collapse modes under quasi-static and dynamic mixed shear-compression loading(a) mode I and (b) mode II. [Hou 11a] 22
1.15 The FE-model of the VHS and the boundary conditions. [Mohr 04a] 23
1.16 The collapse mechanisms of honeycomb under quasi-static uni-axial compression and mixed shear-compression loadings. [Mohr 04a] 24
1.17 The virtual honeycomb specimen, the simplified FEM models, the boundary conditions and the pressure-crush curve under mixed shear-compression loading. [Hou 11b] 25
1.18 Comparison between the experimental results and the numerical ones under quasi-static and dynamic biaxial loading. [Hou 11b] 26
1.19 The comparison between the experimental collapse mechanisms and the numerical ones under quasi-static and dynamic mixed shear-compression loading. [Hou 11b] . . . 26
1.20 The material symmetry axes on the regular hexagonal cell honeycomb structure 27
1.21 The macroscopic yield criterion of honeycomb under quasi-static mixed shear-compression loading based on the numerical results. [Mohr 04a] 29
1.22 The macroscopic yield criterion under quasi-static and dynamic mixed shear-compression loading. [Hong 06a] and [Hong 08] 30
1.23 The macroscopic yield criterion for aluminium honeycombs under quasi-static and dynamic mixed shear-compression loading. [Hou 11b] 31
1.24 The macroscopic yield criterion for the Nomex honeycombs taking into account the effect of the in-plane orientation angle. [Zhou 12] 32

2.1 The honeycomb specimen geometry and cell parameters 37
2.2 The Al5056-N-6.0-1/4-0.003 honeycomb : geometry and cell parameters 37
2.3 Scheme of the in-plane orientation angles 38
2.4 Scheme of the loading angles 38
2.5 Scheme of the combined shear-compression device. [Hou 11a] . 40
2.6 Improvement of the testing conditions 43
2.7 The input and output pulses with beveled **(WB)** and without beveled bars under uni-axial loading $\psi = 0°$ 44
2.8 The separation phenomenon under mixed loading $\psi = 60°$ . . 45

2.9 The improvement of the shortening measurement using an electro optical extensometer under mixed loading $\psi = 60°$ . . 45
2.10 Scheme of the combined shear-compression device and the details of SHPB 46
2.11 The experimental and numerical elastic waves system and the beveled bars effects 48
2.12 Experimental testing conditions for honeycomb samples under dynamic loading 48
2.13 Comparison between the input and the output forces using David© and the extensometer technique 49
2.14 The experimental and numerical three elastic waves under uni-axial loading $\psi = 0°$ 50
2.15 The experimental and numerical three elastic waves under mixed loading $\psi = 60°$ 50
2.16 Forces validation under uni-axial compression loading ($\psi = 0°$) 51
2.17 Forces under mixed shear-compression loading ($\psi = 30°$) . . . 52
2.18 Correction details of the David© output force under mixed shear-compression loading 52
2.19 Correction of the David© output force under mixed shear-compression loading for $\psi = 30°$ 53
2.20 Comparison between three experiments on honeycomb under **quasi-static** ($V_T = 1$ mm/min) uni-axial compression loading ($\psi = 0°$) 54
2.21 Comparison between three impact experiments on honeycomb under **dynamic** ($V_{imp} = 15$ m/s) uni-axial compression loading ($\psi = 0°$) 54
2.22 Comparison between three experiments on honeycomb under **quasi-static** ($V_T = 1$ mm/min) mixed shear-compression loading ($\psi = 30°$ and $\beta = 30°$) 55
2.23 Comparison between three impact experiments on honeycomb under **dynamic** ($V_{imp} = 15$ m/s) mixed shear-compression loading ($\psi = 30°$ and $\beta = 30°$) 55
2.24 The average crushing response of the three experiments and the highlight of standard deviation 56
2.25 The crushing Force-displacement response of honeycomb structure 56
2.26 The quasi-static set-up with the shear-compression loading device 57
2.27 The in-plane orientation angles ($\beta = 0° / 30° / 60° / 90°$) . . 58
2.28 The loading angle ψ effects under **quasi-static** mixed shear-compression loading for $\beta = 0°$ 59
2.29 The in-plane orientation angle β effects under **quasi-static** mixed shear-compression loading for $\psi = 30°$ 60
2.30 The SHPB dynamic set-up with the shear-compression loading device 61

2.31 The measurement technique tools for data processing under dynamic loading . . . 61
2.32 The loading angle ψ effects under **dynamic** mixed shear-compression loading for $\beta = 90°$ . . . 62
2.33 The in-plane orientation angle β effects under **dynamic** mixed shear-compression loading for $\psi = 45°$ . . . 63
2.34 Quasi-static and dynamic force-displacement curves under **uni-axial compression** loading for $\psi = 0°$ . . . 65
2.35 Quasi-static and dynamic force-displacement curves under **mixed shear-compression** loading for $\psi = 30°$ and $\beta = 0°$ . . . 65
2.36 The loading and the in-plane orientation angles effects on the initial peak force under **quasi-static** mixed shear-compression loading. . . . 67
2.37 The loading and the in-plane orientation angles effects on the initial peak force under **dynamic** mixed shear-compression loading. . . . 68
2.38 The competition between the impact velocity, the loading angle and the in-plane orientation angle effect on **the initial peak force** under mixed shear-compression loading. . . . 68
2.39 Comparison between quasi-static and dynamic **initial peak force** : β effects . . . 69
2.40 The combined effect of the loading and the in-plane orientation angles on the average crushing force under **quasi-static** mixed shear-compression loading. . . . 71
2.41 The combined effect of the loading and the in-plane orientation angles on the average crushing force under **dynamic** mixed shear-compression loading. . . . 72
2.42 The competition between the impact velocity, the loading angle and the in-plane orientation angle effect on **the average crushing force** under mixed shear-compression loading. . . . 72
2.43 Comparison between quasi-static and dynamic **average crushing force** : β effects . . . 73
2.44 Comparison between quasi-static and dynamic collapse mechanisms for $\psi = 60°$ . . . 74
2.45 The scheme of the collapse mechanisms under quasi-static and dynamic loading for $\psi = 60°$ . . . 75
2.46 Collapse mechanisms under dynamic uni-axial compression loading . . . 76
2.47 Collapse mechanisms under dynamic mixed shear-compression loading : top views ($\psi = 30°$) . . . 77
2.48 Collapse mechanisms under dynamic mixed shear-compression loading : Mode I . . . 77
2.49 Collapse mechanisms under dynamic mixed shear-compression loading : Mode II . . . 78

2.50 Collapse mechanisms under dynamic mixed shear-compression loading : Mode III . . . 78
2.51 Collapse mechanisms under dynamic mixed shear-compression loading : scheme of the three deforming pattern modes I, II and III . . . 79
2.52 The in-plane orientation angle effect on the deforming pattern modes . . . 81

3.1 Scheme of the force components under mixed loading . . . 86
3.2 Scheme of the numerical model and the boundary conditions under mixed loading . . . 87
3.3 Scheme of the numerical honeycomb specimen and the geometry parameters . . . 88
3.4 FE Model: Mesh . . . 89
3.5 The in-plane orientation angle β on the numerical simulations 89
3.6 The choice of the loading velocity under quasi-static loading . 91
3.7 The loading angle ψ effects under **numerical quasi-static** mixed shear-compression loading for $\beta = 0°$ . . . 91
3.8 The in-plane orientation angle β effects under **numerical quasi-static** mixed shear-compression loading for $\psi = 60°$ . . 92
3.9 Comparison between the experimental and numerical crushing responses under **quasi-static** (a) uni-axial compression $\psi = 0°$ and (b) mixed shear-compression $\psi = 30°$ and $\beta = 0°$ . . . 93
3.10 Numerical and experimental initial peak and average crushing forces under **quasi-static** mixed shear-compression loading for $\beta = 0°$ . . . 95
3.11 Numerical and experimental initial peak and average crushing forces under **quasi-static** mixed shear-compression loading for $\beta = 30°$ . . . 95
3.12 Numerical and experimental initial peak and average crushing forces under **quasi-static** mixed shear-compression loading for $\beta = 60°$ . . . 96
3.13 Numerical and experimental initial peak and average crushing forces under **quasi-static** mixed shear-compression loading for $\beta = 90°$ . . . 96
3.14 The loading angle ψ effects under **numerical dynamic** mixed shear-compression loading for $\beta = 0°$ . . . 97
3.15 The in-plane orientation angle β effects under **numerical dynamic** mixed shear-compression loading for $\psi = 15°$ . . . 98
3.16 Comparison between the experimental and numerical crushing responses under **dynamic** (a) uni-axial compression $\psi = 0°$ and (b) mixed shear-compression $\psi = 30\ °$ and $\beta = 60°$ . . . 99
3.17 Numerical and experimental initial peak and average crushing forces under **dynamic** mixed shear-compression loading for $\beta = 0°$ . . . 101

3.18 Numerical and experimental initial peak and average crushing forces under **dynamic** mixed shear-compression loading for β= 30° . . . 101
3.19 Numerical and experimental initial peak and average crushing forces under **dynamic** mixed shear-compression loading for β= 60° . . . 102
3.20 Numerical and experimental initial peak and average crushing forces under **dynamic** mixed shear-compression loading for β= 90° . . . 102
3.21 The collapse mechanisms under dynamic uni-axial compression loading for $\psi = 0°$: numerical results . . . 103
3.22 The deforming pattern mode under dynamic uni-axial compression loading for $\psi = 0°$: numerical results . . . 104
3.23 The collapse mechanisms under dynamic mixed shear-compression loading for $\psi = 15°$ and $\beta = 90°$: numerical results 104
3.24 The deforming pattern **mode I** under dynamic mixed shear-compression loading for $\psi = 15°$ and $\beta = 90°$: numerical results 105
3.25 The collapse mechanisms under dynamic mixed shear-compression loading for $\psi = 45°$ and $\beta = 0°$: numerical results 105
3.26 The deforming pattern **mode II** under dynamic mixed shear-compression loading for $\psi = 45°$ and $\beta = 0°$: numerical results 106
3.27 The collapse mechanisms under dynamic mixed shear-compression loading for $\psi = 30°$ and $\beta = 90°$: numerical results 106
3.28 The deforming pattern **mode III** under dynamic mixed shear-compression loading for $\psi = 30°$ and $\beta = 90°$: numerical results 107
3.29 The deforming pattern **mode I** at the cell level for $\beta = 90°$. 108
3.30 The deforming pattern **mode II** at the cell level for $\beta = 0°$ . . 108
3.31 The deforming pattern **mode III** at the cell level for $\beta = 30°$ 109
3.32 Good correlation between the experimental and numerical deforming pattern modes . . . 110
3.33 The comparison between the experimental and numerical local collapse mechanisms under quasi-static mixed shear-compression loading . . . 112
3.34 The side effect on the collapse mechanisms under mixed shear-compression loading . . . 113
3.35 The **numerical** crushing force components under dynamic mixed shear-compression loading for $\psi = 45°$ with various β: $\mathbf{F}_Z$ **force component** . . . 115
3.36 The **numerical** crushing force components under dynamic mixed shear-compression loading for $\psi = 45°$ with various β: $\mathbf{F}_Y$ **force component** . . . 115
3.37 The **numerical** crushing force components under dynamic mixed shear-compression loading for $\psi = 45°$ with various β: $\mathbf{F}_N$ **normal force component** . . . 116

3.38 The **numerical** crushing force components under dynamic mixed shear-compression loading for $\psi = 45°$ with various β: **F_S shear force component** 116
3.39 The **numerical** average crushing force components under mixed shear-compression loading for $\psi = 30°$ and $\beta = 0°$: the normal and shear average crushing forces 117
3.40 The macroscopic yield criterion under **quasi-static** mixed shear-compression loading 119
3.41 The macroscopic yield criterion under **dynamic** mixed shear-compression loading 120
3.42 The macroscopic yield criterion under mixed shear-compression loading as function of ψ, β and V_{Imp} 121

4.1 Periodicity of the collapse mechanisms under uni-axial compression loading ($\psi = 0°$) and mixed loading ($\psi = 15°$ and $\beta = 90°$). 127
4.2 Scheme of numerical reduced model. 129
4.3 Comparison between the complete and reduced models: the pressure-crush curves (uni-axial loading $\psi = 0°$). 130
4.4 Comparison between the complete and reduced models: the collapse mechanisms at 1.5, 7.5 and 15 mm of crush (uni-axial loading $\psi = 0°$). 131
4.5 Comparison between the complete and reduced models: the normal pressure-crush curves (mixed loading $\psi = 15°$ and $\beta = 0°$). 133
4.6 Comparison between the complete and reduced models: the shear pressure-crush curves (mixed loading $\psi = 15°$ and $\beta = 0°$). 133
4.7 Comparison between the complete and reduced models: the total pressure-crush curves (mixed loading $\psi = 15°$ and $\beta = 0°$). 134
4.8 Comparison between the complete and reduced models: the collapse mechanisms (mixed loading $\psi = 15°$ and $\beta = 0°$). . . 135
4.9 The comparison between the complete and reduced models in term of the total pressure-crush curves $\psi = 30°$ and $\beta = 30°$. . 138
4.10 The comparison between the complete and reduced models in term of the total pressure-crush curves $\psi = 45°$ and $\beta = 60°$. . 138
4.11 The comparison between the complete and reduced models in term of the total pressure-crush curves $\psi = 60°$ and $\beta = 30°$. . 139
4.12 The comparison between the complete and reduced models in terms of the normal pressure-crush curves $\psi = 30°$ and $\beta = 30°$. 139
4.13 The comparison between the complete and reduced models in terms of the shear pressure-crush curves $\psi = 30°$ and $\beta = 30°$. 140
4.14 The comparison between the complete and reduced models in terms of the normal pressure-crush curves $\psi = 45°$ and $\beta = 60°$. 140

4.15 The comparison between the complete and reduced models in terms of the shear pressure-crush curves $\psi = 45°$ and $\beta = 60°$. 141
4.16 The comparison between the complete and reduced models in terms of the normal pressure-crush curves $\psi = 60°$ and $\beta = 30°$. 141
4.17 The comparison between the complete and reduced models in terms of the shear pressure-crush curves $\psi = 60°$ and $\beta = 30°$. 142
4.18 The comparison between the complete and reduced models in terms of collapse mechanisms ($\psi = 30°$ and $\beta = 30°$). 143
4.19 The comparison between the complete and reduced models in terms of collapse mechanisms ($\psi = 45°$ and $\beta = 60°$). 143
4.20 The comparison between the complete and reduced models in terms of collapse mechanisms ($\psi = 60°$ and $\beta = 30°$). 144
4.21 The boundary conditions and the side effects on the collapse mechanisms in the complete model ($\psi = 60°$ and $\beta = 30°$). . . 145

A.1 The loading angle ψ effects under **quasi-static** mixed shear-compression loading for $\beta = 30°$ 153
A.2 The loading angle ψ effects under **quasi-static** mixed shear-compression loading for $\beta = 60°$ 154
A.3 The loading angle ψ effects under **quasi-static** mixed shear-compression loading for $\beta = 90°$ 154
A.4 The in-plane orientation angle β effects under **quasi-static** mixed shear-compression loading for $\psi = 15°$ 155
A.5 The in-plane orientation angle β effects under **quasi-static** mixed shear-compression loading for $\psi = 45°$ 155
A.6 The in-plane orientation angle β effects under **quasi-static** mixed shear-compression loading for $\psi = 60°$ 156
A.7 The loading angle ψ effects under **dynamic** mixed shear-compression loading for $\beta = 0°$ 156
A.8 The loading angle ψ effects under **dynamic** mixed shear-compression loading for $\beta = 30°$ 157
A.9 The loading angle ψ effects under **dynamic** mixed shear-compression loading for $\beta = 60°$ 157
A.10 The in-plane orientation angle β effects under **dynamic** mixed shear-compression loading for $\psi = 15°$ 158
A.11 The in-plane orientation angle β effects under **dynamic** mixed shear-compression loading for $\psi = 30°$ 158
A.12 The in-plane orientation angle β effects under **dynamic** mixed shear-compression loading for $\psi = 60°$ 159

B.1 The loading angle ψ **numerical** effects under **quasi-static** mixed shear-compression loading for $\beta = 30°$ 161
B.2 The loading angle ψ **numerical** effects under **quasi-static** mixed shear-compression loading for $\beta = 60°$ 162

B.3 The loading angle ψ **numerical** effects under **quasi-static** mixed shear-compression loading for $\beta = 90°$ 162
B.4 The in-plane orientation angle β **numerical** effects under **quasi-static** mixed shear-compression loading for $\psi = 15°$ . . 163
B.5 The in-plane orientation angle β **numerical** effects under **quasi-static** mixed shear-compression loading for $\psi = 30°$ . . 163
B.6 The in-plane orientation angle β **numerical** effects under **quasi-static** mixed shear-compression loading for $\psi = 45°$ . . 164
B.7 The loading angle ψ **numerical** effects under **dynamic** mixed shear-compression loading for $\beta = 30°$ 164
B.8 The loading angle ψ **numerical** effects under **dynamic** mixed shear-compression loading for $\beta = 60°$ 165
B.9 The loading angle ψ **numerical** effects under **dynamic** mixed shear-compression loading for $\beta = 90°$ 165
B.10 The in-plane orientation angle β **numerical** effects under **dynamic** mixed shear-compression loading for $\psi = 30°$ 166
B.11 The in-plane orientation angle β **numerical** effects under **dynamic** mixed shear-compression loading for $\psi = 45°$ 166
B.12 The in-plane orientation angle β **numerical** effects under **dynamic** mixed shear-compression loading for $\psi = 60°$ 167

List of Tables

1.1 Previous works for honeycomb under mixed shear compression loading . . . 33
1.2 Existing simplified models. . . . 33

2.1 Material properties of specimen honeycomb . . . 41
2.2 The material properties of Nylon, Teflon, Steel and Aluminium 42
2.3 Stiffness improvement of the sleeves under mixed loading with $\psi = 60°$ . . . 42
2.4 **Initial peak force** (kN) under quasi-static mixed shear-compression loading . . . 60
2.5 **Average crushing force** (kN) under quasi-static mixed shear-compression loading . . . 60
2.6 **Initial peak force** (kN) under dynamic mixed shear-compression loading . . . 64
2.7 **Average crushing force** (kN) under dynamic mixed shear-compression loading . . . 64
2.8 Comparison between dynamic and quasi-static results under mixed shear-compression loading at **the initial peak force** . 66
2.9 Comparison between dynamic and quasi-static results under mixed shear-compression loading at **the average crushing force** . . . 70
2.10 The deforming pattern modes under quasi-static and dynamic mixed shear-compression loading . . . 80
2.11 The competition between ψ and β on the deforming pattern modes under mixed shear-compression loading . . . 81

3.1 Aluminium honeycomb specimen and bars material properties 88
3.2 Numerical and experimental initial peak force and average crushing force under **quasi-static** mixed shear-compression loading . . . 94
3.3 Numerical and experimental initial peak force and average crushing force (kN) under **dynamic** mixed shear-compression loading . . . 100

3.4 The deforming patterns modes under **quasi-static** mixed shear-compression loading: numerical and experimental results 111
3.5 The deforming pattern modes under **dynamic** mixed shear-compression loading: numerical and experimental results . . . 111

4.1 Existing simplified models. 126
4.2 Initial peaks and average crushing pressures under uni-axial loading. 131
4.3 Initial peaks and average crushing pressures under mixed loading. 134
4.4 CPU-time values for 2.66 GHz 135
4.5 Comparison of the initial peak and the average pressure (reduced and complete models). 137

General introduction

In order to improve sustainable development in the transport sector, the use of lightweight structures is one way to reduce energy consumption and greenhouse gas emission. Reducing vehicle mass has however to be done while at least maintaining the same safety levels. Cellular materials are good candidates because they present a well balanced energy absorption capability-to-mass ratio (specific energy). Nowadays, they are increasingly used as energy absorber structures and/or protective structures in many transport applications.

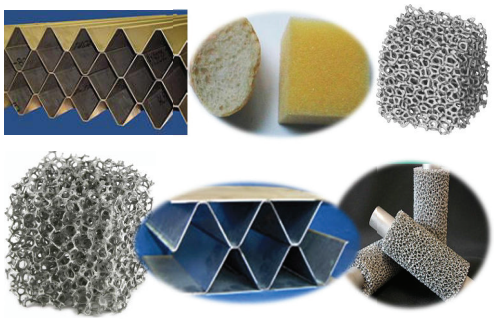

Figure 1: *Different kind of cellular materials*

Cellular materials may be based on a periodic or non periodic cells technology (figure 1). Honeycombs such as one of the periodic cellular materials are considered here. They can be made from different kind of constitutive materials such as metallic, polymer (thermoplastics). Nomex honeycombs made from aramid fiber paper coated with heat resistant phenolic resin offers excellent resiliency, low density, lower pricing and high strength to weight ratio. They are used in numerous engineering and scientific applications in transport industries including the automotive, marine, military, railway and especially for composite aircraft structures

(aircraft parts including sidewalls, galleys, seating, ailerons, flooring and ceiling). Aluminium honeycombs such as metallic honeycombs are made from aluminium alloy offers maximum stiffness and it is one of the highest strength to weight ratios of any structural honeycomb material available. They are used in many transport sectors as aircraft, marine and specifically in the automotive and the railway industries (energy absorption structures, protective structures in cars, crash barriers and rail parts as doors, floors and ceilings). Honeycombs and applications are presented in figure 2.



Figure 2: *Honeycomb structures and applications*

In this thesis, we focus on the aluminium honeycombs. The main use of the aluminium honeycomb structures is in the transport automotive/railway parts. They are introduced to reduce the weight of vehicle, to ensure a good specific energy ratio and to increases occupant protection level (figure 3).



Figure 3: *Aluminium honeycomb energy absorbers*

Aluminium honeycombs are also used in crash barriers for the automotive safety testing requirements (ECE regulation or EURONCAP consumers tests). Crash barriers are used to represent the impacted vehicle (frontal crash tests) or the impacting vehicle (side impact crash tests). They are composed by an assembly of honeycombs with different crushing properties in order to surrogate levels of deceleration and energy dissipation capability experienced by the real impacted or impacting vehicles (figure 4).

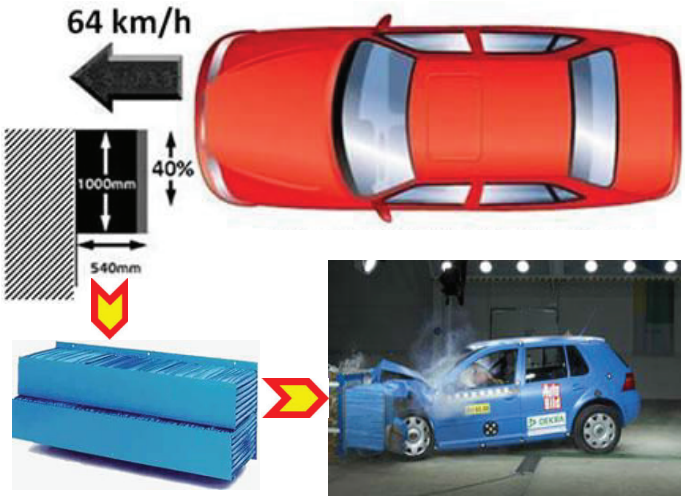

Figure 4: *Aluminium honeycomb and crash test barriers*

In both cases of these applications, honeycombs are subjected to dynamic complex loadings. The challenge is to understand in depth their mechanical behaviour and to simulate numerically under realistic work conditions. Thus, FE models have been developed in the commercial FE codes (ABAQUS crushable foam material or PAM-CRASH crushable foam for solid elements & improved side impact barrier material for solid elements material cards), while correlation between numerical simulations and experiments highlight limitations mainly due to a lack of representation of the honeycomb behaviour under multi-axial loading. Indeed, under multi-axial loading, implementation of the most appropriate honeycomb material card, needs to consider the following parameters as the loading angle and the in-plane orientation cells.

In this context, the uni-axial compression behaviour of aluminium honeycombs have been largely studied in the last decades. Results show that many parameters as the cell size, the cell wall thickness, the cell angle, the height of cell wall and the constitutive material influence their behaviour. However, aluminium honeycomb are subjected on both compression and

shear loads in the realistic working conditions. More recently, the complex behaviour of honeycomb under mixed shear-compression loading has been investigated. While, the influence of two parameters defined by the loading angle (ψ) and the in-plane orientation angle (β) has not been investigated in depth. Note that the loading angle is defined as the angle between the out-of-plane direction of the honeycomb and the load direction. The in-plane orientation angle is defined as the angle between the shear load direction and the double wall thickness direction (figure 5).

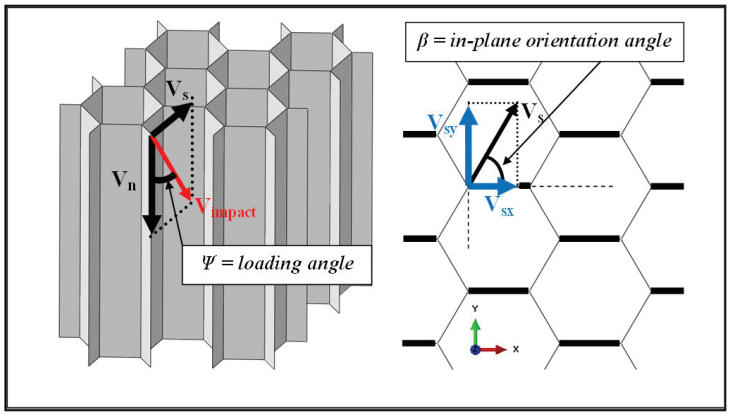

Figure 5: *The loading angle and the in-plane orientation angle under mixed loading*

The thesis works are divided into four main chapters. Chapter 1 deals with the literature review study on honeycomb structure behaviour. This chapter highlights that the combined effect of the loading angle (ψ), the in-plane orientation angle(β) and the impact velocity has not been deeply investigated. Chapter 2 deals with the experimental programme for the aluminium honeycomb specimens under mixed shear-compression loading which have been chosen for the easy analysis of the in-plane orientation angle, loading angle and impact velocity. Chapter 3 deals with the numerical modelling of the mixed shear-compression behaviour taking into account the loading angle, the in-plane orientation angle and the impact velocity. A validation between numerical and experimental results under different configurations of loading taking the in-plane orientation angle into consideration for both loading conditions quasi-static and dynamic is carried out. The separation of the normal and shear behaviours is performed. Thus, the parameters of a macroscopic yield criterion as a function of the loading angle, the in-plane orientation angle and the impact velocity are identified. Finally, the last chapter 4 is devoted to the development of

the reduced numerical model and its validity range under mixed loading in order to reduce the CPU-time and to determine the periodicity procedure limitation. This chapter allows to carry out a reduced numerical programmes of various experimental campaign, which are cheaper than the physical experimental programmes and cheaper than the detailed numerical model (complete model) presented in chapter 3.

Figure 6 presents the summary of this thesis works.

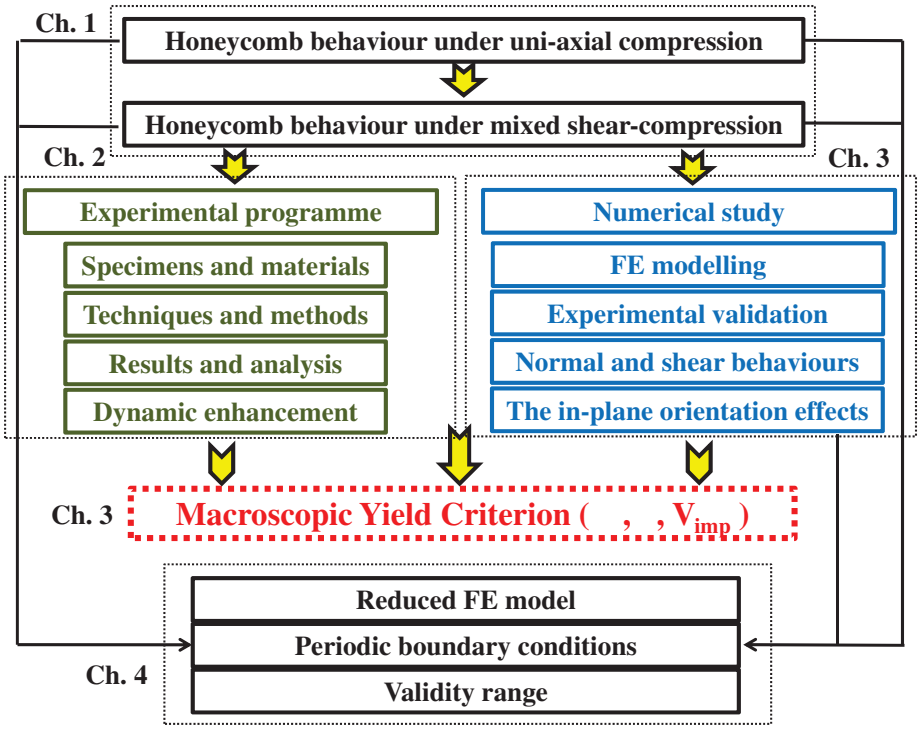

Figure 6: *The thesis outline*

This research was conducted through a joint PhD thesis between the University of Valenciennes and the National Engineering School of Sfax. This collaboration is jointly financed by the National Centre of Scientific Research and the General Direction of Scientific Research in Tunisia. The present research work has also been supported by the International Campus on Safety and Intermodality in Transportation, the Nord-Pas-de-Calais region, the European Community, the Regional Delegation for Research and Technology, The Agence Universitaire de la Francophonie and by the Ministry of Higher Education and Research. I would like to gratefully acknowledge the support of these institutions.

- Chapter 1 -

Literature review on honeycomb behaviour

Resume

The aim of this chapter is to present the state of the art of experimental studies and numerical modelling to investigate the quasi-static and dynamic honeycomb behaviours under uni-axial loading and under mixed shear-compression loading. It's concluded that a macroscopic yield criterion expressed as function of the impact velocity, the loading angle and the in-plane orientation angle is needed to better model the honeycomb behaviour for FE models used to study structural crashworthiness problems.

1.1 Introduction

Cellular materials are extensively used in many sectors of transports industry for their efficiency in term of stiffness-to-weight, strength-to-weight and specific energy absorption.

Cellular materials can be classified into two categories as a homogeneous materials (foams, ...) and structural materials (honeycombs, ...).

In this PhD works, we focus on honeycombs used as energy absorbers in many fields of the transport industry. The geometry of honeycomb structures is an array of hollow cells formed between thin vertical walls. The cells are often columnar and hexagonal in shape that provides a structure with minimal density and high out-of-plane compression properties.

Honeycombs are manufactured via the expansion process and the corrugation process from composite materials such as glass-reinforced plastic (thermoplastic honeycomb), from Nomex paper (Nomex honeycomb), or from a metal (usually aluminium honeycomb).

Indeed, aluminium honeycomb produces one of the highest strength/weight ratios of any structural material. Therefore, the aluminium honeycomb structures are considered here and we focus on their behaviour under the realistic loading conditions and the difficulty to numerically model this behaviour for structural crashworthiness FEA (finite element analysis).

The uni-axial compression honeycomb behaviour was extensively investigated in the past decades. However, investigations on the behaviour under mixed shear-compression, to face realistic conditions, are more recent.

In this chapter, a short selection of the main experimental and numerical works under uni-axial loading is first presented. A detailed description of the existing works under mixed shear-compression loading is after that presented. This description starts by the experimental techniques and methods and is followed by the numerical models in order to understand in depth the mixed behaviour.

Finally, a macroscopic yield criterion is proposed. All these studies are listed focusing on the impact velocity effect (quasi-static and dynamic) and the influence of the loading angle and in-plane orientation angle.

1.2 Honeycomb behaviour under uni-axial compression

The objective of this section is to present a selection of the main works focusing on the honeycomb behaviour under quasi-static and dynamic uni-axial compression loadings.

1.2.1 Experimental investigations

Under uni-axial compression loading, numerous studies have been realized in the past decades (Wierzbicki [Wier 83a, Wier 83b], Goldsmith et al. [Gold 92, Gold 95], ...). Two aspects were studied. The first one is focused on the geometry parameters and material properties effects. The second one is interested to study the impact velocity effect (dynamic enhancement).

In terms of geometry parameters and material properties effects, an experimental investigation on six types of honeycomb structures is achieved by Wu and Jiang [Wu 97]. Their specimens were loaded by blunt impactors and were all back-supported with a steel block. Experimental results suggest that a smaller cell size with core height and made of a stronger material give a better energy-absorbing capability per areal density. In terms of impact velocity effect, a dynamic enhancement of the crush strength about 74 % is observed between the quasi-static and dynamic results of Wu and Jiang [Wu 97]. This dynamic enhancement is proportional to the initial striking velocity of the projectile (impact velocity).

A dynamic enhancement of about 50 % is also observed for both materials (thick-walled aluminium and stainless-steel honeycomb) by comparing the plateau stress for the quasi-static and dynamic experiments realized by Baker et al. [Bake 98] using a high-pressure gas gun which fired projectiles into the fixed specimen.

Previous works were based on the use of classical testing devices (drop mass,...) and are not always able to supply a reasonable accuracy for testing honeycombs. Zhao and Gary [Zhao 98] presented a new development of the Split Hopkinson Pressure Bar (SHPB) with viscoelastic bars. The accuracy of the measurements is greatly improved. Results of an original experimental campaign under quasi-static and dynamic is reported where the dynamic enhancement of the crush strength is also observed.

To understand the dynamic enhancement phenomenon observed on aluminium honeycombs reputed to be not strain rate sensitive, Abdennadher et al. [Abde 03] investigated experimentally the effect of inertia of cellular structures under impact loading. Static and dynamic experimental results are presented for square tubes made of a strain rate insensitive material (brass). Experimental results based on the modified split Hopkinson pressure bar technique show that the dynamic enhancement behaviour of cellular structures such as honeycomb could be explain by the inertia effect. This results followed by the experimental study performed by Zhao et al. [Zhao 05] suggest that significant rate sensitivities for most of the cellular materials are observed and their analysis show that the micro-inertia effect in the successive folding process could be an important factor on this dynamic enhancement.

1.2.2 Numerical investigations

In order to understand in depth the crushing behaviour of honeycomb structures and their collapse mechanisms at the cell level, numerical simulations are required. The literature review shows that several numerical studies (Santosa et al. [Sant 98], Chawla et al. [Chaw 03], ...) have been realized based on the finite element method (FEM). In this section, we will focus on only few of these studies with chronological evolution of modelling techniques.

Numerical simulations are carried out by Chawla et al. [Chaw 03] using the explicit FE code PAM-CRASH^{TM}. A good agreement between the numerical and the experimental results is observed in term of the geometry parameters and material properties. Their numerical results suggest that the crushing strength depends on the foil thickness, the cell size and the material properties. Moreover, the dynamic enhancement on the crushing strength is observed numerically. Their validation between experimental and numerical results is limited to an impact velocity of 5.496 m/s. By contrast, Yamashita and Gotoh [Yama 05] investigated the effect of the cell shape, the foil thickness and the impact velocity (dynamic enhancement) using DYNA3D Explicit FE code in their simulations with an impact velocity equal to 10 m/s. A simplified numerical model composed by one "Y" cross-sectional column (figure1.1) is used based on the symmetry boundary conditions. The simplified model is developed in order to reduce the CPU-time. A good agreement between the numerical simplified model results and

their experimental results is observed. Numerical results suggest that the maximum value of the crush strength is attained for a regular hexagonal cell shape.

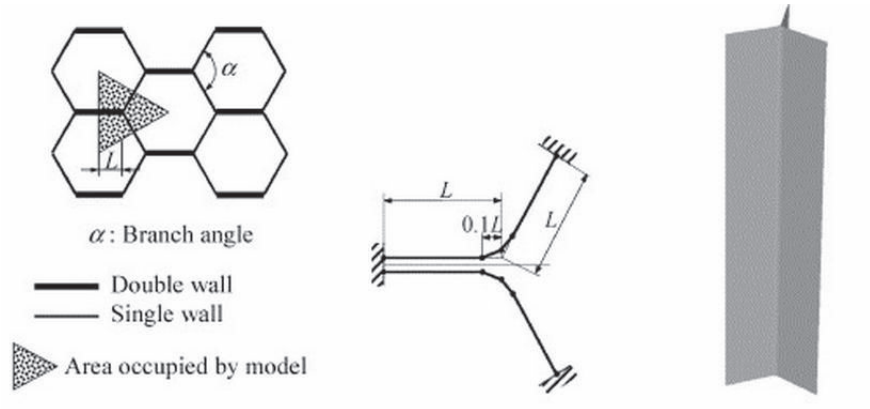

Figure 1.1: *The numerical model of one "Y" cross-sectional.*

In order to reduce the cost of the time calculations, a comparison between three numerical models is realized by Aktay et al.[Akta 08]. The first is a detailed honeycomb micromechanics model, the second is a homogenised material model which is suitable for use in FE code solid elements. The third is a homogenised discrete/finite element model used in a semi-adaptive numerical coupling (SAC) technique.

Their simulations suggest that fine micromechanical model based on shell elements to model the large honeycomb structures required a high quality of mesh and a lot of CPU-time. It is suitable for computing the crush energy absorption taking into account the honeycomb cell sizes, cell wall thickness and cell materials. So as, homogenised core models are carried out using solid elements. The homogenised material model may be used for honeycomb structures, but gives poor agreement when failure is due to core crushing. However, the SAC technique with a homogenised discrete/finite element model has a CPU-time efficient and gave good correlation with the experimental data. Indeed, it is shown to be most appropriate for use in structural simulations with extensive compression core crushing failures.

All these simplified numerical models are suitable to reproduce the honeycomb behaviour under uni-axial compression loading with a good accuracy, but are they suitable under mixed shear-compression loading taking into account the in-plane orientation cells ?

1.3 Honeycomb behaviour under mixed shear-compression

In this section, the quasi-static and dynamic mixed shear-compression loadings on the aluminium honeycomb is considered. The quasi-static honeycomb behaviour has been extensively studied experimentally whereas only a limited number of studies dealt with dynamic behaviour. For numerical modelling, only a few works are reported in the literature. In this section, we investigate the effects of the loading angle and the in-plane orientation angle in addition to the impact velocity on the mixed shear-compression behaviour. We present the influence of these parameters (ψ, β *and* V_{imp}) on the crushing responses, the collapse mechanisms and finally a macroscopic yield criterion which will be useful to model honeycomb behaviour.

1.3.1 Experimental investigations

In this part, the different experimental studies on the quasi-static and dynamic behaviours of aluminium honeycombs are classified and presented by the experimental set-up used.

1.3.1.1 The Enhanced Arcan Apparatus

The experimental techniques and methods on the crushing response of aluminium honeycomb under quasi-static mixed shear-compression with respect to out-of-plane loading are investigated by Doyoyo and Mohr [Doyo 03] and [Mohr 04b]. An Enhanced Arcan Apparatus (EAA) [M Ar 78] was used to apply a controlled biaxial displacement field to the boundaries of a butterfly-shaped honeycomb specimen. Figure 1.2 presents the schematic of the EAA with the butterfly-shaped honeycomb specimen that is made up of a single row of six cells.

The specimen is a 5056-H39 aluminium alloy honeycomb. The relative density (the ratio of the honeycomb density and the base material density) is $\rho^* = 1.8$ %. The width and the length of cell walls are D = 2.4 mm and L=3.1 mm respectively, the angle is $\alpha = 100°$, the single cell wall thickness is t = 33 μ m (figure 1.3).

Two reaction force components related to all the stresses acting on the

specimen were directly measured during the experiments: a vertical force corresponding to the shear force is measured by the load cell of the standard universal testing machine and the normal force is measured by an additional EAA-integrated load cell. They performed uni-axial compression and tension tests as well as the pure shear tests in addition to combined shear-compression tests.

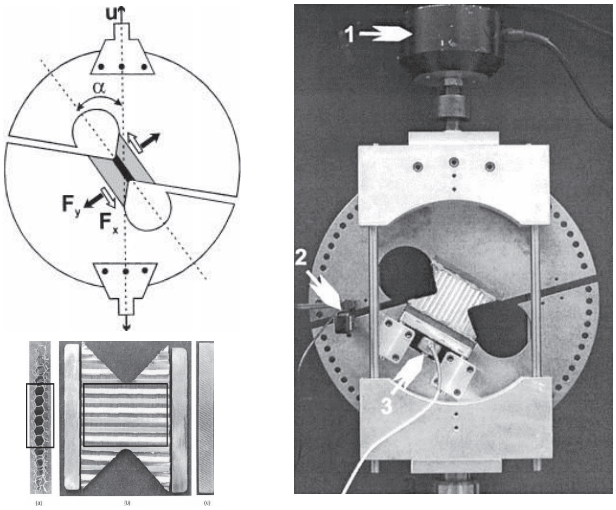

Figure 1.2: *The honeycomb specimen, the schematic of the EAA with the butterfly-shaped honeycomb specimen and photography of the test-setup.[Doyo 03]*

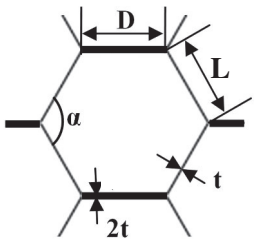

Figure 1.3: *The honeycomb specimen: the cell parameters. [Mohr 04b]*

Their experimental tests have been realized for only one specific in-plane orientation angle.

Recently, Zhou et al.[Zhou 12] investigated experimentally the quasi-static behaviour of Nomex honeycombs under mixed shear-compression

loading using the Arcan set-up. They are interested to analyse the in-plane orientation angle effects. Four in-plane orientation angles with various loading angle are tested (figure 1.4).

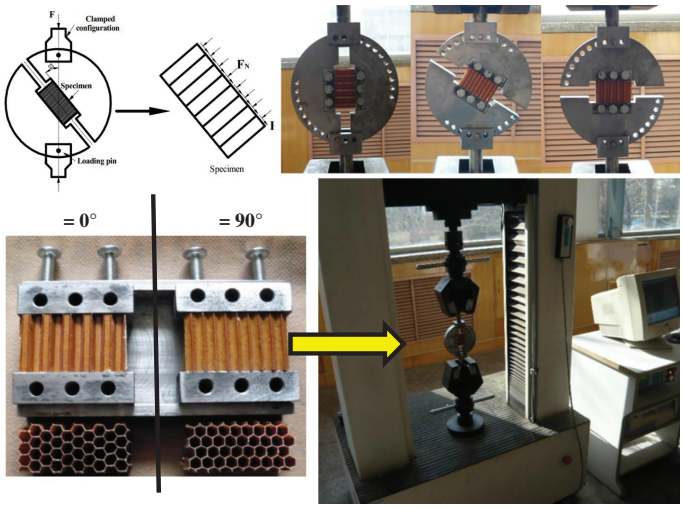

Figure 1.4: *The experimental set-up under quasi-static mixed shear-compression loading for the Nomex honeycombs. [Zhou 12]*

Two co-existing deforming pattern modes of honeycomb specimens are observed under mixed shear-compression.

A significant effect of the in-plane orientation angle is reported on their macroscopic yield criterion which is presented in the section (1.4.2) under quasi-static loading. But what about this effect under dynamic loading?

1.3.1.2 The bi-axial test machine

Hong et al. [Hong 03], [Hong 04], [Hong 06a] and [Hong 06b] have investigated the quasi-static behaviour of aluminium honeycomb under mixed shear-compression loading taking into account the in-plane orientation angle effects using a bi-axial test machine.

The honeycomb specimen is a 5052-H38 aluminium alloy honeycomb. The relative density is $\rho^* = 1$ %. The regular hexagonal cell wall width is equal to D = L = 5.5 mm, the angle is $\alpha = 120°$, the single cell wall thickness is t = 25 μ m.

Under combined shear-compression loading, the length of the honeycomb specimen needs to be at least 10 times larger than the height of specimen in order to minimize the secondary stresses, ([OCon 89] and [ASTM 00]). In

addition they pointed that the width of the specimen needs to be at least 7 times of the cell size in order to minimize the specimen size effect ([Bitz 97] and [Ashb 00]). So that, two different types of specimens are used : the first one, with a larger load carrying area and a larger height, is used to investigate the crush behaviour under mixed loading (figure 1.5) . The second one, with a smaller load carrying area and a smaller height, is used to analyse the effects of the specimen height.

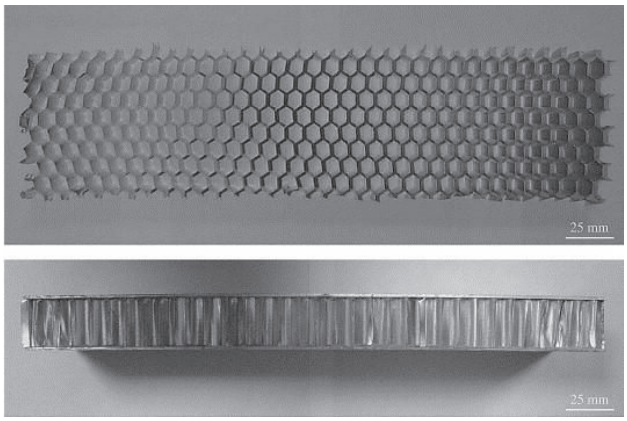

Figure 1.5: *The aluminium honeycomb specimen.[Hong 06a]*

After that, an experimental set-up is developed in order to apply combined compressive and shear loads with respect to the strongest material symmetry direction. The compressive and the shear loads can be controlled and applied independently by two actuators (figure 1.6).

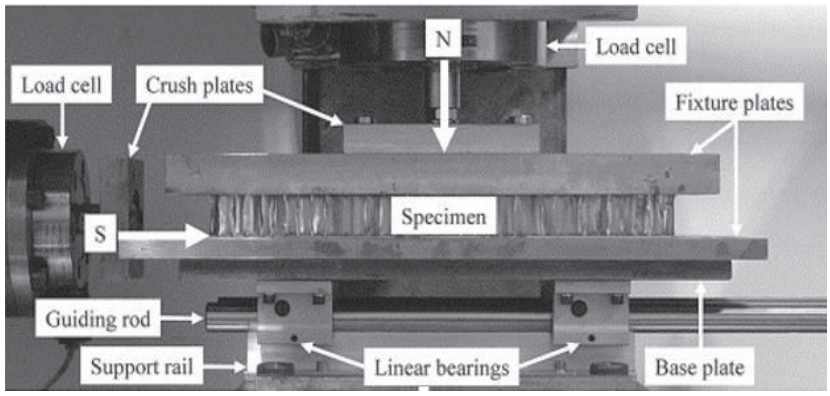

Figure 1.6: *A test set-up for crush tests under quasi-static mixed shear-compression loading. [Hong 06a]*

Using this experimental set-up, the influence of the shear load and the shear load direction (the in-plane orientation) on the quasi-static crush behaviour of aluminium honeycomb structures is investigated. Their experimental results ([Hong 06a]) suggest that the normal crush strengths under mixed shear-compression loading are lower than that under uni-axial compression loading. The effect of the in-plane orientation angle on the phenomenological yield criterion under mixed shear-compression with quasi-static loading conditions is studied based on the experimental results. Their experimental results present the effect of the in-plane orientation angle β and the ratio of shear stress by the compressive stress on the energy absorption capacity. The normalized energy absorption rate increases as the shear stress ratio increases for $\beta = 0°$ but decreases as the shear stress ratio increases for $\beta = 30°$ and $\beta = 90°$ (figure 1.7).

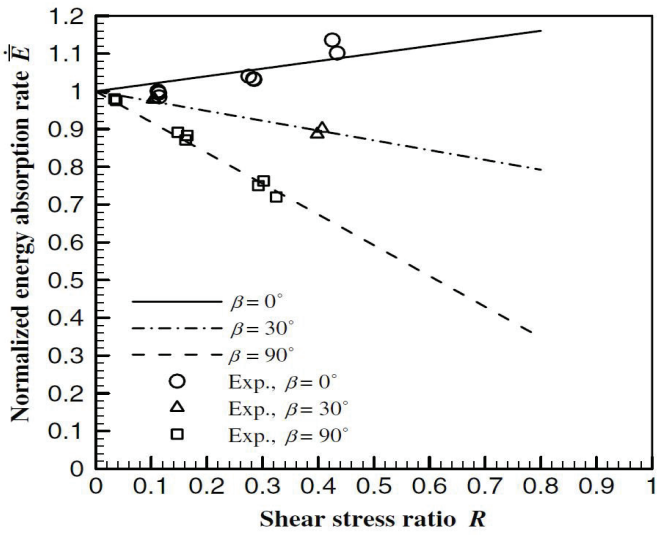

Figure 1.7: *The influence of the in-plane orientation angle on normalized energy absorption rate under quasi-static mixed shear-compression loading. [Hong 06a]*

The influence of the shear load on the collapse mechanisms is also investigated and is shown in figure 1.8. Under pure compressive loads, the aluminium honeycombs shows a progressive folding of cell walls stacking on top of each other. By contrast, under mixed shear-compression loading, the aluminium honeycomb shows an inclined stacking patterns of folds in contrast to the stacking of folds on top of each other. The inclined stacking patterns are formed due to the consequences of the asymmetric location of horizontal plastic hinge lines and the presence of shear loads.

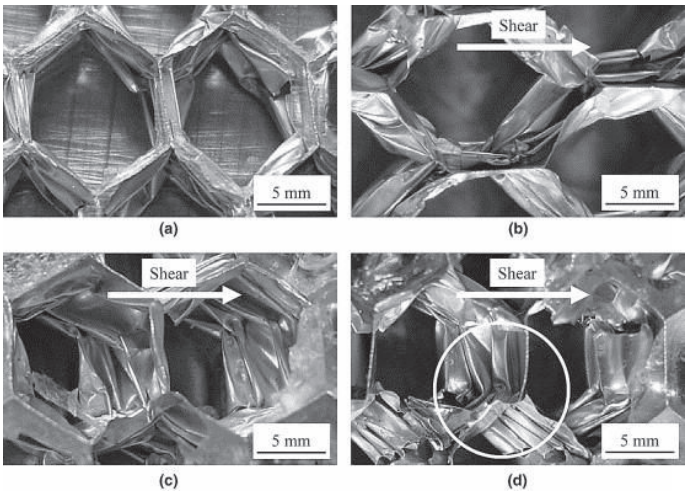

Figure 1.8: *The influence of the shear loads on the collapse mechanisms under quasi-static uni-axial compression (a) and mixed shear-compression loading (b) $\beta = 0°$, (c) $\beta = 30°$ and (d) $\beta = 90°$. [Hong 06a]*

1.3.1.3 Mixed shear-compression device

Under dynamic mixed shear-compression loading conditions, an impact test machine with a gas gun (figure 1.9) was used to investigate the crush behaviour of aluminium honeycomb structures taking into account the effects of the impact velocity and the in-plane orientation angle but for only one loading angle [Hong 08].

The same specimens used for quasi-static experiments are used for the dynamic tests. In their works, they investigate only one loading angle ψ that is fixed at 15°. This experimental set-up is used to analyse the effect of the in-plane orientation angle β under quasi-static loading condition with a loading velocity equal to 0.1 mm/s and under dynamic loading with an impact velocity equal to 6.7 m/s (figure 1.9).

The quasi-static and dynamic results show that the normal crush strength increases when the impact velocity increases but no effect on the shear strength is observed. The trends of the normalized normal crush strengths under mixed shear-compression loading taking the in-plane orientation angle into consideration are very similar to each other. They have also investigated the influence of the in-plane orientation angle β on the macroscopic yield criterion which is presented in the next section.

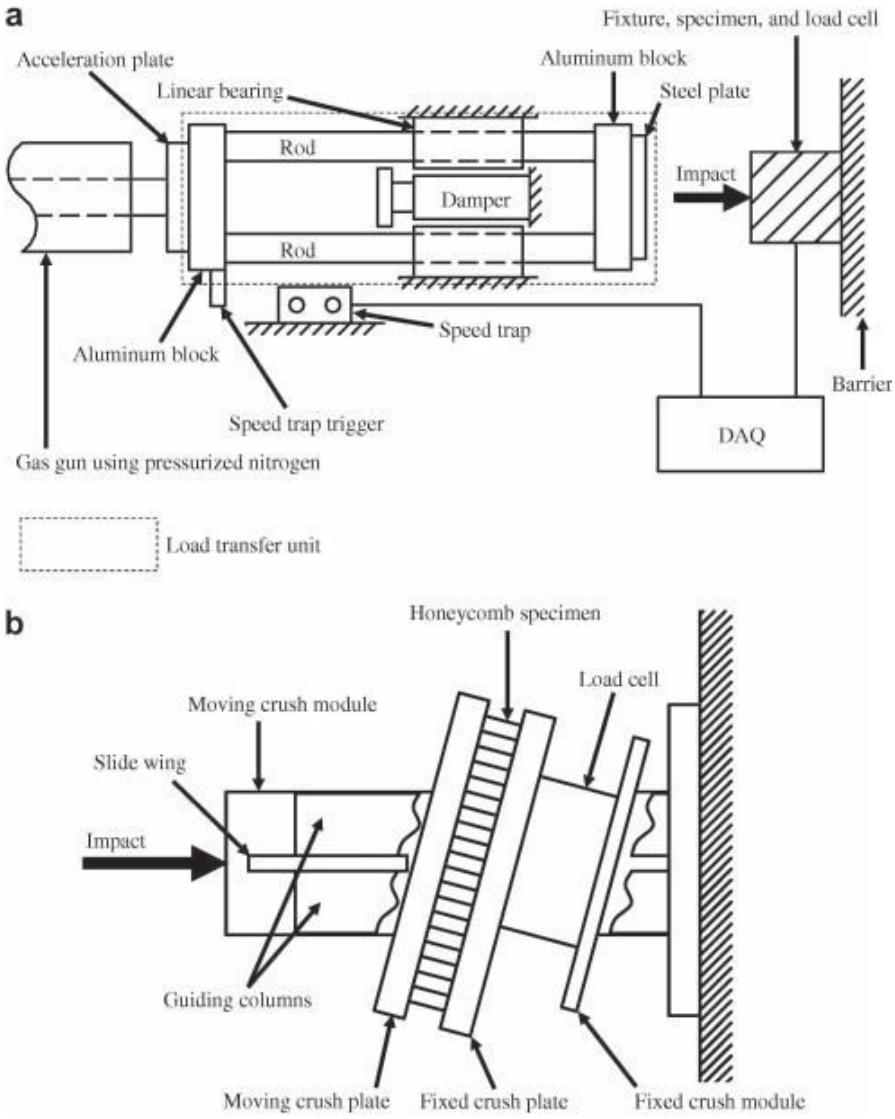

Figure 1.9: *Experiment set-up for crush tests under dynamic mixed shear-compression loading (a) whole testing set-up (b) loading device (specimen and load cell). [Hong 08]*

Due to the weak ψ angle, the experimental progressive folding mechanisms under mixed shear-compression loading are similar to the mechanisms observed under uni-axial compression (figure 1.10).

But, the crushed honeycomb specimens under mixed shear-compression loading show the inclined stacking patterns of folds due to the asymmetric location of horizontal plastic hinge lines.

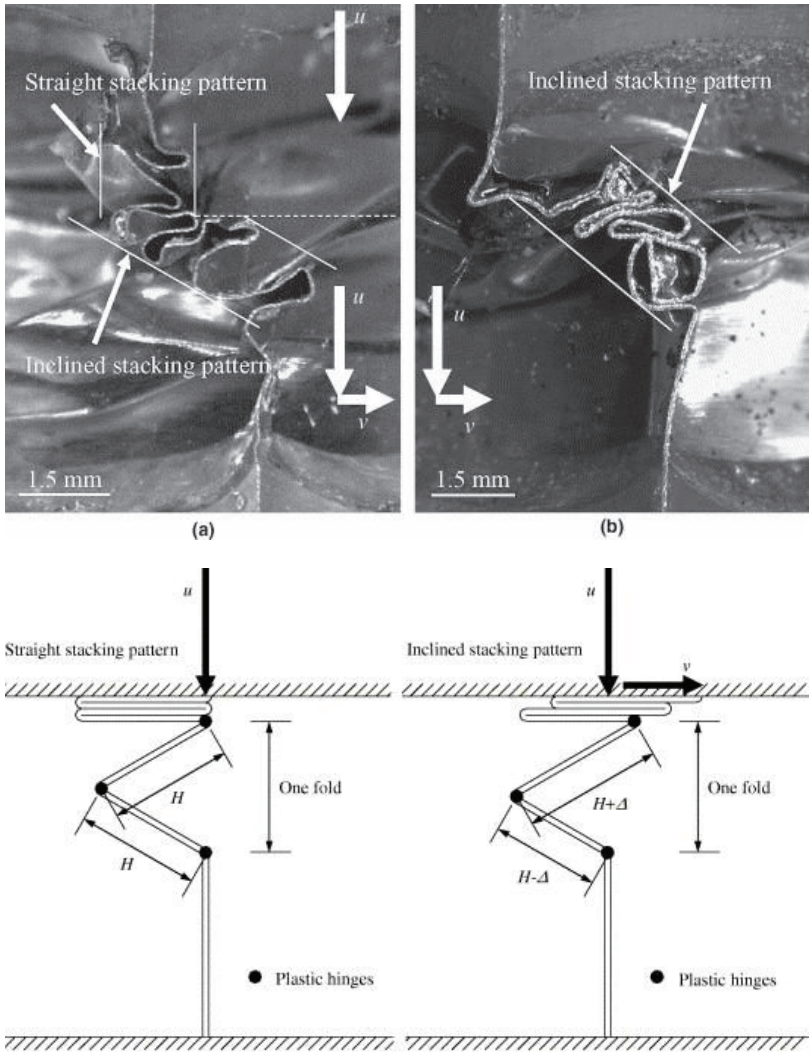

Figure 1.10: *The collapse mechanisms under quasi-static and dynamic mixed shear-compression loading. [Hong 08]*

In order to perform dynamic experiments at a higher impact velocity and to study the effect of the loading angle ψ on a larger range, Hou [Hou 11] developed a new experimental techniques for testing the aluminium honeycomb behaviour under mixed quasi-static and dynamic shear-compression loadings.

1.3.1.4 Advanced mixed shear-compression loading device

Recently, Hou et al. [Hou 11] and [Hou 11a] presented a mixed shear-compression loading device. It is composed by two short cylindrical bars with one bevel end. They are made of the same material (Nylon) and have the same diameter as the Hopkinson bars set-up. The honeycomb specimen is placed between the two short bars with inclined ends (beveled bars). A Teflon sleeve and two aluminium supports are used to ensure the good alignment of the beveled bars and the Hopkinson bars and to fix the whole device (figure 1.11). The aluminium honeycomb specimens are crushed

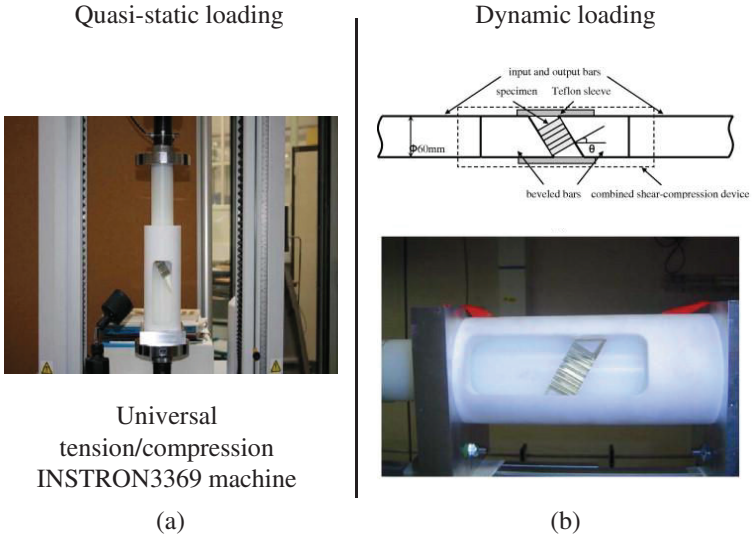

Figure 1.11: *The experimental test set-up under quasi-static (a) and dynamic (b) mixed shear-compression loading. [Hou 11a]*

under quasi-static loading conditions using the mixed shear-compression loading device on a universal tension/compression INSTRON3369 machine with a loading velocity of about 1 mm/min (figure 1.11 (a)). The experiments were performed under dynamic loading conditions at the impact velocity of about 15 m/s by introducing the mixed shear-compression loading device on a large-diameter Nylon Split Hopkinson Pressure Bar system (SHPB) with beveled ends of different angles (figure 1.11 (b)). The loading angle ranged from $\psi = 0°$ that presents the uni-axial compression loading case to $\psi = 60°$ by steps of 10° with two in-plane orientation angles $\beta = 0°$ and $\beta = 90°$.

The specimen is an Al5052 aluminium alloy honeycomb. The relative density is $\rho^* = 3\%$. The single cell wall thickness is t = 76 μm, the angle is α = 120° and the cell size is d = 6.35 mm. The specimen contains 39 complete

cells on the honeycomb cross-section. The specimen dimensions are 40*40*25 mm in the directions of L, W and T respectively (figure 1.12). There is then more than 6 cells in any direction so that the size effect may be considered as not significant.

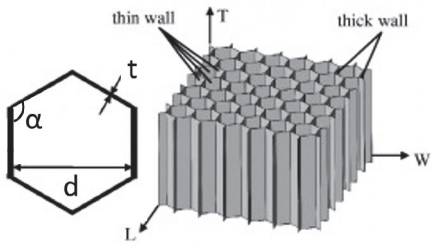

Figure 1.12: *The aluminium honeycomb specimen used by Hou.[Hou 11]*

Their experimental results analysed two parameters : the initial peak force and the crush strength such as presented by figure 1.13.

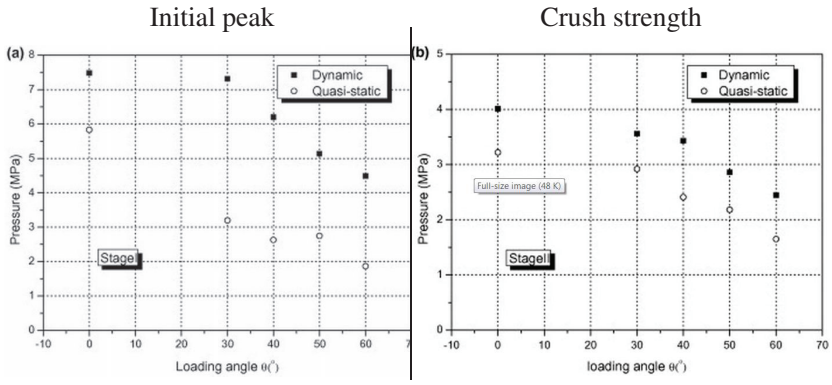

Figure 1.13: *The initial peak and the crush strength under quasi-static and dynamic mixed shear-compression loading in the two stages: (a) Stage I and (b) Stage II. [Hou 11a]*

The loading angle ψ has a strong effect on both the initial peak and the average crush strength that decrease with increasing loading angles. Comparing their quasi-static and dynamic results, a noticeable dynamic strength enhancement is observed. At the initial collapse, the strength of honeycomb under dynamic loading is significantly higher than under quasi-static loadings. An enhancement of the average crushing strength varying from 22% to 48% is found from the dynamic curves to the quasi-static ones (figure 1.13).

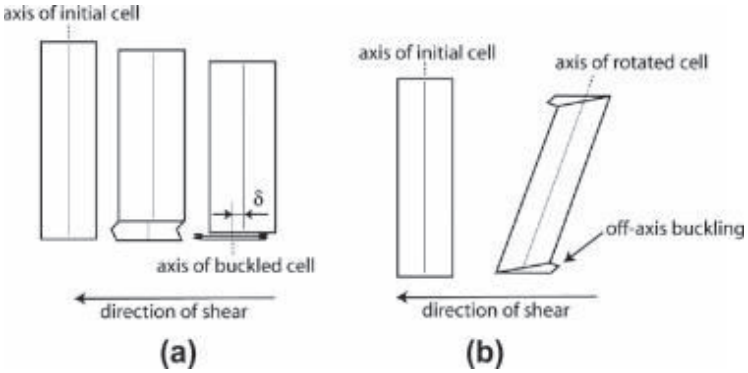

Figure 1.14: *The collapse modes under quasi-static and dynamic mixed shear-compression loading(a) mode I and (b) mode II. [Hou 11a]*

From photographies captured by a high-speed camera during the quasi-static and dynamic tests, the difference between the collapse mechanisms and modes under uni-axial compression and combined shear-compression loading are identified. Two co-existing deforming pattern modes under combined shear-compression are identified (figure 1.14) and the influence of loading rate on the occurrence of these two deforming modes is studied. The first one maintains the central part with no rotation such as under uni-axial compression loading, but the additional shear load allows to an overall translation of the buckled cell relative to the non compacted cell. The second one presents an off-axis local buckling mechanism and allow to incline the rotation of the central part during the crash test. The origin of the two co-existing modes was however not further explained. Moreover, the influence of the in-plane orientation angle ($\beta = 0°$ and $\beta = 90°$) is analysed and no significant effect is reported.

1.3.2 Numerical investigations

In order to understand in depth the mixed honeycomb behaviour and to enrich the experimental results especially in the local collapse mechanisms under dynamic loading, numerical simulations are needed. The numerical simulations allow to study the geometry parameters, the material properties, the impact velocity, ... and to perform numerically an experimental programme with a minimum cost as possible. The numerical results serve also to complete the experimental data and give more information to identify the parameters of the macroscopic yield criterion.

The 'Y' finite element model presented in section 1.2.2 used by Yamashita [Yama 05] is available only for the uni-axial compression loading due to

symmetric boundary conditions. Under mixed shear-compression loading, it is not suitable to simulate the real crash test because the normal and the shear loads are combined and the symmetric boundary conditions are no longer verified.

A few numerical studies under mixed shear-compression loading are reported in the literature. The mixed honeycomb behaviour has been investigated numerically by Mohr and Doyoyo [Mohr 04a] under quasi-static loading and by Hou et al. [Hou 11b] under both quasi-static and dynamic loadings.

A virtual honeycomb specimen (VHS) is used by Mohr and Doyoyo [Mohr 04a] to perform numerical biaxial tests based on finite elements method. The numerical tests are performed only under quasi-static loading conditions for various loadings angle but for only one in-plane orientation angle $\beta = 90°$ due to the limitation of the symmetric boundary conditions applied in their FE model. So the influence of the in-plane orientation angle β was not investigated.

Based on the periodicity of honeycomb specimen, the VHS defined as "row-model" is composed by a row of cells such as presented in figure 1.15. The same honeycomb specimen used in their experiments [Doyo 03] is used in their simulations. It is an 5056-H39 aluminium alloy honeycomb. The relative density is $\rho^* = 1.8$ %. The width and the length of cell walls are D = 2.4 mm and L=3.1 mm respectively, the angle is $\alpha = 100°$, the single cell wall thickness is t = 33 μ m, (figure 1.15).

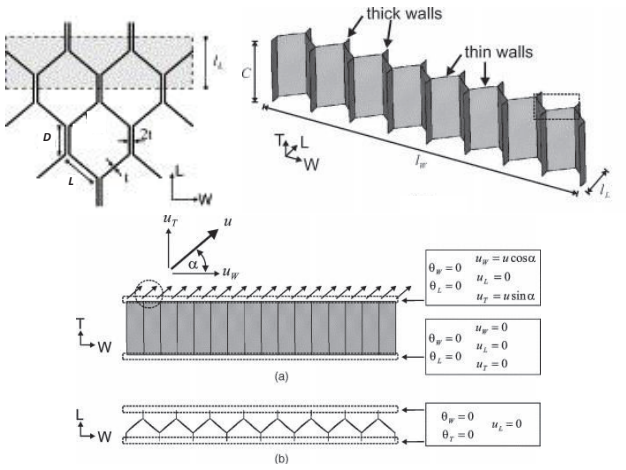

Figure 1.15: *The FE-model of the VHS and the boundary conditions. [Mohr 04a]*

In addition to the symmetric boundary conditions, all degrees of freedom are restricted at the bottom of the specimen, whereas a homogeneous displacement field is applied at the top of the specimen. LS-DYNA v960/Explicit FE code is used and the parameters of the time and time step are chosen such as guarantee the quasi-static loading conditions. The virtual honeycomb specimen (VHS) involves a detailed finite element model with 3d shell elements obeying an elastic–plastic constitutive law.

The numerical results suggest a good description of the local collapse mechanisms for the honeycomb crushed specimen under quasi-static mixed shear-compression loading.

The collapse mechanisms begin by the elastic regime followed by the plastic collapse point that activates the progressive folding systems. The folding system at the cell level is characterised by the folding plane, folding direction and hinge line orientation (figure 1.16).

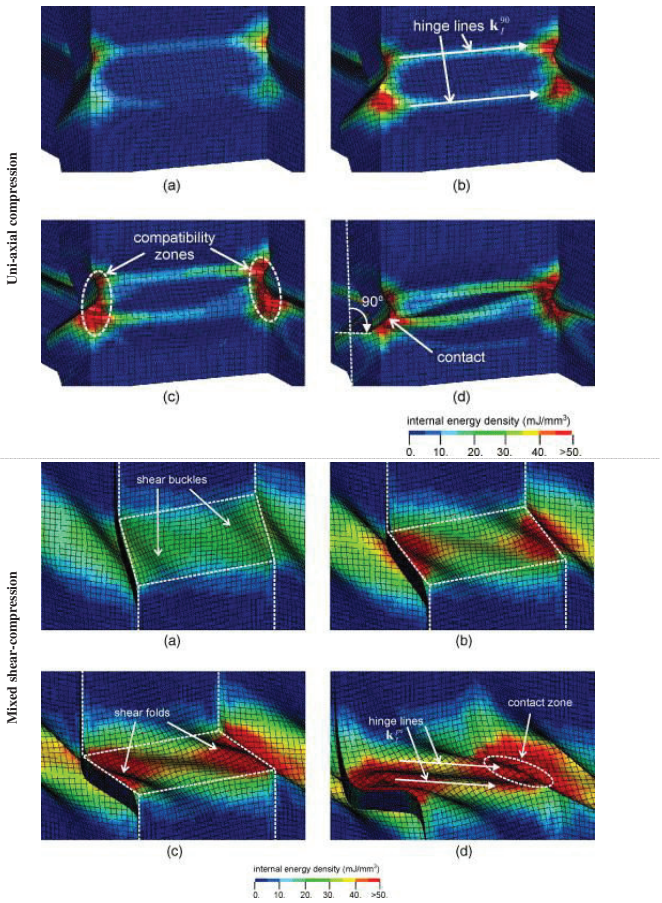

Figure 1.16: *The collapse mechanisms of honeycomb under quasi-static uni-axial compression and mixed shear-compression loadings. [Mohr 04a]*

The numerical simulations are performed only under quasi-static loading conditions, therefore, numerical simulation are required under dynamic loading to observe and analyse the effect on local collapse mechanisms. So that, Hou et al.[Hou 11b] have used the same simplified "row-model" in their simulations under both quasi-static and dynamic loadings. The same cell geometry and dimensions of the hexagonal aluminium 5052 honeycomb specimen used in their experiments are applied. Under dynamic loading, the specimen is placed between two rigid planes which are moved using the experimental input and output bars velocities (denoted as Vinput and Voutput in figure 1.17). Under quasi-static loading, one rigid plane is fixed and the second is moved with the loading velocity of 0.1 mm/s. Automatic mass scaling technique is used to overcome the difficulty of the enormous computing calculation time.

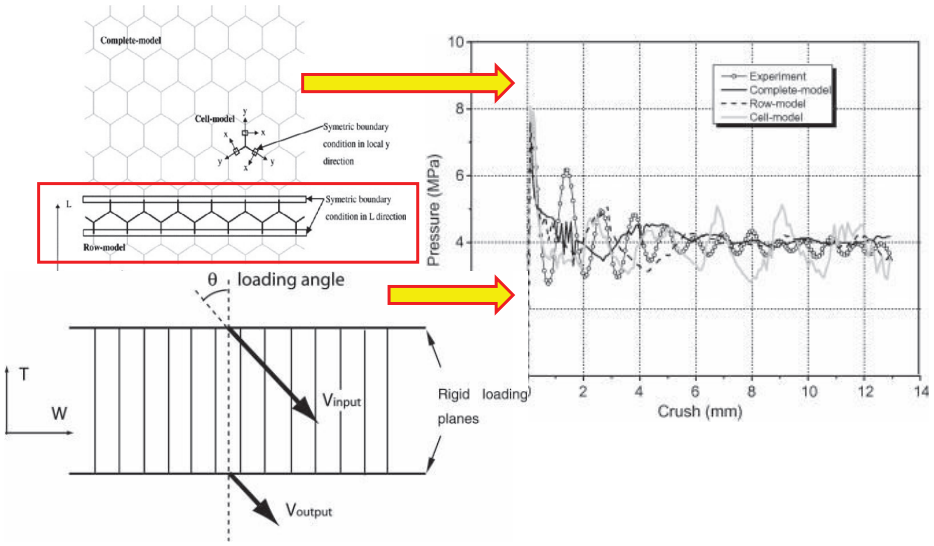

Figure 1.17: *The virtual honeycomb specimen, the simplified FEM models, the boundary conditions and the pressure-crush curve under mixed shear-compression loading. [Hou 11b]*

Under uni-axial compression loading, the accuracy of this simplified model is verified by comparing its crushing response to a complete detailed model and the experimental responses (figure 1.17). So that, the simplified "row-model" is used under mixed shear-compression loading in their simulations with various loading angle ψ but for only one in-plane orientation angle $\beta = 90°$.

Under mixed shear-compression loading, an experimental validation is realised in the crushing responses focusing on the initial peak pressure and

the average crushing pressure. Figure 1.18 shows a good correlation between experimental and numerical results under both quasi-static and dynamic loadings with a fixed in-plane orientation angle $\beta = 90°$.

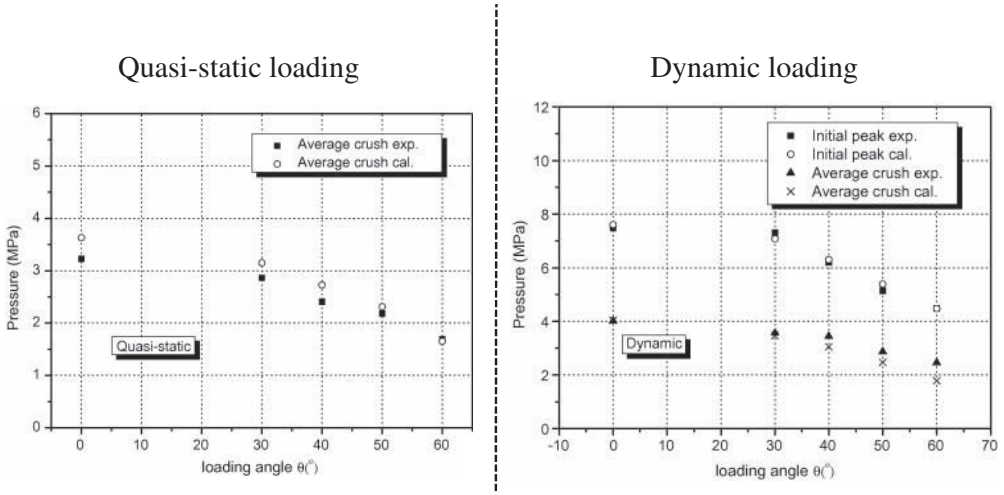

Figure 1.18: *Comparison between the experimental results and the numerical ones under quasi-static and dynamic biaxial loading. [Hou 11b]*

An experimental validation is also performed concerning the collapse mechanisms. The two co-existing pattern modes observed experimentally are verified during their simulations (figure 1.19). The folding mechanisms including the inclined plastic hinge lines are observed numerically for each loading angle ψ and they are in a good agreement with the experimental mechanisms.

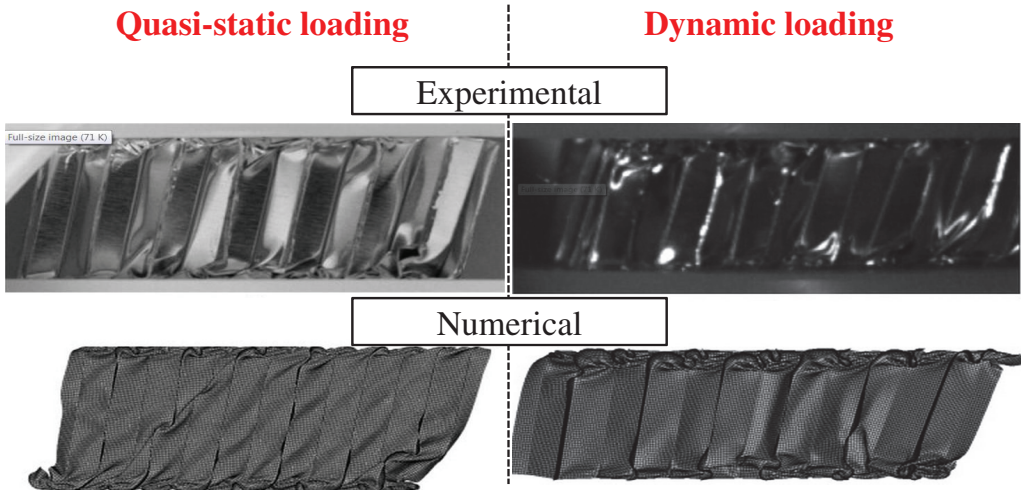

Figure 1.19: *The comparison between the experimental collapse mechanisms and the numerical ones under quasi-static and dynamic mixed shear-compression loading. [Hou 11b]*

1.4 Macroscopic yield criterion

To model the behaviour of honeycombs in large structural crashworthiness FEA, a macroscopic constitutive law is required to be implemented into a solid FE (3D) with a reasonable CPU-time consuming. For that, a macroscopic yield criterion that gives a good description of honeycomb behaviour under realistic (mixed shear-compression) loading conditions is needed.

1.4.1 Description of the macroscopic yield criterion for honeycomb structure

The aluminium honeycomb structures are orthotropic and they are characterised by three symmetry planes due to the manufacturing process. Here, we briefly present the development of a macroscopic yield criterion proposed by Hong et al. [Hong 06a] for the aluminium honeycomb under mixed shear-compression loading. Their criterion takes the in-plane orientation angle into account.

The macroscopic yield behaviour of incompressible orthotropic materials is described by Hill's quadratic yield criterion [Hill 50]:

$$F(\sigma_{22}-\sigma_{33})^2+G(\sigma_{33}-\sigma_{11})^2+H(\sigma_{11}-\sigma_{22})^2+2L\sigma_{23}^2+2M\sigma_{31}^2+2N\sigma_{12}^2=\sigma_{ge}^2 \tag{1.1}$$

where F, G, H, L, M and N are material constants, which can be determined from experiments. Here, σ_{11}, σ_{22} and σ_{33} are the normal stresses and σ_{23}, σ_{31} and σ_{12} are the shear stresses with respect to the material symmetry axes X1, X2 and X3 (figure 1.20). σ_{ge} represents the generalized effective stress.

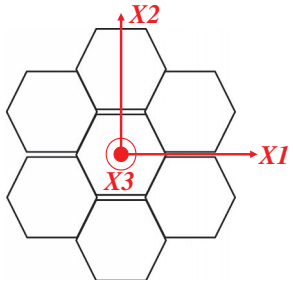

Figure 1.20: *The material symmetry axes on the regular hexagonal cell honeycomb structure*

Under mixed shear-compression when the loading conditions involve only mixed compressive and shear stresses ($\sigma_{11} = \sigma_{22} = \sigma_{12} = 0$), the Hill's yield criterion can be rewritten as :

$$\sigma_{33}^2 + F'\sigma_{32}^2 + G'\sigma_{31}^2 = H'\sigma_{ge}^2 \tag{1.2}$$

The equation 1.1 presents a yield criterion for orthotropic incompressible materials. But, aluminium honeycombs under realistic crash conditions are compressible. Only one normal stress is involved in the experiment. The only normal stress σ_{33} in equation 1.2 produces the normal strain ϵ_{33}. An assumed zero plastic poisson's ratio can give the plastic compressibility. In this context, the yield surface for aluminium honeycomb specimens is investigated when both the normal and shear loads reach the plateau. This definition of the yield surface seems reasonable since aluminium honeycombs are frequently modelled as rigid-plastic materials ([Harr 99] ; [Zhan 92]) and the main applications of aluminium honeycombs are as structural reinforcements and energy absorbers. Different definitions of the yield surface ([Doyo 03]; [Mohr 04a]; [Mohr 04c] and [Mohr 04b]) are possible depending on the objectives of the investigations. Therefore, the normal and shear stresses in equation 1.2 can be replaced by the normal crush strength and the appropriate shear strengths:

$$\sigma^2 + A\tau_{31}^2 + B\tau_{32}^2 = \sigma_{cr}^2 \tag{1.3}$$

where A and B are material constants. σ is the normal crush strength, τ_{31} and τ_{32} are the shear strengths with respect to the material symmetry axes and σ_{cr} is the normal crush strength under uni-axial compression loading determined by experimental results. For a given in-plane orientation angle β , the shear crush strength τ can be decomposed into τ_{31} and τ_{32} with respect to the material symmetry axes. So, equation 1.3 can be rewritten by:

$$\sigma^2 + (A\cos^2(\beta) + B\sin^2(\beta))\tau^2 = \sigma_{cr}^2 \tag{1.4}$$

The normalized form of the equation 1.4 becomes :

$$(\frac{\sigma}{\sigma_{cr}})^2 + (A\cos^2(\beta) + B\sin^2(\beta))(\frac{\tau}{\sigma_{cr}})^2 = 1 \tag{1.5}$$

For a given β angle, equation 1.5 represents a quadratic curve in the

normalized τ-σ plane that defines the macroscopic yield criterion of the aluminium honeycomb under mixed shear-compression loading taking into account the in-plane orientation angle β.

1.4.2 Application of the macroscopic yield criterion for honeycomb structure

In this section, a selection of the main works dealing with the identification of a macroscopic yield criterion for the honeycomb behaviour under mixed shear-compression loading is listed.

In 2004, based on the analysis of numerical simulations realised by Mohr and Doyoyo [Mohr 04a], an elliptic macroscopic plastic collapse envelope corresponding to the initial peak is evaluated and defined by this equation:

$$(\frac{\tau}{\tau^0})^2 + (\frac{\sigma}{\sigma^0})^2 = 1 \tag{1.6}$$

where τ^0 is the macroscopic yield stress under pure shear loading and σ^0 is the macroscopic yield stress under uni-axial compression loading.

When the crushing regime is activated, a linear crushing envelope that defines the post-collapse behaviour is described by the equation :

$$(\frac{|\bar{\tau}|}{\bar{\tau^0}}) + (\frac{\bar{\sigma}}{\bar{\sigma^0}}) = 1 \tag{1.7}$$

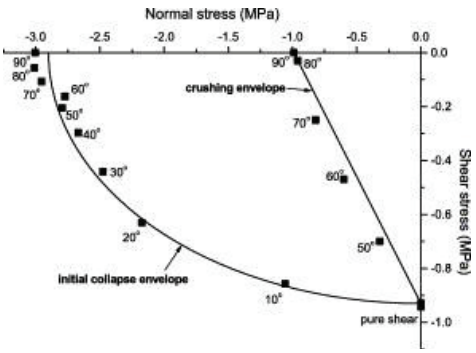

Figure 1.21: *The macroscopic yield criterion of honeycomb under quasi-static mixed shear-compression loading based on the numerical results. [Mohr 04a]*

The macroscopic yield criterion defined by the equations 1.6 and 1.7 is presented (figure 1.21).

Their macroscopic yield criterion shows that when the loading angle decreases, the average crushing force (crushing envelope) decreases linearly and the initial peak force (initial collapse envelope) decreases elliptically.

In 2006-2008, Hong et al. [Hong 06a] and [Hong 08] proposed a macroscopic yield criterion under quasi-static mixed shear-compression loading based on an elliptical crushing envelope. This criterion taking into account the in-plane orientation angle is based on the equation 1.5.

Under dynamic loading, this yield criterion is generalized as :

$$(\frac{\sigma}{\sigma_{crd}(V_{Imp})})^2 + (A_d(V_{Imp})\cos^2(\beta) + B_d(V_{Imp})\sin^2(\beta))(\frac{\tau}{\sigma_{crd}(V_{Imp})})^2 = 1 \tag{1.8}$$

where the material constants $A_d(V_{Imp})$ and $B_d(V_{Imp})$ are functions of the impact velocity V_{Imp}. $\sigma_{crd}(V_{Imp})$ represents the crush strength of honeycomb specimens under dynamic uni-axial compression loading.

Their experimental works show that the effect of the in-plane orientation angle under quasi-static and dynamic is very significant on the curvature of the criterion, the curvature of the yield surface decreases when the in-plane orientation angle β increases. This means that the energy absorption performance decreases with the increases of the in-plane orientation angle (figure 1.22).

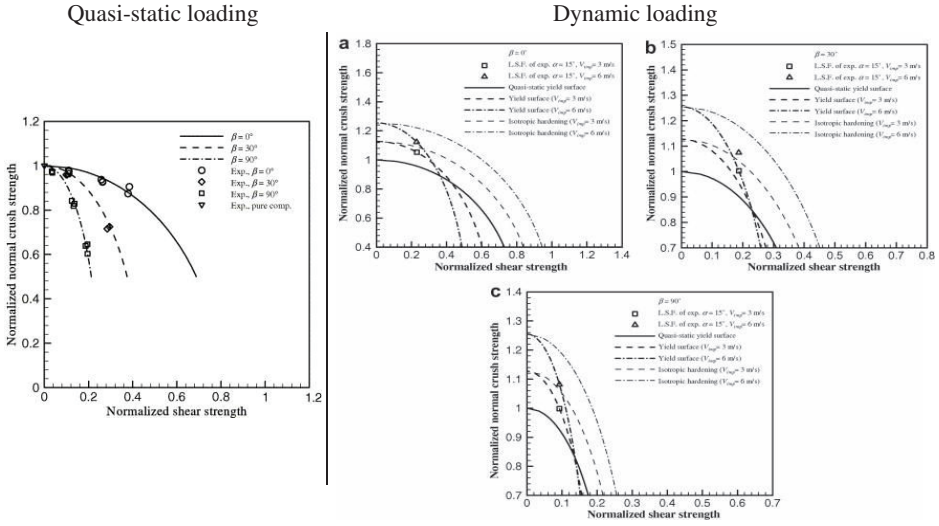

Figure 1.22: *The macroscopic yield criterion under quasi-static and dynamic mixed shear-compression loading. [Hong 06a] and [Hong 08]*

Recently, a macroscopic yield criterion on the aluminium honeycomb behaviour was proposed by Hou et al. [Hou 11, Hou 11a, Hou 11b]. It is based on a numerical study using a detailed FEM model for honeycomb specimen crushed under quasi-static and dynamic mixed shear-compression loadings. The numerical simulations allow to obtain the normal and the shear behaviours separately under mixed shear-compression loading and to identify the parameters of the macroscopic yield criterion.

The macroscopic yield criterion defined by the equation 1.4 is developed based on the normal average strength vs. shear average strength. The numerical simulations suggest an elliptical shape plotted for both the quasi-static and dynamic loading cases with various loading angle ψ (figure 1.23).

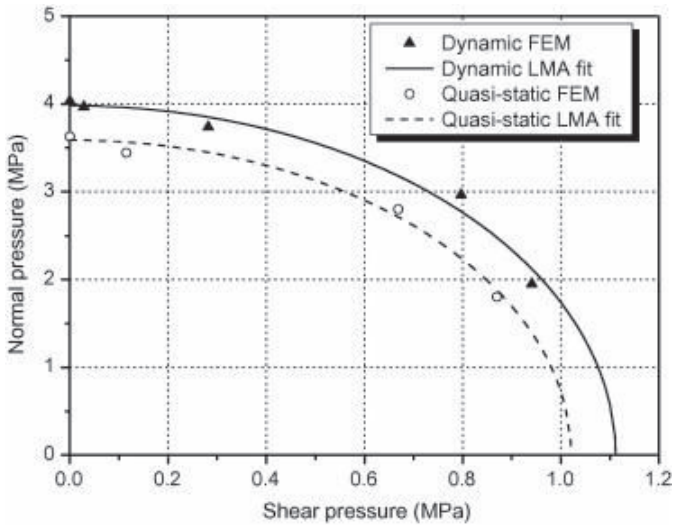

Figure 1.23: *The macroscopic yield criterion for aluminium honeycombs under quasi-static and dynamic mixed shear-compression loading. [Hou 11b]*

This macroscopic yield criterion suggests that the expansion of the elliptical crushing envelope is isotropic from the quasi-static loading to the dynamic loading. Indeed, the dynamic enhancement was observed independently of the in-plane orientation angle β.

More recently, Zhou et al. [Zhou 12] presented the macroscopic yield criterion in figure 1.24 for the Nomex honeycomb based on quasi-static experimental results and described by the equation 1.8.

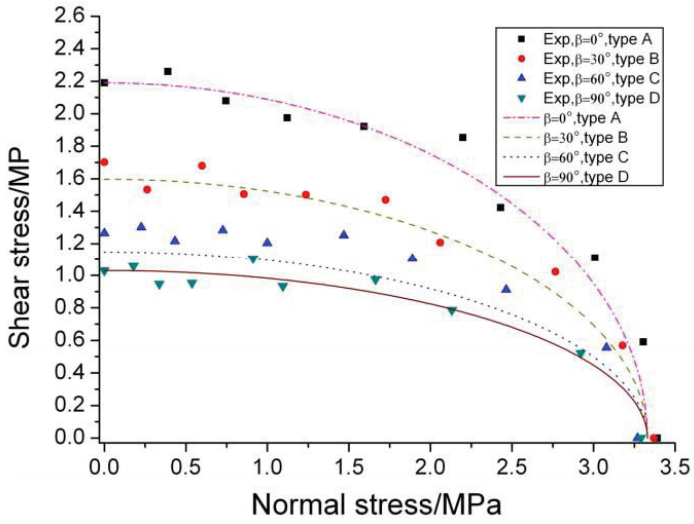

Figure 1.24: *The macroscopic yield criterion for the Nomex honeycombs taking into account the effect of the in-plane orientation angle. [Zhou 12]*

This macroscopic yield criterion indicates that the in-plane orientation angle β has a significant effect but only quasi-static loading was investigated.

Finally, some works have suggested that the in-plane orientation angle has a significant effect on the macroscopic yield criterion, other works suggested no effect.

1.5 Summary of the literature study and conclusion

The mechanical behaviour of honeycombs under real working conditions loading is linked not only to the cellular structure geometry and constitutive material but also to the loading angle, the in-plane orientation angle and the impact velocity.

Table 1.1 summarises the experimental results reported in the literature taking the effects of the loading angle, the in-plane orientation angle and the impact velocity on the macroscopic yield criterion into account. This table 1.1 also indicates if the collapse mechanisms have been analysed and what kind of deforming modes was observed.

Table 1.1: *Previous works for honeycomb under mixed shear compression loading*

	Macroscopic Yield Criterion			Collapse mechanisms	
	ψ	β	V_{imp}	Mode I	Mode II
Mohr et al.(02/04)	Yes	No	No	Yes	No
Hong et al.(06/08)	No	Yes	Yes	Yes	No
Hou et al.(10/11)	Yes	No	Yes	Yes	Yes
Zhou et al.(12)	Yes	Yes	No	No	No

Under mixed loading, the different investigations on the in-plane orientation angle effect present a contradiction. Thus, it will be interesting to further study in depth the influence of this parameters (β) coupled with the effect of the loading angle (ψ) and the impact velocity (V_{imp}). This can be best analysed through combination of dedicated experimental campaign and subsequent computational simulations.

For numerical simulations, as found in the open literature, a virtual honeycomb specimen called 'cell-model' may be considered as a three conjoint half walls in "Y" configuration model. This configurations is however only valid for uni-axial compression loading. In their numerical study, Mohr and Doyoyo [Mohr 04a], as well as Hou et al.[Hou 11a] used a virtual honeycomb specimen called 'row-model' made up of a row of cells. Unfortunately, their model is only valid under combined shear-compression loading with a single in-plane orientation angle ($\beta = 90\ °$) and the influence of this angle β is consequently not investigated.

Table 1.2: *Existing simplified models.*

Existing simplified models	Boundary conditions	Uni-xial	Mixed	
		$\psi = 0°$	ψ	β
Cell model	Local symmetric BC's	Yes	No	No
Row model	Local symmetric BC's	Yes	Yes	No

The existing simplified finite element models in the open literature are summarized in table 1.2. These simplified models are unable to simulate correctly the mixed shear-compression behaviour by taking the in-plane orientation angle β into account.

As a conclusion, the honeycomb behaviour was extensively investigated under quasi-static and dynamic uni-axial compression loadings

Under mixed shear-compression loading, none of the published works have investigated in depth the combined effects of the loading angle ψ, the in-plane orientation angle β and the impact velocity V_{Imp} on the honeycomb crush behaviour. Moreover, concerning the β angle effect , contradictory conclusions appear in the literature.

To better understand the honeycomb crush behaviour under realistic conditions by combining experiments and numerical simulations (detailed and reduced models) and to propose a macroscopic yield criterion expressed as a function of (ψ, β and V_{Imp}) useful for structural crashworthiness FEA are the challenges that this PhD work proposes to take up.

- Chapter 2 -

Honeycomb behaviour under quasi-static and dynamic mixed shear-compression loading

Resume

This chapter presents the experimental techniques and methods used for the study of the mixed shear-compression honeycomb behaviour under quasi-static and dynamic loading conditions. An improvement of an existing experimental set-up is performed and a new measurement technique based on an electro optical extensometer is used to overcome a separation phenomenon between the input bar and the input beveled bar. Experimental results focus on the analysis of triple effect of the impact velocity (V_{imp}), the loading angle (ψ) and the in-plane orientation angle (β) on the crushing responses. The triple effect is investigated on the initial peak force and the average crushing force. A significant effect of the loading angle is reported. The influence of the in-plane orientation angle becomes more significant when the loading angle increases. Concerning the effect of the impact velocity, a dynamic enhancement is observed under mixed shear-compression loading for $\psi \leq 45°$. For $\psi = 60°$, the quasi-static responses are higher than the dynamic ones. It is explained through an investigation of collapse mechanisms. Three existing deforming pattern modes are identified and it is shown that their distribution is related to the coupled effect of the in-plane orientation angle and the loading angle.

2.1 Introduction

This chapter investigates in details the honeycomb behaviour under mixed shear-compression loading where three parameters are studied : the loading angle (ψ), the in-plane orientation angle (β) and the impact velocity (V_{imp}). Quasi-static and dynamic loadings are performed to quantify the velocity effect on crushing responses.

Based on the previous works developed by Hou et al.[Hou 11a, Hou 11b] for the experimental techniques, an improvement is suggested on the mixed shear-compression loading device in order to increase the accuracy of the experimental results. In the first part of this chapter, specimens preparation is presented. In the second part, the improved testing technique for the mixed shear-compression loading is presented to lead quasi-static and dynamic experiments. For that, numerical approach is developed to design the experimental set-up with objective to have a good accuracy of the results. After the FE validation of the set-up under dynamic conditions, the experiments using the SHPB set-up are carried out with an impact velocity close to real conditions ($V_{imp} = 15$ m/s). In the last part of the chapter, the experimental results are presented as function of the loading angle (ψ), the in-plane orientation (β) and the impact velocity. Results are analysed and discussed by investigating the parameters effects on the crushing responses and on the collapse mechanisms of the aluminium honeycomb structures.

2.2 Specimens and materials preparation

Hexagonal honeycomb specimens are extracted from Al5056-N-6.0-1/4-0.003 aluminium alloy commercial honeycomb sandwich panel core. The relative density (the ratio of the honeycomb density and the base material density) is $\rho^* = 3$ %. The cell wall width is D = 3.67 mm, the single cell wall thickness is t = 76 μm , the cell angle is $\alpha = 120°$ and the cell size is d = 6.35 mm (figures 2.1 and 2.2). It contains 39 complete cells on the honeycomb cross-section (figure 2.2). The specimen dimensions are $44 * 41 * 25$ mm in the directions of X, Y and Z respectively. The X and Y direction are the in-plane directions. The X is the ribbon direction and the Y is the width direction. The Z direction is the strongest direction of honeycomb structure used for energy absorption performances. It is defined by the out-of-plane direction.

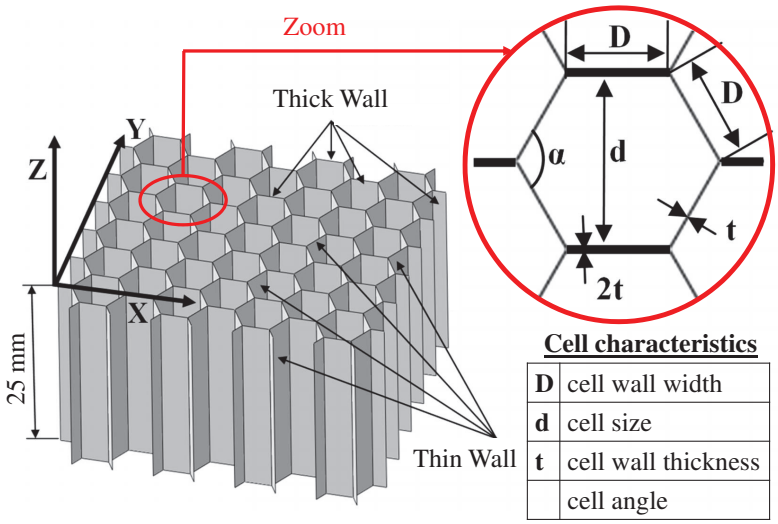

Figure 2.1: *The honeycomb specimen geometry and cell parameters*

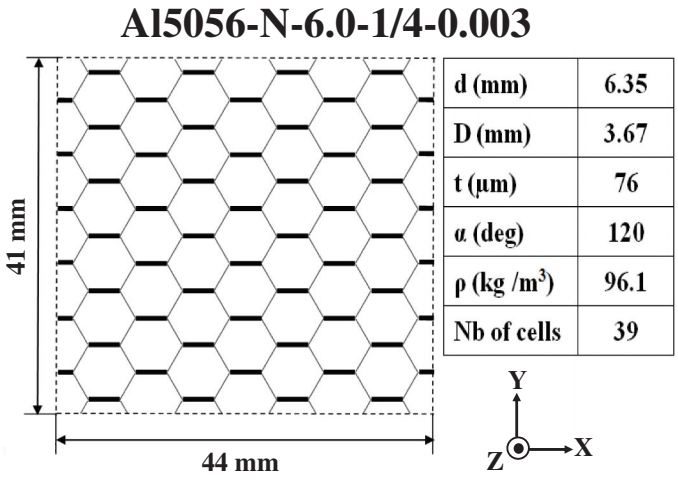

Figure 2.2: *The Al5056-N-6.0-1/4-0.003 honeycomb : geometry and cell parameters*

The specimen dimensions are chosen such that the specimen is a representative elementary volume as referred by Hou et al.[Hou 11a].

By changing the cutting direction of the specimens using a water-jet cutting system, the influence of the in-plane orientation angle using four different angles $\beta = 0°$, $\beta = 30°$, $\beta = 60°$ and $\beta = 90°$ can be studied (figure 2.3).

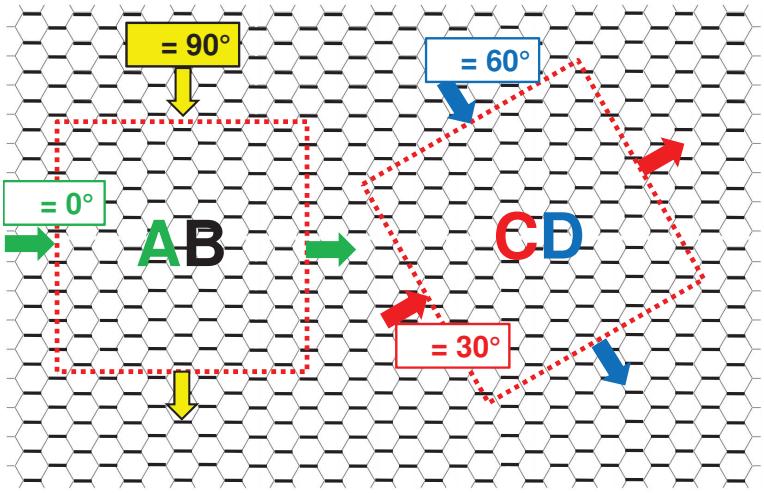

Figure 2.3: *Scheme of the in-plane orientation angles*

The two short beveled bars are machined so as to modify the loading angle from $\psi = 0°$ to $\psi = 60°$ (figure 2.4).

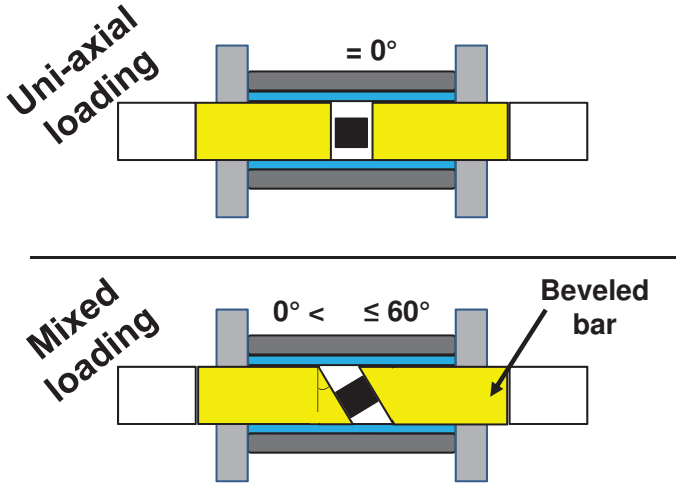

Figure 2.4: *Scheme of the loading angles*

The experimental programme is divided into 2 parts : The specimens are crushed with an impact velocity of 15 m/s for the dynamic experiments and with a loading velocity of 1 mm/min for the quasi-static experiments. This study investigates the dynamic enhancement behaviour by comparing the quasi-static and dynamic crushing responses under similar conditions.

2.3 Experimental techniques and methods

Based on a combined shear-compression device developed by Hou et al. [Hou 11a] introduced in SHPB system, numerical simulations are performed in order to analyse the whole testing system. Numerical results show an expansion at the Teflon sleeve during test. So that, a numerical study is carried out to limit the expansion phenomenon by increasing the sleeve stiffness. In addition, a separation phenomenon between the input bar and input beveled bar is observed numerically and during experiments. So as, an electro optical extensometer is used. Comparison between experimental and numerical elastic waves system shows that a correction is needed for the transmuted elastic wave under mixed loadings.

2.3.1 Mixed shear-compression device

A new combined shear-compression loading device was developed by Hou et al. [Hou 11a] and [Hou 11b] and introduced in the SHPB system in order to realise mixed loading experiments. It is based on two short beveled bars inclined with different angles in order to achieve five loading angles ψ from 0° to 60° with a step close to 15°. The device is positioned between two large diameter ($\emptyset$ = 60 mm) bars made of Pa66 with 3 m in length (figure 2.5).

The combined shear-compression loading device composed by two short cylindrical beveled bars made of the same material and diameter as the Hopkinson bars, a Teflon sleeve and two aluminium supports (figure 2.5). A Teflon sleeve with 20 mm of thickness ensures the alignment of the loading during the test. Two aluminium supports are used to guide the loading device in the SHBP set-up.

Each specimen is placed between the two beveled bars before the test with respect to the wave propagation principle along the device, so that reflections or disturbances must be limited as possible.

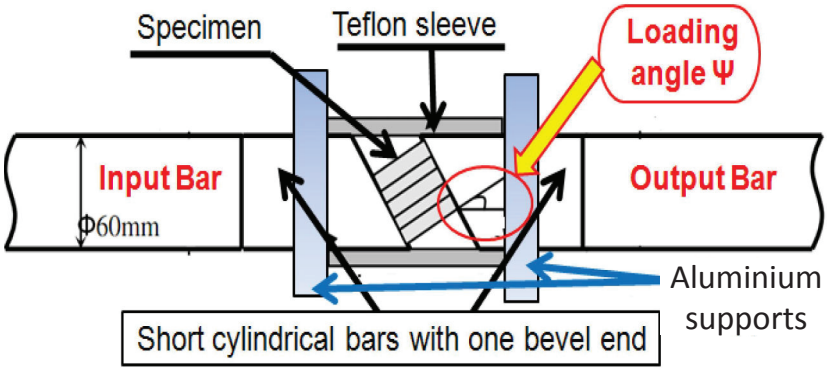

Figure 2.5: *Scheme of the combined shear-compression device. [Hou 11a]*

Same measurement method as classical Hopkinson testing is used based on the 3D-dimensional elastic wave theory. A numerical study of this device was performed. In all loading cases, especially in the most severe loading case (loading angle $\psi = 60°$), the two short beveled are no longer aligned during the test. An expansion in the Teflon sleeve and a misalignment of the two beveled bars are observed.

2.3.2 FE analysis of the whole testing system

2.3.2.1 FE model and details

Numerical simulations of the set specimen/beveled bars are carried out in order to observe the elastic waves system and its propagation along the set-up in function of time. In addition, optimal conditions are attended with respect to the stiffness of sleeves and the testing conditions. The influence of the two short beveled bars must be negligible during the loading of the specimen so as to accurately capture the mechanical responses of honeycomb.

A FE model of the whole testing system is realised. It is composed by a cylindrical projectile, incident bar (input) and transmitted bar (output). At the interface between the input and output bars, a combined shear-compression loading device is introduced (figure 2.5). The components of this device are as following :

- two short beveled bars,
- Teflon and steel sleeves,
- two metallic supports and
- the specimen.

The efficiency of the testing system is validated. The most severe case with loading angle $\psi = 60°$ is considered. The dimensions and materials properties of the FE model are similar to properties wished for the experimental device.

The ABAQUS/Explicit code is used to simulate numerically the experiments with the SHPB set-up. Elements with 8-node linear brick with reduced integration formulation (C3D8R) are used. The element size is 5 mm for the bars, the sleeves and supports, 3 mm for the bevels and 1.5 mm for the honeycomb specimen.

For the specimen, the constitutive behaviour is described as a crushable foam model [Hou 11a] (table 2.1).

Table 2.1: *Material properties of specimen honeycomb*

	Honeycomb
Density ρ (kg/m^3)	82.6
Young's Modulus E (MPa)	450
Poisson's Ratio ν	0.35
Plastic Poisson's Ratio ν_p	0
Yield Stress σ_s (MPa)	3.22
Lock Strain ε_{lock}	0.72

For the projectile, Hopkinson bars and beveled bars, a linear behaviour material with elastic properties of Nylon is used. For the Teflon sleeve, steel sleeve and supports, a linear behaviour material with elastic properties of Teflon, steel and aluminium respectively is also defined. All material properties are given in table 2.2.

Surface to surface contact is chosen between the interface of projectile/input Hopkinson bar and Hopkinson bars/beveled bars with frictionless contact conditions. At the interfaces between the specimen and the beveled bars, surface-to-surface contact with penalty contact method is applied. A Coulomb friction coefficient equal to 0.5 is given for these contact conditions. The penalty contact method is applied between the Steel sleeve, the Teflon sleeve and the Nylon bars with a friction coefficient equal to 0.05.

An impact velocity close to 15 m/s is applied to the projectile in the axial (Z) direction. It is chosen to be in accordance with results given by Hou et al.[Hou 11a, Hou 11b]. The bottom surface of the two supports is restricted on three translational displacements that correspond to the realistic boundary loading conditions. Two elements located on the external

Table 2.2: *The material properties of Nylon, Teflon, Steel and Aluminium*

	Density ρ (kg/m^3)	Young's Modulus E (MPa)	Poisson's Ratio ν
Nylon	1120	3370	0.3
Teflon	2200	1500	0.46
Steel	7800	210000	0.295
Aluminium	2700	70000	0.35

surface of the input and output bars corresponding to the positions of strain gages are chosen. The first gage is placed at mid length of the input bar and the second is placed at 0.4 m of the output bar to avoid any superposition of the elastic waves system (figure 2.10).

2.3.2.2 Improvement of the testing device

Under mixed shear-compression loading with $\psi = 60°$ (the most severe case of mixed loading), numerical simulations investigating a Teflon sleeve with 20 mm of thickness (Hou et al.[Hou 11a, Hou 11b]) show an expansion of 2 mm at the window zone and $\simeq$ 1 mm at the top of sleeve (figure 2.6-(a)). This is due to the shear load component. For that, a stiffens steel sleeve is proposed in order to limit the expansion. Numerical tests suggest that a thickness of 5 mm of Teflon sleeve and 10 mm of Steel sleeve limit the expansion phenomenon and ensure a good alignment during the test such as presented in figure 2.6-(b).

The comparison between the results is presented by table 2.3.

Table 2.3: *Stiffness improvement of the sleeves under mixed loading with ψ = 60°*

	Teflon (20 mm) sleeve	Teflon + Steel (5 mm)+(10 mm) sleeves
Expansion (mm) at the top	0.95	**0.07**
Expansion (mm) at the window zone	2	**0.13**

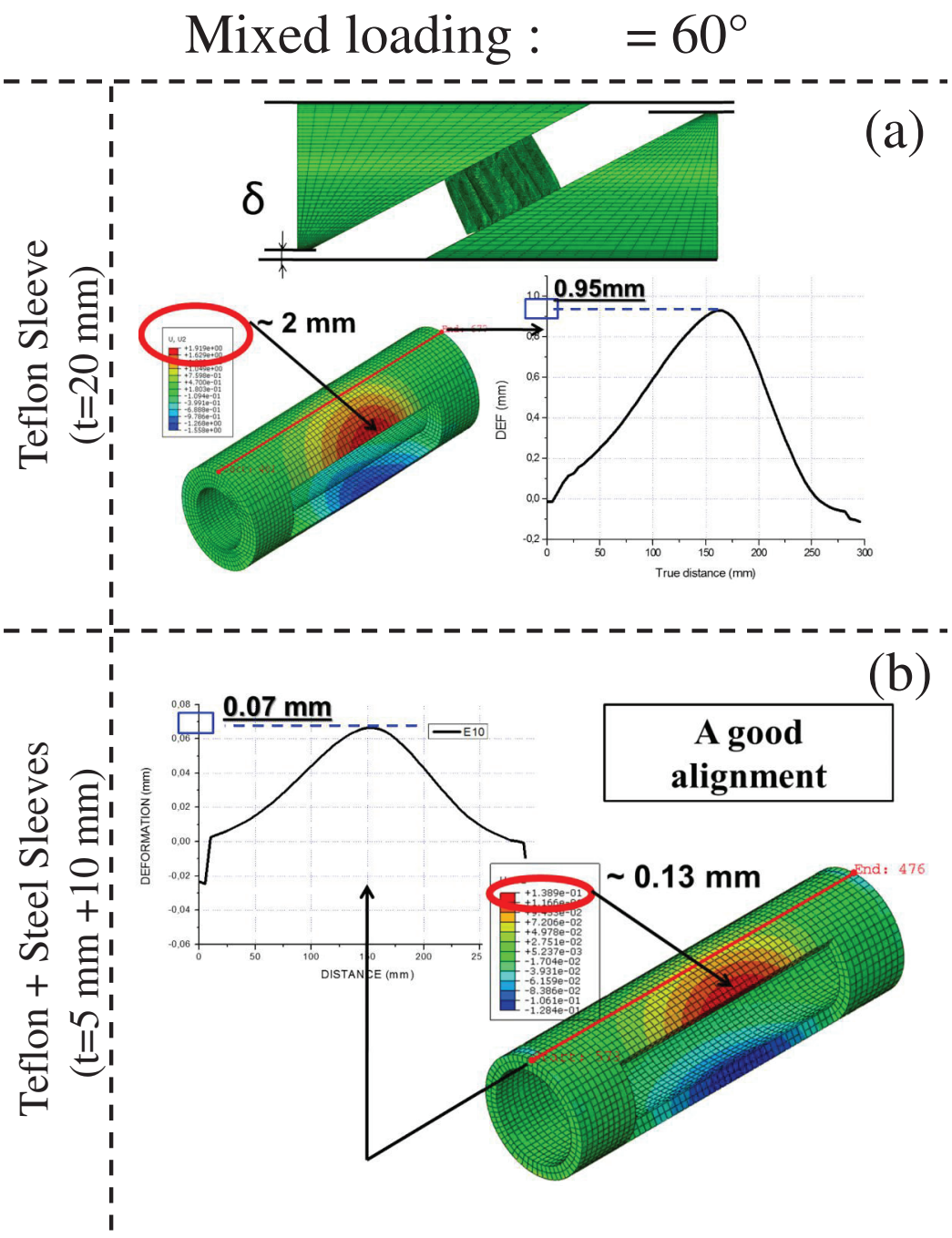

Figure 2.6: *Improvement of the testing conditions*

2.3.2.3 Analysis and improvement of the data processing

In order to verify the data processing, the FE numerical elastic pulses under uni-axial compression loading with beveled **(WB)** and without beveled are analysed.

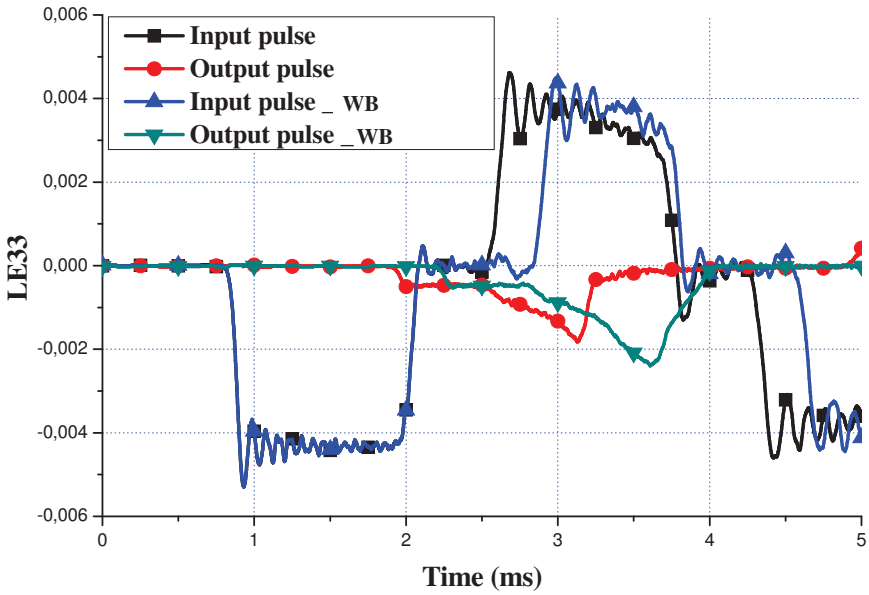

Figure 2.7: *The input and output pulses with beveled **(WB)** and without beveled bars under uni-axial loading $\psi = 0°$*

Figure 2.7 displays the beveled bars effect on the elastic pluses. The reflected wave obtained by the set-up with beveled bars shows a shorter duration time compared to the reflected wave given by the set-up without beveled bars. Longer transmitted wave is observed by the set-up with beveled bars. This can be explain by the output beveled bar that continues to push the output Hopkinson bar.

Figure 2.8 shows that a separation phenomenon between the input bar and the input beveled bar appears. This phenomenon has an effect on the reflected elastic wave and causes the cutting of this elastic wave. To overcome this limitation, an electro optical extensometer is used during experiments in order to focus the measurement near the specimen and not by using the strain gage signals (figure 2.9).

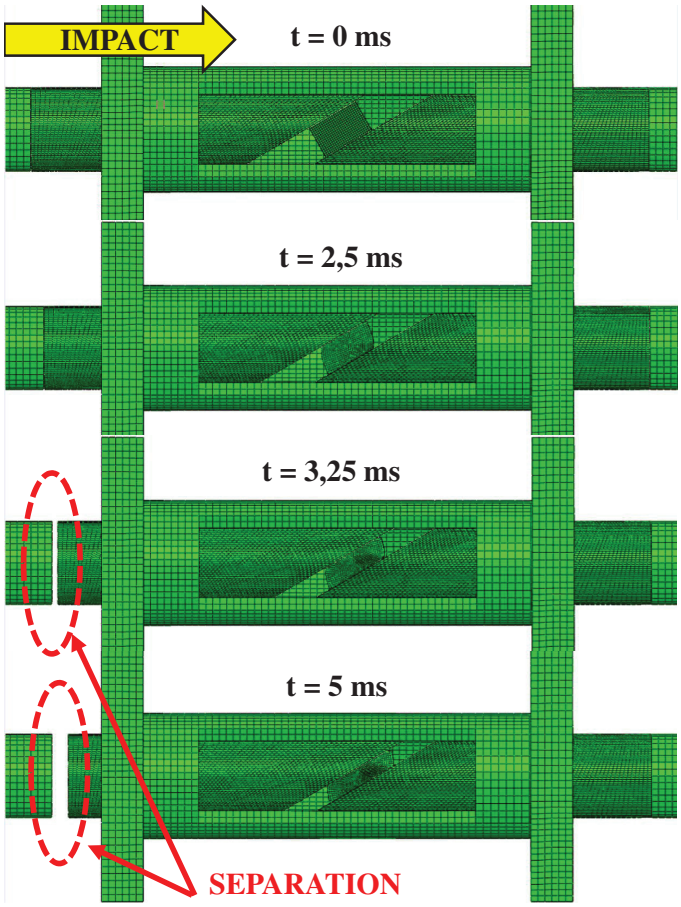

Figure 2.8: *The separation phenomenon under mixed loading $\psi = 60°$*

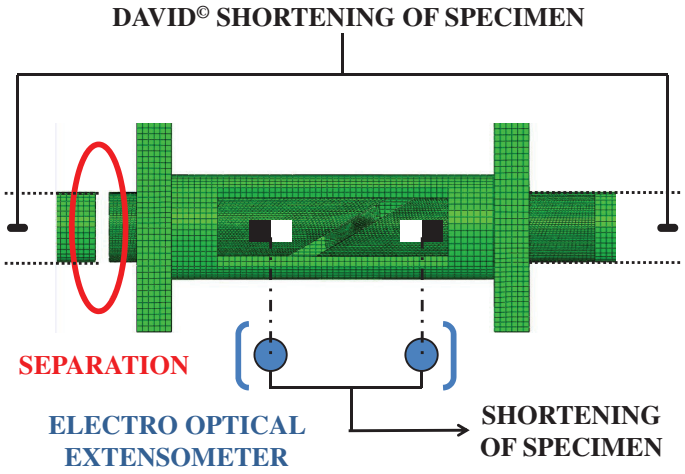

Figure 2.9: *The improvement of the shortening measurement using an electro optical extensometer under mixed loading $\psi = 60°$*

2.3.3 Experimental set-up

The improved mixed shear-compression device was manufactured and introduced into a Pa66 SHPB set-up composed by two bars of 3 m in length and a striker (1 m), all with a diameter of 60 mm (figure 2.10). The gages positions are similar to than of the FE model conditions. Strain gages are used to detect the three elastic waves after ampli-conditioning process (Vishay 2210B) and recorded using a numerical oscilloscope. An electro optical extensometer (Rudolph XR 200) is used to complete the data needed to compute the output force [Toun 12].

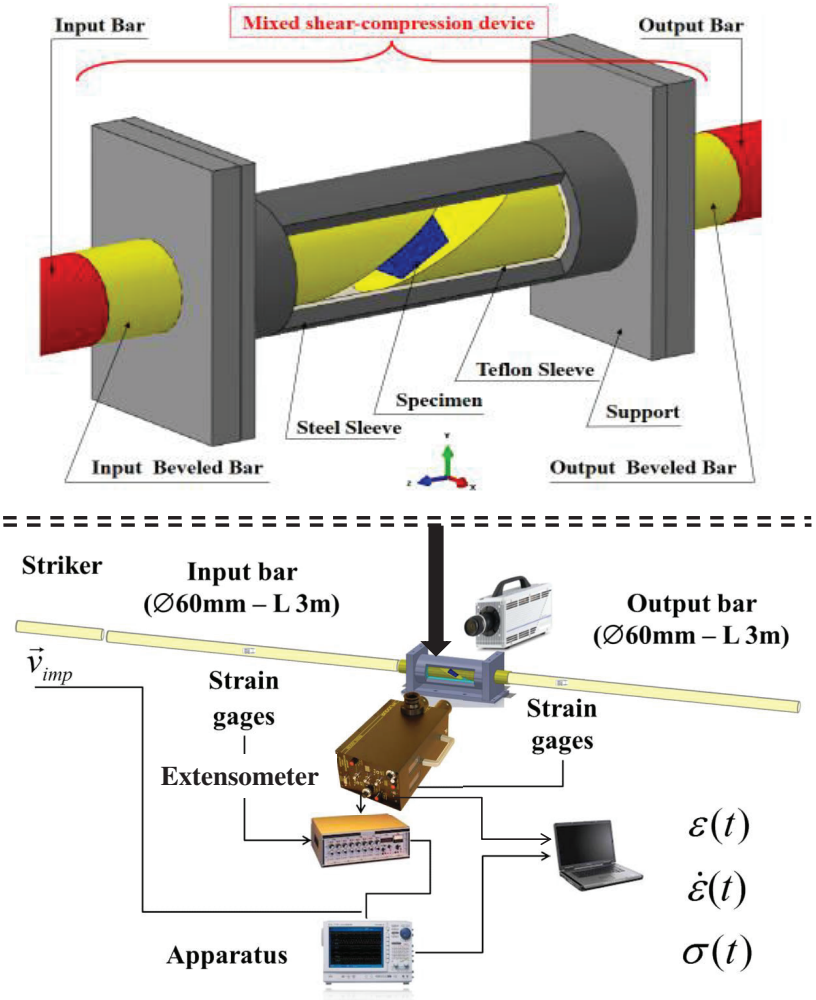

Figure 2.10: *Scheme of the combined shear-compression device and the details of SHPB*

A projectile launched by a gas gun strikes the free end of the input bar. A compressive longitudinal incident wave ε_i(t) is generated in the input bar just after the impact with the striker. Once this wave reaches the bar/specimen interface, a part of it called ε_r(t) is reflected, whereas an other elastic wave is generated through the specimen and develops as the transmitted wave ε_t(t) in the output bar.

Some assumptions should be respected such as the 3D-dimensional wave propagation theory, the inertia effect and the neglected friction between the specimen and the ends of bars. Based on the three elastic waves, the input and output forces and velocities can be calculated directly by the following equations:

$$F_{input}(t) = A_{IB}E_{IB}(\varepsilon_i(t) + \varepsilon_r(t)) \tag{2.1}$$

$$F_{output}(t) = A_{OB}E_{OB}\varepsilon_t(t) \tag{2.2}$$

$$V_{input}(t) = C_{IB}(\varepsilon_i(t) - \varepsilon_r(t)) \tag{2.3}$$

$$V_{output}(t) = C_{OB}\varepsilon_t(t) \tag{2.4}$$

$$\delta(t) = \int_0^\tau V_{output}(t) - V_{input}(t)dt \tag{2.5}$$

where F_{input}(t), F_{output}(t), V_{input}(t), V_{output}(t) and δ(t) are forces, particle velocities on specimen/bar interfaces and the shortening of the crushed specimen in function of time. A_{IB} / E_{IB} and A_{OB} / E_{OB} are respectively the cross section area and Young's Modulus of the input and output bars. C_{IB} and C_{OB} are respectively the elastic wave speed in the input and output bars.

2.3.4 Analysis of beveled bars effects and validation of the whole testing system

2.3.4.1 Beveled bars effects

To verity FE numerical observations, a serie of experiments is performed in the uni-axial loading direction using only the SHBP set-up (input bar/specimen/output bar) and using the SHBP set-up with the loading device (input bar/input beveled bar/specimen/output beveled bar/output bar).

The influence of the beveled bars on the data calculations and the validation of the testing system are performed under both uni-axial

and mixed loadings. A comparative study between the numerical and experimental results is achieved based on the elastic waves system.

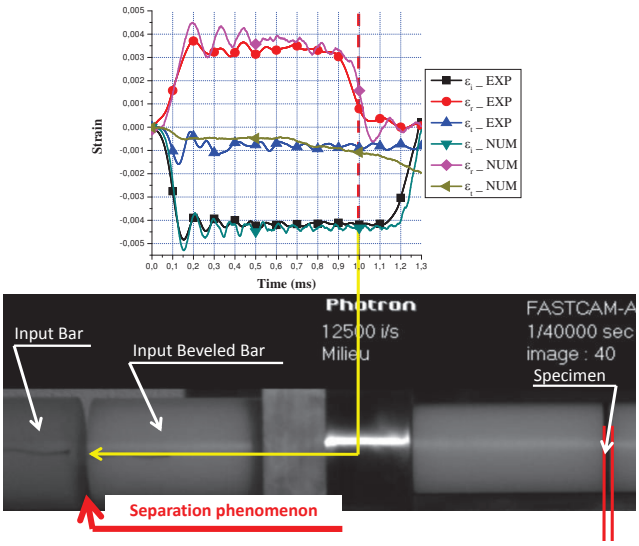

Figure 2.11: *The experimental and numerical elastic waves system and the beveled bars effects*

The loading device introduced in the SHPB set-up has the same effects highlighted in the numerical simulations on the three elastic waves system as shown in figure 2.11. The separation phenomenon of the input bar and the input short beveled bar is also confirmed during experimental tests (figures 2.11 and 2.12).

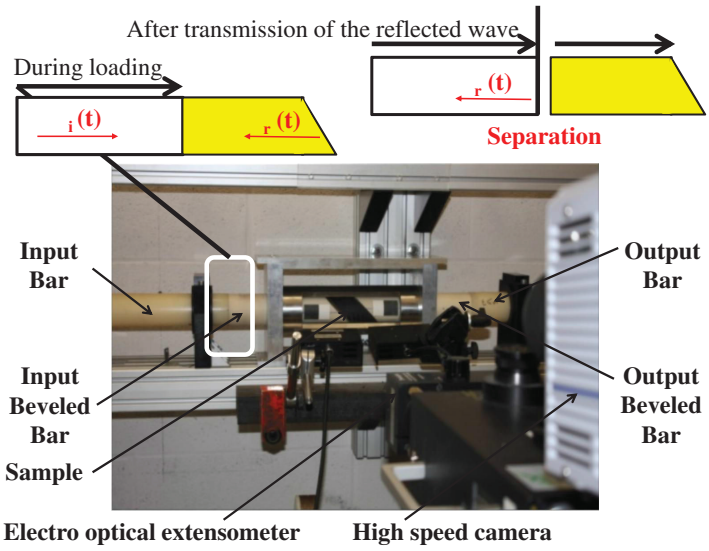

Figure 2.12: *Experimental testing conditions for honeycomb samples under dynamic loading*

It's leads to a restriction of the data measuring to compute the global force and velocity and a disequilibrium is generated due to the cut of the reflected wave. Indeed, this phenomenon is achieved by the transfer of energy from the input bar to the input beveled bar. Thus, the equilibrium of the forces can not be verified (figure 2.13). So that, the input displacement and the input force in the real duration of loading can not be calculated with respect to the governing equations used in the software David©. Therefore, a comparison between the input and output forces using the software David© and using the extensometer technique is presented in figure 2.13. The input force and the output force calculated by David© are limited to a specimen crushing of 10 mm. Although, more informations could be added when an electro optical extensometer technique is used.

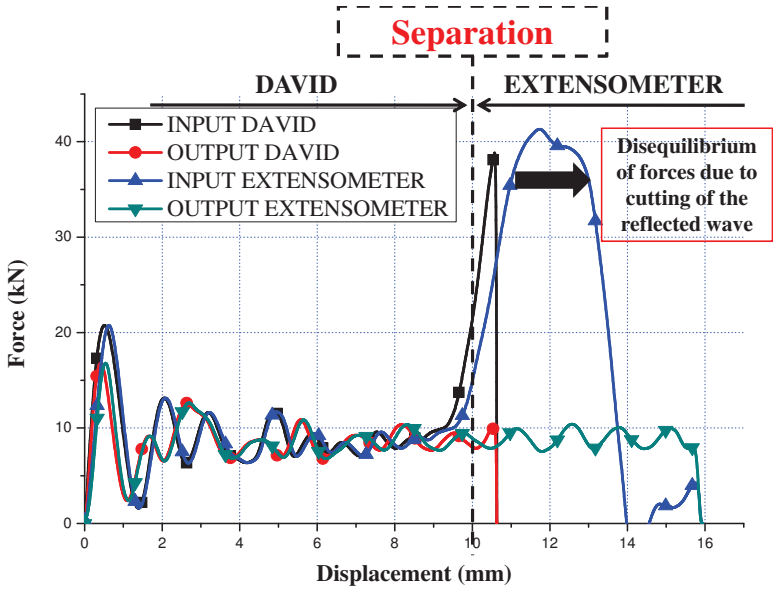

Figure 2.13: *Comparison between the input and the output forces using David© and the extensometer technique*

Due to the separation phenomenon between the input bar and input beveled bar and the cutting of the reflected elastic wave, the use of the input force is limited. Thus, the use of the output force is motivated and believed to be more accurate.

2.3.4.2 Validation of the whole testing system

The elastic pulses are analysed so as to present separately the elastic wave system (incident, reflected and transmitted) obtained numerically and experimentally.

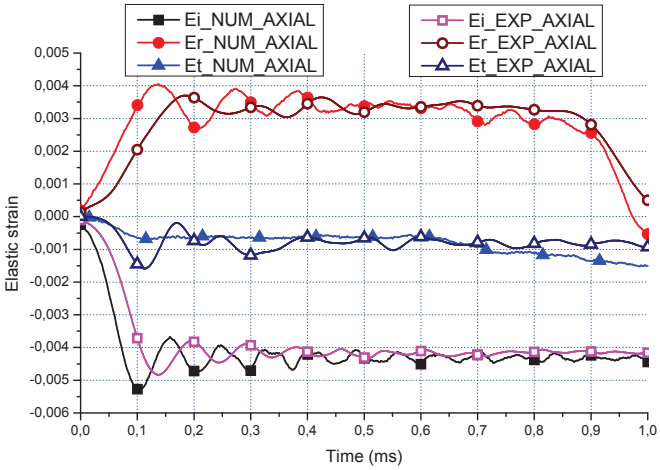

Figure 2.14: *The experimental and numerical three elastic waves under uni-axial loading $\psi = 0°$*

Under uni-axial loading ($\psi = 0°$), a good correlation between the numerical and experimental elastic waves is observed in figure 2.14. However, under mixed shear-compression with a loading angle $\psi = 60°$, a good agreement is verified for the incident elastic wave whereas a disagreement is observed for the elastic reflected and transmitted waves (figure 2.15).

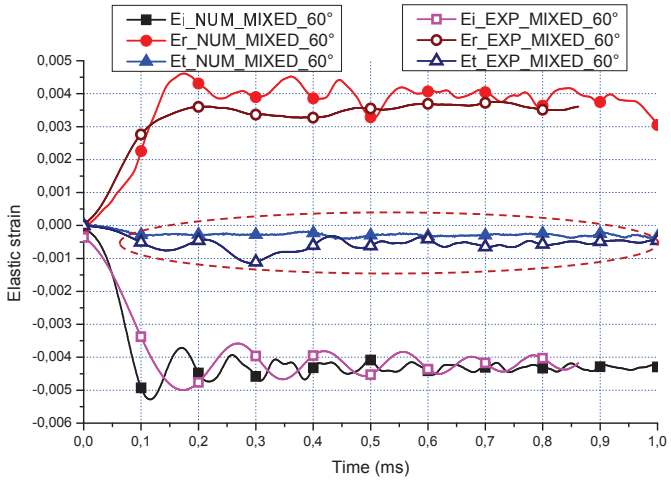

Figure 2.15: *The experimental and numerical three elastic waves under mixed loading $\psi = 60°$*

To understand the disagreement under mixed shear-compression loading, numerical and experimental studies are realized. For that, a piezoelectric cell load (measurement range : 30 kN) is introduced in the testing system and

data analysis are focused on three forces :

- F_{NUM} : the numerical output force,
- $F_{Cellload}$: the experimental cell load force and
- $F_{David©}$: the experimental David© output force.

Figure 2.16 presents a schematic of the experimental test realised which the output force is directly measured by the piezoelectric cell load and compared with the numerical output force and the output force extracted from the David© software. A good agreement between all the three forces is observed.

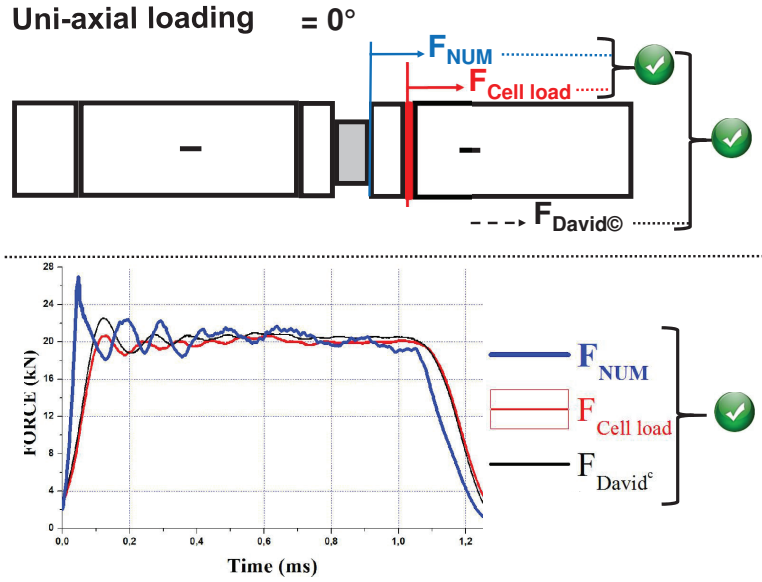

Figure 2.16: *Forces validation under uni-axial compression loading ($\psi = 0°$)*

In figure 2.17, the same test is used under mixed shear-compression loading with a loading angle ($\psi = 30°$).

A good correlation between the numerical output force and the experimental cell load force is observed. Whereas, a disagreement with the David© output force is observed. For that, numerical simulations and experiments with different loading angles are realized. The present testing conditions are not usually validated with respect to governing equations standards. Basically, David© software is developed for an accurate analysis under uni-axial loading regarding gage dimensions of samples. Then two calculations are done at the same time based on the linear momentum conservation and on the energy conservation. To ensure the conservation

process during the propagation of the elastic waves system, a transmission coefficient for each bar is determined.

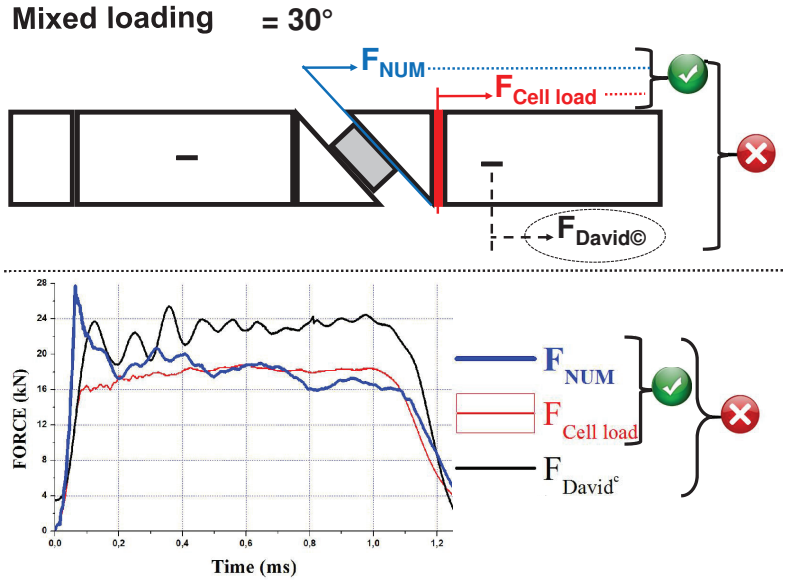

Figure 2.17: *Forces under mixed shear-compression loading ($\psi = 30°$)*

In the present mixed shear-compression loading conditions, a tangential force component (related to the loading angle ψ) is generated (figure 2.18) and leads to the no conservation of the energy balance. Thus, the transmission coefficient of the output bar is significantly modified.

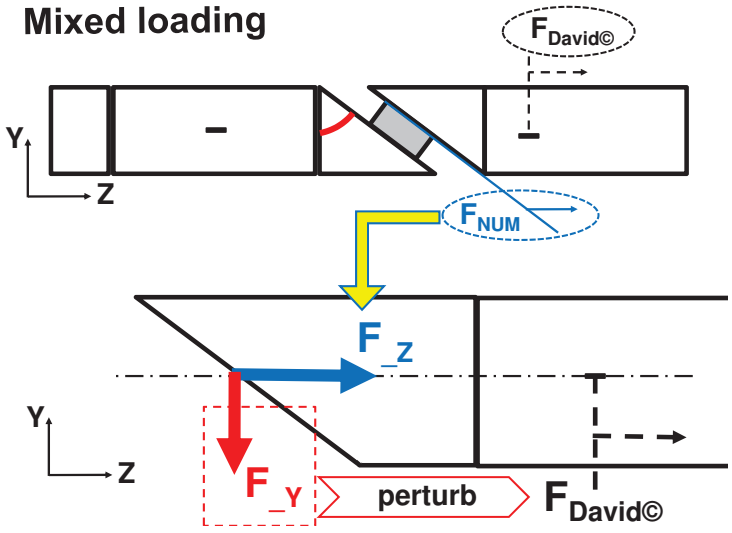

Figure 2.18: *Correction details of the David© output force under mixed shear-compression loading*

Based on the comparison between numerical and experimental results, a difference corresponding to $\cos(\psi)$ is observed for all cases of mixed loading. Thus, a good correlation between the forces can be reached by applying such a correction factor (figure 2.19).

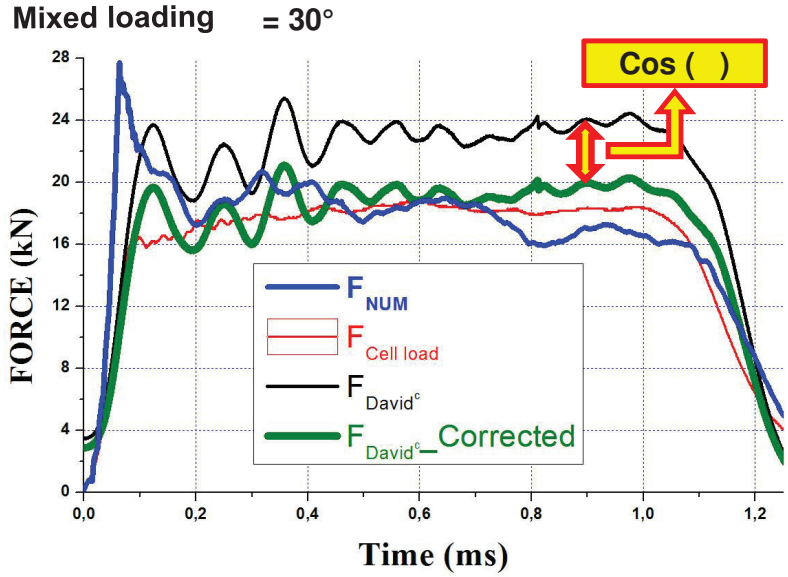

Figure 2.19: *Correction of the David© output force under mixed shear-compression loading for $\psi = 30°$*

Finally, for the experimental programme, three experimental tests per velocity are performed for each combination of loading. The average of the three force-displacement curves is calculated to present the mean crushing behaviour. For quasi-static and dynamic loadings, an electro optical extensometer is used to give the current displacement evolution. In addition, a high-speed camera and a CCD camera are triggered in function of the loading conditions to observe the collapse mechanisms.

2.4 Experimental results and analysis

In this section, the quasi-static and dynamic results of experiments are presented. The main objective is to investigate the combined effects of the loading angle ψ, the in-plane orientation angle β and the impact velocity V_{imp} on the initial peak force, the average crushing force and the collapse mechanisms.

2.4.1 Crushing responses

2.4.1.1 Reproducibility of the crushing responses

Due to the complexity of the experiments using the mixed shear-compression loading device in the SHPB set-up, the reproducibility must be verified. Three tests are performed for each loading configuration.

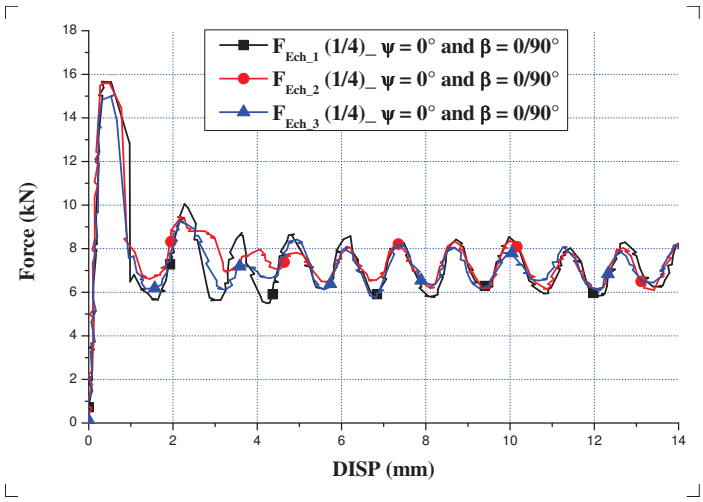

Figure 2.20: *Comparison between three experiments on honeycomb under* ***quasi-static*** *(V_T = 1 mm/min) uni-axial compression loading (ψ = 0°)*

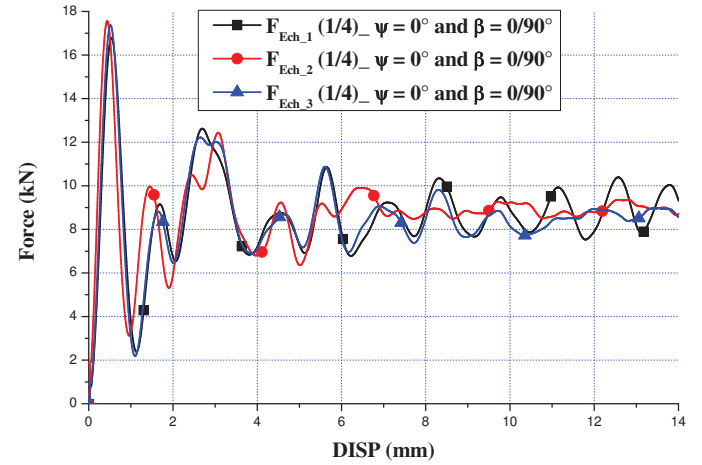

Figure 2.21: *Comparison between three impact experiments on honeycomb under* ***dynamic*** *(V_{imp} = 15 m/s) uni-axial compression loading (ψ = 0°)*

Figures 2.20 and 2.21 illustrate a good reproducibility of the force-displacement curves for $\psi = 0°$ under uni-axial quasi-static (1 mm/min) and dynamic (15 m/s) compression loading conditions.

Under mixed shear-compression loading, figures 2.22 and 2.23 show the force-displacement curves for a loading angle $\psi = 30°$ with $\beta = 30°$ under quasi-static and dynamic loadings. Once again, a good repeatability is verified.

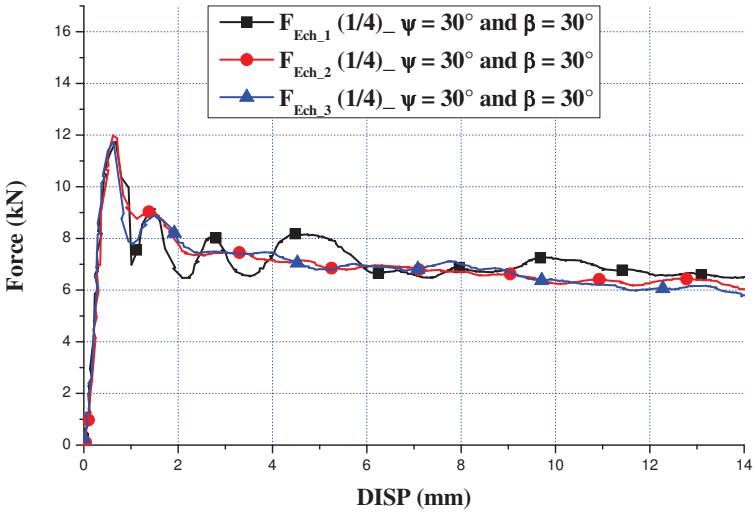

Figure 2.22: *Comparison between three experiments on honeycomb under* ***quasi-static*** *(V_T = 1 mm/min) mixed shear-compression loading ($\psi = 30°$ and $\beta = 30°$)*

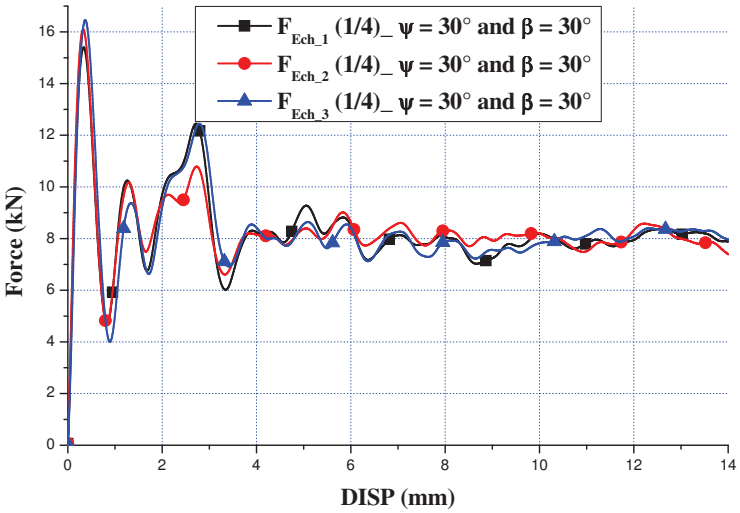

Figure 2.23: *Comparison between three impact experiments on honeycomb under* ***dynamic*** *(V_{imp} = 15 m/s) mixed shear-compression loading ($\psi = 30°$ and $\beta = 30°$)*

Finally, the average of the three force-displacement responses will be systematically calculated to present the mean crushing behaviour as given in figure 2.24.

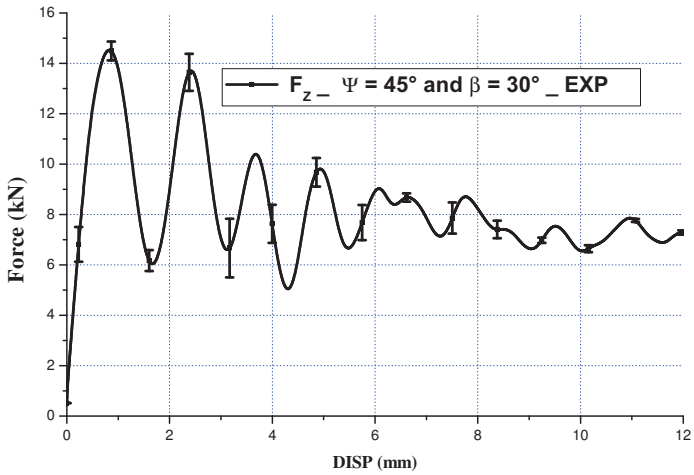

Figure 2.24: *The average crushing response of the three experiments and the highlight of standard deviation*

2.4.1.2 Analysis of the crushing responses

A typical response of honeycomb under uni-axial compression loading starts with an elastic part up to an initial peak which correspond to the localisation of the first plastic fold, then a serie of folding mechanisms characterises the average crushing force (plateau force).

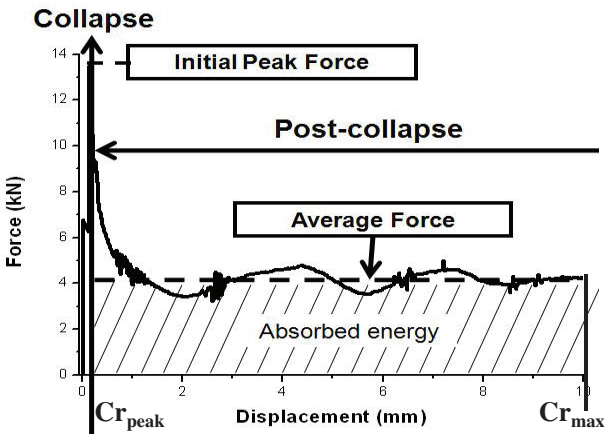

Figure 2.25: *The crushing Force-displacement response of honeycomb structure*

The plateau area informs about energy absorption performance. Densification stage at the end is developed as soon as all folds are developed (figure 2.25).

Further analyses are focused on the initial peak force and the average crushing force. The initial peak force F^{Peak} corresponds to the first maximum force value in the force-displacement curve such as shown in figure 2.25. The average crushing force $F^{Average}$ (figure 2.25) is defined by this following equation :

$$F^{Average} = \frac{1}{Cr_{max} - Cr_{peak}} \int_{Cr_{peak}}^{Cr_{max}} F(Cr)\mathrm{d}Cr \tag{2.6}$$

where Cr_{peak} is the crush value at the initial peak, Cr_{max} is the final crush value and F(Cr) is the axial force component (F_z).

The quasi-static and dynamic crushing experimental responses of the ***Al5056-N-6-1/4-0.003*** honeycomb behaviour are presented in the next sections.

2.4.1.3 Quasi-static crushing responses

The quasi-static experiments are performed using a " Sintech 20/D " tensile/compression machine with a speed loading equal to 1 mm/min (figure 2.26).

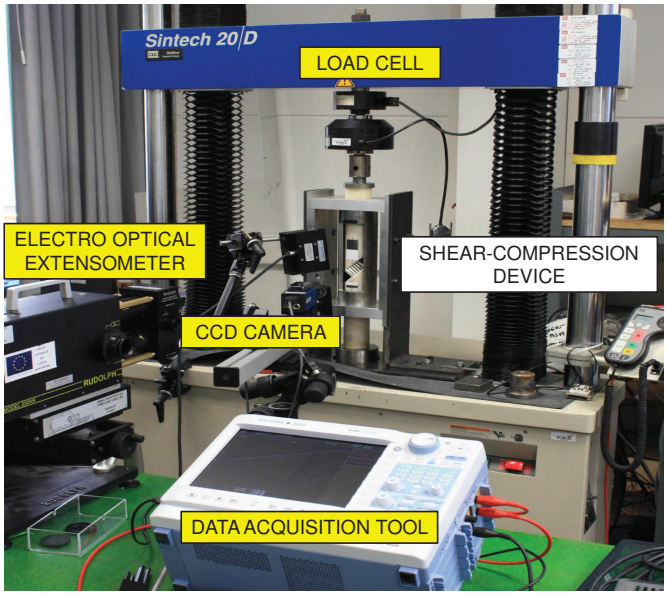

Figure 2.26: *The quasi-static set-up with the shear-compression loading device*

The force-displacement curves of aluminium honeycomb under uni-axial and mixed shear-compression loadings are presented. Five loading angles are investigated in this experimental study : $\psi = 0°$ correspond to uni-axial compression loading and $\psi = 15°$ / $\psi = 30°$ / $\psi = 45°$ / $\psi = 60°$ correspond to mixed shear-compression loadings.

For each loading angle ψ , the in-plane orientation angle β is modified. A set of four in-plane orientation angles ($\beta = 0° / 30° / 60° / 90°$) is investigated in this study. The in-plane orientation angle $\beta = 0°$ correspond to the shear load parallel to the double wall thickness, $\beta = 30°$ correspond to the shear load perpendicular to the single wall thickness, $\beta = 60°$ correspond to the shear load parallel to the single wall thickness and $\beta = 90°$ correspond to the shear load perpendicular to the double wall thickness as given in figure 2.27. The loading angle ψ effects is studied in the first step and the in-plane orientation angle β is studied in the second step.

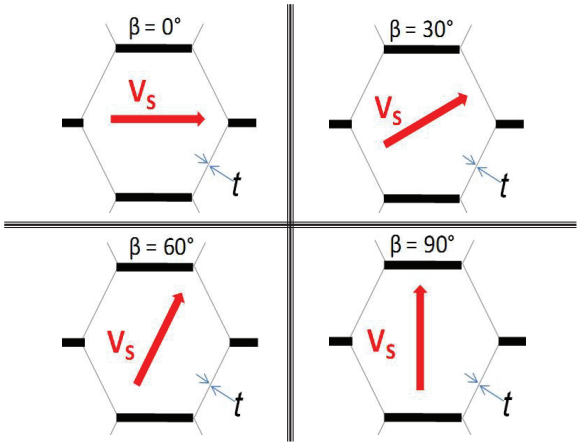

Figure 2.27: *The in-plane orientation angles ($\beta = 0° / 30° / 60° / 90°$)*

The loading angle ψ effects

The loading angle ψ effects on the quasi-static mixed shear-compression honeycomb behaviour is studied. For each in-plane orientation angle, the crushing responses are presented taking into account the loading angle ψ (figures 2.28 for $\beta = 0°$ and appendices A.1, A.2 and A.3 for the other β angle values).

For all in-plane orientation angles, the slope of the elastic part and the initial peak force decreases when the loading angle ψ increases. Moreover, when the loading angle ψ increases the level of the average crushing force decreases. Under uni-axial compression loading, the second stage is composed

by oscillations that correspond to the fold process.

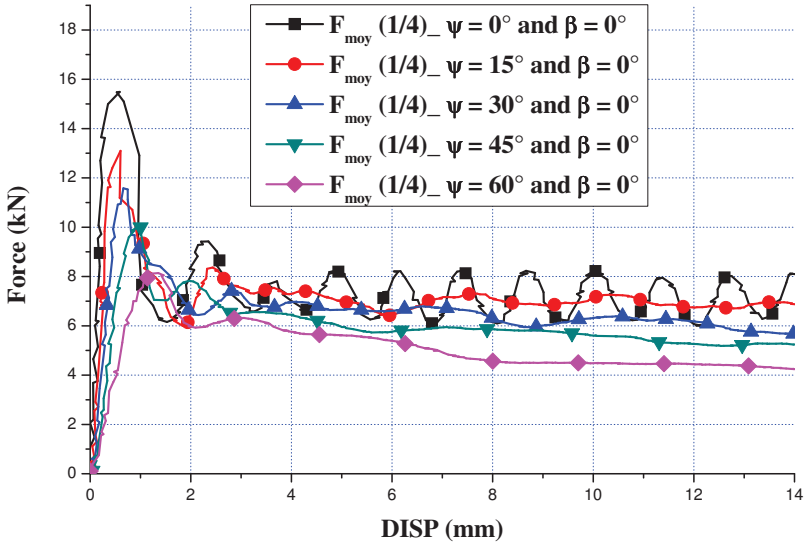

Figure 2.28: *The loading angle ψ effects under **quasi-static** mixed shear-compression loading for $\beta = 0°$*

Under mixed shear-compression loading, oscillations are disappeared progressively when the loading angle ψ increases. This phenomenon could be explain by the phase shift created by the loading angle ψ in the folding system progress.

The in-plane orientation angle effects β

The in-plane orientation angle β effects on the mixed shear-compression honeycomb behaviour is studied. The force-displacement curves are displayed for the each loading angle with four in-plane orientation angles under quasi-static loadings (figures 2.29 for $\psi = 30°$ and appendices A.4, A.5, and A.6 for the other ψ angle values).

For the mixed shear-compression loading, these force-displacement curves show that the influence of the in-plane orientation angle depends on the loading angle. The effects of the in-plane orientation becomes more pronounced on the initial peak for the loading angle $\psi \geqslant 45°$.

The in-plane orientation angle effects on the crushing force stage is very clear and could be explained by the difference on the collapse mechanisms and the deforming pattern modes listed in the section 2.4.3.

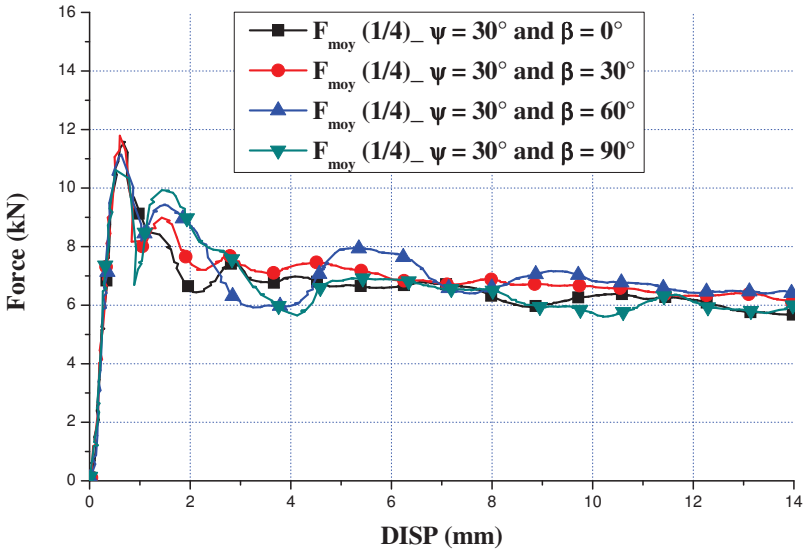

Figure 2.29: *The in-plane orientation angle β effects under* ***quasi-static*** *mixed shear-compression loading for $\psi = 30°$*

Based on the previous experimental results, the in-plane orientation angle as well as the loading angle effects are summarised in table 2.4 for the initial peak force and in table 2.5 for the average crushing force.

Table 2.4: ***Initial peak force*** *(kN) under quasi-static mixed shear-compression loading*

	$\beta = 0°$	$\beta = 30°$	$\beta = 60°$	$\beta = 90°$
$\psi = 0°$	15.52	15.52	15.52	15.52
$\psi = 15°$	13.13	13.38	12.98	12.72
$\psi = 30°$	11.60	11.82	11.15	10.83
$\psi = 45°$	10.04	9.78	9.40	9.48
$\psi = 60°$	8.15	7.23	6.68	6.46

Table 2.5: ***Average crushing force*** *(kN) under quasi-static mixed shear-compression loading*

	$\beta = 0°$	$\beta = 30°$	$\beta = 60°$	$\beta = 90°$
$\psi = 0°$	7.27	7.27	7.27	7.27
$\psi = 15°$	7.15	7.03	7.18	7.09
$\psi = 30°$	6.51	6.65	6.43	6.50
$\psi = 45°$	5.14	5.43	5.77	5.29
$\psi = 60°$	3.70	4.04	3.63	3.57

2.4.1.4 Dynamic crushing responses

The dynamic experiments are performed using the shear-compression loading device introduced in the SHPB set-up with an impact velocity equal to 15 m/s (figure 2.30 and 2.31).

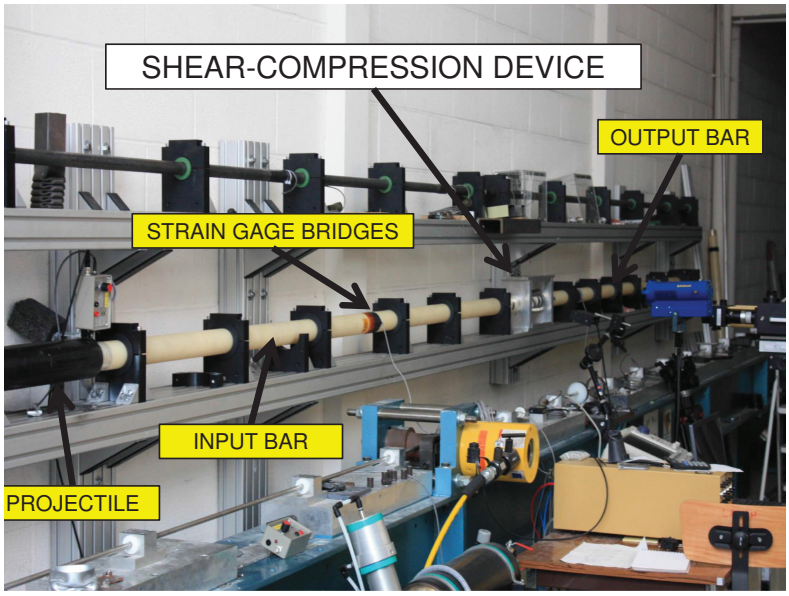

Figure 2.30: *The SHPB dynamic set-up with the shear-compression loading device*

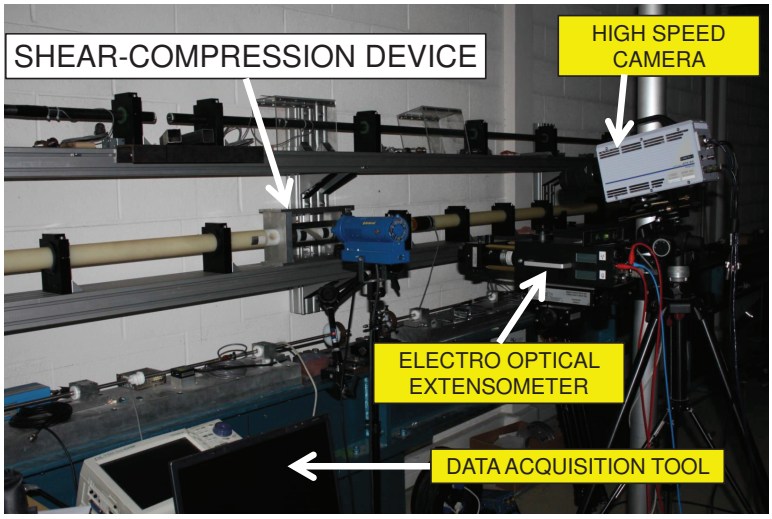

Figure 2.31: *The measurement technique tools for data processing under dynamic loading*

The same loading configurations than the quasi-static experiments are investigated in this study. But under dynamic loading conditions, the densification stage is not presented due to the limitation of the data processing using the SHPB technique related to the loading duration. So, all force-displacement curves are plotted at 14 mm of crushing displacement to be in accordance with the quasi-static results.

The loading angle ψ effects

Figures A.7,A.8, A.9 and 2.32 present the effect of the loading angle ψ on the mixed shear-compression honeycomb behaviour for the aluminium ***Al5056-N-6-1/4-0.003*** honeycomb specimen.

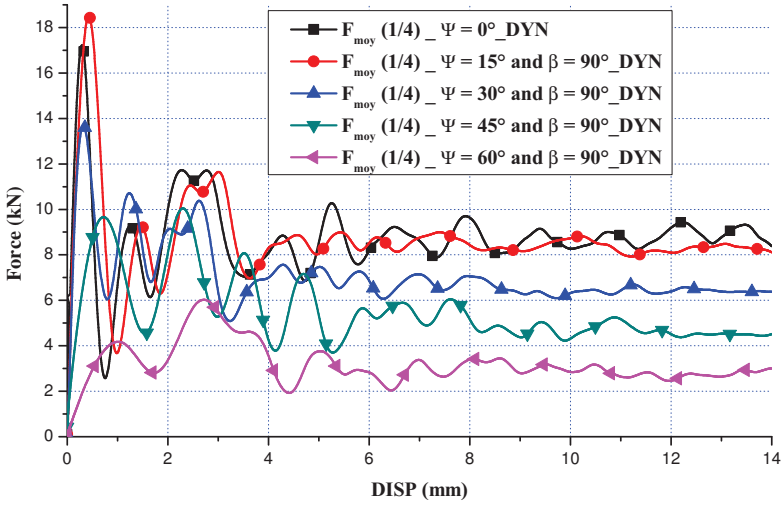

Figure 2.32: *The loading angle ψ effects under **dynamic** mixed shear-compression loading for $\beta = 90°$*

For each in plane orientation angle, the same observations as under quasi-static loadings are addressed under dynamic loading. By analysing these force-displacement responses, it can be noted that the level of these dynamic responses decreases with loading angle ψ, which is similar to the quasi-static trends. For ψ ranged between 0° and 15°, the influence of ψ on the average crushing force (plateau) is not significant whereas it becomes more pronounced for $\psi \geq 15°$.

The in-plane orientation angle β effects

The effects of the in-plane orientation angle on the mixed shear-compression honeycomb behaviour is studied. The force-displacement curves with different in-plane orientation angles are presented for the aluminium ***Al5056-N-6-1/4-0.003*** honeycomb specimen in figures A.10, A.11, 2.33 and A.12.

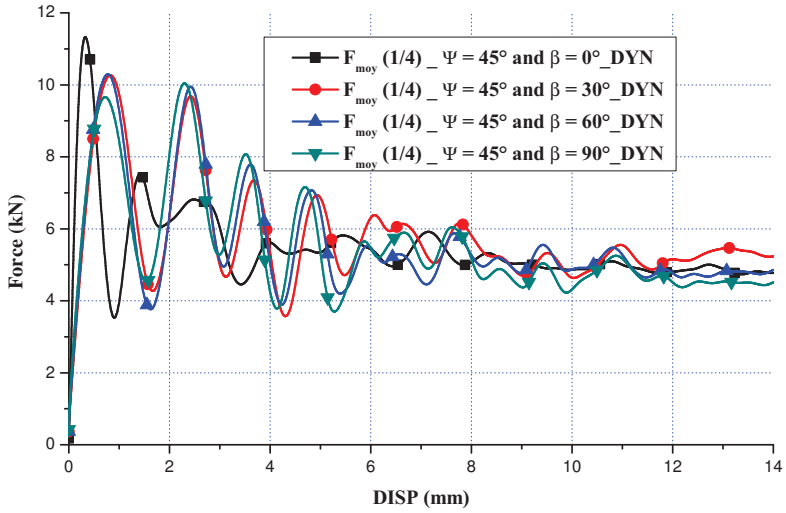

Figure 2.33: *The in-plane orientation angle β effects under* ***dynamic*** *mixed shear-compression loading for $\psi = 45°$*

Under dynamic mixed shear-compression loading, the in-plane orientation angle have a similar effect than quasi-static loading. The effect of the in-plane orientation depends on the loading angle ψ and becomes more pronounced on the initial peak and on the average crushing force for the loading angle $\psi \geqslant 45°$. Indeed, the influence of the loading angle on the collapse mechanisms is investigated in the section 2.4.3.

Under dynamic loading conditions, table 2.6 and 2.7 present the effects of the in-plane orientation angle and the loading angle on the initial peak force and on the average crushing force, respectively.

Table 2.6: ***Initial peak force*** *(kN) under dynamic mixed shear-compression loading*

	$\beta = 0°$	$\beta = 30°$	$\beta = 60°$	$\beta = 90°$
$\psi = 0°$	16.92	16.92	16.92	16.92
$\psi = 15°$	17.96	16.83	16.95	18.35
$\psi = 30°$	13.61	13.80	13.77	13.76
$\psi = 45°$	11.29	9.96	10.28	9.65
$\psi = 60°$	7.88	6.18	5.86	6.00

Table 2.7: ***Average crushing force*** *(kN) under dynamic mixed shear-compression loading*

	$\beta = 0°$	$\beta = 30°$	$\beta = 60°$	$\beta = 90°$
$\psi = 0°$	8.70	8.70	8.70	8.70
$\psi = 15°$	8.93	8.55	8.61	8.47
$\psi = 30°$	6.77	6.80	6.59	6.79
$\psi = 45°$	5.16	5.50	5.80	5.30
$\psi = 60°$	3.42	2.84	2.97	2.93

2.4.2 Dynamic enhancement

The dynamic enhancement of honeycombs under uni-axial compression loading has been extensively investigated in open literatures. Comparison studies between the quasi-static and dynamic behaviours of honeycomb structures indicate that these structures show a dynamic enhancement when the loading velocity increases under out-of-plane crushing of metallic honeycombs such as reported by Wu and Jiang [Wu 97], Zhao and Gary [Zhao 98], Goldsmith and Sackman [Gold 92], Baker et al.[Bake 98] , Harrigan et al.[Harr 99], Zhao et al.[Zhao 05] and Zhou and Mayer [Zhou 02]. In energy absorbing applications, for these cases, the dynamic enhancement is mainly attributed to the inertia effects. Thus, Zhao and Gary [Zhao 98] observed the dynamic enhancement of the honeycomb strength in their Hopkinson experimental results under the out-of-plane compression loading. The honeycomb strength increased by 40% when the loading rate increased from 5.10^{-4} m/s to 30 m/s, but the dynamic enhancement seems to be not significant under in-plane compression loading. Therefore, the effect of inertia is important under out-of-plane compression, while is limited for the in-plane compression loading.

In this section, the dynamic enhancement is verified under uni-axial compression loading and is studied under mixed shear-compression loading taking into account the variations of the loading angle ψ and of the in-plane orientation angle β. Figure 2.34 shows the force-displacement curve for the ***Al5056-N-6-1/4-0.003*** aluminium honeycomb under quasi-static and dynamic uni-axial compression loading.

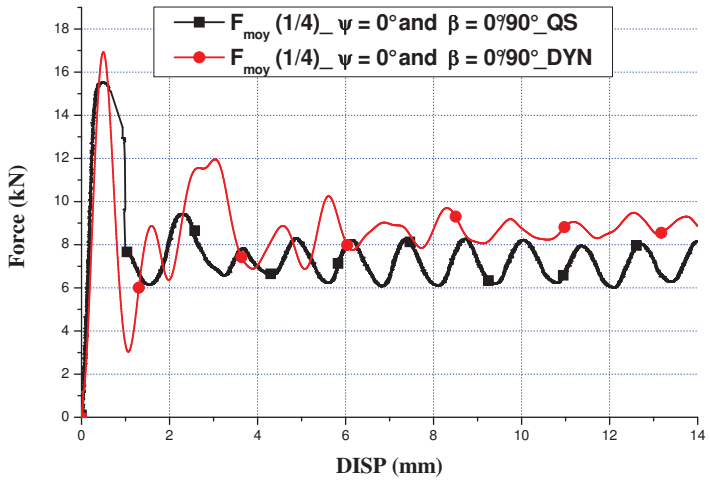

Figure 2.34: *Quasi-static and dynamic force-displacement curves under* ***uni-axial compression*** *loading for $\psi = 0°$*

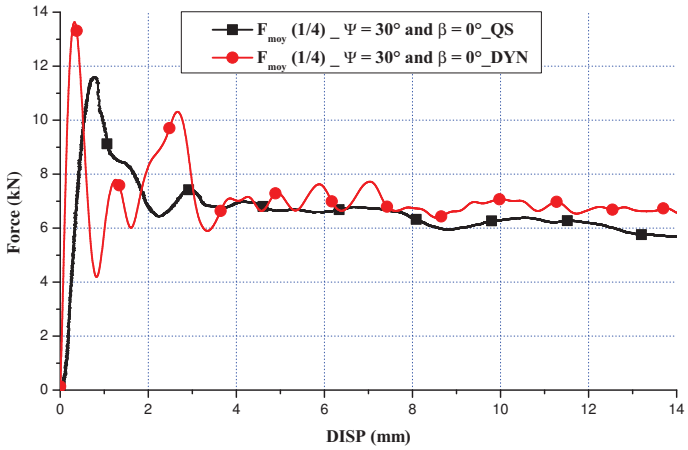

Figure 2.35: *Quasi-static and dynamic force-displacement curves under* ***mixed shear-compression*** *loading for $\psi = 30°$ and $\beta = 0°$*

For instance, under mixed shear-compression loading, the dynamic enhancement is observed for one configuration of loading ($\psi = 30°$ and β

= 0°) as an example in figure 2.35. For both cases of loading, the dynamic responses are higher than the quasi-static ones on the initial peak force and the average crushing force.

To study the dynamic enhancement behaviour in details and to quantify the force enhanced of the honeycomb from quasi-static to dynamic loading, the comparison between the experimental quasi-static and dynamic results is presented for the initial peak force and for the average crushing force. The dynamic enhancement rate γ could be defined by the following equation [Hou 11]:

$$\gamma = \frac{F_{DYN} - F_{QS}}{F_{QS}} \tag{2.7}$$

2.4.2.1 Initial peak force

Based on the tables 2.4 and 2.6, the dynamic enhancement rate γ is calculated for the initial peak force and tables 2.8 show the results for the ***Al5056-N-6-1/4-0.003*** aluminium honeycomb under mixed shear-compression loading.

Table 2.8: *Comparison between dynamic and quasi-static results under mixed shear-compression loading at* ***the initial peak force***

Loading configuration	Quasi-static (kN)	Dynamic (kN)	Dynamic enhancement rate
$\psi = 0°$	15.52	16.92	9.02 %
$\psi = 15° \ / \ \beta = 0°$	13.13	17.96	36.78%
$\psi = 15° \ / \ \beta = 30°$	13.38	16.83	25.78%
$\psi = 15° \ / \ \beta = 60°$	12.98	16.95	30.68%
$\psi = 15° \ / \ \beta = 90°$	12.72	18.35	44.26%
$\psi = 30° \ / \ \beta = 0°$	11.60	13.61	17.42%
$\psi = 30° \ / \ \beta = 30°$	11.82	13.80	16.75%
$\psi = 30° \ / \ \beta = 60°$	11.15	13.77	23.49%
$\psi = 30° \ / \ \beta = 90°$	10.83	13.76	27.05%
$\psi = 45° \ / \ \beta = 0°$	10.04	11.29	12.45%
$\psi = 45° \ / \ \beta = 30°$	9.78	9.96	1.84 %
$\psi = 45° \ / \ \beta = 60°$	9.40	10.28	9.36 %
$\psi = 45° \ / \ \beta = 90°$	9.48	9.65	13.79 %
$\psi = 60° \ / \ \beta = 0°$	8.15	7.88	**-3.19**%
$\psi = 60° \ / \ \beta = 30°$	7.23	6.18	**-14.52**%
$\psi = 60° \ / \ \beta = 60°$	6.68	5.86	**-12.27**%
$\psi = 60° \ / \ \beta = 90°$	6.46	6.00	**-7.12**%

The dynamic enhancement phenomenon of aluminium honeycomb strength is not only observed under uni-axial compression loading but also under mixed shear-compression loading. The initial peak forces show a large difference between quasi-static and dynamic results. The dynamic enhancement rate is equal to 9.02 % under uni-axial compression loading. It's significant under mixed shear-compression loading for a loading angle $\psi \leq 45°$. For instance, it's reached 44.2 % for the loading configuration ($\psi = 15°$ / $\beta = 30°$). For $\psi = 60°$, the quasi-static initial peak forces are higher than the dynamic ones. So, these results suggest that the dynamic enhancement behaviour depends on the loading angle ψ. The dynamic enhancement ratio for the initial peak force decreases when the loading angle increases linearly, ($\gamma \approx 35$ % for $\psi = 15°$, $\gamma \approx 20$ % for $\psi = 30°$ and $\gamma \approx 10$ % for $\psi = 45°$). For $\psi = 60°$, the dynamic enhancement is not observed. Instead, we observe a dynamic initial peak force lower than the quasi-static one. This suggests that the first stage of the folding mechanisms is different. Based on the tables 2.4 and 2.6, the coupled influence of the loading angle and the in-plane orientation angle on the initial peak force is presented by figure 2.36 under quasi-static conditions and by figure 2.37 under dynamic conditions.

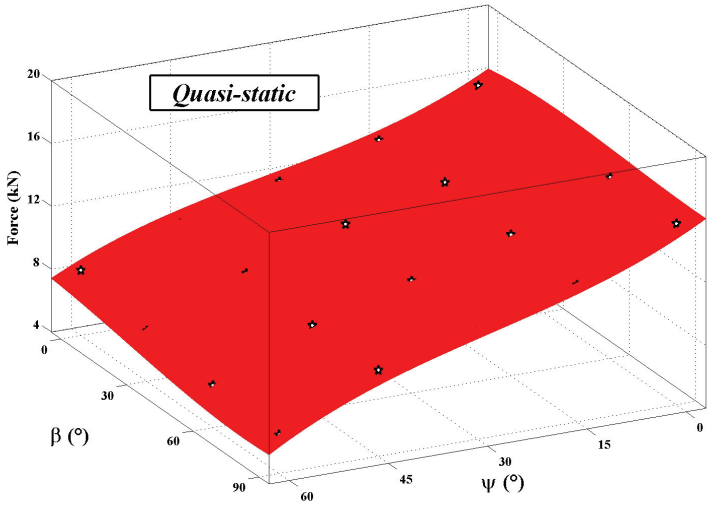

Figure 2.36: *The loading and the in-plane orientation angles effects on the initial peak force under* ***quasi-static*** *mixed shear-compression loading.*

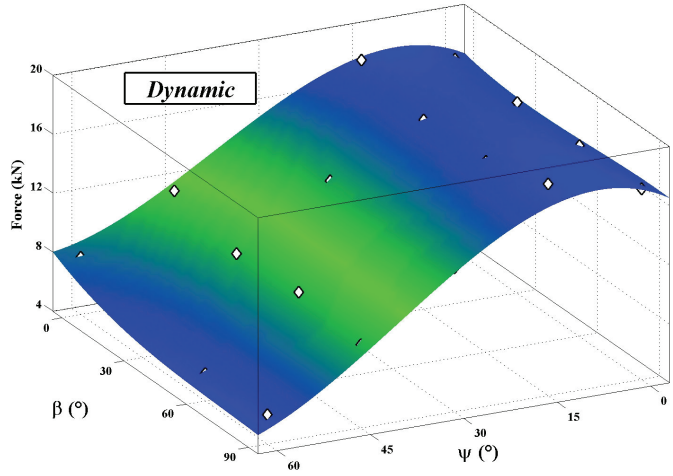

Figure 2.37: *The loading and the in-plane orientation angles effects on the initial peak force under* ***dynamic*** *mixed shear-compression loading.*

Under quasi-static and dynamic loadings, the initial peak force decreases significantly when the loading angle $\psi > 15°$.

The quasi-static and dynamic responses for the ***Al5056-N-6-1/4-0.003*** aluminium honeycomb specimen are superposed with the combined effects of ψ and β (figure 2.38).

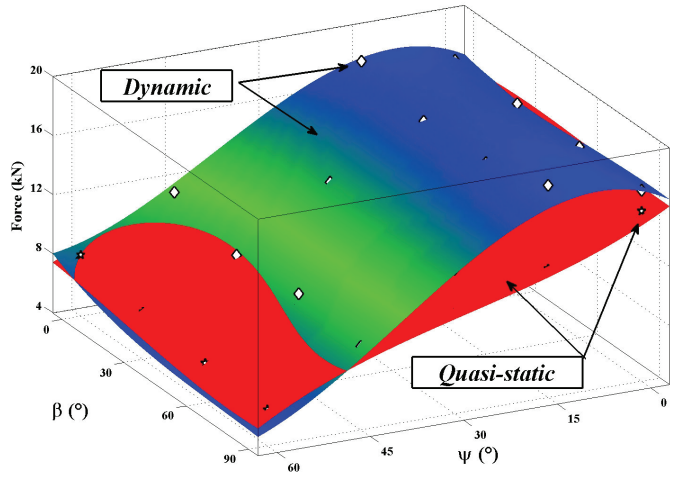

Figure 2.38: *The competition between the impact velocity, the loading angle and the in-plane orientation angle effect on* ***the initial peak force*** *under mixed shear-compression loading.*

Analysing the aluminium honeycomb crushing response surfaces for the initial peak force, a significant effect of the impact velocity is observed under mixed shear-compression loading until a loading angle $\psi = 45°$. For the crushed specimen, the dynamic enhancement is observed from $\psi = 0°$ to $\psi = 45°$. This enhancement phenomenon is mainly attributed to the inertia effect [Zhao 04]. For $\psi > 45°$, this tendency is inversed and the difference observed on the quasi-static and dynamic initial peak forces could be explained by the difference of initial collapse mechanisms. This will be investigated in section 2.4.2.3.

Now, the influence of the in-plane orientation angle β on the initial peak force is studied. To confirm this influence and to investigate the effect of the impact velocity on the influence of the in-plane orientation angle, the dynamic enhancement behaviour for the initial peak force is presented as a function of β for each loading angle ψ. It is presented focusing on the β effects for the ***Al5056-N-6-1/4-0.003*** aluminium honeycomb in figure 2.39.

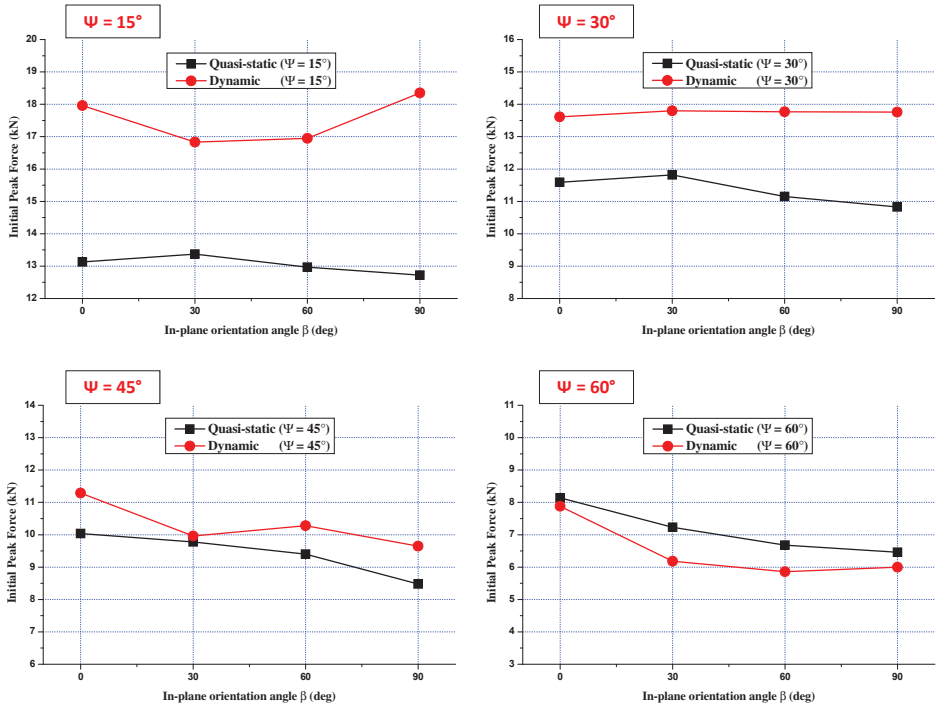

Figure 2.39: *Comparison between quasi-static and dynamic* ***initial peak force*** *: β effects*

Figure 2.39 shows that the in-plane orientation angle β has a negligible effect on the initial peak force under both loading conditions quasi-static and dynamic for $\psi = 15°$ and $30°$. When the loading angle $\psi \geq 45°$, the effect of β becomes more significant. Moreover, the influence of the in-plane orientation angle is not affected by the impact velocity effect.

2.4.2.2 Average crushing force

Based on the tables 2.5 and 2.7, the dynamic enhancement rate γ is calculated for the average crushing force. Table 2.9 shows the results for the ***Al5056-N-6-1/4-0.003*** aluminium honeycomb under mixed shear-compression loading.

Table 2.9: *Comparison between dynamic and quasi-static results under mixed shear-compression loading at* ***the average crushing force***

Loading configuration	Quasi-static (kN)	Dynamic (kN)	Dynamic enhancement rate
$\psi = 0°$	7.27	8.70	19.67 %
$\psi = 15° \ / \ \beta = 0°$	7.15	8.93	24.89%
$\psi = 15° \ / \ \beta = 30°$	7.03	8.55	21.62%
$\psi = 15° \ / \ \beta = 60°$	7.18	8.61	19.91%
$\psi = 15° \ / \ \beta = 90°$	7.09	8.47	19.46%
$\psi = 30° \ / \ \beta = 0°$	6.51	6.77	3.99%
$\psi = 30° \ / \ \beta = 30°$	6.65	6.80	2.25%
$\psi = 30° \ / \ \beta = 60°$	6.43	6.59	2.48%
$\psi = 30° \ / \ \beta = 90°$	6.50	6.79	4.46%
$\psi = 45° \ / \ \beta = 0°$	5.14	5.16	0.38%
$\psi = 45° \ / \ \beta = 30°$	5.43	5.50	1.28%
$\psi = 45° \ / \ \beta = 60°$	5.77	5.80	0.51%
$\psi = 45° \ / \ \beta = 90°$	5.29	5.30	0.18%
$\psi = 60° \ / \ \beta = 0°$	3.70	3.42	**-7.56**%
$\psi = 60° \ / \ \beta = 30°$	4.04	2.84	**-29.70**%
$\psi = 60° \ / \ \beta = 60°$	3.63	2.97	**-18.18**%
$\psi = 60° \ / \ \beta = 90°$	3.57	2.93	**-17.92**%

The dynamic enhancement on the average crushing force also depends on the loading angle ψ such as observed on the initial peak force. Table 2.9 shows a large difference between quasi-static and dynamic results. The dynamic enhancement rate is equal to 19.67 % under uni-axial compression loading. It reaches 21% for $\psi = 15°$ that is the approximately the same rate

under uni-axial compression loading. When the loading angle increases, the dynamic enhancement rate shows a drop to decrease to $\gamma \approx 3.5$ % for $\psi = 30°$ and $\gamma \approx 0.5$ % for $\psi = 45°$. The effect of the impact velocity is cancelled by the loading angle effect until $\psi = 45°$. It is inverted at the loading angle $\psi = 60°$. Moreover, it can be noted the dynamic enhancement ratio is significantly higher for the initial peak force than the average crushing force.

Based on the tables 2.5 and 2.7, the combined effects of the loading angle ψ and the in-plane orientation angle β on the average crushing force are plotted under quasi-static (figure 2.40) and under dynamic (figure 2.41) separately at the first step.

The average crushing force globally decreases when the loading angle ψ increases under quasi-static and dynamic conditions (figures 2.40 and 2.41). The combined effect of the impact velocity, the loading angle and the in-plane orientation is presented for the ***Al5056-N-6-1/4-0.003*** aluminium honeycomb in figure 2.42.

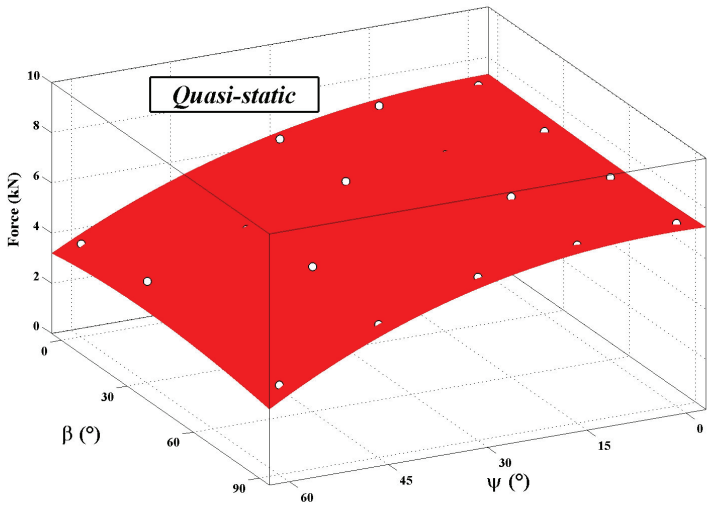

Figure 2.40: *The combined effect of the loading and the in-plane orientation angles on the average crushing force under* ***quasi-static*** *mixed shear-compression loading.*

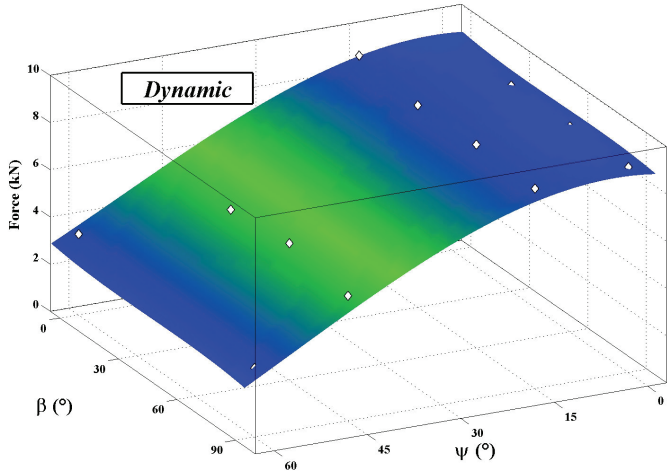

Figure 2.41: *The combined effect of the loading and the in-plane orientation angles on the average crushing force under* ***dynamic*** *mixed shear-compression loading.*

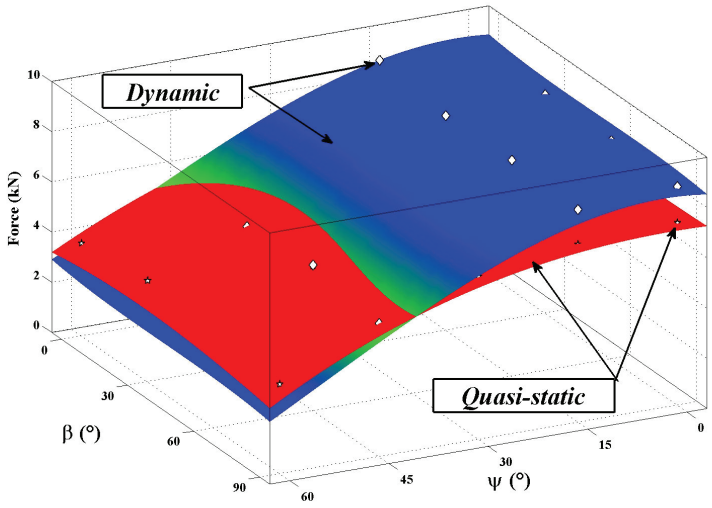

Figure 2.42: *The competition between the impact velocity, the loading angle and the in-plane orientation angle effect on* ***the average crushing force*** *under mixed shear-compression loading.*

For the average crushing force, the dynamic enhancement decreases when the loading angle increase until it becomes $\gamma \approx 0$ % for $\psi = 45°$. This dynamic

enhancement phenomenon can be explained by the inertia effect [Zhao 04] and may be the air entrapped effects [Hong 08]. For $\psi > 45°$, the dynamic enhancement is not observed. On the contrary, the quasi-static responses are higher than the dynamic ones. The collapse mechanisms have to be examined carefully and will allow to explain this phenomenon.

Such as performed for the initial peak force, the influence of the in-plane orientation angle β is investigated on the average crushing force taking into consideration the impact velocity. So, the dynamic enhancement behaviour for the average crushing force is presented as a function of β for each loading angle ψ in figure 2.43.

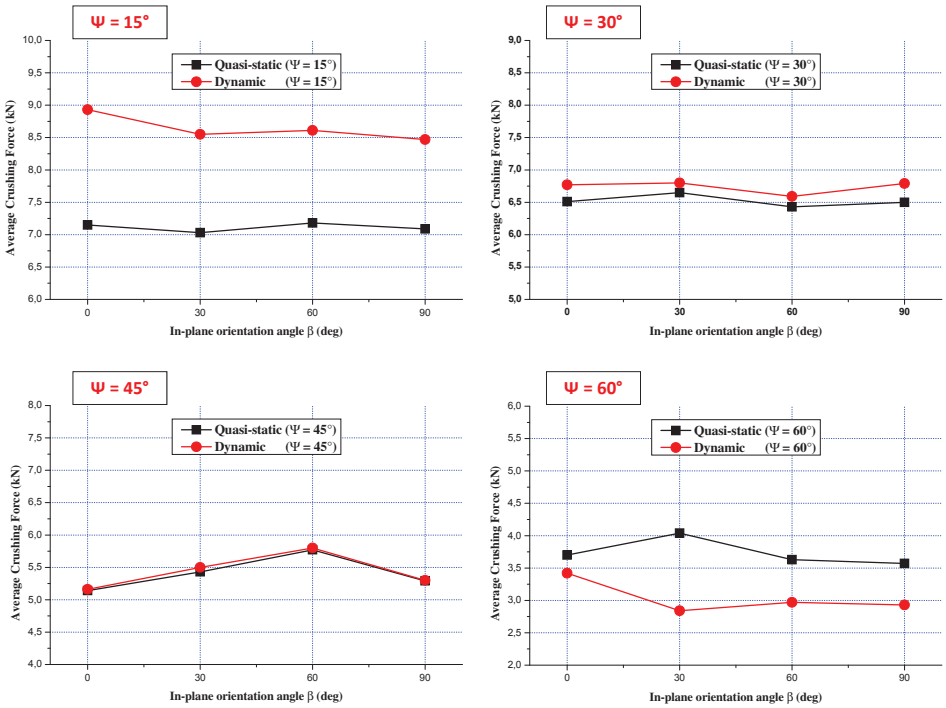

Figure 2.43: *Comparison between quasi-static and dynamic* ***average crushing force*** *: β effects*

Under quasi-static and dynamic loadings, an insignificant effect of the in-plane orientation angle is observed for ψ varying from 0° to 30°. More significant effect of this angle β is observed for $\psi \geq 45°$ (for $\psi = 45°$ and $\beta = 0° \ / \ \beta = 60°$). The impact velocity has insignificant effect on the influence of the in-plane orientation angle (similar tendency of β effect is observed under quasi-static and dynamic).

2.4.2.3 Impact velocity effect for a higher loading angle

In order to understand in depth the phenomenon of the inverse effect of the impact velocity for loading angles $\psi \geq 45°$, an analysis of the collapse mechanisms for a loading angle $\psi = 60°$ is carried out under both quasi-static and dynamic loading conditions.

Figure 2.44 presents the collapse mechanisms of a crushed specimen under quasi-static loading and under dynamic loading for $\psi = 60°$. The final stage of the crushed specimen under dynamic loading show that the honeycomb specimen begins by the formation of the first fold followed by the global rotation of the cell axis due to the impact velocity. On the contrary, the crushed specimen under quasi-static loading shows a progressive folding system at both sides of the specimen that causes the global rotation of the cell axis.

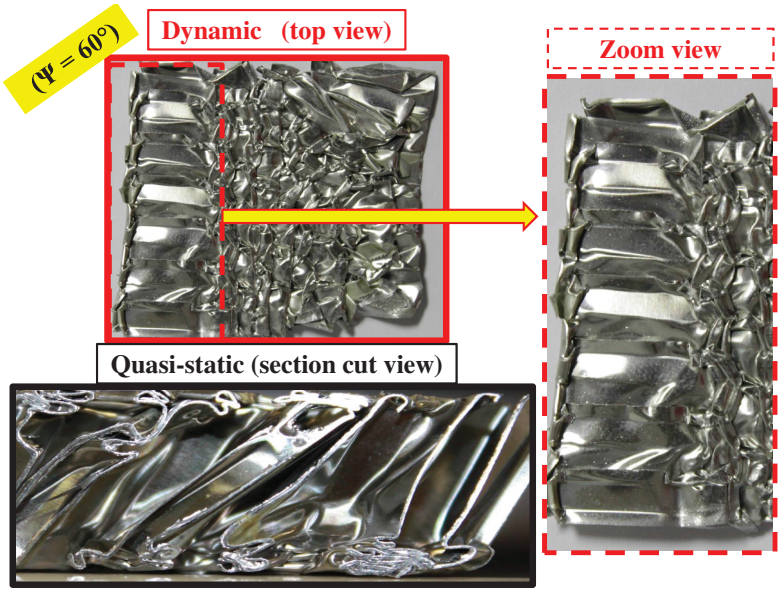

Figure 2.44: *Comparison between quasi-static and dynamic collapse mechanisms for $\psi = 60°$*

In order to explain this phenomenon, figure 2.45 presents a schematic of quasi-static and dynamic collapse mechanisms. The collapse mechanisms under quasi-static loading required more quantity of energy than under dynamic loading. This is explained by the difference on the fold number formation that it is more higher under quasi-static than under dynamic. Indeed, inertia effects promote the global rotation of the cell axis rather than the formation of folds.

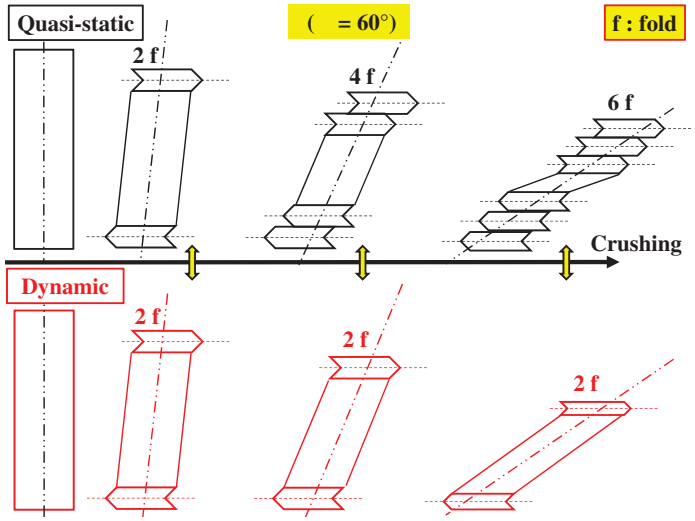

Figure 2.45: *The scheme of the collapse mechanisms under quasi-static and dynamic loading for $\psi = 60°$*

More details of the collapse mechanisms are presented in the next section for all cases of the mixed shear-compression loading.

2.4.3 Collapse mechanisms analysis

In order to investigate the collapse mechanisms, a high speed camera is used for the dynamic experiments and a CCD camera for quasi-static experiments. Crushed honeycomb specimens are presented at the top view to observe clearly the influence of the shear load direction on the collapse mechanisms under mixed shear-compression loading. Three deforming pattern modes are identified. The schemes of these modes are addressed to illustrate the collapse mechanisms. The combined effect of the in-plane orientation and the loading angle is studied on the deforming pattern modes for both quasi-static and dynamic loading conditions.

2.4.3.1 Experimental collapse mechanisms under uni-axial compression

Under uni-axial compression loading for quasi-static and dynamic conditions, similar collapse mechanisms are observed. The collapse mechanisms start by elastic buckling followed by post-buckling till an initial peak that represents the collapse point. The formation of the first fold shows the apparition of plastic mechanisms mainly characterized by horizontal hinge lines. The end of the development of the first fold initiates the formation of the second one

which leads to the activation of a progressive folding system. It takes place in the crushing regime (post-collapse) and it is characterised by the average crushing force that represents the energy absorption quantity. The formation of the first fold is characterised by the random wave instability localisation that could be at the top or the bottom honeycomb specimen such as shown in figure 2.46.

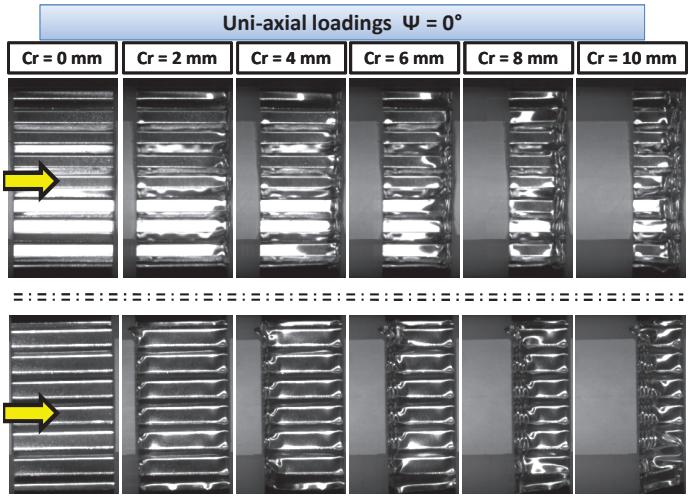

Figure 2.46: *Collapse mechanisms under dynamic uni-axial compression loading*

2.4.3.2 Experimental collapse mechanisms under mixed shear-compression

The formation of the first fold under mixed shear-compression loading could be localised at the top or the bottom of the honeycomb specimen such as under uni-axial loading. Figure 2.47 shows the top views of the collapse mechanisms under dynamic mixed shear-compression loading for only one loading angle $\psi = 30°$ as an example with different in-plane orientation angles ($\beta = 0°$, $30°$, $60°$ and $90°$).

Aluminium honeycomb specimens crushed under dynamic and quasi-static mixed shear-compression loading show progressive folding of cell walls such as under uni-axial compression loading. Under mixed loading, the collapse mechanisms depend on the loading angle ψ in addition to the in-plane orientation angle β (figure 2.47). The honeycomb specimens crushed under mixed shear-compression loading for $\psi = 30°$ with various in-

plane orientation angle β show similar progressive folding mechanisms with different deforming pattern modes (I, II, and III) depending of the shear load direction i.e the β angle.

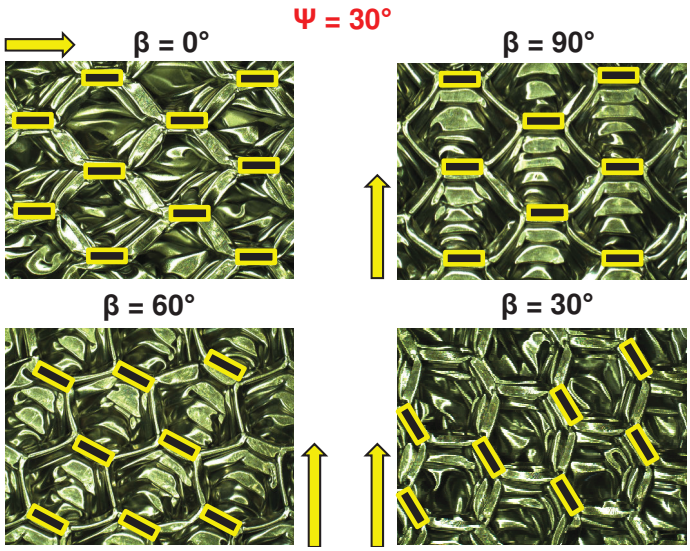

Figure 2.47: *Collapse mechanisms under dynamic mixed shear-compression loading : top views ($\psi = 30°$)*

The deforming pattern modes are the consequence of the symmetric or asymmetric location of horizontal or inclined plastic hinge lines for folding due to the presence of mixed shear-compression loading. They are presented by figures 2.48, 2.49 and 2.50.

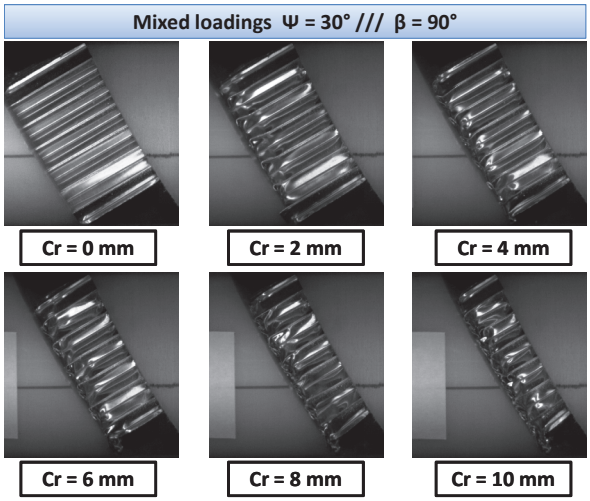

Figure 2.48: *Collapse mechanisms under dynamic mixed shear-compression loading : Mode I*

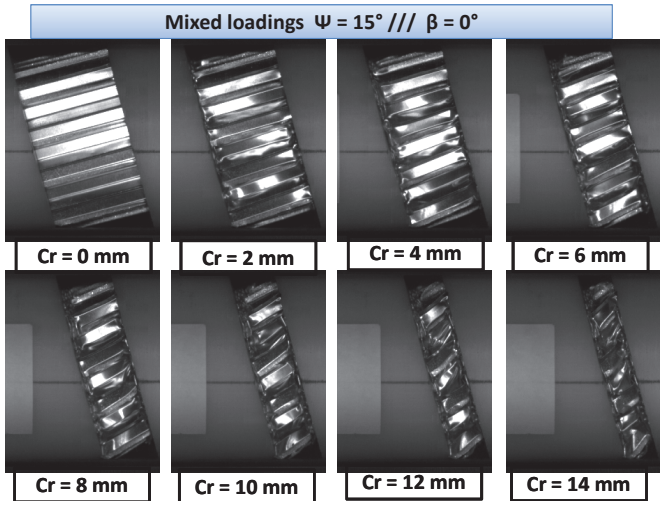

Figure 2.49: *Collapse mechanisms under dynamic mixed shear-compression loading : Mode II*

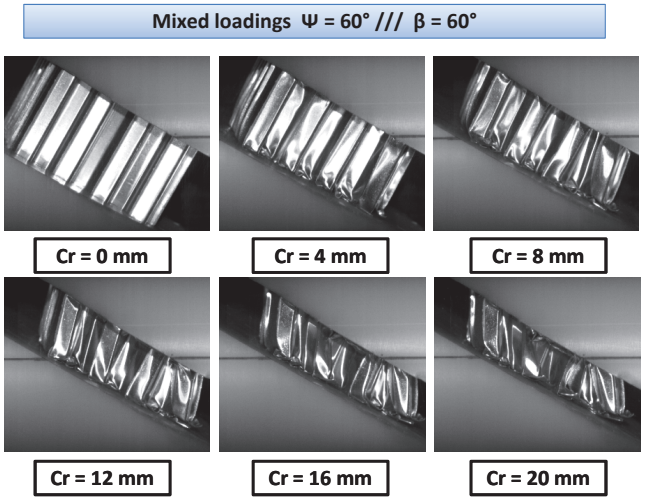

Figure 2.50: *Collapse mechanisms under dynamic mixed shear-compression loading : Mode III*

Such as reported by Mohr and Doyoyo [Mohr 04a, Mohr 04b, Mohr 04c], Hong et al.[Hong 06a, Hong 06b, Hong 08] and Hou et al.[Hou 11a, Hou 11b], the first deforming pattern mode (mode I) is verified in our experiments (figure 2.48). In addition, a second deforming mode (mode II) identified by Hou et al.[Hou 11a, Hou 11b] is also verified (figure 2.49). But, a new deforming pattern mode (mode III) is identified during our experiments (figure 2.50).

Figure 2.51 illustrates the scheme of the three deforming pattern modes under mixed shear-compression loading. The first mode is characterised by horizontal plastic hinge lines and the fold formation on a single side of the specimen which promotes the no rotation of the cell axis. The second mode is characterised by inclined plastic hinge lines and the fold formation on both sides of specimen that achieves the rotation of the cell axis from the beginning that provided the global rotation of the crushed specimen. The third mode is the combination between the first mode and the second mode when the plastic hinge lines remain horizontal but the formation of the fold in both side of the specimen leads to the global rotation of the crushed specimen is observed.

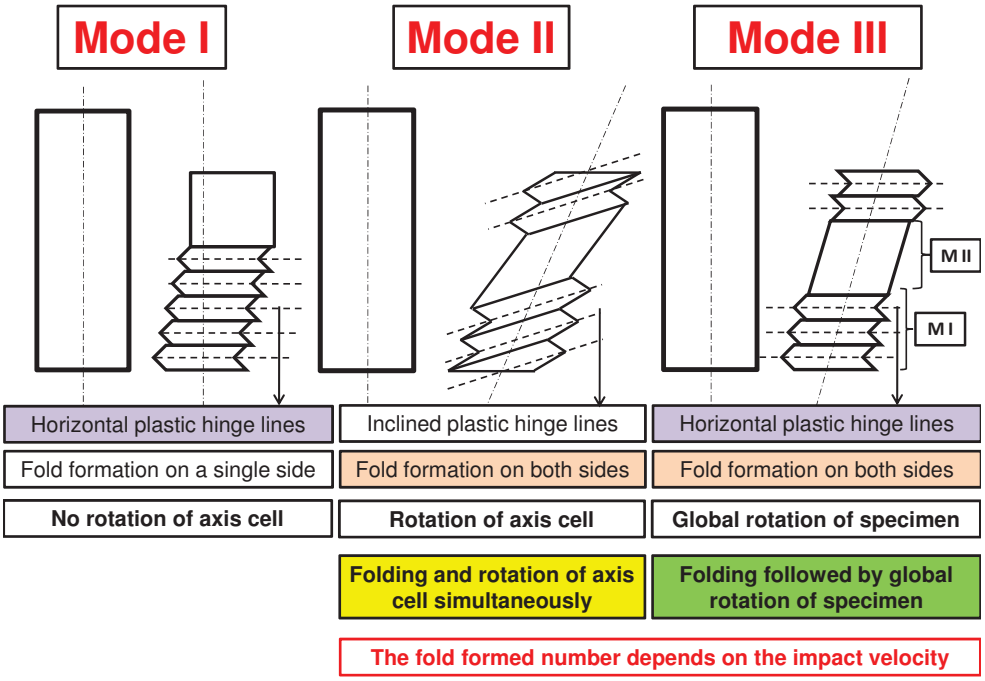

Figure 2.51: *Collapse mechanisms under dynamic mixed shear-compression loading : scheme of the three deforming pattern modes I, II and III*

2.4.3.3 Competition between the loading and in-plane orientation angles effect on the deforming pattern modes

The distribution of the deforming pattern modes as a function of ψ and β angles are presented in table 2.10 under quasi-static and dynamic loadings for the aluminium honeycomb specimen ***Al5056-N-6-1/4-0.003***.

Table 2.10: *The deforming pattern modes under quasi-static and dynamic mixed shear-compression loading*

	$\beta = 0°$		$\beta = 30°$		$\beta = 60°$		$\beta = 90°$	
	QS	DYN	QS	DYN	QS	DYN	QS	DYN
$\psi = 0°$	MI	MI	MI	MI	MI	MI	MI	MI
$\psi = 15°$	***MII***	***MII***	MI	MI	MI	MI	MI	MI
	MI	***MII***	MI	MI	MI	MI	MI	**MIII**
	MI	***MII***	MI	MI	MI	***MII***	MI	**MIII**
$\psi = 30°$	***MII***	***MII***	**MIII**	***MII***	MI	MI	MI	MI
	MII	***MII***	***MII***	MI	MI	***MII***	MI	MI
	MII	***MII***	***MII***	***MII***	MI	***MII***	MI	MI
$\psi = 45°$	***MII***	***MII***	**MIII**	MI	**MIII**	**MIII**	MI	MI
	MII	***MII***	**MIII**	***MII***	**MIII**	**MIII**	MI	**MIII**
	MII	***MII***	**MIII**	**MIII**	**MIII**	**MIII**	**MIII**	MI
$\psi = 60°$	***MII***	***MII***	**MIII**	MI	**MIII**	**MIII**	**MIII**	MI
	MII	***MII***	**MIII**	**MIII**	**MIII**	**MIII**	**MIII**	MI
	MII	***MII***	**MIII**	***MII***	**MIII**	**MIII**	**MIII**	MI

Under uni-axial loadings $\psi = 0°$, mode I is always observed for quasi-static and dynamic conditions. Under mixed shear-compression loading, table 2.10 suggests that the in-plane orientation and loading angles have a significant effects on the deforming pattern modes. Focus on the in-plane orientation angle β effect in the first time followed by the effect of loading angle in the second time, the distribution of the deforming pattern mode is presented by the following remarks:

- For $\beta = \mathbf{0°}$, the mode II is clearly observed regardless of the loading angle ψ.

- For $\beta = \mathbf{30°}$, according to the loading angle, the deforming pattern modes can be classified as mode I for $\psi = 15°$ while the three deforming pattern modes I, II and III are observed for $\psi \geq 30°$. But it can noted that mode III is dominant.

- For $\beta = \mathbf{60°}$, when the $0° \leq \psi \leq 30°$, mode I is usually observed except for some case under dynamic conditions. However mode I is dominant for this range of ψ. Mode III is always observed for $45° \leq \psi \leq 60°$.

- For $\beta = \mathbf{90°}$, mode I is extensively observed irrespective of the loading angle ψ except for a few cases when the mode III is appeared.

To more explain this distribution, figure 2.52 presents the influence of the in-plane orientation angle on the deforming pattern mode.

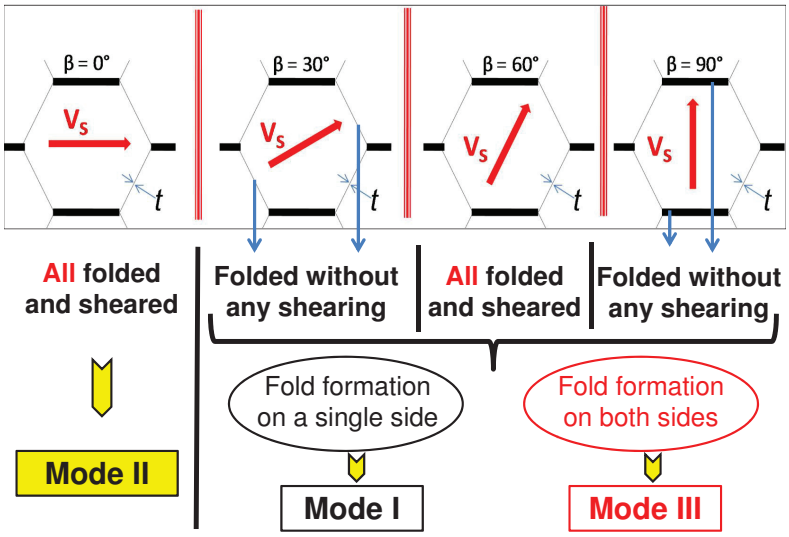

Figure 2.52: *The in-plane orientation angle effect on the deforming pattern modes*

For $\beta = 0°$ when the shear load direction is parallel to the double wall thickness, all cell walls are folded and sheared simultaneously. The shear of double wall thickness requires a lot quantity of energy that leads to the rotation of the cell axis simultaneously with the folding mechanisms characterised by inclined plastic hinge lines at both sides of the specimen.

For $\beta = 30/60/90°$, mode I is always observed. However, when the loading angle increases, the shear load increases and actives the formation of the fold at both sides of the specimen that leads to the global rotation of the specimen. That is why mode III appears when the loading angle increases.

Under quasi-static and dynamic conditions, similar deforming pattern modes are observed for all loading configurations except some cases mainly due to the inertia effects but also due to the geometry imperfections or the specimen position effects.

Table 2.11: *The competition between ψ and β on the deforming pattern modes under mixed shear-compression loading*

<table>
<tr><th></th><th>$\beta = 0°$</th><th>$\beta = 30°$</th><th>$\beta = 60°$</th><th>$\beta = 90°$</th></tr>
<tr><td>$\psi = 0°$</td><td colspan="4">MI</td></tr>
<tr><td>$\psi = 15°$</td><td rowspan="5">MII</td><td colspan="3">MI</td></tr>
<tr><td>$\psi = 30°$</td><td rowspan="3">MIII</td><td colspan="2">MI</td></tr>
<tr><td>$\psi = 45°$</td><td rowspan="2">MIII</td><td>MI</td></tr>
<tr><td>$\psi = 60°$</td><td>MIII/MI</td></tr>
</table>

To summarise, table 2.11 presents the distribution of the three deforming pattern modes I, II and III taking into account the competition between the loading angle and the in-plane orientation angle.

To investigate deeply the collapse mechanisms and the deforming pattern modes at the local cell wall level, cutting section of the crushed specimens are required but under dynamic loading the specimens are completely crushed and a cutting section don't allow us to identify the local collapse mechanisms. So as, numerical simulations are needed (chapter 3).

2.5 Conclusion

The quasi-static and dynamic behaviours of aluminium honeycombs under mixed shear-compression loading is studied taking into account the loading angle ψ and the in-plane orientation angle β effects.

A finite element (FE) study is realised in order to improve the mixed shear-compression loading device. The increased stiffness of the sleeves limits the radial expansion phenomenon and ensures a good alignment of loading and therefore the efficiency in the data processing. A separation phenomenon between the input hopkinson bar and the input beveled bar is observed numerically and is confirmed experimentally. So, an electro optical extensometer is used such as a measurement technique to extend the information needed to compute the output force for a larger crushing displacement of the specimen.

Experimental programme based on the improved mixed shear-compression loading device is performed with four in-plane orientation angles and five loading angles. Three experimental tests per velocity are performed for each combination of loading. A good repeatability is confirmed. The average of the three force-displacement curves is calculated to present the mean crushing behaviour and attention is paid on two parameters : initial peak force and average crushing force. Experimental results show a significant effect of the loading angle ψ on the mixed shear-compression behaviour. The effect of the in-plane orientation angle β is studied and it is more significant when the loading angle increases ($\psi \geqslant 45°$). This is explained by the difference of the collapse mechanisms and the deforming pattern modes.

A dynamic enhancement is observed under mixed shear-compression loading. The dynamic enhancement rate is calculated as a function of the

loading angle ψ and the in-plane orientation angle β. It decreases when the loading angle increases. The dynamic enhancement is more pronounced on the initial peak force than the average crushing force. For both initial peak and average crushing forces, the dynamic enhancement is not observed when the loading angle exceeds 45° ($\psi > 45°$). This phenomenon is explained by the difference between the collapse mechanisms under quasi-static and dynamic loadings.

Quasi-static and dynamic collapse mechanisms are examined and three deforming pattern modes (mode I, II and III) are identified under mixed shear-compression loading. The collapse mechanisms show that the deforming pattern modes depends of the the loading angle ψ and the in-plane orientation angle β.

Due to the limitation of the experimental techniques to measure the tangential force component, to separate the normal and shear behaviours in the frame of the specimen and to develop a macroscopic yield criterion, a numerical study is required. Moreover, it will allow to investigate the collapse mechanisms in depth under mixed shear-compression quasi-static and dynamic loadings and to confirm experimental observations.

- Chapter 3 -

FE modelling of aluminium honeycomb under mixed shear-compression loading

Resume

Due to the limitation of the experimental measurements to investigate the normal and the shear honeycomb behaviours separately, numerical simulations are performed. The aim of this chapter is to present a detailed FE model allowing to simulate the mixed shear-compression honeycomb behaviour. Numerical results suggest that the in-plane orientation angle has a significant effect on the tangential force component. Indeed, the combined influence of the in-plane orientation and loading angles affects the collapse mechanisms and the deforming patterns modes. Finally, a validation between numerical and experimental responses allows to dissociate the normal and shear forces components. They are used to identify the parameters of a macroscopic yield criterion expressed as a function of the impact velocity, the loading angle and the in-plane orientation angle.

3.1 Introduction

In order to investigate in details the mixed shear-compression behaviour of cellular materials, the normal and shear responses are required. The experimental results using the SHPB set-up only provides the axial component force (F_Z) of the crushing responses of aluminium honeycomb under mixed shear-compression. The relationship between the forces obtained by the experimental set-up and the normal and shear forces on honeycomb specimen are presented by figure 3.1 and by the following equations :

$$F_X \approx 0 \tag{3.1}$$

$$F_Y = F_N sin(\psi) - F_S cos(\psi) \tag{3.2}$$

$$F_Z = F_N cos(\psi) + F_S sin(\psi) \tag{3.3}$$

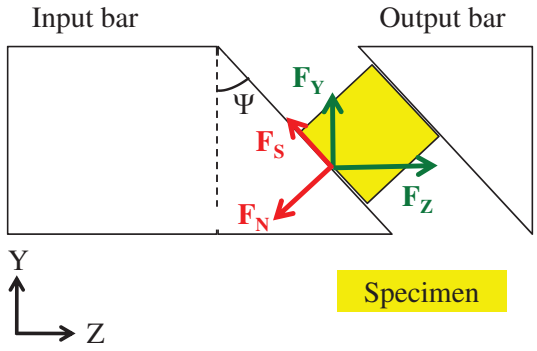

Figure 3.1: *Scheme of the force components under mixed loading*

The device presented in chapter 2 with the Teflon and steel sleeves leads to a transverse component force F_Y which can not be measured experimentally. So, the normal and the shear force components respectively F_N and F_S can not be calculated.

One way to solve this problem is to simulate the experimental tests in order to have acess to local force components. In this chapter, FE numerical simulations are carried out taking the effect of the loading angle ψ and the in-plane orientation angle β into consideration. In addition, an analysis of the crushing responses and the collapse mechanisms is realised to complete experimental observations of the previous chapter.

3.2 General description of the FE numerical model

In numerical tests, it's difficult to simulate with refined mesh the whole experimental set-up including the SHPB system, the mixed shear-compression loading device and the specimen. So, only the honeycomb specimen placed between two beveled bars is modelled. The experimental input and output velocities obtained by using DAVID© are applied in the two beveled bars. The numerical model as well as the boundary conditions are shown in figure 3.2. The FEM commercial code Abaqus/explicit is used for this numerical study.

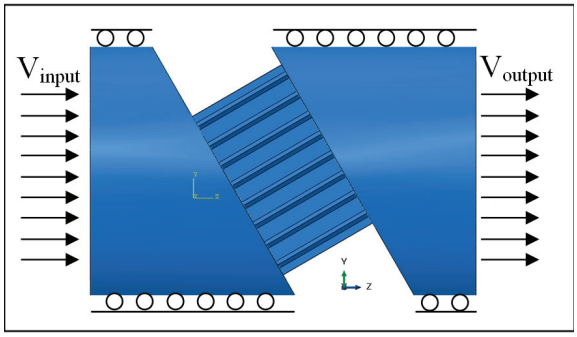

Figure 3.2: *Scheme of the numerical model and the boundary conditions under mixed loading*

3.2.1 The FE numerical model and materials

The aluminium honeycomb specimen used in the experimental study is presented by a virtual honeycomb specimen in the simulations. It's an ***Al5056-N-6.0-1/4-0.003*** aluminium alloy honeycomb. It contains 39 cells on the honeycomb cross-section. The specimen dimensions are 44*41*25 mm in the directions of X, Y and Z respectively. The cell has a regular hexagonal shape, an angle of 120°, with a cell wall thickness t = 76 μm, a cell size d = 6.35 mm, and a cell wall width D = 3.67 mm (figure 3.3).

The material constitutive model parameters is determined using an inverse method of identification based on quasi-static uni-axial crushing responses taking into account the geometry imperfections and the glue effects [Mark 98]. The cell wall material (Al5056-O) with a density 2640 kg/m^3 is assumed to exhibit a bilinear elastic–plastic response with a Young's modulus

E = 70 GPa, a Poisson's ratio $\nu = 0.35$, a yield stress $\sigma_y = 0.38$ GPa, and a hardening modulus $E_t = 0.5$ GPa.

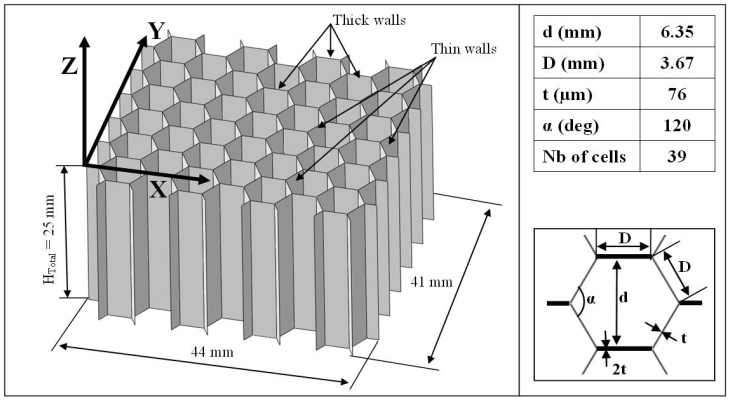

Figure 3.3: *Scheme of the numerical honeycomb specimen and the geometry parameters*

The two short beveled bars are made of Teflon presented by a linear material with elastic properties (Density $\rho = 2200$ kg/m^3, Young's modulus E = 1.5 GPa and Poisson's ratio $\nu = 0.46$). The material properties are presented in table 3.1.

Table 3.1: *Aluminium honeycomb specimen and bars material properties*

	Aluminium honeycomb	Teflon parts
Density ρ (kg/m^3)	2640	2200
Young's Modulus E (GPa)	70	1.5
Poisson's Ratio ν	0.35	0.46
Plastic Poisson's Ratio ν_p	0	-
Yield Stress σ_s (GPa)	0.38	-
Hardening modulus E_t (GPa)	0.5	-

3.2.2 FEM: Mesh and boundary conditions

The honeycomb specimen is modelled using the FE software ABAQUS/explicit. All the honeycomb cells are meshed using four-node-doubly curved thin shell elements with a reduced integration scheme (finite membrane strains, active stiffness hourglass control (S4R) and 5 integration points through cell wall thickness). A sensitivity analysis on the size of the elements was carried out in order to prevent mesh effects on the numerical results. This analysis has led to choose an element size of 0.25

mm corresponding to a discretisation of the complete model geometry with 232,600 elements (figure 3.4).

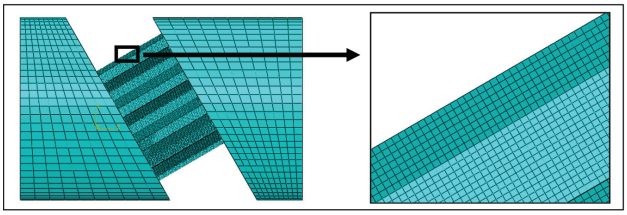

Figure 3.4: *FE Model: Mesh*

A general contact algorithm was used for the whole model with a Coulomb friction coefficient equal to 0.3. At the interfaces between the specimen and the inclined surfaces of the beveled, surface-to-surface contact algorithm with a rough contact method is applied. The double thickness wall in the real honeycomb is composed of two simple thickness walls bonded by a thin adhesive layer. During simulations, these double walls are represented by single shells with double thickness assuming that the bonding is not delaminated [Mohr 04a]. All degrees of freedom of nodes of the two short beveled bars are fixed except the velocity in Z direction in order to ensure the good alignment such as in the experiments. The impact velocities are taken equal to the input velocity and the output velocity obtained in the experimental study on respectively the input and output short beveled bars (figure 3.2). The short beveled bars are meshed with 8-node linear brick elements with reduced integration (C3D8R) with an element size of 3 mm (figure 3.4).

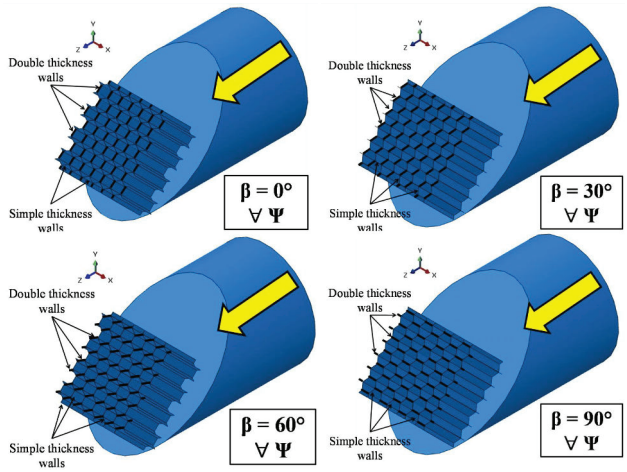

Figure 3.5: *The in-plane orientation angle β on the numerical simulations*

Four configurations are presented in figure 3.5 that illustrate the position and the orientation of the specimen to obtain the four in-plane orientation angles $\beta = 0°$, $\beta = 30°$, $\beta = 60°$ and $\beta = 90°$ for every loading angle ψ such as performed in the experiments.

3.3 Numerical results and experimental validation

The loading configurations of the experimental programme are reproduced in this simulation programme.

The aim of this section is to validate the numerical model developed previously by comparison with the experimental results presented in the chapter 2 under uni-axial compression and mixed shear-compression loadings. The comparison between experimental and numerical crushing responses in the Z direction (Fz) and collapse mechanisms in both cases of loadings are presented. This comparison study is carried out in term of the initial peak force and the average crushing force as well as the deforming patterns modes.

3.3.1 The crushing responses under quasi-static loading

In order to perform the quasi-static numerical tests, the numerical model is used by fixing one of the beveled bars and applying a loading velocity of 1 m/s on the other beveled bar. This loading velocity is chosen after simulations with various loading velocity (0.1, 0.5 and 1 m/s). For this loading velocity, the ratio of the kinetic energy to the strain energy is very small (about 10^{-4}) and inertia effects are insignificant.

A comparison between the three simulated responses with the experimental one suggest that a loading velocity of 1 m/s ensures a gain of the computing time of 75 % for an enhancement of 3 % at the crushing response comparing with 0.5 m/s (figure 3.6).

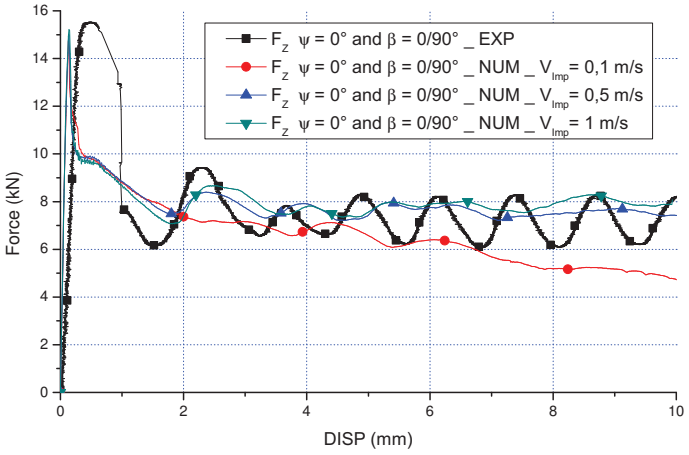

Figure 3.6: *The choice of the loading velocity under quasi-static loading*

In this section, the effects of the loading angle and the in-plane orientation angle are investigated numerically on the F_Z force component. In addition, the experimental validation is presented taking into account ψ and β angles.

3.3.1.1 The loading angle ψ effects

Figures (3.7 for $\beta = 0°$ and appendices B.1, B.2 and B.3 for the other β angle values) present the loading angle ψ effects on the force-displacement responses for the quasi-static mixed shear-compression loading.

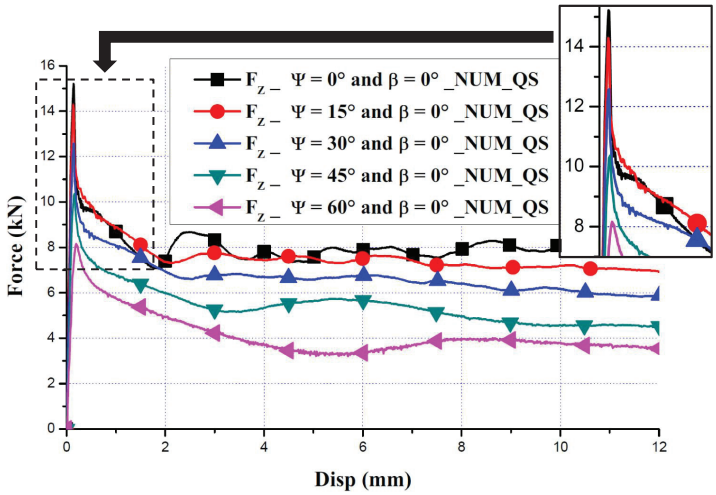

Figure 3.7: *The loading angle ψ effects under* ***numerical quasi-static*** *mixed shear-compression loading for $\beta = 0°$*

For all in plane orientation angles, no significant effect is observed at the slope of the elastic part. However, a significant effect is reported not only on the initial peak force but also on the average crushing force (figure 3.7). It can be noticed that the quasi-static crushing responses decrease with the increase of the loading angle ψ.

3.3.1.2 The in-plane orientation angle β effects

The effects of the angle in-plane orientation angle β on the quasi-static mixed shear-compression honeycomb behaviour is investigated by comparing the force-displacement responses at the four in-plane orientation angles with the fives loading angles. The results are shown for the aluminium ***Al5056-N-6-1/4-0.003*** honeycomb specimen in figures (3.8 for $\psi = 60°$ and appendices B.4, B.5 and B.6 for the other loadings angles.

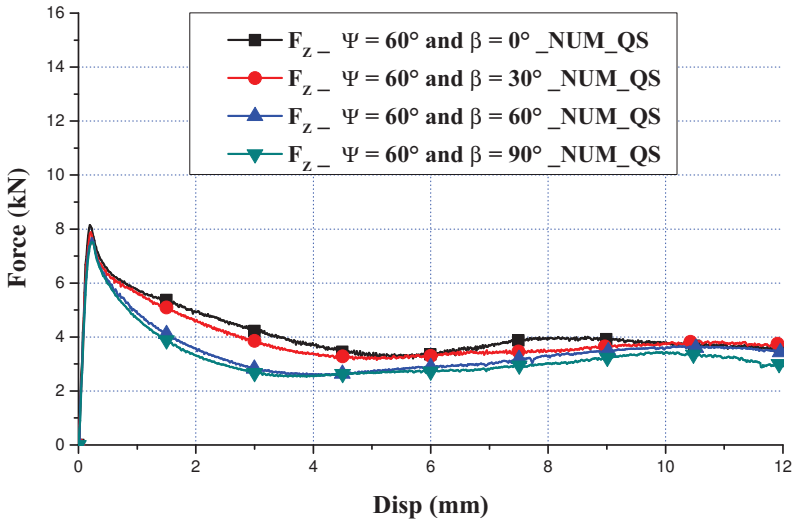

Figure 3.8: *The in-plane orientation angle β effects under **numerical quasi-static** mixed shear-compression loading for $\psi = 60°$*

Under quasi-static mixed shear-compression loading, the effect of in-plane orientation angle is small in general. The effect becomes more pronounced when the shear load becomes more dominant i.e (the loading angle ψ increases) especially on the average crushing force (plateau) such as displayed in the figure 3.8.

3.3.1.3 Experimental validation : β and ψ angles effects

Figure 3.9 presents a comparison between the experimental and numerical crushing responses under uni-axial compression loading and for one configuration of the mixed shear-compression loading. A good agreement is observed between the numerical curve and the experimental one.

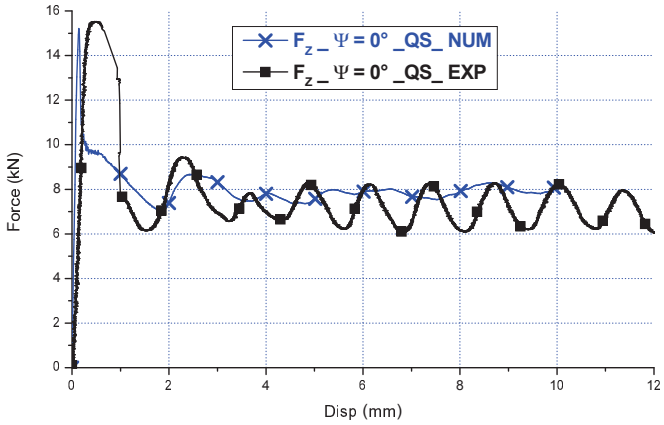

(a) Uni-axial compression = 0 °

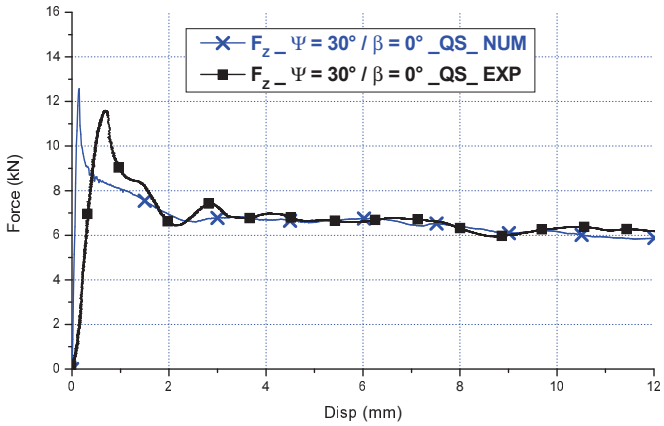

(b) Mixed shear-compression = 30 °/ = 0°

Figure 3.9: *Comparison between the experimental and numerical crushing responses under* ***quasi-static*** *(a) uni-axial compression $\psi = 0°$ and (b) mixed shear-compression $\psi = 30°$ and $\beta = 0°$*

The in-plane orientation angle as well as the loading angle effects are summarised in tables 3.2 and presented in figures 3.10 to 3.13 for the numerical and experimental results (with standard deviation) under quasi-static loading conditions.

Table 3.2: *Numerical and experimental initial peak force and average crushing force under* ***quasi-static*** *mixed shear-compression loading*

ψ	β	Initial peak force (kN)			Average crushing force (kN)		
		EXP	NUM	Error (%)	EXP	NUM	Error (%)
0°	0°	15.52	15.2	2.06	7.3	8.01	9.72
	30°	15.52	15.2	2.06	7.3	8.01	9.72
	60°	15.52	15.2	2.06	7.3	8.01	9.72
	90°	15.52	15.2	2.06	7.3	8.01	9.72
15°	0°	13.13	14.27	8.68	7.15	7.56	5.73
	30°	13.37	14.19	6.13	7.03	7.65	8.82
	60°	12.97	14.25	9.86	7.18	7.51	4.59
	90°	12.72	14.21	11.71	7.09	7.48	5.50
30°	0°	11.59	12.57	8.45	6.51	6.67	2.54
	30°	11.82	12.31	4.14	6.65	6.48	2.55
	60°	11.15	12.26	9.95	6.43	6.39	0.62
	90°	10.83	12.2	12.65	6.51	6.50	0.15
45°	0°	10.04	10.35	3.08	5.14	5.39	4.86
	30°	9.78	10.02	2.45	5.43	5.11	5.89
	60°	9.40	9.94	5.74	5.77	4.89	**15.25**
	90°	8.48	9.74	14.85	5.29	4.91	7.18
60°	0°	8.14	8.14	0	3.70	4.09	10.54
	30°	7.23	7.88	8.99	4.04	3.98	1.48
	60°	6.68	7.66	14.67	3.63	3.41	6.06
	90°	6.46	7.51	**16.25**	3.57	3.20	10.36

A good agreement between experimental and numerical results at the initial peak force and the average crushing force is provided for all configurations under quasi-static loading with an acceptable difference.

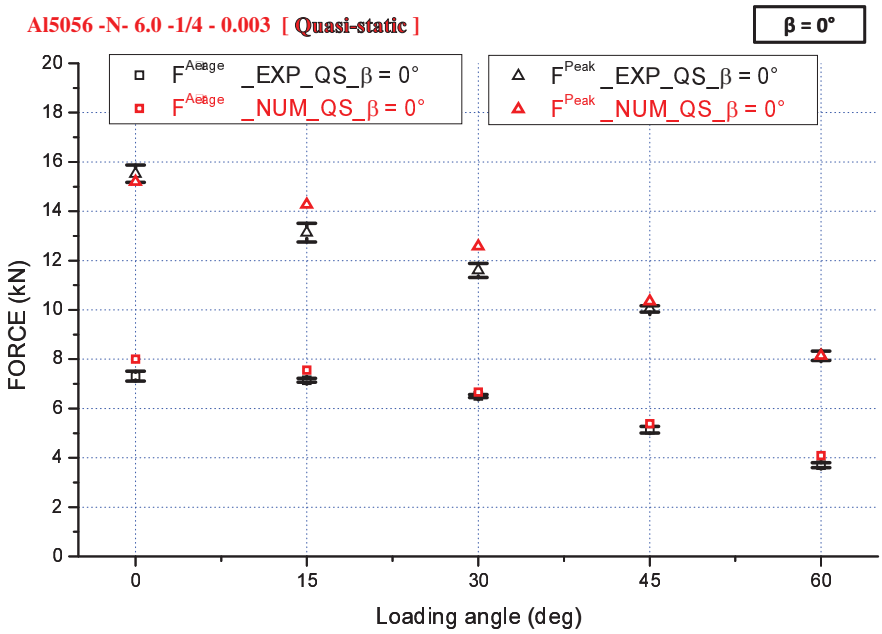

Figure 3.10: *Numerical and experimental initial peak and average crushing forces under* ***quasi-static*** *mixed shear-compression loading for* $\beta = 0°$

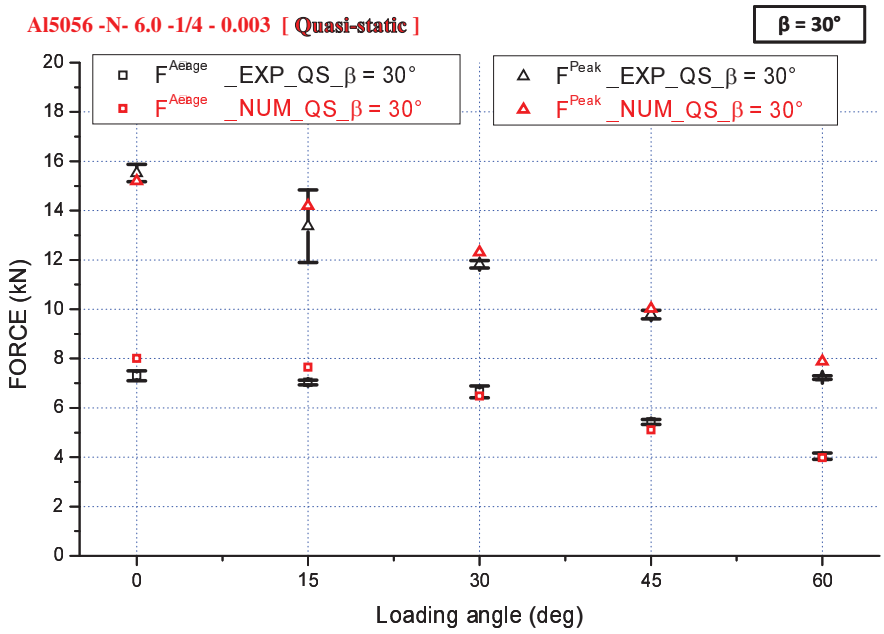

Figure 3.11: *Numerical and experimental initial peak and average crushing forces under* ***quasi-static*** *mixed shear-compression loading for* $\beta = 30°$

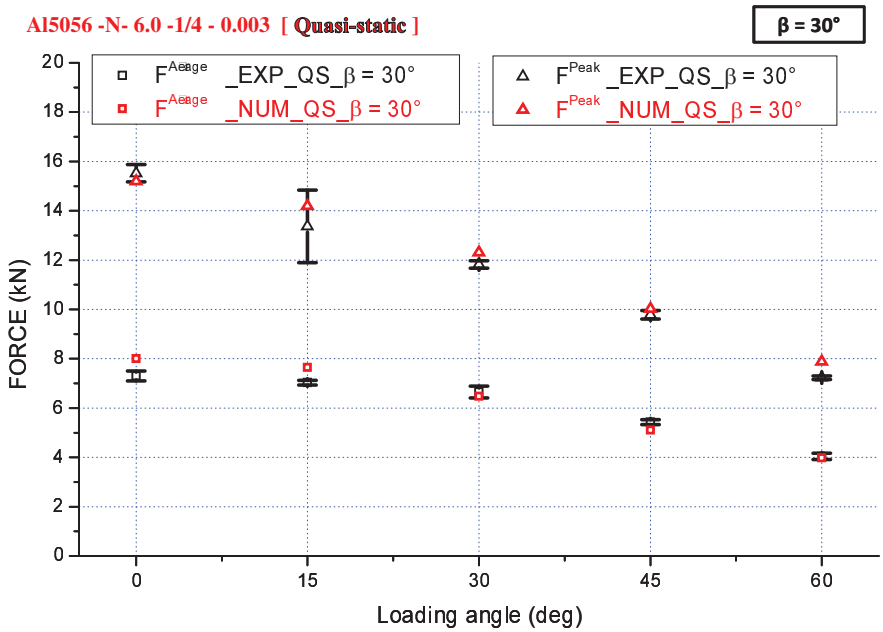

Figure 3.12: *Numerical and experimental initial peak and average crushing forces under* ***quasi-static*** *mixed shear-compression loading for* $\beta = 60°$

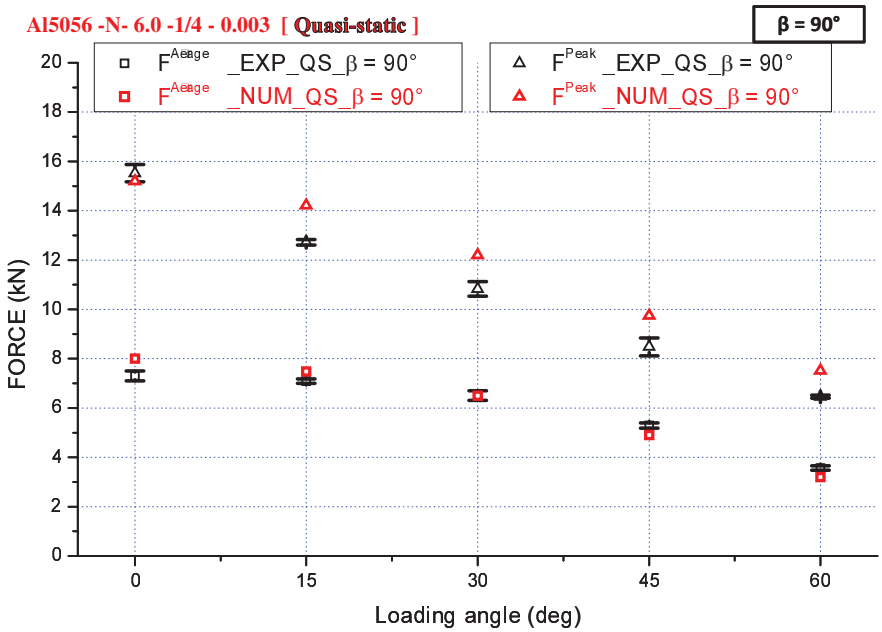

Figure 3.13: *Numerical and experimental initial peak and average crushing forces under* ***quasi-static*** *mixed shear-compression loading for* $\beta = 90°$

3.3.2 The crushing responses under dynamic loading

For the numerical simulations under dynamic loading, the use of the input and the output velocities obtained by the experiments provided a crushing displacement of 11 mm.

3.3.2.1 The loading angle ψ effects

Similarly to quasi-static conditions, the loading angle ψ effects on the mixed shear-compression honeycomb behaviour is studied numerically under dynamic conditions by presenting the force-displacement curves of the fives loading angles and four in-plane orientation angles for the aluminium ***Al5056-N-6-1/4-0.003*** honeycomb specimen (figures 3.14 for $\beta = 0°$ and appendices B.7, B.8 and B.9 for the other β angle values).

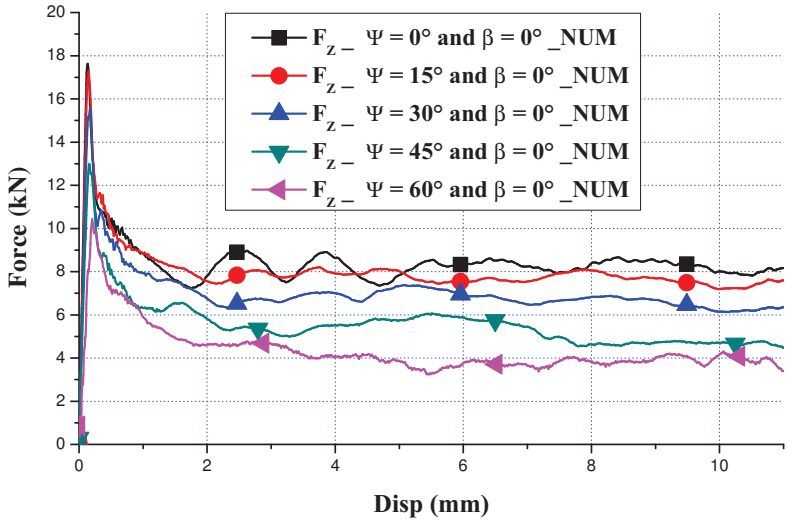

Figure 3.14: *The loading angle ψ effects under **numerical dynamic** mixed shear-compression loading for $\beta = 0°$*

For each in plane orientation angles, the same observations as under quasi-static simulations are obtained. A small difference at the slope of the elastic part is shown on the dynamic crushing responses. However, focusing on the initial peak and the average crushing forces, a significant effect of ψ is observed and the level of the dynamic responses decreases when the loading angle ψ increases.

3.3.2.2 The in-plane orientation angle β effects

For the influence of the in-plane orientation angle, the results are presented for in figures 3.15 for $\psi = 15°$ and appendices B.10, B.11 and B.12 for the other ψ angle values.

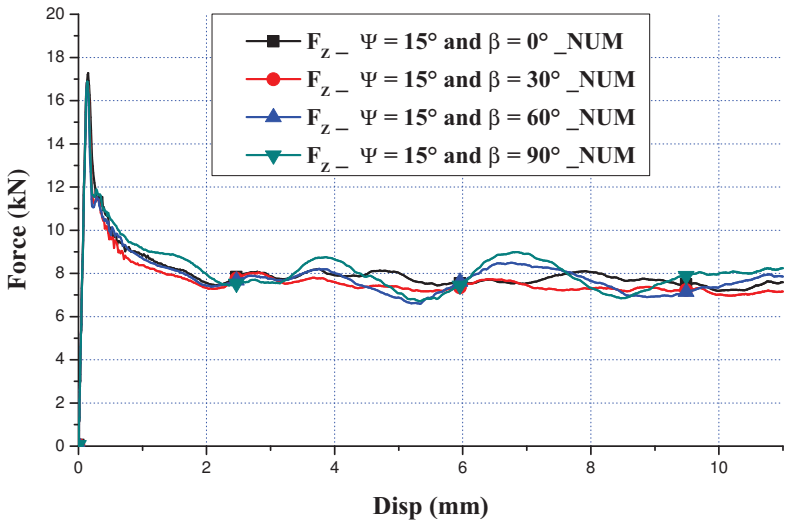

Figure 3.15: *The in-plane orientation angle β effects under* ***numerical dynamic*** *mixed shear-compression loading for $\psi = 15°$*

A negligible effect of the in-plane orientation angle is observed for all loading angles. For $\psi = 15°$, 30° and 45° the influence is not very significant however for the loading angle $\psi = 60°$, the effects of the in-plane orientation becomes more pronounced. In fact, when the loading angle increases the influence on the in-plane orientation angle becomes more significant.

3.3.2.3 Experimental validation : β and ψ angles effects

Figure 3.16 presents the crushing responses under dynamic uni-axial compression loading and dynamic mixed shear-compression loading ($\psi =$ 30 ° and β= 60°). A good agreement is observed between the experimental and numerical responses.

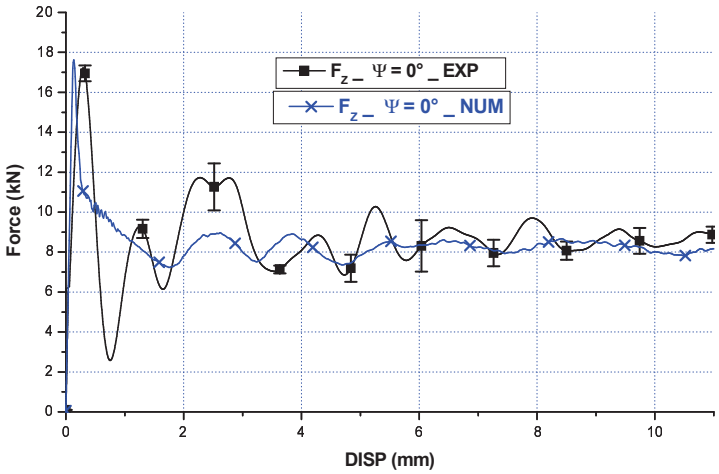

(a) Uni-axial compression = 0 °

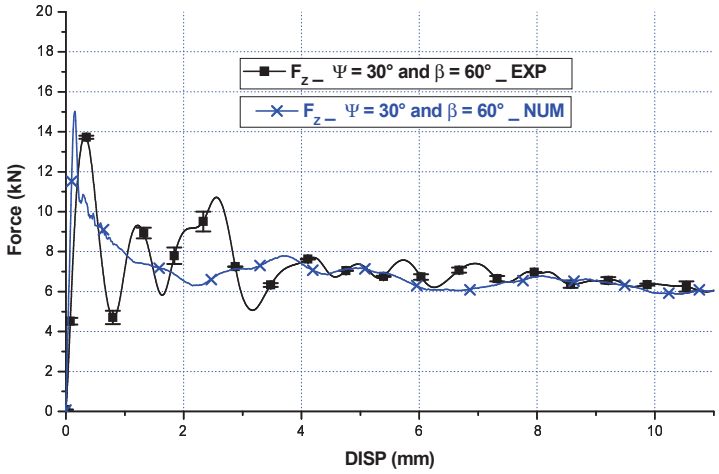

(b) Mixed shear-compression = 30 °/ = 60°

Figure 3.16: *Comparison between the experimental and numerical crushing responses under* ***dynamic*** *(a) uni-axial compression $\psi = 0°$ and (b) mixed shear-compression $\psi = 30°$ and $\beta = 60°$*

Table 3.3 summarises the results for the different loading angles with various in-plane orientation angles.

Table 3.3: *Numerical and experimental initial peak force and average crushing force (kN) under **dynamic** mixed shear-compression loading*

ψ	β	Initial peak force (kN)			Average crushing force (kN)		
		EXP	NUM	Error (%)	EXP	NUM	Error (%)
0°	0°	16.92	17.61	4.07	8.70	8.45	2.87
	30°	16.92	17.61	4.07	8.70	8.45	2.87
	60°	16.92	17.61	4.07	8.70	8.45	2.87
	90°	16.92	17.61	4.07	8.70	8.45	2.87
15°	0°	17.96	17.27	3.84	8.93	7.9	11.53
	30°	16.83	16.84	0.06	8.55	7.59	11.22
	60°	16.95	16.83	0.70	8.61	7.84	8.94
	90°	18.35	16.88	8.01	8.47	8.22	2.95
30°	0°	13.61	15.6	14.62	6.77	6.87	1.47
	30°	13.80	15.39	11.52	6.80	6.71	1.32
	60°	13.77	15.00	8.93	6.59	6.71	1.82
	90°	13.76	14.94	8.57	6.79	6.88	1.32
45°	0°	11.29	12.98	14.97	5.16	5.48	6.20
	30°	9.96	12.75	28.01	5.50	5.27	4.18
	60°	10.28	12.53	21.88	5.80	5.84	0.67
	90°	9.65	12.31	27.56	5.30	5.05	4.71
60°	0°	7.88	10.43	**32.36**	3.42	4.01	17.25
	30°	6.18	10.10	**63.43**	2.84	3.28	15.49
	60°	5.86	9.44	**61.09**	2.97	3.51	**18.18**
	90°	6.00	9.33	**55.50**	2.93	3.31	12.96

Under dynamic conditions, the numerical responses under uni-axial loading and mixed shear-compression loading show a good correlation with experimental results for the loading angle. Nevertheless, when the loading angle increases $\psi \geq 45°$, the initial peak force is overestimated in the numerical responses. The average crushing force shows a good correlation between the numerical results and the experimental ones. The error becomes more pronounced for $\psi = 60°$. This could be explain by the complexity of the experimental collapse mechanisms when the loading angle increases ($\psi = 60°$). For the clarity of the comparison between the experimental and numerical results, figures 3.17, to 3.20 present the initial peak and average crushing forces for all configurations of loading under dynamic condition.

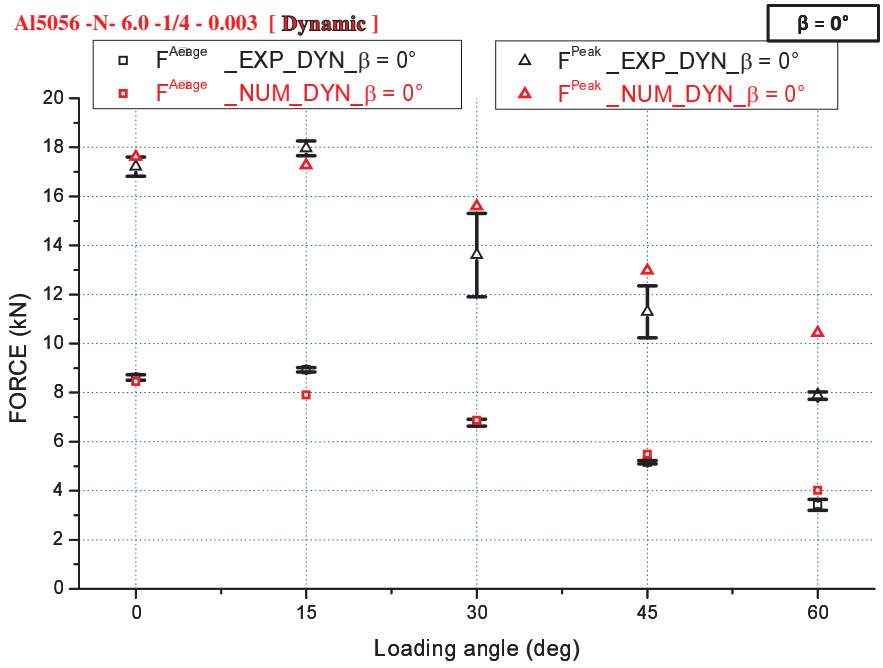

Figure 3.17: *Numerical and experimental initial peak and average crushing forces under* ***dynamic*** *mixed shear-compression loading for* $\beta = 0°$

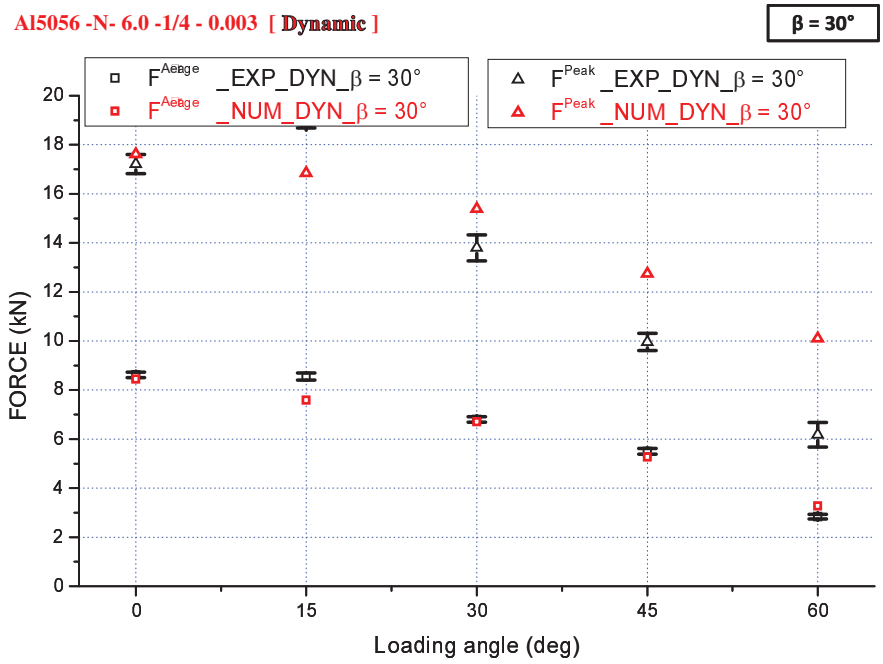

Figure 3.18: *Numerical and experimental initial peak and average crushing forces under* ***dynamic*** *mixed shear-compression loading for* $\beta = 30°$

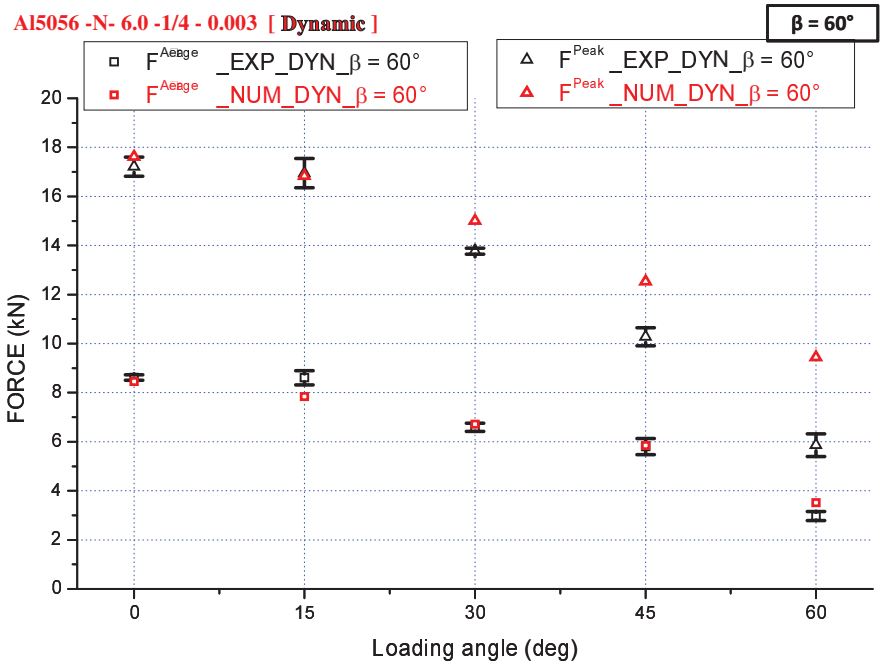

Figure 3.19: *Numerical and experimental initial peak and average crushing forces under* ***dynamic*** *mixed shear-compression loading for* $\beta = 60°$

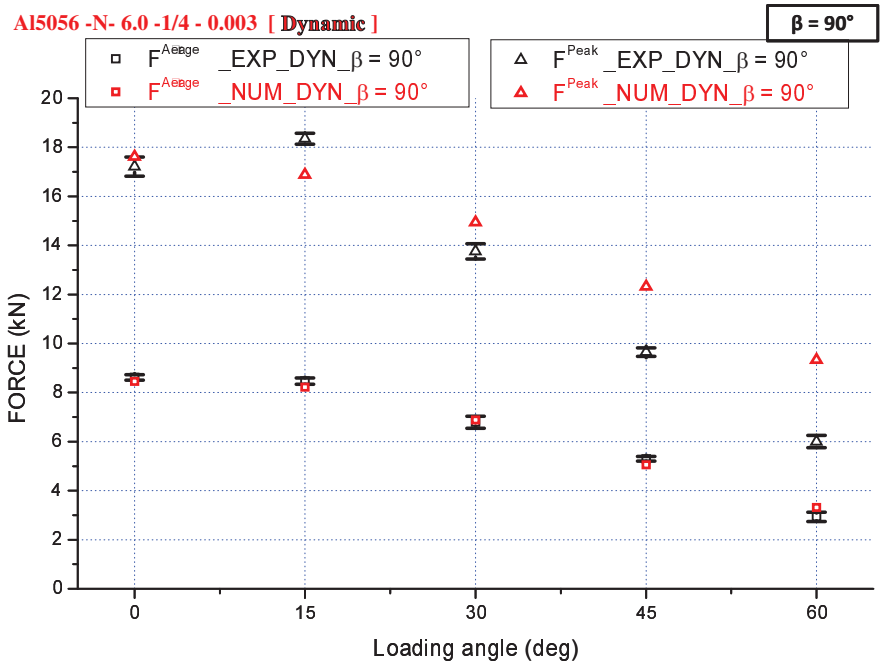

Figure 3.20: *Numerical and experimental initial peak and average crushing forces under* ***dynamic*** *mixed shear-compression loading for* $\beta = 90°$

Based on the comparison between the experimental and numerical results under quasi-static and dynamic mixed loading, a good correlation is reported

in term of initial peak and average crushing forces. The numerical model was less successful on the initial peak force as well as the average crushing force when the loading increases $\psi \geq 45°$. So, to explain this difference, a numerical investigation of the collapse mechanisms including the deforming pattern modes is performed. Under dynamic loading, the collapse mechanisms are observed through the high speed video at the side of the specimen. As the experimental local collapse mechanisms (inside the specimen) are not accessible, they are analysed on the numerical model previously validated.

3.3.3 The collapse mechanisms

The collapse mechanisms including the global deforming pattern modes of the specimens and the local collapse mechanisms at cells level are investigated under quasi-static and dynamic loading conditions. In this section, a full description of the numerical collapse mechanisms is presented. An experimental validation is realised focusing on the deforming pattern modes.

3.3.3.1 Numerical collapse mechanisms under uni-axial compression

The successive folding system is identified with an horizontal plastic hinge lines in addition to the compatibility zones observed by Mohr et al.[Mohr 04a]. The deforming pattern mode I is observed in figure 3.21.

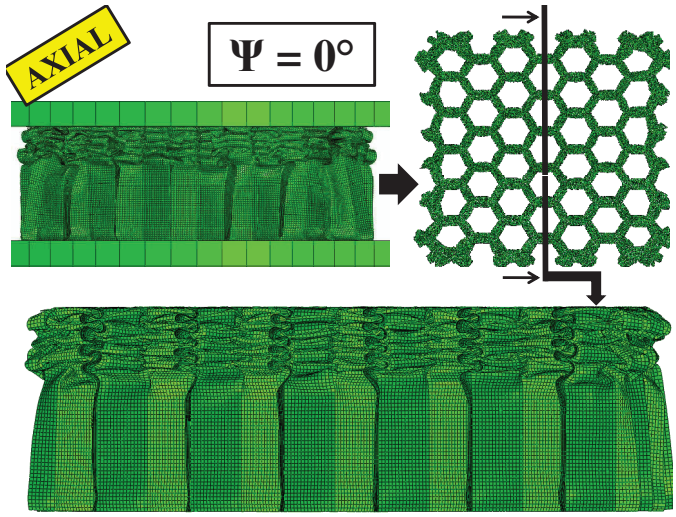

Figure 3.21: *The collapse mechanisms under dynamic uni-axial compression loading for $\psi = 0°$: numerical results*

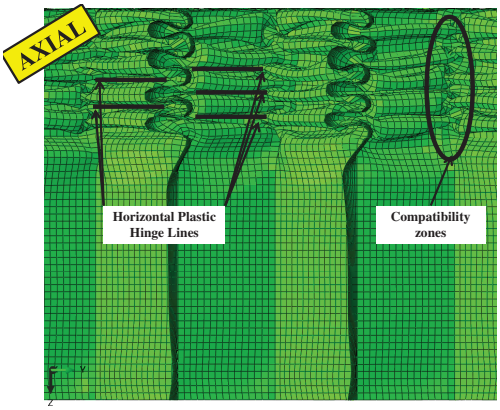

Figure 3.22: *The deforming pattern mode under dynamic uni-axial compression loading for $\psi = 0°$: numerical results*

The section cut of the crushed specimen under uni-axial compression is presented in figure 3.21. A detailed collapse mechanisms of the cell wall is presented by figure 3.22. The plastic hinge lines are horizontal in both simple and double wall thickness. The compatibility zones are localized in the intersection axis of the two cell walls.

3.3.3.2 Numerical collapse mechanisms under mixed shear-compression

Under mixed shear-compression, the collapse mechanisms focusing on the deforming pattern modes are presented in this section. Three deforming pattern modes are identified numerically.

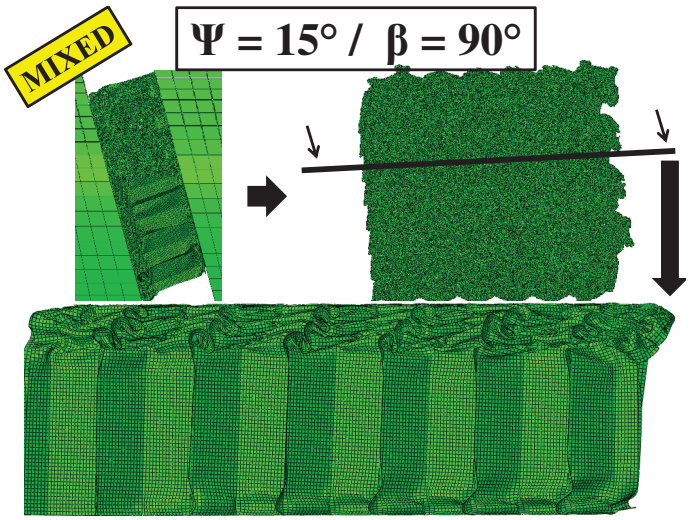

Figure 3.23: *The collapse mechanisms under dynamic mixed shear-compression loading for $\psi = 15°$ and $\beta = 90°$: numerical results*

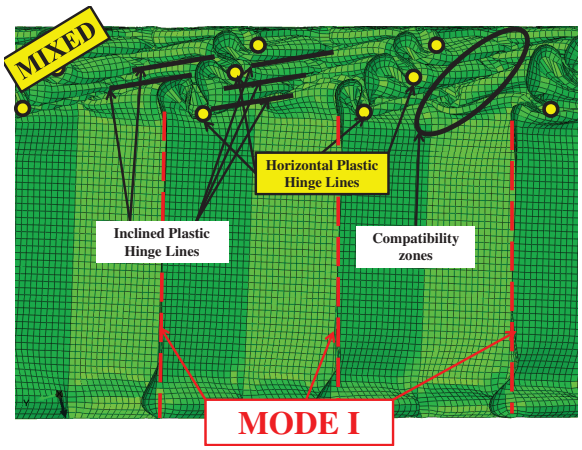

Figure 3.24: *The deforming pattern* ***mode I*** *under dynamic mixed shear-compression loading for $\psi = 15°$ and $\beta = 90°$: numerical results*

Figures 3.23 and 3.24 present the collapse mechanisms and the deforming pattern mode under dynamic mixed shear-compression loading for $\psi = 15°$ and $\beta = 90°$. The deforming pattern mode " **mode I** " is observed. The cut section of the crushed specimen shows horizontal plastic hinge lines on the double wall thickness and inclined plastic hinge lines on the simple wall thickness, no rotation of the cell axis is observed. The compatibility zones are localised on the inclined part of the cell axis.

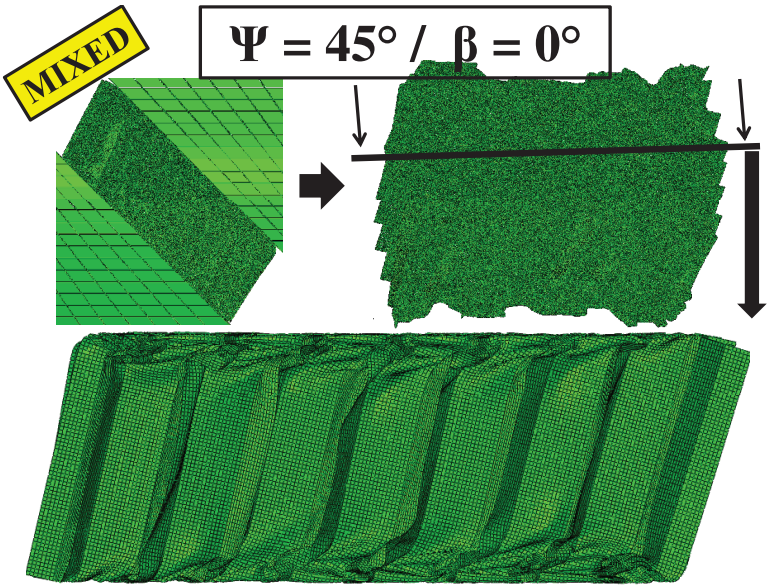

Figure 3.25: *The collapse mechanisms under dynamic mixed shear-compression loading for $\psi = 45°$ and $\beta = 0°$: numerical results*

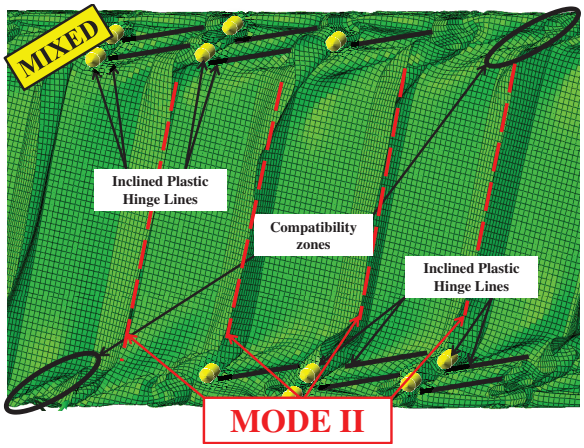

Figure 3.26: *The deforming pattern* ***mode II*** *under dynamic mixed shear-compression loading for $\psi = 45°$ and $\beta = 0°$: numerical results*

Figures 3.25 and 3.26 present the collapse mechanisms and the deforming pattern mode under dynamic mixed shear-compression loading for $\psi = 45°$ and $\beta = 0°$. The deforming pattern mode " **mode II** " is observed. The cut section of the crushed specimen shows inclined plastic hinge lines on both the double cell wall thickness and the simple cell wall thickness. Due to the inclined successive collapse mechanisms, the rotation of the cell axis is observed. Here, the formation of the fold is observed simultaneously at the two sides of the specimen that is different to " **mode I** ". Indeed, the compatibility zones are localised at the both sides of specimen (at the top and at the bottom).

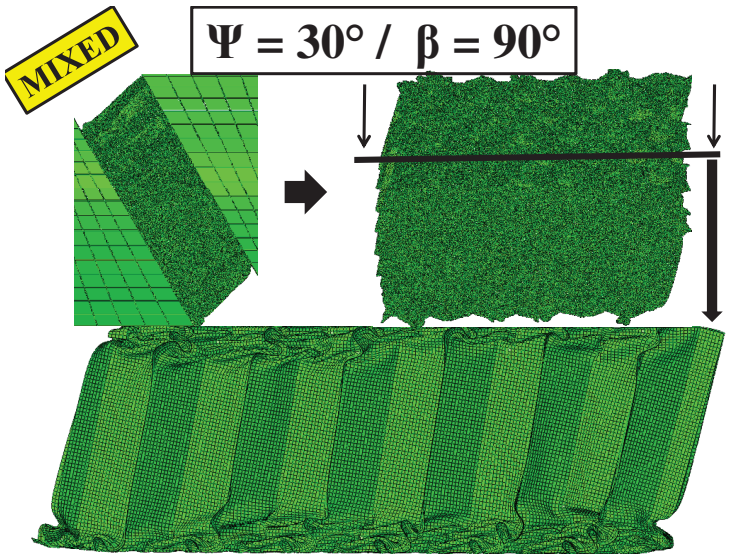

Figure 3.27: *The collapse mechanisms under dynamic mixed shear-compression loading for $\psi = 30°$ and $\beta = 90°$: numerical results*

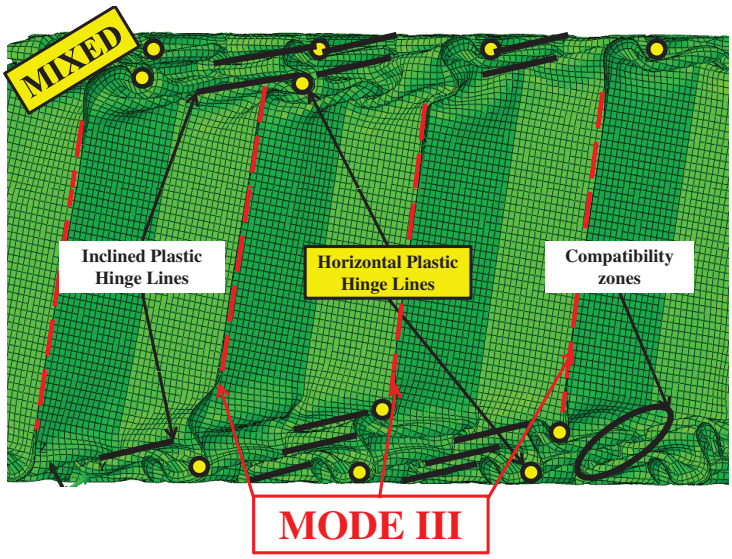

Figure 3.28: *The deforming pattern* ***mode III*** *under dynamic mixed shear-compression loading for $\psi = 30°$ and $\beta = 90°$: numerical results*

Figures 3.27 and 3.28 present the collapse mechanisms and the deforming pattern mode under dynamic mixed shear-compression loading for $\psi = 30°$ and $\beta = 90°$. The deforming pattern mode " **mode III** " is observed. The cut section of the crushed specimen shows horizontal plastic hinge lines on the double wall thickness and inclined plastic hinge lines on the simple wall thickness at the top and bottom of the specimen. The formation of the fold in both sides of specimen leads to the global rotation of the specimen.

3.3.3.3 The in-plane orientation angle effect on the collapse mechanisms

To explain more on details the three existing different deforming pattern modes, the equivalent plastic strain (PEEQ) distribution is analysed at the cell level.

Figure 3.29 presents the mode I. The shear load direction is perpendicular to the double wall thickness ($\beta = 90°$). This leads to the folding of the double wall thickness without any shearing. Thus, the formed plastic hinge lines are horizontal. The progressive folding system is localised at only one side of the specimen (top or bottom).

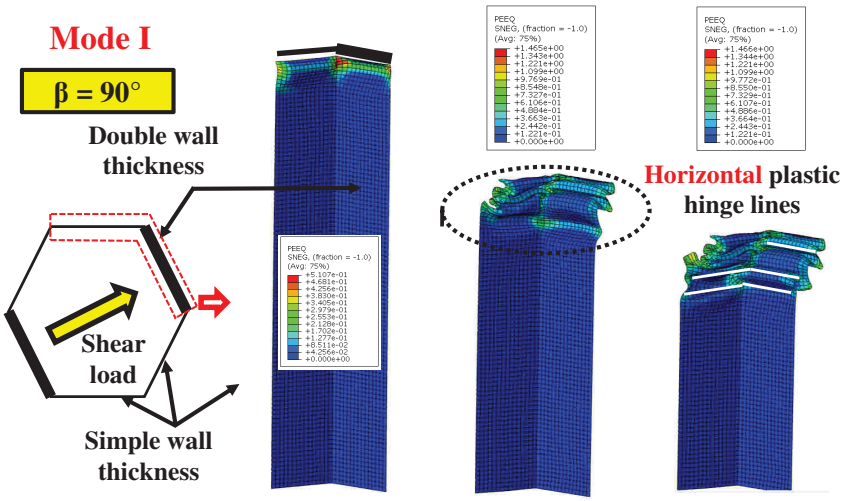

Figure 3.29: *The deforming pattern* ***mode I*** *at the cell level for* $\beta = 90°$

Figure 3.30 presents the mode II. The shear load direction is parallel to the double wall thickness ($\beta = 0°$). This leads to the folding of double and simple wall thickness with shearing. Thus, all the formed plastic hinge lines are inclined. the progressive folding system is localised at the both sides of the specimen that allows the rotation of the cell axis simultaneously with the folding process.

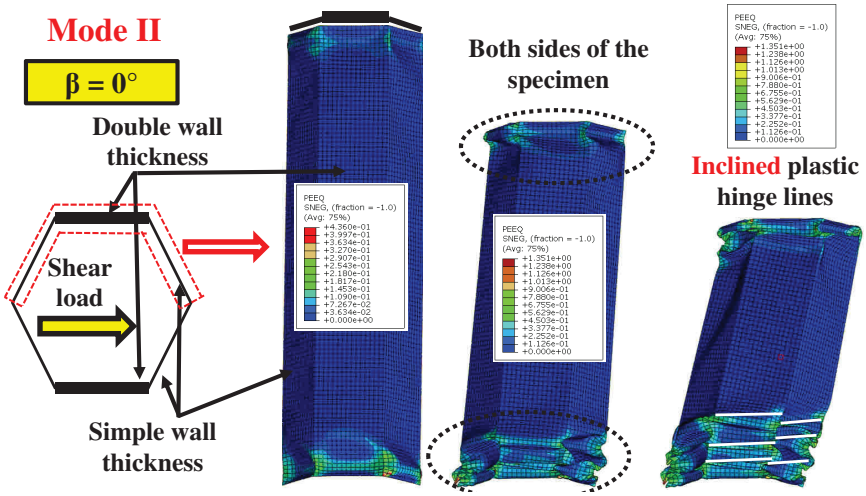

Figure 3.30: *The deforming pattern* ***mode II*** *at the cell level for* $\beta = 0°$

Figure 3.31 presents the mode III. The shear load direction is perpendicular to the simple wall thickness ($\beta = 30°$). This leads to the folding of simple wall thickness without shearing and the double wall thickness with shearing. Thus, the formed plastic hinge lines are horizontal (simple wall thickness) and inclined (double wall thickness). The progressive folding system is localised at the both sides of the specimen that allows to the global rotation of the specimen.

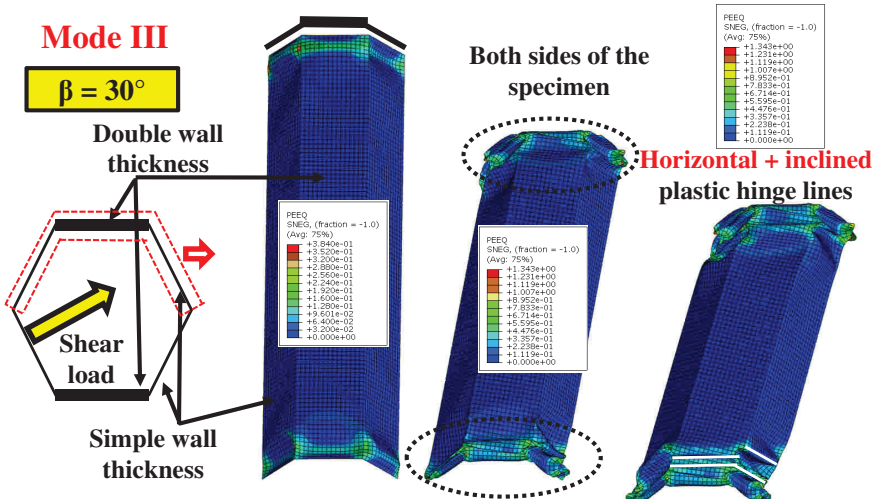

Figure 3.31: *The deforming pattern* ***mode III*** *at the cell level for* $\beta = 30°$

3.3.4 Numerical and experimental deforming pattern modes

In this section, a comparative study is achieved between the experimental and numerical collapse mechanisms. Under both quasi-static and dynamic mixed shear-compression loading, the deforming pattern modes are compared taking into account the coupled effect of the loading angle and the in-plane orientation angle.

The three identified deforming pattern modes are verified both numerically and experimentally and shown in figure 3.32.

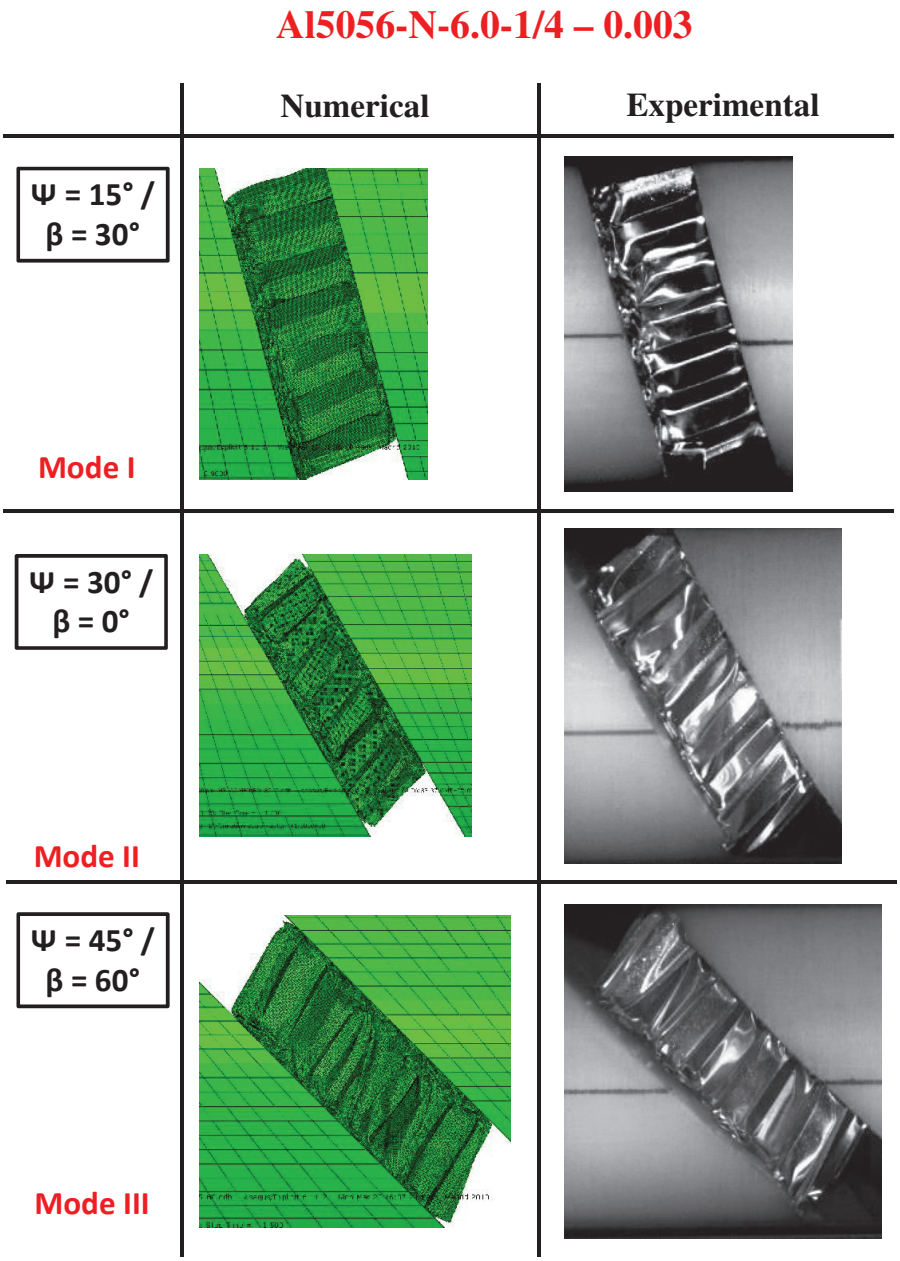

Figure 3.32: *Good correlation between the experimental and numerical deforming pattern modes*

Tables 3.5 and 3.4 present the experimental deforming pattern modes compared to the numerical ones under quasi-static and dynamic loadings, respectively.

Table 3.4: *The deforming patterns modes under* ***quasi-static*** *mixed shear-compression loading: numerical and experimental results*

	$\beta = 0°$		$\beta = 30°$		$\beta = 60°$		$\beta = 90°$	
	NUM	EXP	NUM	EXP	NUM	EXP	NUM	EXP
$\psi = 0°$	MI	MI	MI	MI	MI	MI	MI	MI
$\psi = 15°$	***MII***	***MII***	MI	MI	MI	MI	MI	**MIII**
$\psi = 30°$	***MII***	***MII***	MI	***MII***	**MIII**	***MII***	**MIII**	MI
$\psi = 45°$	***MII***	***MII***	**MIII**	**MIII**	**MIII**	**MIII**	**MIII**	MI
$\psi = 60°$	***MII***	***MII***	**MIII**	**MIII**	**MIII**	**MIII**	**MIII**	MI

Table 3.5: *The deforming pattern modes under* ***dynamic*** *mixed shear-compression loading: numerical and experimental results*

	$\beta = 0°$		$\beta = 30°$		$\beta = 60°$		$\beta = 90°$	
	NUM	EXP	NUM	EXP	NUM	EXP	NUM	EXP
$\psi = 0°$	MI	MI	MI	MI	MI	MI	MI	MI
$\psi = 15°$	***MII***	MI	**MIII**	MI	***MII***	MI	**MIII**	MI
$\psi = 30°$	***MII***	***MII***	**MIII**	***MII***	**MIII**	MI	**MIII**	MI
$\psi = 45°$	***MII***	***MII***	**MIII**	**MIII**	**MIII**	**MIII**	**MIII**	MI
$\psi = 60°$	***MII***	***MII***	**MIII**	**MIII**	**MIII**	**MIII**	**MIII**	**MIII**

For $\beta = 0°$, the deforming pattern mode " **mode II** " is the dominant mode numerically and experimentally for all loading angle under quasi-static and dynamic loading. For $\beta = 30°$ and $\beta = 60°$, the three deforming pattern modes " **mode I** ", " **mode II** " and " **mode III** " are observed. When the loading angle ψ increases the mode " **mode III** " becomes more dominant. For $\beta = 90°$, a difference on the deforming modes is reported between numerical and experimental collapse mechanisms. The most experimental cases under quasi-static and dynamic loadings are folded according to " **mode I** " by contrast according to " **mode III** " for the simulations.

3.3.5 Numerical and experimental local collapse mechanisms

It's difficult to observe the local collapse mechanisms for all configurations. So a set of configurations is chosen to realise a section cut of the experimental crushed specimen under quasi-static loading. Therefore, a comparison

is achieved between the experimental local collapse mechanisms and the simulated ones.

The comparison is performed for the following loading configurations, firstly for the uni-axial loading ($\psi = 0°$), secondly for seven configurations of the mixed shear-compression loading : ($\psi = 15°/\ \beta = 30°$, $\psi = 30°/\ \beta = 0°$, $\psi = 30°/\ \beta = 90°$, $\psi = 45°/\ \beta = 0°$, $\psi = 45°/\ \beta = 60°$, $\psi = 60°/\ \beta = 0°$ and $\psi = 60°/\ \beta = 90°$) such as presented in figure 3.33.

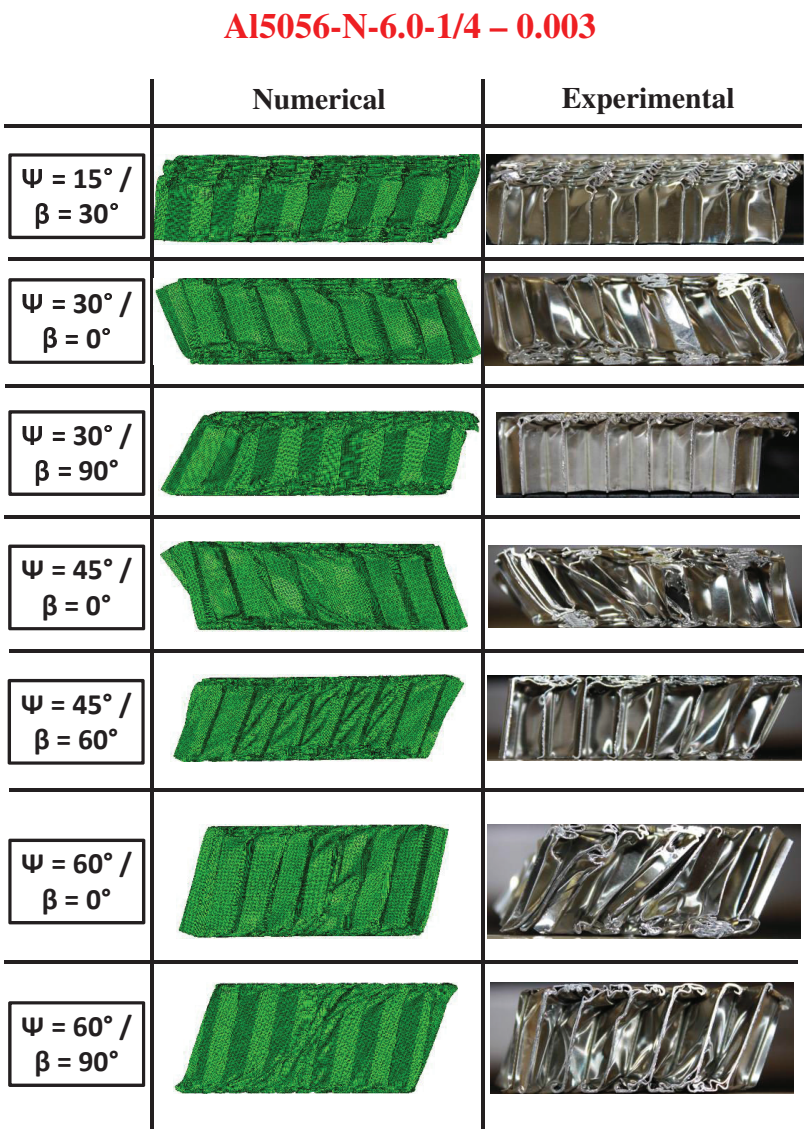

Figure 3.33: *The comparison between the experimental and numerical local collapse mechanisms under quasi-static mixed shear-compression loading*

Figure 3.33 shows that the numerical model is able to reproduce the experimental collapse mechanisms. A good correlation is observed not only for the deforming pattern modes but also for the local collapse mechanisms except for some cases of mixed loading ($\psi = 30°/\ \beta = 90°$).

This difference could be explain by the side effect and the boundary conditions. This phenomenon is observed experimentally under both uniaxial and mixed loadings such as shown in figure 3.34.

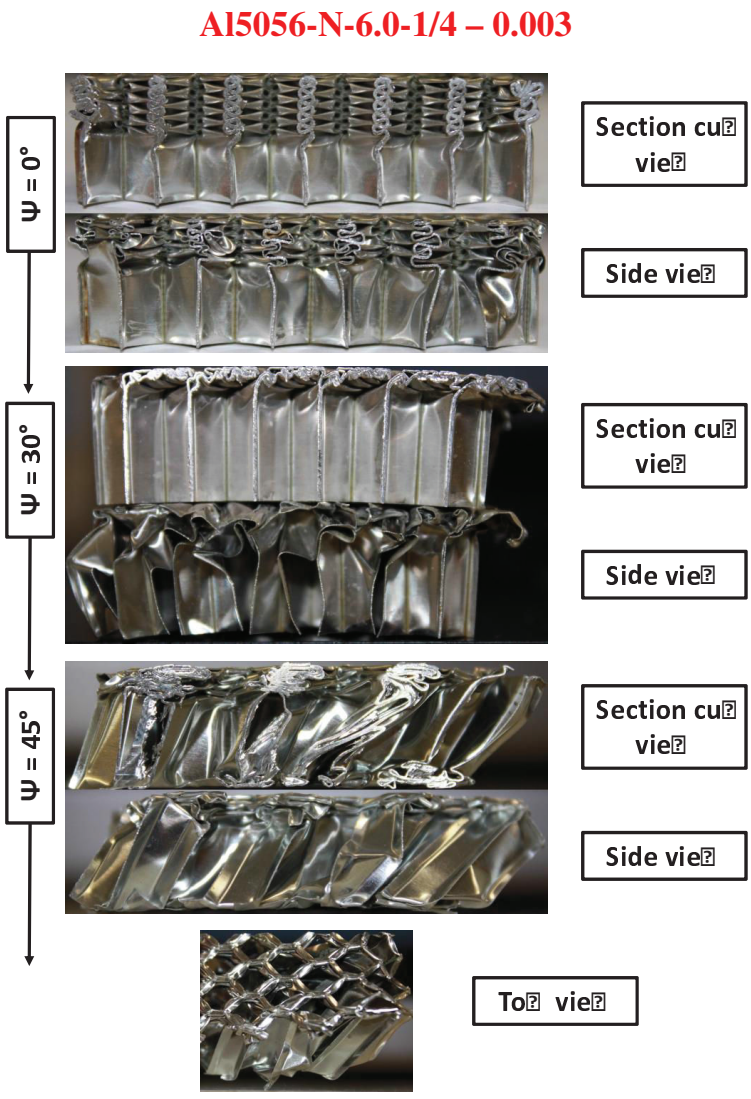

Figure 3.34: *The side effect on the collapse mechanisms under mixed shear-compression loading*

Figure 3.34 suggests that the distribution of collapse mechanisms is different from the side to the middle of the crushed specimen. Moreover, the side effect becomes more significant when the loading angle ψ increases.

As a conclusion, a good correlation between experimental and numerical results is observed on the crushing responses. The finite element model allows to reproduce faithfully the experimental collapse mechanisms with a good agreement in the deforming pattern modes. The validated finite element model is used in the next section to separate the normal and the shear behaviours under mixed shear-compression loading.

3.4 The normal and shear behaviours

The finite element model developed and validated previously is used in this section to get access to the tangential force component F_Y. Therefore, the normal and shear honeycomb behaviours under mixed shear-compression loading are presented separately. In addition, the average crushing normal and shear forces are calculated in order to identify the parameters of a macroscopic yield criterion for the aluminium honeycomb under mixed shear-compression. The macroscopic yield criterion presented in this thesis is depending on three parameters : the in-plane orientation angle β, the loading angle ψ and the impact velocity.

3.4.1 The in-plane orientation angle effects on the tangential force component (F_Y)

The influence of the in-plane orientation angle on the axial force component F_Z is investigated experimentally and numerically. A negligible effect is reported. So what about the effect of this angle on the tangential force component?

Figures 3.35 and 3.36 present the crushing force components for one loading angle $\psi = 45°$ with four in-plane orientation angles ($\beta = 0$ / 30 / 60 / 90°). The component force F_X was verified to be negligible and is not presented here. Figures 3.35 and 3.36 suggest that the influence of the in-plane orientation angle β is more pronounced at the tangential force component F_Y than at the axial force component F_Z.

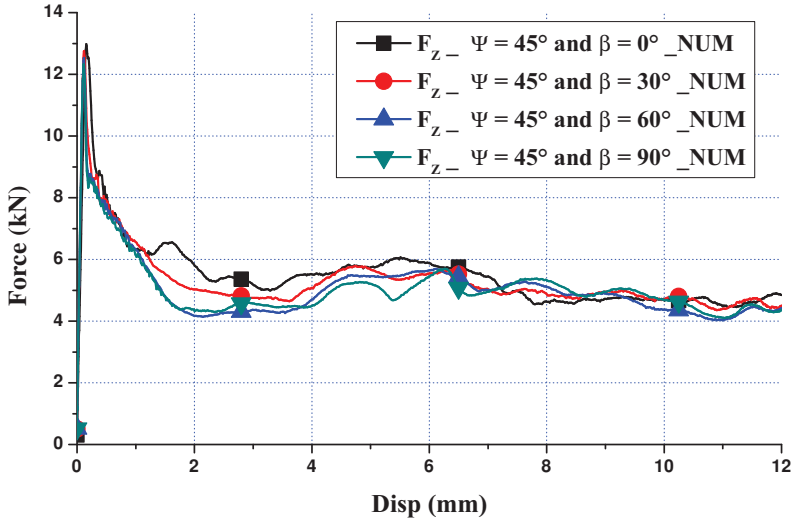

Figure 3.35: *The **numerical** crushing force components under dynamic mixed shear-compression loading for $\psi = 45°$ with various β: **F_Z force component***

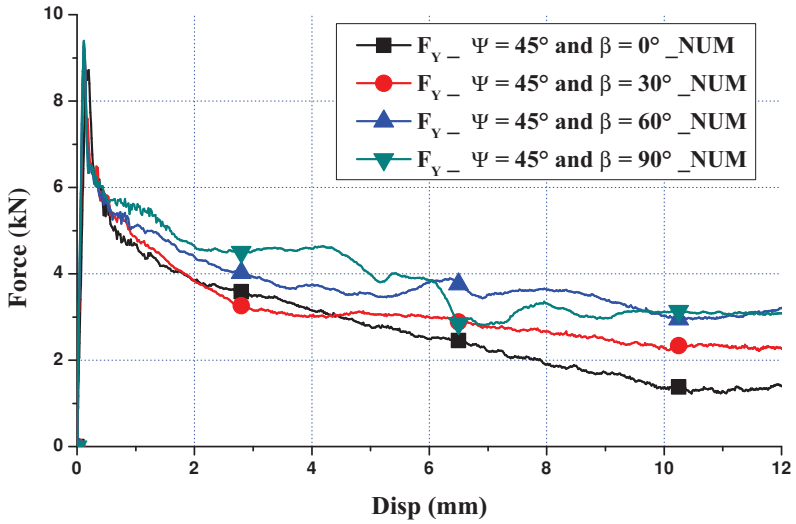

Figure 3.36: *The **numerical** crushing force components under dynamic mixed shear-compression loading for $\psi = 45°$ with various β: **F_Y force component***

3.4.2 Normal and shear crushing responses

Based on the numerical simulations, the normal and the shear forces in the frame of the specimen (figure 3.1) are calculated using the following equations

:

$$F_N = F_Z cos(\psi) + F_Y sin(\psi) \tag{3.4}$$

$$F_S = F_Z sin(\psi) - F_Y cos(\psi) \tag{3.5}$$

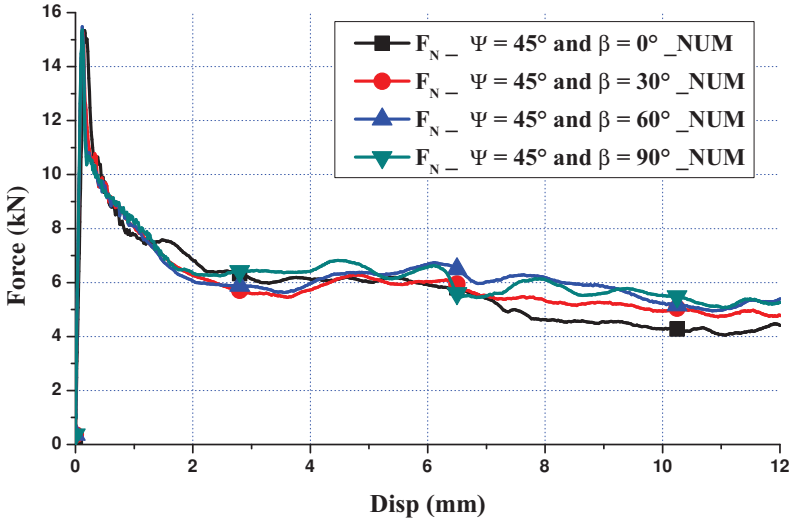

Figure 3.37: *The **numerical** crushing force components under dynamic mixed shear-compression loading for $\psi = 45°$ with various β: **F_N normal force component***

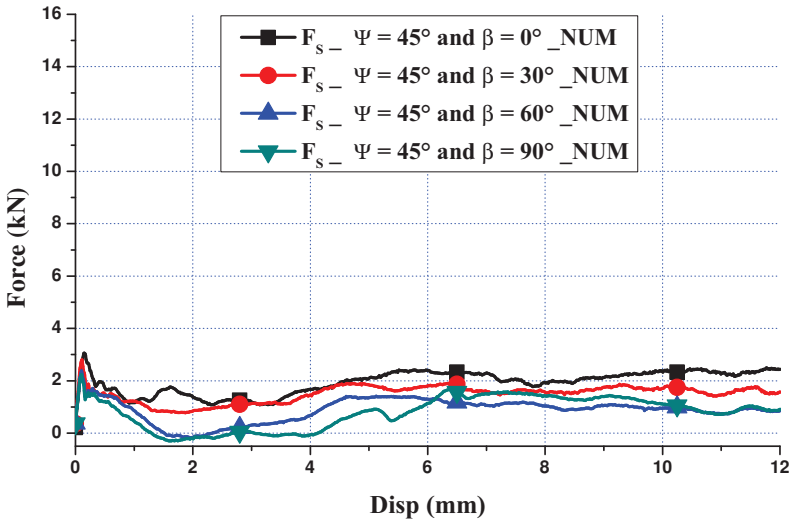

Figure 3.38: *The **numerical** crushing force components under dynamic mixed shear-compression loading for $\psi = 45°$ with various β: **F_S shear force component***

The influence of the in-plane orientation angle is fairly significant in the tangential force component F_Y. As a result, a significant effect is reported in the normal force component F_N and the shear force component F_S for a loading angle $\psi = 45°$ with four in-plane orientation angles. It is illustrated by figures 3.37 and 3.38. The in-plane orientation angle effect is more pronounced in the shear force F_S than in the normal force F_N.

Now, to study the combined effect of the three parameters: the in-plane orientation angle, the loading angle and the impact velocity for all loading configurations, a macroscopic yield criterion is suggested. It is based on the normal and shear crushing forces. The average crushing normal and shear forces are presented in the figure 3.39. and they are calculated by the following equations :

$$F_N^{Average} = \frac{1}{Cr_{max} - Cr_{peak}} \int_{Cr_{peak}}^{Cr_{max}} F_N(Cr)\mathrm{d}Cr \tag{3.6}$$

$$F_S^{Average} = \frac{1}{Cr_{max} - Cr_{peak}} \int_{Cr_{peak}}^{Cr_{max}} F_S(Cr)\mathrm{d}Cr \tag{3.7}$$

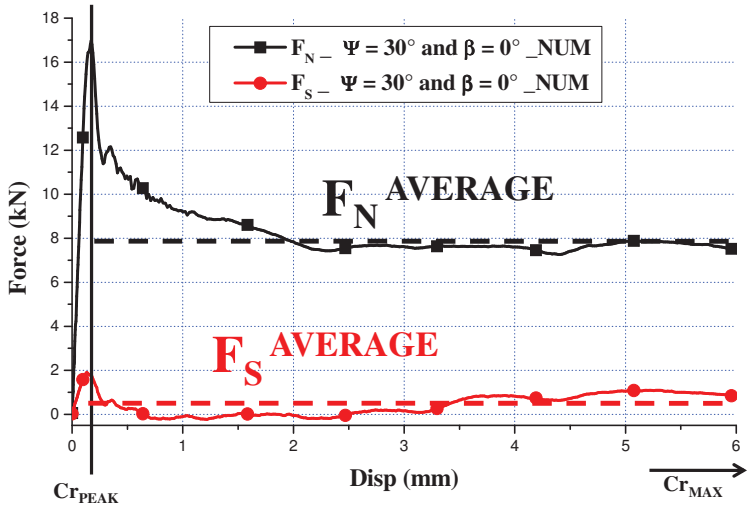

Figure 3.39: *The **numerical** average crushing force components under mixed shear-compression loading for $\psi = 30°$ and $\beta = 0°$: the normal and shear average crushing forces*

Finally, based on the numerical results validated by the experimental ones for all loading configurations, the numerical simulations allow to determine

the average crushing normal and shear forces. In addition, the identification of the macroscopic yield criterion parameters is performed.

3.5 Macroscopic Yield Criterion

Mohr and Doyoyo [Mohr 04a] suggested a linear fit for the crushing envelope for their honeycomb specimens with only one in-plane orientation angle $\beta = 90°$ based on their finite element analysis. However, the quadratic yield criterion developed by Hong et al.[Hong 06a, Hong 08] gives a good description of the macroscopic crush behaviour of honeycomb specimens under quasi-static and dynamic loading conditions with different in-plane orientation angles ($\beta = 0°$; $\beta = 30°$ and $\beta = 90°$). They investigated the impact velocity for only one loading angle $\psi = 15°$. Recently, an elliptical yield envelope is found for both the quasi-static and dynamic loading cases by Hou et al.[Hou 11b] using the Levenberg-Marquardt Algorithm (LMA). Their macroscopic yield criterion takes into account the loading angle ψ and the impact velocity but the influence of the in-plane orientation angle ($\beta = 0°$ and $\beta = 90°$) is investigated and no effect is reported. More recently, a significant effect of the in-plane orientation angle on the experimental yield surfaces of Nomex honeycomb was reported by Zhou et al.[Zhou 12].

As mentioned previously, the aluminium honeycomb behaviour under mixed shear-compression loading is characterized by the normal crush strength σ and the shear crush strength τ defined by:

$$\sigma = \frac{F_N^{Average}}{S_{Specimen}} \tag{3.8}$$

and

$$\tau = \frac{F_S^{Average}}{S_{Specimen}} \tag{3.9}$$

where $S_{Specimen}$ represents the cross specimen section area.

Under mixed shear-compression quasi-static loading, equation 3.10 defines the macroscopic yield criterion of the aluminium honeycomb taking into account the in-plane orientation angle β.

$$(\frac{\sigma}{\sigma_{QS}})^2 + (A\cos^2(\beta) + B\sin^2(\beta))(\frac{\tau}{\sigma_{QS}})^2 = 1 \tag{3.10}$$

where σ_{QS} is the crush strength under quasi-static uni-axial compression

loading. Based on the fitted strength contours, the values of A and B parameters could be determined by the non linear least squares fits method with Levenberg-Marquardt Algorithm (LMA) for the specimens with β= 0° and β= 90°, respectively. Therefore, the material constants identified are A = 8.62 with R^2 = 0.972 and B = 22.44 with R^2 = 0.991.

For a validation of the proposed yield criterion, the normalized strength contour for β= 30° and β= 60° are determined. The proposed yield criterion seems to give a very good description of the quasi-static honeycomb behaviour. Based on equation 3.10, figure 3.40 presents the macroscopic yield criterion for the ***Al5056-N-6-1/4-0.003*** aluminium honeycomb under quasi-static loading based on the equation 3.10.

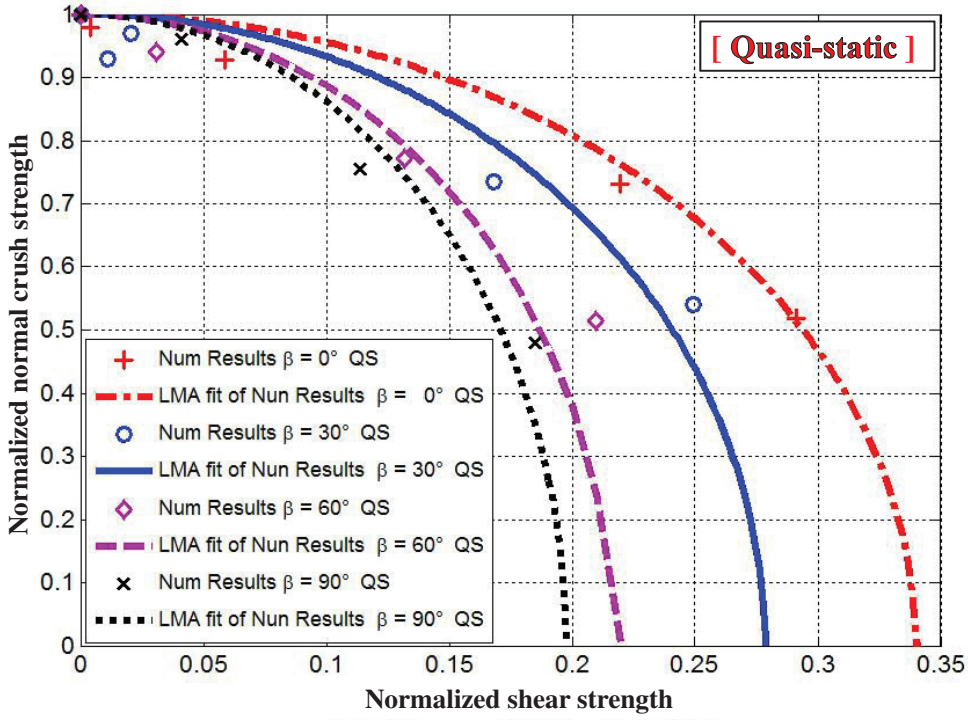

Figure 3.40: *The macroscopic yield criterion under* ***quasi-static*** *mixed shear-compression loading*

Under dynamic loading, the equation 3.10 presents the quadratic yield criterion generalised to be valid at different impact velocities. It is defined by the following equation:

$$\left(\frac{\sigma}{\sigma_{DYN}(V_{Imp})}\right)^2 + \left(A_d(V_{Imp})\cos^2(\beta) + B_d(V_{Imp})\sin^2(\beta)\right)\left(\frac{\tau}{\sigma_{DYN}(V_{Imp})}\right)^2 = 1 \tag{3.11}$$

where σ_{DYN} the crush strength under dynamic uni-axial compression loading. The material constants $A_d(V_{Imp})$ and $B_d(V_{Imp})$ at the impact velocity V_{Imp} = 15 m/s are obtained from the normal and shear crush strengths for β= 0° and β= 90°. Such as under quasi-static conditions, the non linear least squares fits method with Levenberg-Marquardt Algorithm (LMA) of the numerical results suggests the following material constants identified as A_d = 10.04 with R^2 = 0.972 and B_d = 28.73 with R^2 = 0.915.

Based on equation 3.11, figure 3.41 presents the macroscopic yield criterion for the ***Al5056-N-6-1/4-0.003*** aluminium honeycomb under dynamic loading.

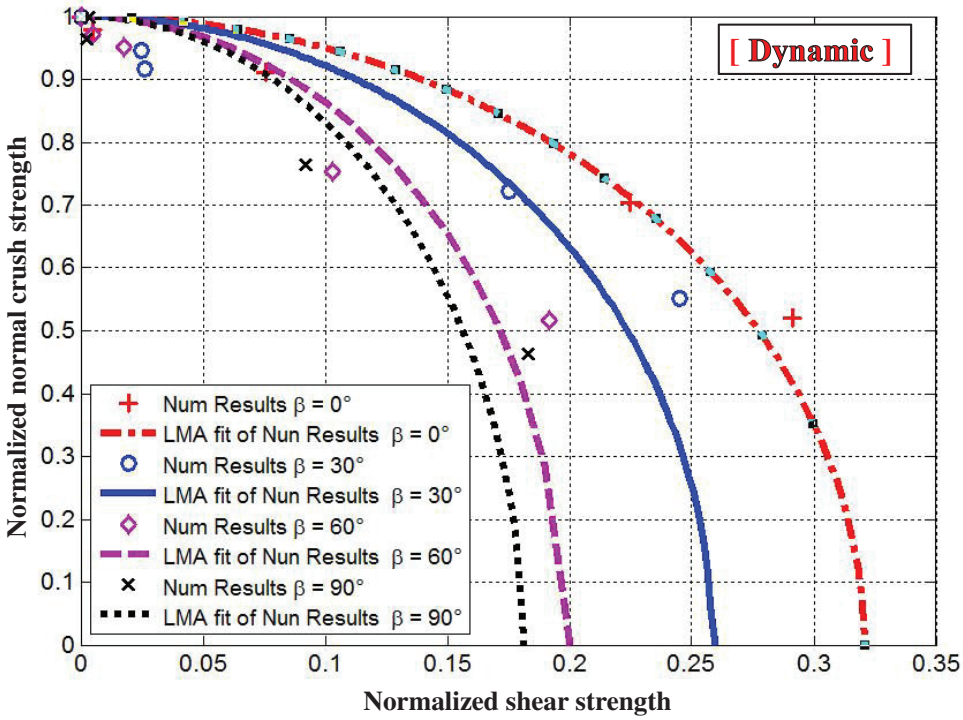

Figure 3.41: *The macroscopic yield criterion under* ***dynamic*** *mixed shear-compression loading*

The symbols in the two figures 3.40 and 3.41 represent the normalized normal crush and shear strengths (quasi-static and dynamic, respectively). The lines represent the macroscopic yield envelope based on the non linear least squares fits method of the numerical results.

A significant effect of the in-plane orientation angle on the macroscopic yield criterion from β= 0° to β= 90° is confirmed. When the in-plane orientation angle increases the area of the surface surrounded by the curve becomes larger. Indeed, the most case required a lot quantity of energy is

for β= 0°.

Finally, to analysis the impact velocity effect, the superposition of the macroscopic yield criterion under quasi-static and dynamic loading requires that the dynamic macroscopic yield criterion must be normalised by the crush strength under quasi-static uni-axial compression loading such as defined by the following equation:

$$(\frac{\sigma}{\sigma_{QS}})^2 + (A_d(V_{Imp})\cos^2(\beta) + B_d(V_{Imp})\sin^2(\beta))(\frac{\tau}{\sigma_{QS}})^2 = (\frac{\sigma_{DYN}}{\sigma_{QS}})^2 \quad (3.12)$$

Thus, equations 3.10 and 3.12 leads to present the macroscopic yield criterion as a function of the loading angle ψ, the in-plane orientation angle β and the impact velocity V_{Imp} (figure 3.42).

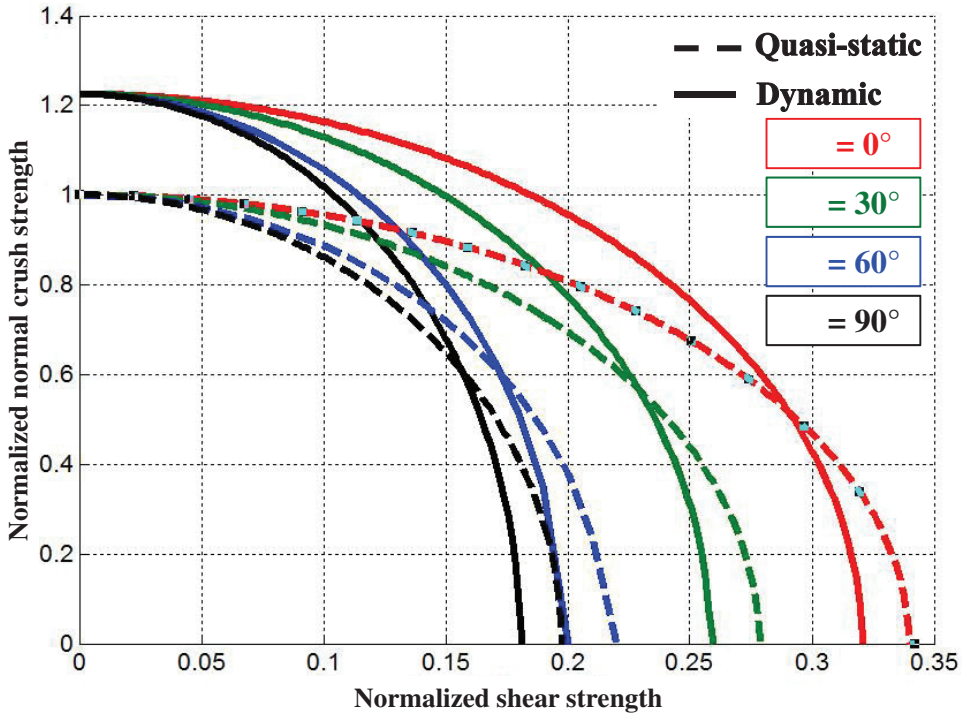

Figure 3.42: *The macroscopic yield criterion under mixed shear-compression loading as function of ψ, β and V_{Imp}*

The dynamic enhancement is also confirmed by the macroscopic yield criterion up to a critical loading angle $\psi_{critical}$ determined through the solution of the equations system (3.10 and 3.12) and given by :

$$\psi_{critical} = \arctan(\frac{\tau_{critical}}{\sigma_{critical}}) \quad (3.13)$$

where

$$\frac{\tau_{critical}}{\sigma_{critical}} = \sqrt{\frac{R^2 - 1}{K_{DYN} - K_{QS}R^2}} \tag{3.14}$$

$$R = \frac{\sigma_{DYN}}{\sigma_{QS}} \tag{3.15}$$

$$K_{DYN} = A_d(V_{Imp})\cos^2(\beta) + B_d(V_{Imp})\sin^2(\beta) \tag{3.16}$$

$$K_{QS} = A\cos^2(\beta) + B\sin^2(\beta) \tag{3.17}$$

For $\psi > \psi_{critical}$, the dynamic crushing responses become higher than the dynamic ones. This phenomenon is explained by the difference of the collapse mechanisms presented in section 2.4.2.

As a conclusion, the mixed shear-compression honeycomb behaviour described by the macroscopic yield criterion depends not only of the loading angle ψ but also of the in-plane orientation angle β and the impact velocity.

3.6 Conclusion

The mixed shear-compression experiments are reproduced using detailed FE simulations by modelling the specimen placed between two beveled bars and using the experimental input and output velocities.

The numerical results are presented in term of force-displacement crushing responses and in term of collapse mechanisms. The effects of the loading angle ψ and the in-plane orientation angle β are investigated numerically under quasi-static and dynamic conditions. Such as reported by the experimental exploitations, a small influence of the in-plane orientation angle β is reported on the axial force component F_Z (the only accessible force component by experimental measurement). Numerical results confirm that when the loading angle increases, the effect of the in-plane orientation angle becomes more pronounced.

A comparison between the numerical results and the experimental ones are carried out on the initial peak force and on the average crushing force. A good correlation is observed under quasi-static and dynamic mixed shear-compression loadings.

The collapse mechanisms are investigated numerically and the three deforming pattern modes experimentally observed are also identified. Numerical results suggest that the combined effect of the in-plane orientation

angle and the loading angle has an influence on the deforming pattern modes and therefore an influence on the crushing force responses.

Finally, using the validated numerical model, it is possible to separate the normal and the shear behaviours and to determine the parameters of a macroscopic yield criterion. A significant effect of the in-plane orientation angle is highlighted on the mixed shear-compression behaviour by the macroscopic yield criterion. The superposition of quasi-static and dynamic macroscopic yield criterion confirms the dynamic enhancement up to a critical loading angle $\psi_{critical}$ depending of the in-plane orientation angle β and the impact velocity. It decreases for the loading angle $0° \lneq \psi < \psi_{critical}$ and a negative enhancement is observed for $\psi > \psi_{critical}$. This surprising phenomenon is attributed to the combined effect of the loading angle, the in-plane orientation angle and the impact velocity which affects the collapse mechanisms.

- Chapter 4 -

Reduced FE model of honeycomb specimen and its validity range

Resume

The aim of this chapter is to develop a reduced FE model used for the simulation of the mixed shear-compression honeycomb behaviour under quasi-static and dynamic loading conditions with a minimum computing time and taking into account the in-plane orientation angle β. Reduced FE model based on the periodicity procedure is proposed and its validity range is evaluated. The numerical results show that in terms of pressure-crush curve and collapse mechanisms, the reduced model is consistent with a complete FE model composed of 39 cells with a CPU-time gain efficiency about 97.17 %. The reduced model is valid from a loading angle $\psi = 0°$ to a loading angle ψ_{limit} contained between $\psi = 30°$ and $\psi = 45°$. The reduced model allows investigating in depth the crush honeycomb behaviour with minimum time calculations in accord with its validity range.

4.1 Introduction

In order to well understand the mixed shear-compression behaviour of cellular materials, the normal and shear behaviours are required to be studied separately. As it is very difficult to experimentally resume the normal and shear forces components, especially under dynamic conditions. The use of a refined FE model detailed in the previous chapter has given successful results. However, such detailed FE model requires a lot of computing time which does not allow to perform numerical design of experiment by varying cells geometry, wall thickness, constitutive material ...

From previous numerical simulations, as found in the open literature, a virtual honeycomb specimen called 'cell-model' may be considered as a three conjoint half walls in "Y" configuration model. This configurations is however only valid for uni-axial compression loading. In their numerical study, Mohr and Doyoyo [Mohr 04a], as well as Hou et al.[Hou 11a] used a virtual honeycomb specimen called 'row-model' made up of a row of cells. Unfortunately, their model is only valid under combined shear-compression loading with only one in-plane orientation angle ($\beta = 90\ ^\circ$). So, the β angle effect can not be investigated numerically. The existing simplified finite element models in the open literature are summarized in table 4.1.

Table 4.1: *Existing simplified models.*

Existing simplified models	Boundary conditions	Uni-axial	Mixed	
		$\psi = 0°$	ψ	β
Cell model	Local symmetric BC's	Yes	No	No
Row model	Local symmetric BC's	Yes	Yes	No

The goal of this chapter is to develop a reduced finite element model which allow to quickly study the influence of the loading angle ψ and the in-plane orientation angle β on the honeycomb crush behaviour under mixed shear-compression loading. A reduced model involving a representative elementary cell of honeycomb structure, based on the periodicity procedure, is proposed by Tounsi et al. [Toun 13] in order to reduce the CPU-time of calculations . Different loading configurations are carried in order to evaluate the validity range of the reduced model and to test its performances under mixed loading.

4.2 Reduced FE Model

Based on the validation between the experimental and the numerical results presented previously, this study is carried out using the same virtual honeycomb specimen Al5056-N-6.0-1/4-0.003.

The complete FE honeycomb model used in the previous chapter taking into account the loading angle, the in-plane orientation angle, the impact velocity, the cell geometry and the material properties requires a lot of computing time. On the basis of the periodicity of the honeycomb structure as well as the periodicity of the collapse mechanisms under mixed loading at the two directions (X and Y) observed in the complete model, we propose to develop a reduced numerical model. Figure 4.1 shows the collapse mechanisms under uni-axial compression loading ($\psi = 0°$) and mixed shear compression loading ($\psi = 15°$ and $\beta = 90°$).

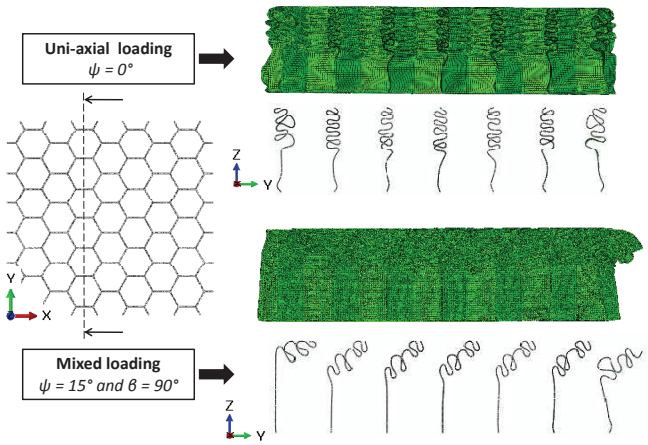

Figure 4.1: *Periodicity of the collapse mechanisms under uni-axial compression loading ($\psi = 0°$) and mixed loading ($\psi = 15°$ and $\beta = 90°$).*

Careful examination of the collapse mechanisms in the complete model shows a progressive crushing mode on the specimen. The mechanisms of plastic deformation were assumed to be identical on each cell. But in reality, under both cases uni-axial and mixed loadings, it can be noted that at the cell level, the collapse mechanisms are not perfectly periodic due to the boundary conditions, calculations errors, the formation of the first fold is caused by

the waves propagation phenomena (the go back of the waves), the geometry defects, the initial imperfections and the numerical rounding. The collapse modes as well as the plastic folding wave length are slightly different (figure 4.1). Under uni-axial loading, the boundary conditions and the side effects are considered to have a small influence on the global force-displacement response. However, under mixed shear-compression loading, the boundary conditions and the side effects become more important. In particular, the side effect will perturb the deforming pattern modes and the influence becomes more significant on the global response. So, with the increase of the loading angle the periodicity of the collapse mechanisms will be lost at a critical angle. In this context, this study is achieved with an objective to test the performance of the reduced model and to investigate its validity range under mixed shear-compression loading with taking the in-plane orientation angle β into consideration.

In order to simplify the geometry model, the two short beveled bars are represented by two rigid walls. The specimen is placed between two parallel rigid walls that represent the loading boundary conditions. An impact loading velocity V_{imp} = 15 m/s is assigned to the top rigid wall while the bottom rigid wall is fixed. The normal and shear velocities are defined respectively by:

$$V_n(t) = V_{imp}(t)\cos\psi \tag{4.1}$$

and

$$V_s(t) = V_{imp}(t)\sin\psi \tag{4.2}$$

As the shear velocity depends on the in-plane orientation angle β, two velocity components are introduced:

$$V_{sx}(t) = V_{imp}(t)\sin\psi\cos\beta \tag{4.3}$$

and

$$V_{sy}(t) = V_{imp}(t)\sin\psi\sin\beta \tag{4.4}$$

4.2.1 Cell model and periodic boundary conditions

In order to optimise the computer run time, the periodicity of the honeycomb meso-structure is used to develop a reduced model representing an elementary cell. The reduced model has the same height as the complete model. In the

first step, periodic boundary conditions are applied to the reduced model with an elementary cell dimension is equal to 3D length and d width (figure 4.2), submitted to uni-axial compression loading. In the second step, the reduced model was used to simulate the crush behaviour under mixed shear-compression loading.

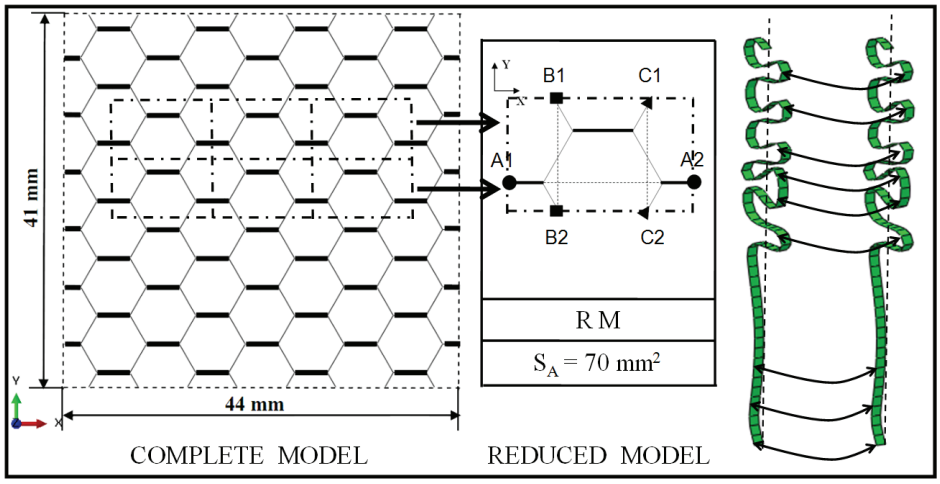

Figure 4.2: *Scheme of numerical reduced model.*

The following periodicity conditions are applied on the free lateral edges ((A1, A2), (B1, B2) and (C1, C2)) of the reduced model (figure 4.2). The degrees of freedom of nodes on these edges are presented by the displacements (U_i) and the rotations (U_{Ri}). The following equations (4.5) and (4.6) define the relationships between all degrees of freedom of nodes on each pair of free edges to make sure that they have the same displacements and rotations [Wilb 11]:

$$U_{i1} - U_{i2} = U_{i1}^{ref} - U_{i2}^{ref} \qquad i = 1, 2, 3 \tag{4.5}$$

and

$$U_{Ri1} = U_{Ri2} \qquad i = 1, 2, 3 \tag{4.6}$$

where U_{ij}^{ref} are displacements of conjugate nodes on opposite sides chosen as reference nodes. The previously explained constraint equations (4.5) and (4.6) are assigned on edge nodes in an ABAQUS/Explicit input file. The simulations are carried out on the reduced model having the same height, cell dimensions, material properties, mesh size, boundary conditions and contact algorithm as the complete model.

4.2.2 Validation of the reduced model under uni-axial loading

4.2.2.1 Pressure-crush curves

A comparison between the pressure-crush curves (defined as the force-displacement curves divided by cross-sectional area) of the complete and reduced models is made in this section in order to validate the reduced model under uni-axial compression. The comparison study was carried out the initial peak pressure and the average crushing pressure. The initial peak pressure P^{Peak} corresponds to the first maximum pressure value in the pressure-crush curve. The average crushing pressure $P^{Average}$ is defined by the following equation:

$$P^{Average} = \frac{1}{Cr_{max} - Cr_{peak}} \int_{Cr_{peak}}^{Cr_{max}} P(Cr)dCr \tag{4.7}$$

where Cr_{peak} is the crush value at the initial peak, Cr_{max} is the final crush value and P(Cr) is the axial force component (F_z) divided by specimen cross-sectional area.

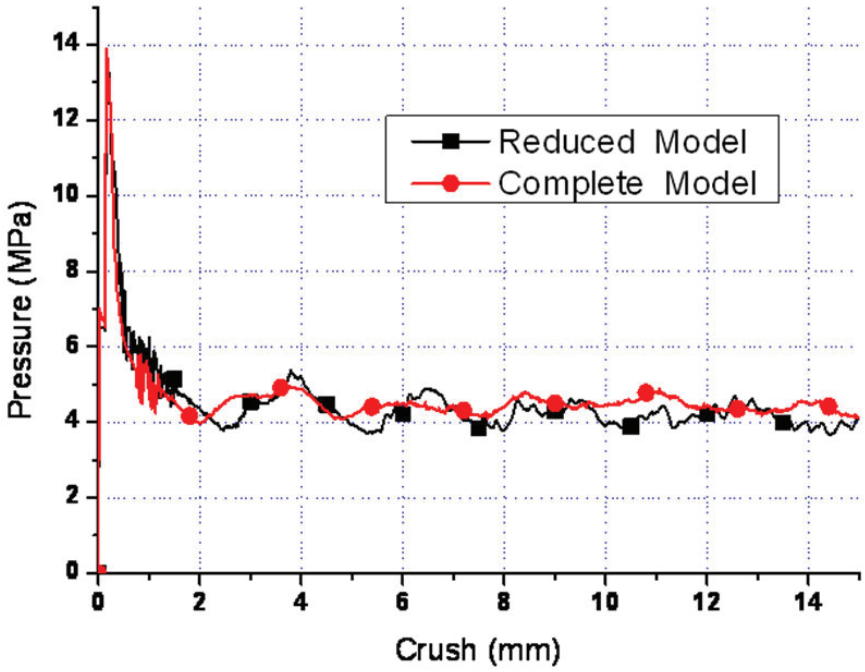

Figure 4.3: *Comparison between the complete and reduced models: the pressure-crush curves (uni-axial loading $\psi = 0°$).*

Figure 4.3 shows that the reduced model is in good agreement with the complete model under uni-axial compression loading.

Table 4.2: *Initial peaks and average crushing pressures under uni-axial loading.*

	C M	R M	Error
Initial peak pressure (MPa)	13.9	13.41	3.5 %
Average crushing pressure (MPa)	4.61	4.46	3.25 %

Table 4.2 shows that the reduced model (R M) results are close to the complete model (C M) ones (3.5 % error on the initial peak and 3.25 % error on the average crushing pressure).

4.2.2.2 Collapse mechanisms

The collapse mechanisms that include buckling part, collapse and post collapse parts by the formation of successive folding systems are analysed in both complete and reduced models.

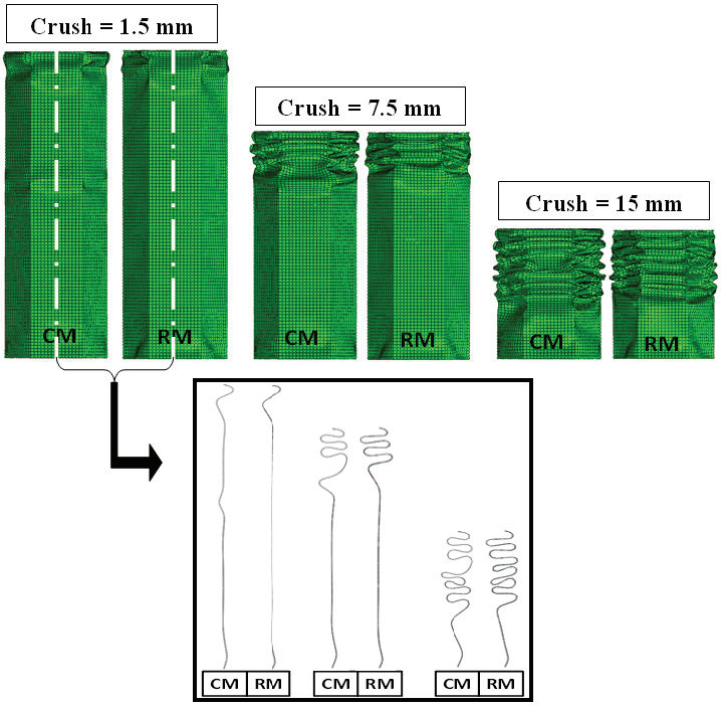

Figure 4.4: *Comparison between the complete and reduced models: the collapse mechanisms at 1.5, 7.5 and 15 mm of crush (uni-axial loading ψ = 0°).*

After the initial peak, the formation of the first fold takes place in the softening regime and conducts to the activation of the folding systems. The mechanisms are presented in three stages of crush distance (1.5; 7.5 and 15 mm). The same number of folds is observed in both reduced and complete models. Folding begins at the specimen top for the two models (figure 4.4).

As a result of the pressure-crush curves and collapse mechanisms comparison, the reduced model using periodic boundary conditions is validated under uni-axial compression loading. Only small acceptable differences on the collapse mechanisms are observed.

4.2.3 Validation of the reduced model under mixed shear-compression loading

In order to make sure that the reduced model is valid under mixed shear-compression loading, one configuration is analysed corresponding to a loading angle ($\psi = 15°$) with an in-plane orientation angle ($\beta = 0°$). To realize this mixed shear-compression loading configuration, the boundary conditions are applied using equations (4.1, 4.3 and 4.4).

4.2.3.1 Pressure-crush curves

For the evaluation of the reduced model under mixed shear-compression loading, the pressure-crush responses (figures 4.5, 4.6 and 4.7) as well as the comparison between collapse mechanisms of reduced and complete models (figure 4.8) are presented.

The different parts of the pressure are defined by P_n referred to as the normal pressure and P_s referred to as the shear pressure. Figure 4.5 shows a good agreement in terms of normal pressure-crush curves between both models (reduced and complete). Knowing that each oscillation on the pressure-crush curve represents the formation of one fold, the figure 4.6 showing the shear pressure-curves make appear the same number of folds with a difference in the amplitude of the oscillations. The shear pressure-crush curve of the complete model is smoother than the reduced model; this could be explained by the influence of the side effects and boundary conditions. To evaluate the overall pressure under mixed shear-compression loading, the total pressure is defined by the following equation:

$$P_{Total}(Cr_T) = P_n(Cr_T)\cos\psi + P_s(Cr_T)\sin\psi \tag{4.8}$$

and

$$Cr_T = \frac{NormalCrush}{\cos\psi} = \frac{ShearCrush}{\sin\psi} \tag{4.9}$$

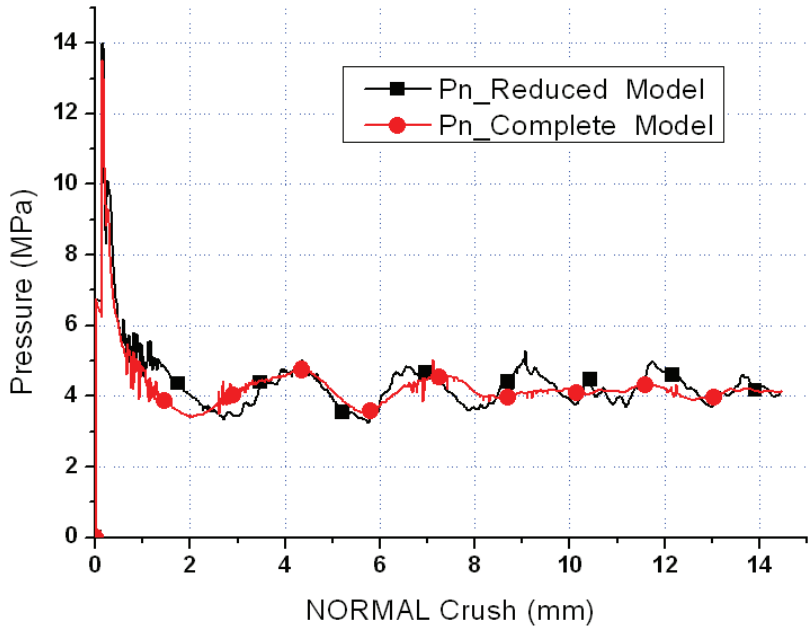

Figure 4.5: *Comparison between the complete and reduced models: the normal pressure-crush curves (mixed loading $\psi = 15°$ and $\beta = 0°$).*

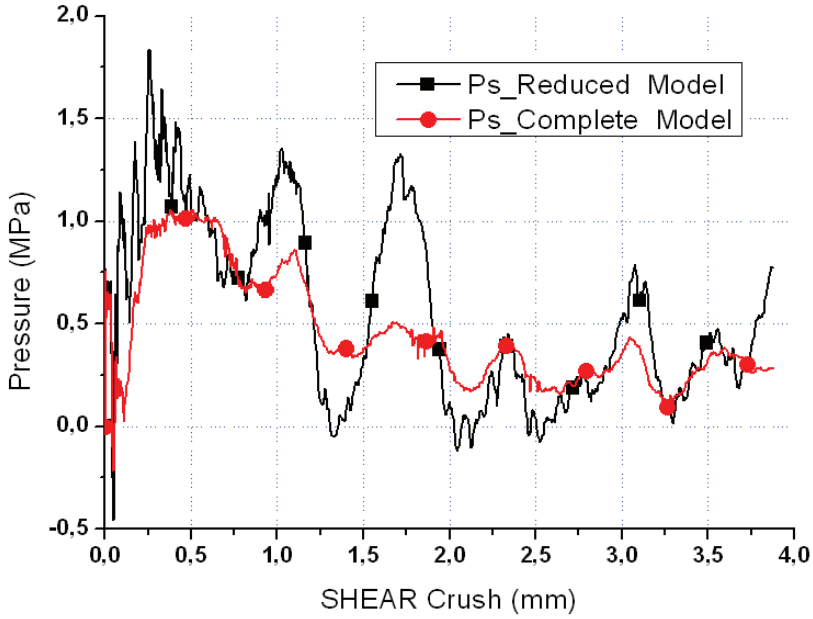

Figure 4.6: *Comparison between the complete and reduced models: the shear pressure-crush curves (mixed loading $\psi = 15°$ and $\beta = 0°$).*

Figure 4.7 and table 4.3 show a good agreement on the total pressure, the initial peak pressure as well as the average crushing pressure values between the reduced and the complete models are presented.

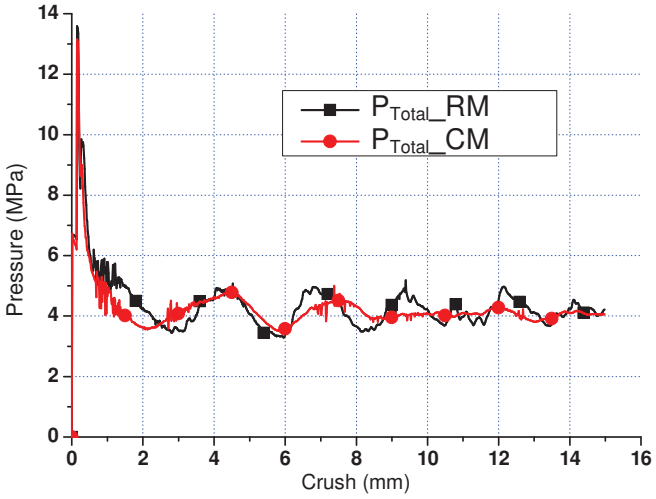

Figure 4.7: *Comparison between the complete and reduced models: the total pressure-crush curves (mixed loading $\psi = 15°$ and $\beta = 0°$).*

Table 4.3: *Initial peaks and average crushing pressures under mixed loading.*

	C M	R M	Error
Initial peak pressure (MPa)	13.15	13.41	3.35 %
Average crushing pressure (MPa)	4.22	4.36	2.85 %

4.2.3.2 Collapse mechanisms

The collapse mechanisms under mixed shear-compression dynamic loading are investigated by comparing the complete model to the reduced one.

Figure 4.8 shows the collapse mechanisms of the reduced and complete models under mixed loading ($\psi = 15°$ and $\beta = 0°$) at three normal crush distances. A small variation in the orientation of the first fold formation is observed after a normal crush of 1.488 mm. This could be explained by the the wave phenomena that initializes the location and the formation of the first fold in addition to the numerical rounding. At the normal crush distance 7.24 mm, a fold appears at the bottom side of specimen in the complete model but it does not appear in the reduced model. The occurrence of this fold on

the bottom side of the complete model is caused by the boundary conditions and the side effect and the fold becomes more remarkable at the final normal crush distance (14.48).

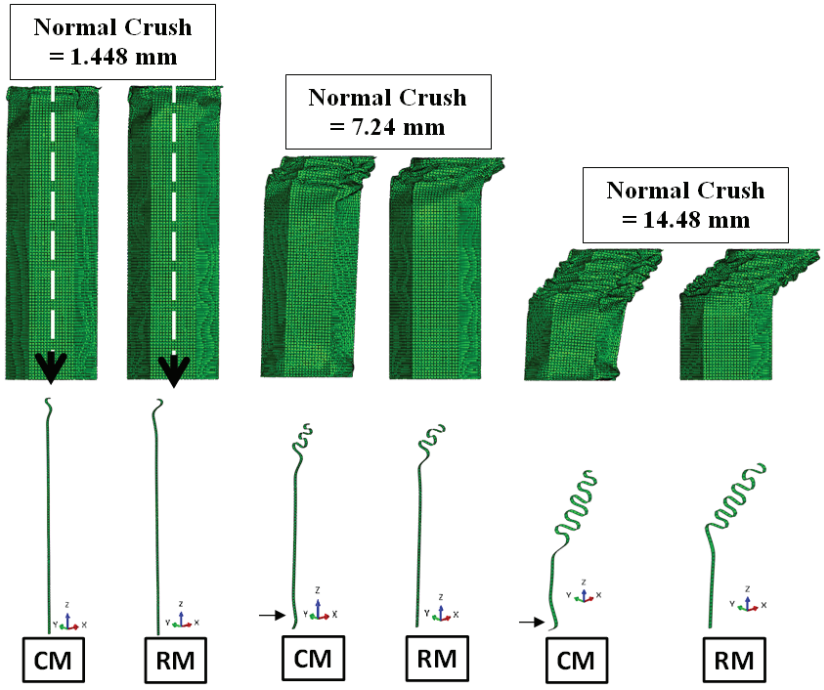

Figure 4.8: *Comparison between the complete and reduced models: the collapse mechanisms (mixed loading $\psi = 15°$ and $\beta = 0°$).*

Comparing the both models, there is a small difference in the plastic folding wave length but it is not significant. The difference observed on the shear pressure displayed in figure 4.6 can be explained by the effect of the difference in the collapse mechanisms. Thus, these differences have an influence on the total pressure (an error about 3.35 % at the initial peak pressure and 2.85 % at the average crushing pressure) but it remains acceptable.

Table 4.4: *CPU-time values for 2.66 GHz*

	C M	R M
Uni-axial loading ($\psi = 0°$)	19236 s	507 s
Mixed loading ($\psi = 15°$ and $\beta = 0°$)	17639 s	498 s

As a conclusion, the reduced model is tested and validated under mixed shear-compression loading with a loading angle ($\psi = 15°$) and an in-plane orientation angle ($\beta = 0°$) despite some small difference in collapse

mechanisms that are not significant on the global crushing response. Thus, the reduced model provides a significant gain of CPU time (97.17 %) such as shown in the table 4.4.

The reduced model produces a good compromise in terms of CPU-time gain efficiency and accuracy of results under uni-axial loading and under only one case of mixed loading ($\psi = 15°$ and $\beta = 0°$). Which brings us to extend our study to investigate the performance and the validity range of the reduced model under different configurations of mixed shear-compression loading taking the in-plane orientation angle β and the loading angle ψ effects into consideration.

4.3 Reduced model validity range

A validation is necessary to verify if the reduced model is able to simulate a large range of mixed shear-compression behaviour by taking the in-plane orientation angle into consideration. Numerical simulations were performed on both reduced and complete models for many configurations of the loading angle ψ and the in-plane orientation angle β. This study was carried out in order to define the validity range of the reduced model or in other words, the limit angle of loading for which the periodicity conditions remain verified.

4.3.1 Comparison between the reduced and complete models results

Different combinations of the loading angle from 0° to 60° by 15° and the in-plane orientation angle from 0° to 90° by 30° were tested numerically. The impact velocity of 15 m/s was applied to the simulations.

Table 4.5 shows a comparison study between the complete and reduced models focused on the initial peak and average crushing pressure values. The reduced model is less efficient and the error increases when the loading angle increases. For a loading angle lower than 30°, the reduced model is able to have the consistent results in term of pressure-crush curves given by the complete model with an error that does not exceed about 6 %. For a loading angle 45°, the error is between 1.7 % and 7.27 % on the initial peak pressure and between 8.45 % and 20.14 % on the average crushing pressure. For a loading angle 60°, the error becomes more important due to the fact that shear load becomes more dominant than the normal one. This result can be

explained by the difference between the collapse mechanisms reported by the reduced and complete models.

Table 4.5: *Comparison of the initial peak and the average pressure (reduced and complete models).*

ψ	β	Initial peak pressure (MPa)			Average crushing pressure (MPa)		
		C M	R M	Error (%)	C M	R M	Error (%)
0°	0°	13.9	13.41	3.52	4.61	4.46	3.25
	30°	13.9	13.41	3.52	4.61	4.46	3.25
	60°	13.9	13.41	3.52	4.61	4.46	3.25
	90°	13.9	13.41	3.52	4.61	4.46	3.25
15°	0°	13.15	13.41	1.97	4.22	4.36	3.31
	30°	13.16	13.4	1.82	4.21	4.29	1.9
	60°	13.25	13.4	1.13	4.32	4.39	1.62
	90°	13.23	13.39	1.28	4.33	4.45	2.77
30°	0°	11.53	11.27	2.25	3.67	3.84	4.63
	30°	11.6	11.29	2.67	3.6	3.82	6.11
	60°	11.81	11.68	1.1	3.62	3.76	3.86
	90°	11.84	11.83	0.04	3.65	3.62	0.82
45°	0°	9.37	9.53	1.7	2.97	3.42	15.15
	30°	9.34	9.67	3.53	2.9	3.47	19.65
	60°	9.48	10.09	6.43	2.78	3.34	20.14
	90°	9.49	10.18	7.27	2.72	2.95	8.45
60°	0°	6.39	7.91	23.78	2.29	3.05	33.18
	30°	6.22	7.75	24.59	2.22	3.35	50.90
	60°	6.15	7.8	26.82	2.01	2.85	41.79
	90°	6.15	7.91	28.59	1.78	2.14	20.22

From table 4.5, we notice that configurations between the loading angle ψ and the in-plane orientation angle β (ψ =30°/ β = 30°, ψ =45°/ β = 60° and ψ =60°/ β = 30°) present large errors. In the next section, the pressure-crush curves and collapse mechanisms are studied for these cases to understand the origin of this disparity.

4.3.2 Pressure-crush curves

The evolution, versus the crush distance, of the total pressure in the case of the following combinations of loading angle and in-plane orientation angle is presented in figures 4.9, 4.10 and 4.11.

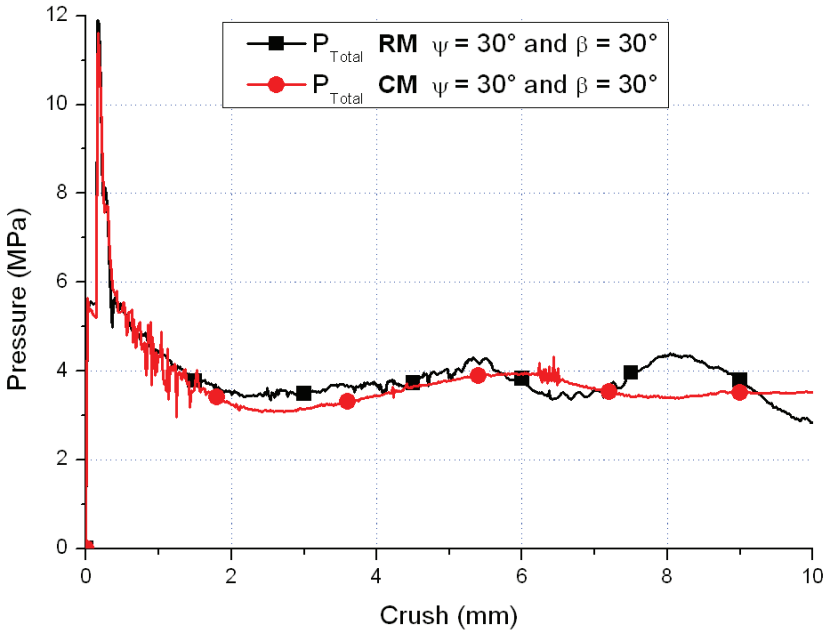

Figure 4.9: *The comparison between the complete and reduced models in term of the total pressure-crush curves $\psi = 30°$ and $\beta = 30°$.*

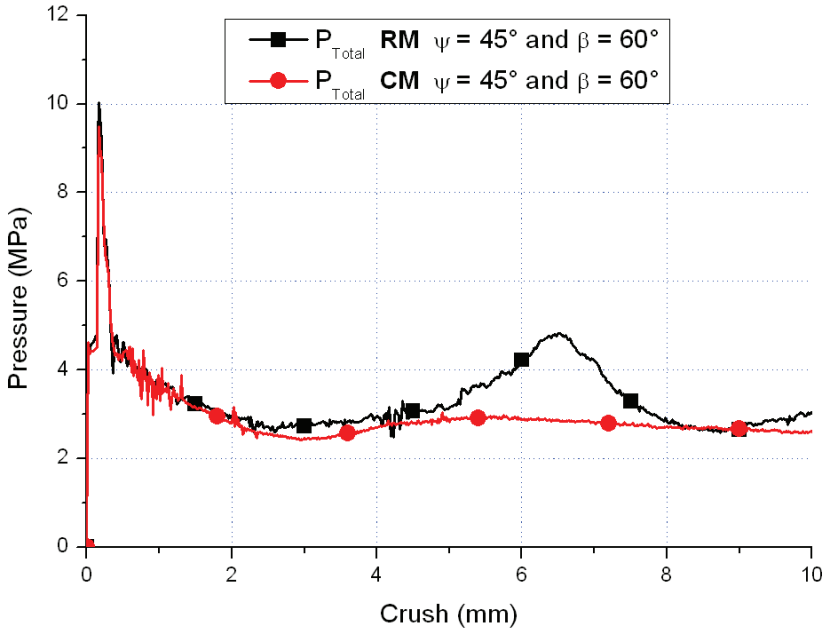

Figure 4.10: *The comparison between the complete and reduced models in term of the total pressure-crush curves $\psi = 45°$ and $\beta = 60°$.*

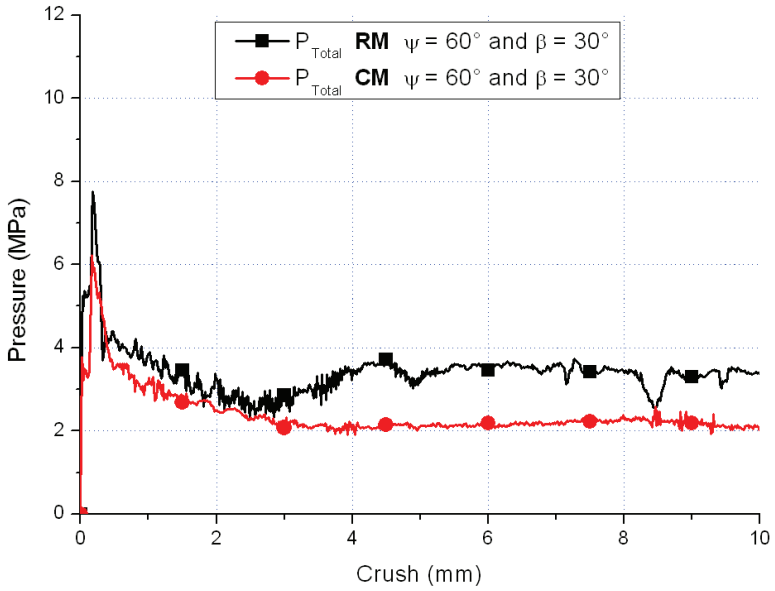

Figure 4.11: *The comparison between the complete and reduced models in term of the total pressure-crush curves $\psi = 60°$ and $\beta = 30°$.*

A good agreement with a small difference is observed between the reduced model and the complete model results in terms of total pressure at ψ =30°/ β = 30° and ψ =45°/ β = 60°. But at ψ =60°/ β = 30° the difference becomes more pronounced. To understand the origin of the increase difference with the increase loading angle, the normal and the shear pressures are displayed in figures 4.12/4.13 , 4.14/4.15 and 4.16/4.17.

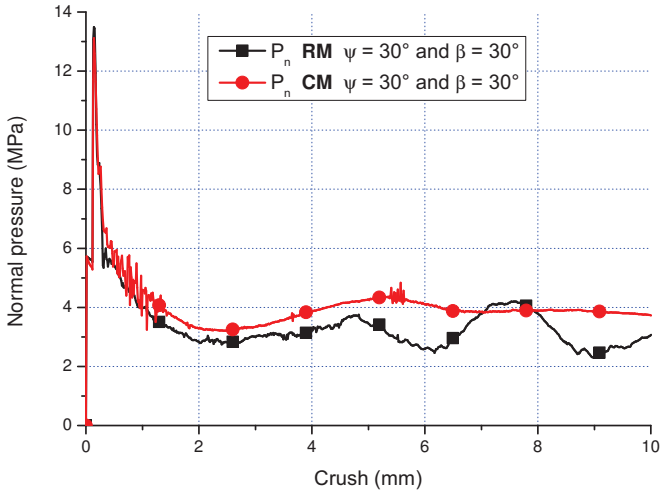

Figure 4.12: *The comparison between the complete and reduced models in terms of the normal pressure-crush curves $\psi = 30°$ and $\beta = 30°$.*

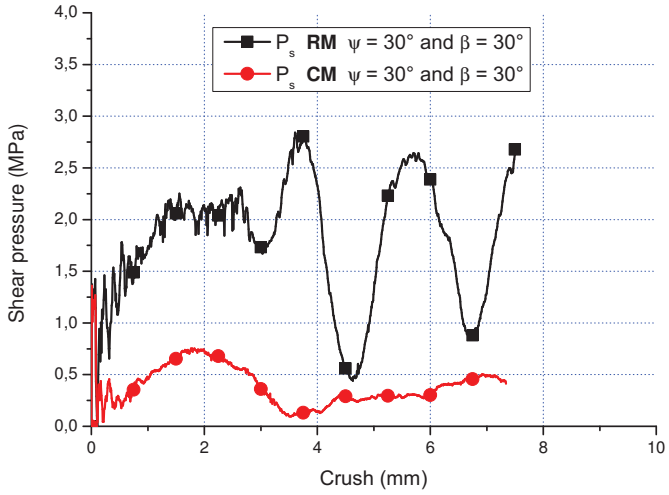

Figure 4.13: *The comparison between the complete and reduced models in terms of the shear pressure-crush curves $\psi = 30°$ and $\beta = 30°$.*

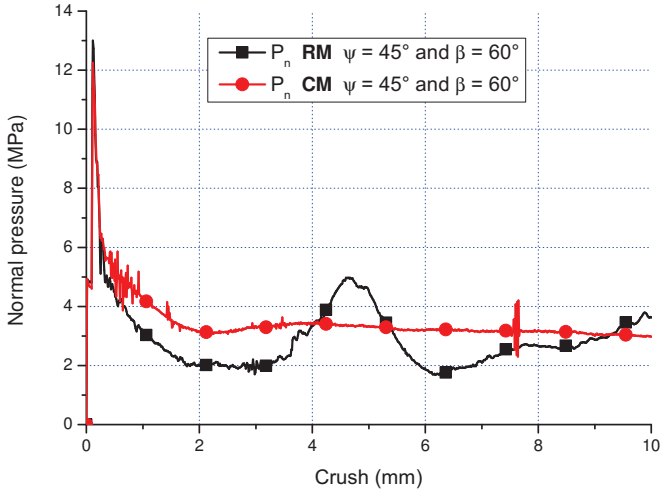

Figure 4.14: *The comparison between the complete and reduced models in terms of the normal pressure-crush curves $\psi = 45°$ and $\beta = 60°$.*

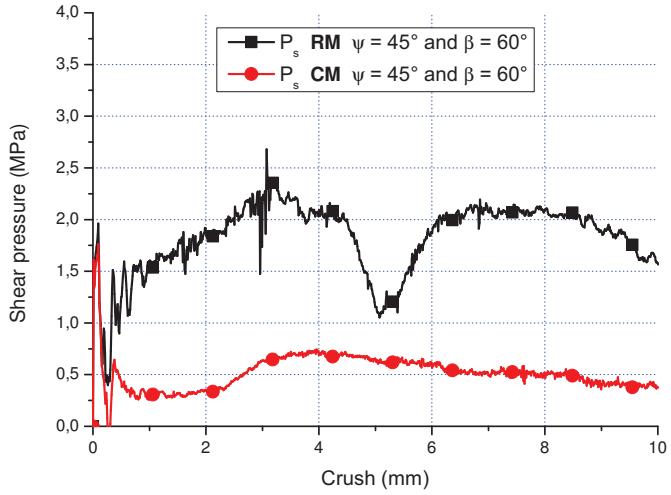

Figure 4.15: *The comparison between the complete and reduced models in terms of the shear pressure-crush curves $\psi = 45°$ and $\beta = 60°$.*

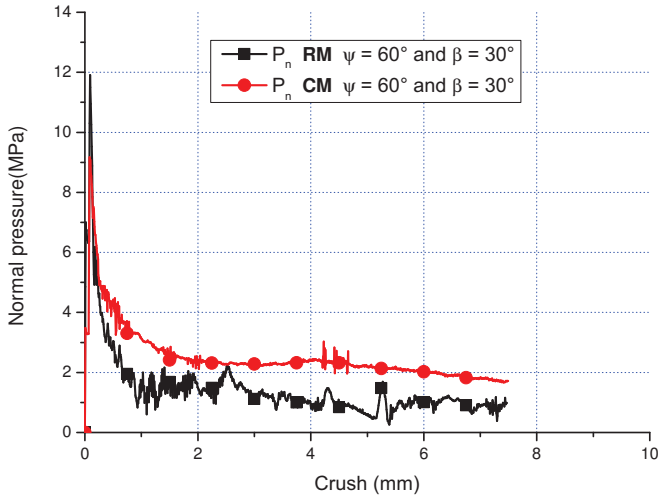

Figure 4.16: *The comparison between the complete and reduced models in terms of the normal pressure-crush curves $\psi = 60°$ and $\beta = 30°$.*

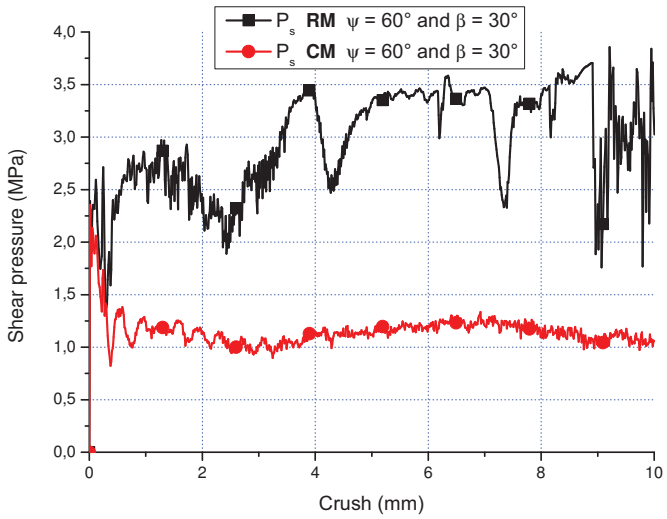

Figure 4.17: *The comparison between the complete and reduced models in terms of the shear pressure-crush curves $\psi = 60°$ and $\beta = 30°$.*

In the normal pressure-crush curves, the reduced model has a normal pressure smaller than the complete model. In the shear pressure-crush curves, the difference in the average amplitude between the reduced and complete models becomes more pronounced than in the normal pressure-crush curves. The reduced model shows some oscillations and peaks at the normal and shear pressures that are not observed in the complete model. As a conclusion, the difference in the total pressure is related to the difference in the shear stress that becomes more important when the loading angle ψ increases. The origin of this difference is related to the boundary conditions and the side effect and it could be more explaining by the collapse mechanisms investigated in the next part.

4.3.3 Collapse mechanisms

To understand deeply the origin of the difference between the results given by complete and reduced models and to justify the idea of the boundary conditions effect, a study of collapse mechanisms in the two models is achieved. The collapse mechanisms begin by elastic buckling followed by post-buckling till an initial peak that represents the collapse point. The formation of the first fold shows the apparition of the plastic hinge line highlighted in figure 4.18. The end of the development of the first fold initiates the formation of the second one which leads to the activation

of the successive folding systems. It takes place in the crushing regime (post-collapse) and it is characterised by the average crushing pressure that represents the energy absorption quantity.

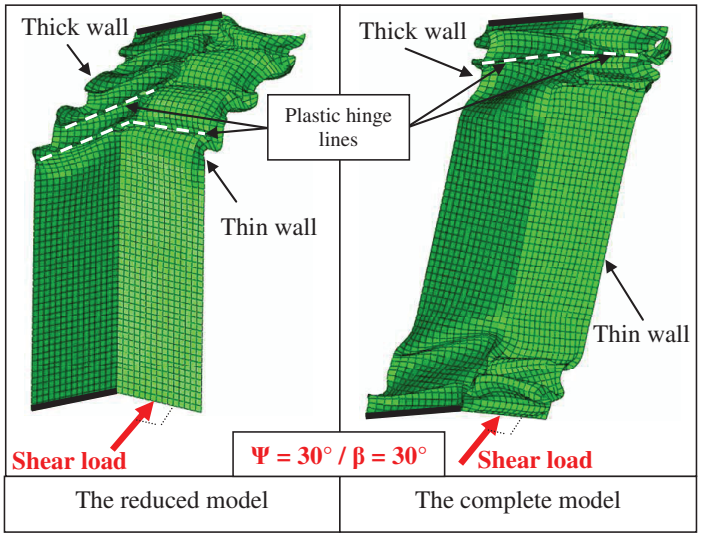

Figure 4.18: *The comparison between the complete and reduced models in terms of collapse mechanisms ($\psi = 30°$ and $\beta = 30°$).*

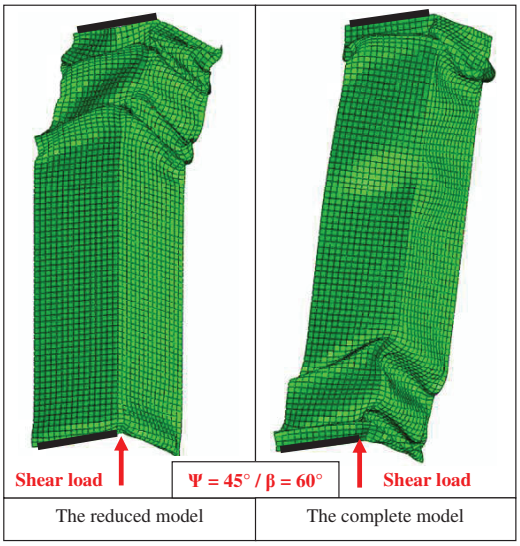

Figure 4.19: *The comparison between the complete and reduced models in terms of collapse mechanisms ($\psi = 45°$ and $\beta = 60°$).*

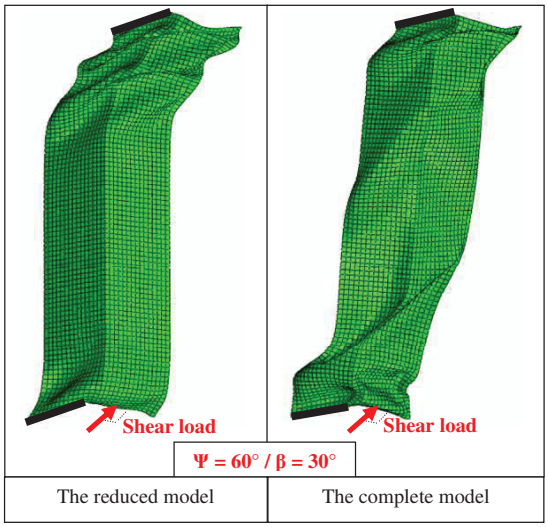

Figure 4.20: *The comparison between the complete and reduced models in terms of collapse mechanisms ($\psi = 60°$ and $\beta = 30°$).*

For these cases of mixed shear-compression loading, the collapse mechanisms are presented at the final step of crushing in figures 4.18, 4.19 and 4.20 respectively ($\psi = 30°$ and $\beta = 30°$), ($\psi = 45°$ and $\beta = 30°$) and ($\psi = 60°$ and $\beta = 30°$). The number of folds for the reduced and complete models is similar but the location of these folds is different. The reduced model shows the formation of folds at the top of the specimen and this causes the no rotation of the cell axis. The complete model shows the formation of the folds at the top and the bottom of specimen and this causes the rotation of the cell axis.

When the shear load becomes equal or superior to the normal load ($\psi \geq 45°$), the boundary conditions and the side effects become more important and perturb the collapse mechanisms of the complete model that loses its periodicity (figure 4.21). As a result, the reduced model is unable to produce the same collapse mechanisms that the complete model and has reached its limits of validity. The periodicity procedure is no longer verified in this case and this define the limit of the reduced model validity range.

To summarise, the difference observed at the shear pressure as well as the total pressure could be explained by the difference in the collapse mechanisms.

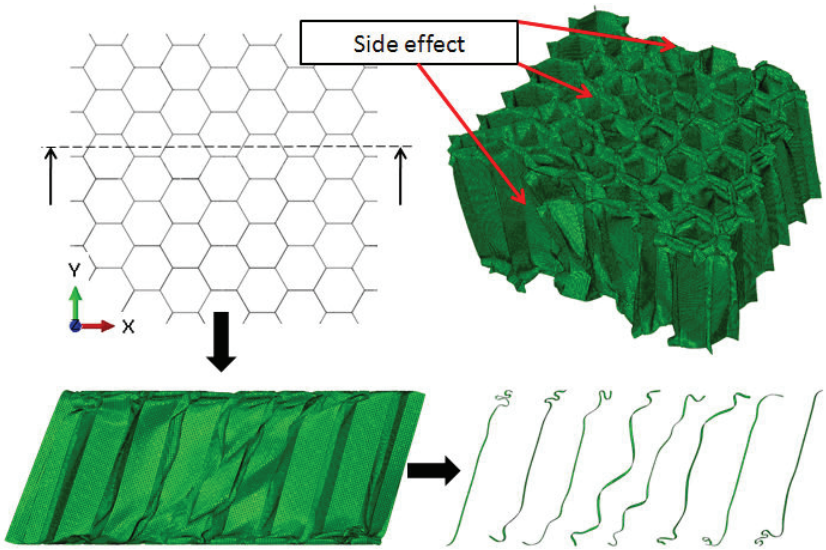

Figure 4.21: *The boundary conditions and the side effects on the collapse mechanisms in the complete model ($\psi = 60°$ and $\beta = 30°$).*

The difference of the collapse mechanisms could be explained by the calculation errors, the waves propagation phenomena, the geometry defects, the initial imperfections and the numerical rounding, but especially by the boundary conditions and the side effect. The influence of the boundary conditions and the side effect become significant when the loading angle increases. So, a loading angle limit ψ_{limit} for the validity of the reduced model may be defined between $\psi = 30°$ and $\psi = 45°$. Noting that, in the most real applications of the honeycomb, the loading angle ψ will be contained between $\psi = 0°$ and ψ_{limit}. Therefore, the validity range of the reduced model allows one to cover a wide range of real applications.

4.4 Conclusion

The numerical simulation of aluminium honeycomb behaviour under mixed shear-compression loading taking the in-plane orientation angle into account needs a large CPU-time. The existing simplified models are valid under uni-axial compression and under mixed shear-compression loading with only one in-plane orientation angle. In this chapter, a reduced model based on the periodicity conditions has been developed in order to reduce the calculations cost and to take into consideration the in-plane orientation angle β effects. The validity range of the reduced model has been analysed under both cases of loadings, uni-axial compression and mixed shear-compression taking into

account the in-plane orientation angle β. The reduced model gives a good compromise in terms of CPU time gain efficiency (97.17 %) and accuracy of results. The comparison between the complete and reduced models in terms of pressure-crush curves shows a small error until a loading angle of 30°. From a loading angle ψ =45°, the error becomes more important. This could be explained by the side effect and the boundary conditions. The shear loading becomes more dominant than the normal loading, the side effect increases and the differences in the collapse mechanisms become more significant. A loading angle limit ψ_{limit} for the validity of the reduced model is included between $\psi = 30°$ and $\psi = 45°$. The validity of the reduced model is however provided for a range of loading angles commonly encountered in real applications. Indeed, honeycombs are not designed to be efficient under high shear loadings. According to its range of validity, this reduced model can be used as a quick tool for numerical design of experiment of new honeycomb material configurations by the variation of cell size, cell shape, cell wall thickness, material properties and the impact velocity.

Conclusions and perspectives

Nowadays, cellular materials are widely used in many transport industries. In the particular context of the automotive industry, cellular materials such as aluminium honeycomb are used as energy absorbers. So, understanding in depth the honeycomb behaviour under realistic loading conditions useful for FEA structural crashworthiness presents the main aim of this thesis.

Under mixed shear-compression loading, none of the published works have investigated in depth the combined effects of the loading angle ψ, the in-plane orientation angle β and the impact velocity V_{Imp} on the honeycomb crush behaviour. Moreover, concerning the β angle effect , contradictory conclusions appear in the literature.

So that, combined experiments and numerical simulations (detailed and reduced models) are realised and a macroscopic yield criterion expressed as a function of (ψ, β and V_{Imp}) is proposed.

For the experimental set-up, a finite element (FE) study is realised in order to improve the mixed shear-compression loading device. The increased stiffness of the sleeves limits the radial expansion phenomenon and ensures a good alignment of loading and therefore the efficiency in the data processing. A separation phenomenon between the input Hopkinson bar and the input beveled bar is observed numerically and is confirmed experimentally. So, an electro optical extensometer is used as a measurement technique to extend the information needed to compute the output force for a larger crushing displacement of the specimen. Experimental programme is performed with four in-plane orientation angles and five loading angles. The crushing responses analysis are focused on two parameters : the initial peak force and the average crushing force. Experimental results show a significant effect of the loading angle ψ and an effect of the in-plane orientation angle β (more significant when the loading angle increases) on the mixed shear-compression

behaviour. Based on a comparison between quasi-static and dynamic results, a dynamic enhancement is observed under mixed shear-compression loading. The dynamic enhancement rate is calculated as a function of the loading angle ψ and the in-plane orientation angle β. It decreases when the loading angle increases and it becomes negative when the loading angle exceeds 45° ($\psi > 45°$). This phenomenon is explained by the difference between the collapse mechanisms under quasi-static and dynamic loadings.

Three deforming pattern modes (mode I, II and III) depending of the the loading angle ψ and the in-plane orientation angle β are identified under mixed shear-compression loading.

The experimental set-up is limited to only measure the axial component force. A detailed FE model is developed to separate the normal and the shear force components in the frame of the specimen. A good correlation between the numerical results and the experimental ones on the initial peak force and on the average crushing force is observed. Such as reported by the experimental exploitations, a small influence of the in-plane orientation angle β is reported on the axial force component F_Z. Numerical results confirm also that when the loading angle increases, the effect of the in-plane orientation angle becomes more pronounced.

The collapse mechanisms are investigated numerically and the three deforming pattern modes experimentally observed are also identified. Numerical results suggest that the combined effect of the in-plane orientation angle and the loading angle has an influence on the deforming pattern modes and therefore an influence on the crushing force responses.

After that, the normal and the shear forces are calculated separately. They are used to determine the parameters of the proposed macroscopic yield criterion. A significant effect of the in-plane orientation angle on the dynamic enhancement is highlighted. The superposition of quasi-static and dynamic macroscopic yield criterions confirms that the dynamic enhancement is verified up to a critical loading angle $\psi_{critical}$ depending of the in-plane orientation angle β and the impact velocity. It decreases for the loading angle $0° \lesssim \psi < \psi_{critical}$ and a negative enhancement is observed for $\psi > \psi_{critical}$. This surprising phenomenon is attributed to the combined effect of the loading angle, the in-plane orientation angle and the impact velocity which affects the collapse mechanisms.

Finally, as the numerical simulations using the detailed FE model need a large CPU-time, a reduced model based on the periodicity conditions

has been developed. The comparison between the detailed (complete) and reduced models shows that a limit loading angle ψ_{limit} (]30°, 45°[) defines the validity of the reduced model. The reduced model is however valid for a range of loading angles commonly encountered in real applications. Indeed, honeycombs are not designed to be efficient under high shear loadings. According to its range of validity, this reduced model can be used as a quick tool for numerical design of experiment of new honeycomb material configurations by the variation of cell size, cell shape, cell wall thickness, material properties and the impact velocity.

Future perspectives

Honeycombs used as crash energy absorber may be of various constitutive materials and of different cell geometry parameters (cell size, cell shape, cell wall thickness). Future researches can be focused on the extension of the macroscopic yield criterion to take the geometry parameters and material properties into account.

The combined effect of the loading angle and the in-plane orientation angle will be implemented in a FE honeycomb macro model useful for FEA structural crashworthiness.

In the thesis work, only the honeycomb cores have been considered. For the use of honeycomb cores into sandwich panels, it would be interesting to investigate if the same effects of (ψ, β and V_{Imp}) are verified.

Annexes

- Appendix A -

The experimental honeycomb behaviour

A.1 Quasi-static crushing responses

The loading angle ψ effects

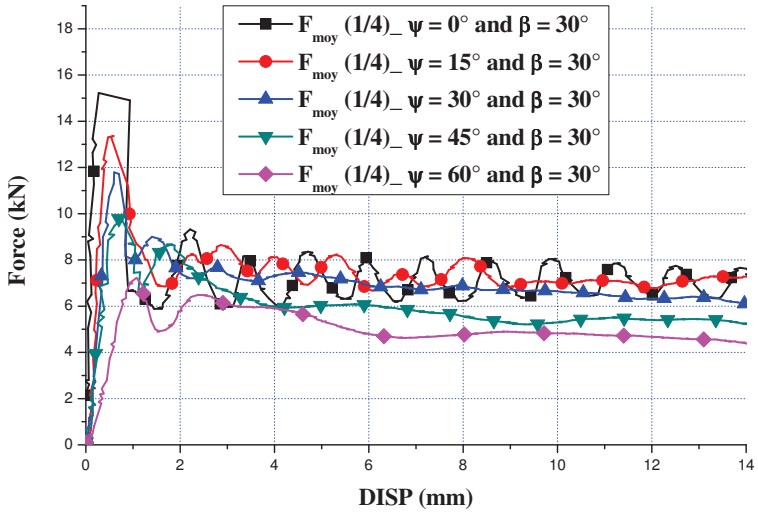

Figure A.1: *The loading angle ψ effects under **quasi-static** mixed shear-compression loading for $\beta = 30°$*

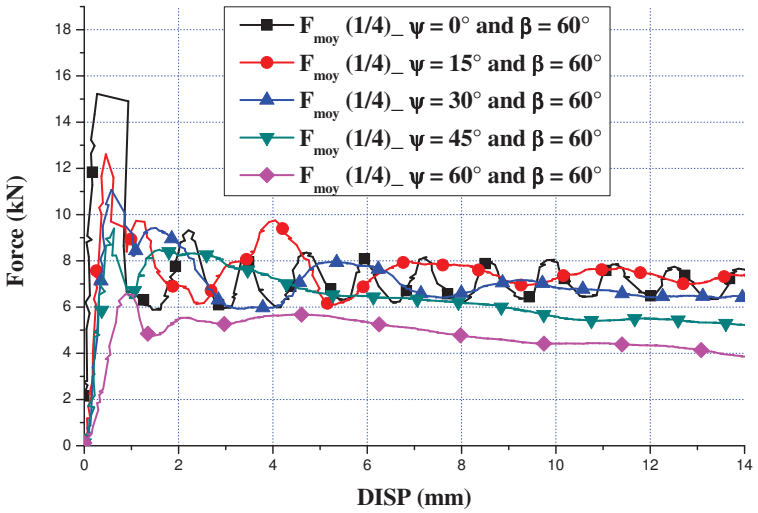

Figure A.2: *The loading angle ψ effects under* ***quasi-static*** *mixed shear-compression loading for $\beta = 60°$*

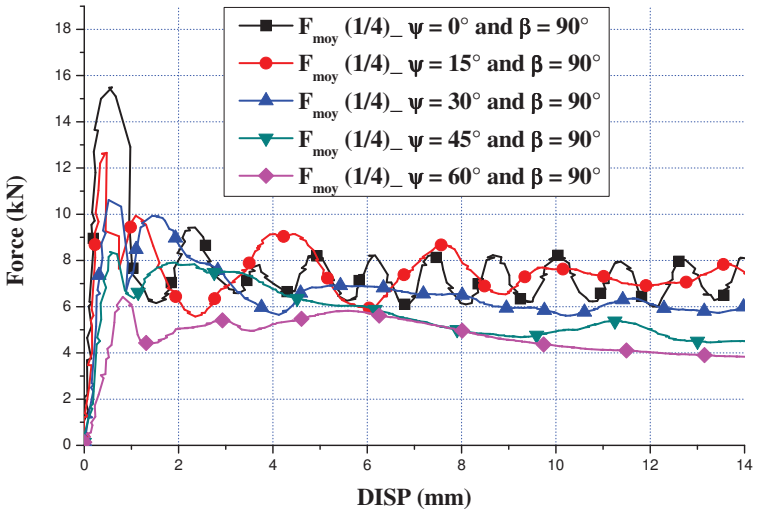

Figure A.3: *The loading angle ψ effects under* ***quasi-static*** *mixed shear-compression loading for $\beta = 90°$*

The in-plane orientation angle β effects

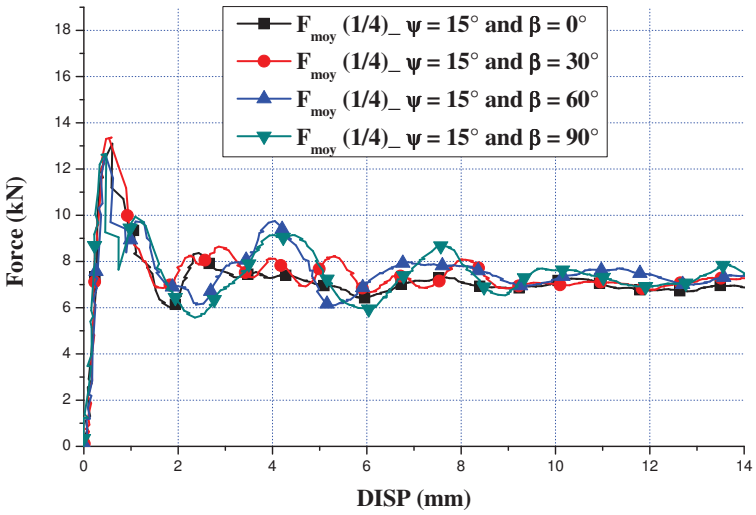

Figure A.4: *The in-plane orientation angle β effects under* ***quasi-static*** *mixed shear-compression loading for $\psi = 15°$*

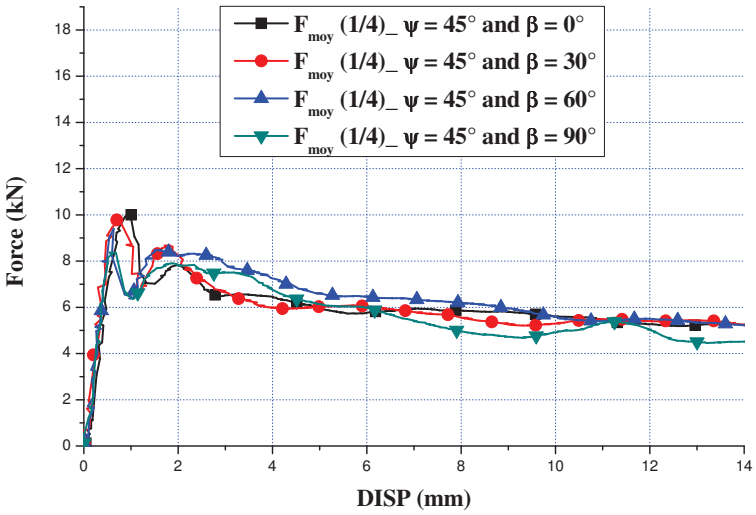

Figure A.5: *The in-plane orientation angle β effects under* ***quasi-static*** *mixed shear-compression loading for $\psi = 45°$*

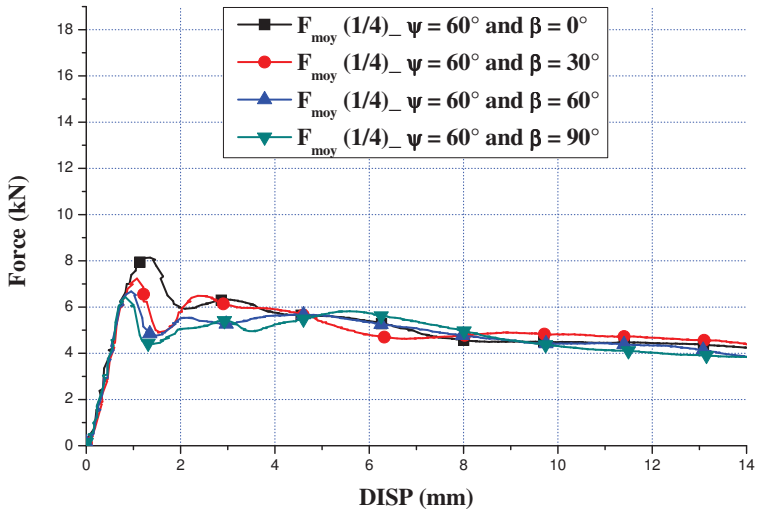

Figure A.6: *The in-plane orientation angle β effects under* ***quasi-static*** *mixed shear-compression loading for $\psi = 60°$*

A.2 Dynamic crushing responses

The loading angle ψ effects

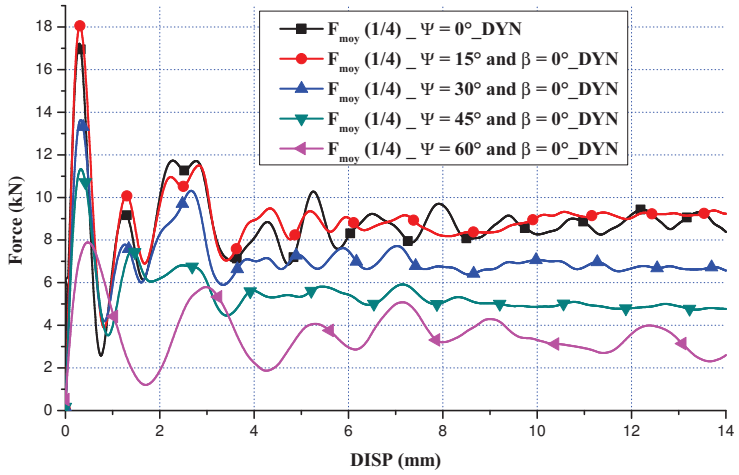

Figure A.7: *The loading angle ψ effects under* ***dynamic*** *mixed shear-compression loading for $\beta = 0°$*

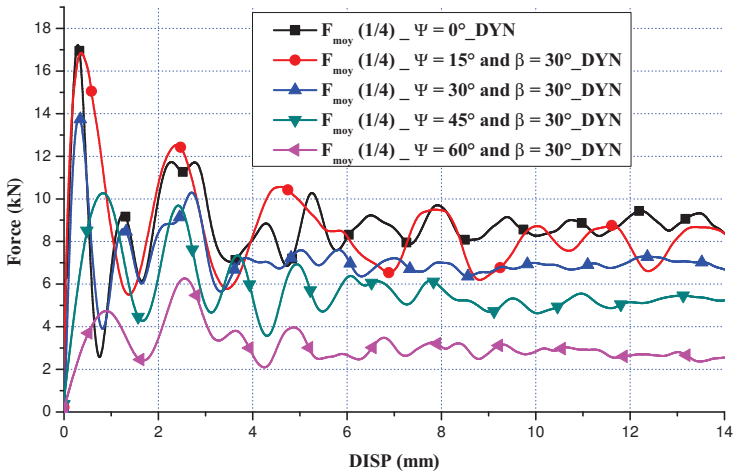

Figure A.8: *The loading angle ψ effects under **dynamic** mixed shear-compression loading for $\beta = 30°$*

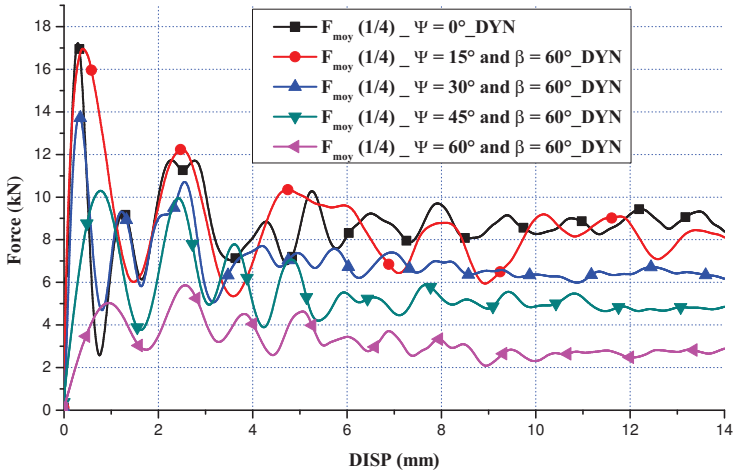

Figure A.9: *The loading angle ψ effects under **dynamic** mixed shear-compression loading for $\beta = 60°$*

The in-plane orientation angle β effects

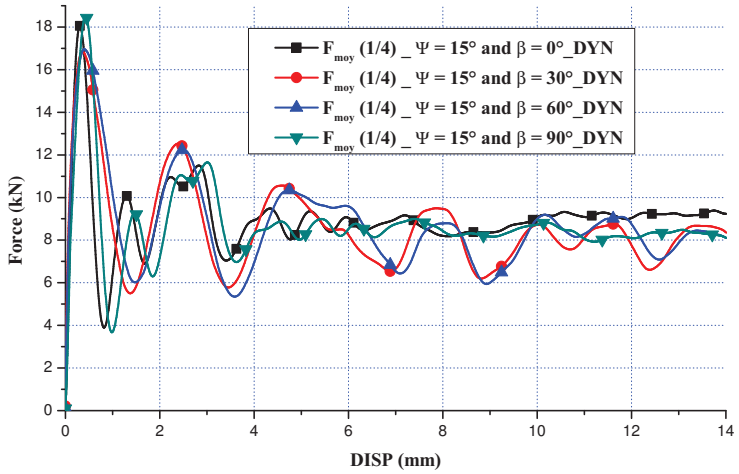

Figure A.10: *The in-plane orientation angle β effects under **dynamic** mixed shear-compression loading for $\psi = 15°$*

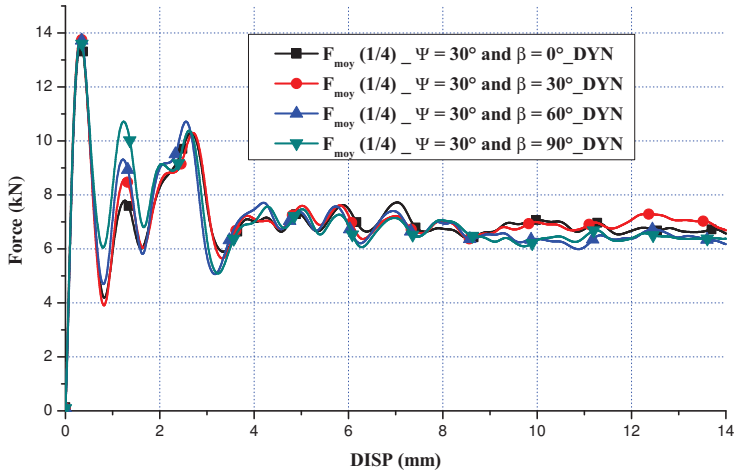

Figure A.11: *The in-plane orientation angle β effects under **dynamic** mixed shear-compression loading for $\psi = 30°$*

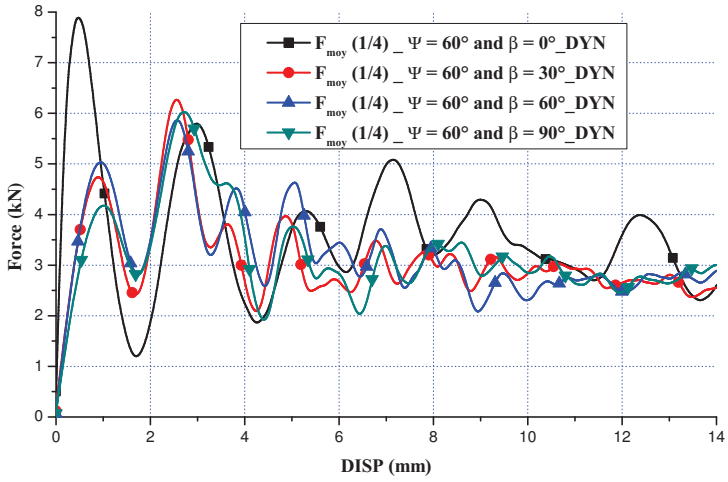

Figure A.12: *The in-plane orientation angle β effects under* ***dynamic*** *mixed shear-compression loading for $\psi = 60°$*

- Appendix B -

The numerical honeycomb behaviour

B.1 Quasi-static crushing responses

The loading angle ψ effects on the F_Z force component

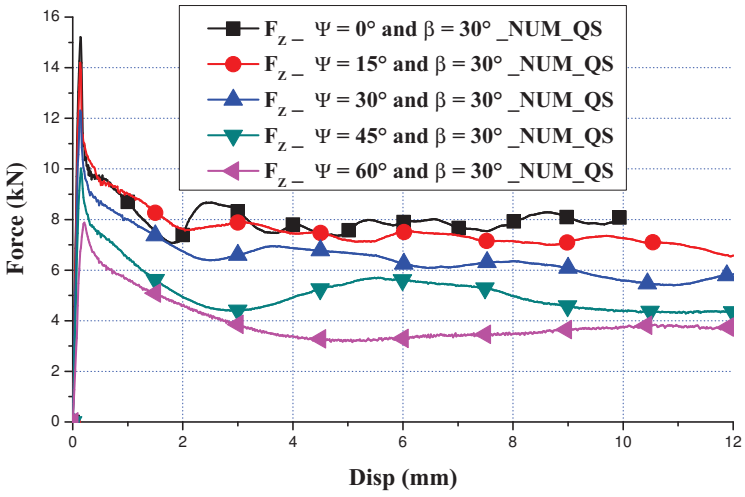

Figure B.1: *The loading angle ψ* ***numerical*** *effects under* ***quasi-static*** *mixed shear-compression loading for $\beta = 30°$*

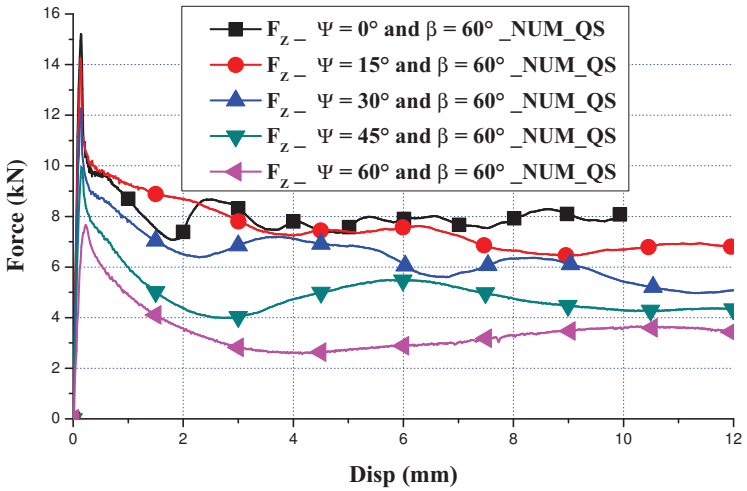

Figure B.2: *The loading angle ψ* ***numerical*** *effects under* ***quasi-static*** *mixed shear-compression loading for $\beta = 60°$*

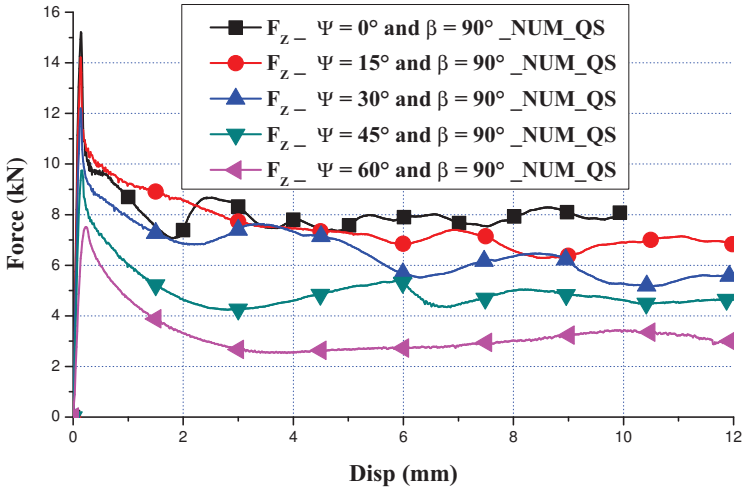

Figure B.3: *The loading angle ψ* ***numerical*** *effects under* ***quasi-static*** *mixed shear-compression loading for $\beta = 90°$*

The in-plane orientation angle β effects on the F_Z force component

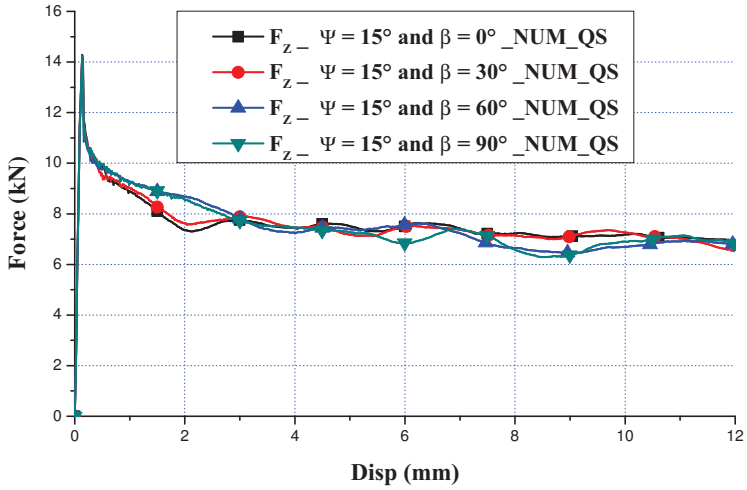

Figure B.4: *The in-plane orientation angle β* ***numerical*** *effects under* ***quasi-static*** *mixed shear-compression loading for $\psi = 15°$*

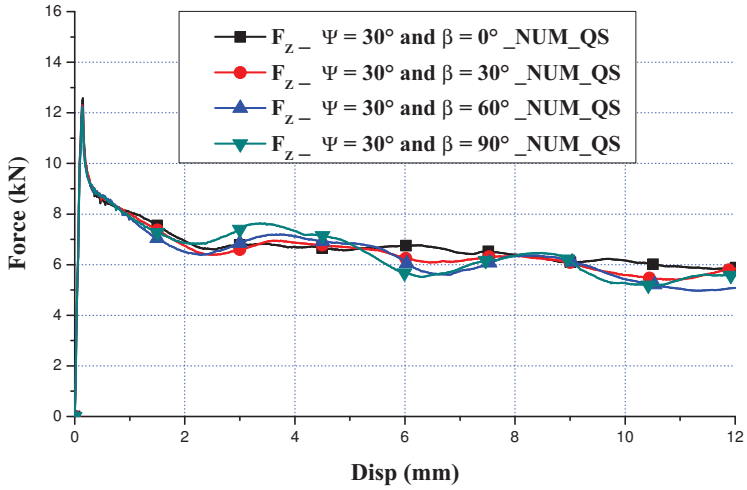

Figure B.5: *The in-plane orientation angle β* ***numerical*** *effects under* ***quasi-static*** *mixed shear-compression loading for $\psi = 30°$*

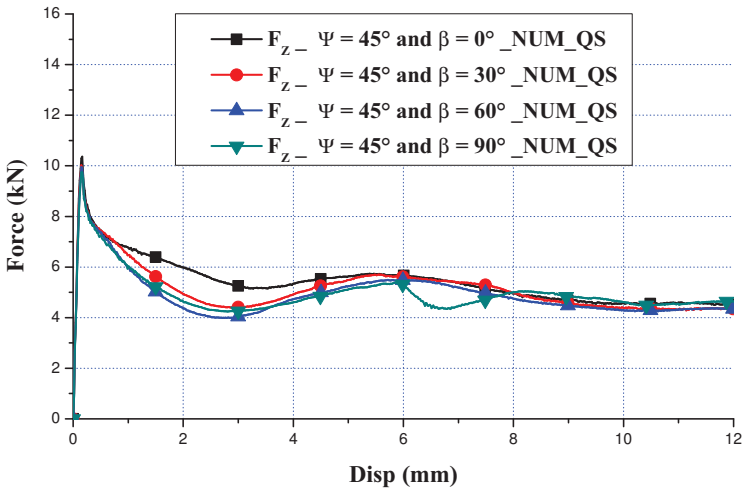

Figure B.6: *The in-plane orientation angle β* ***numerical*** *effects under* ***quasi-static*** *mixed shear-compression loading for $\psi = 45°$*

B.2 Dynamic crushing responses

The loading angle ψ effects on the F_Z force component

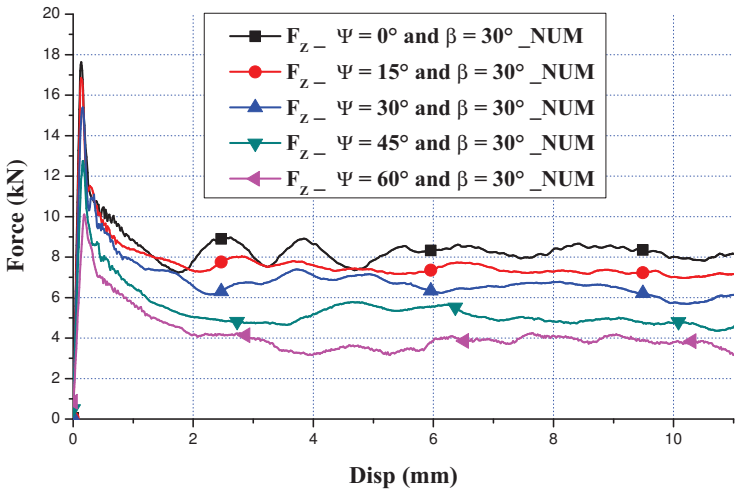

Figure B.7: *The loading angle ψ* ***numerical*** *effects under* ***dynamic*** *mixed shear-compression loading for $\beta = 30°$*

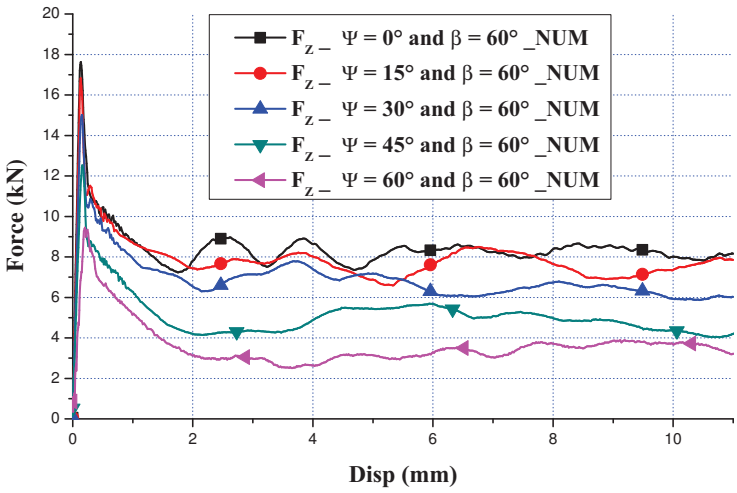

Figure B.8: *The loading angle ψ* ***numerical*** *effects under* ***dynamic*** *mixed shear-compression loading for $\beta = 60°$*

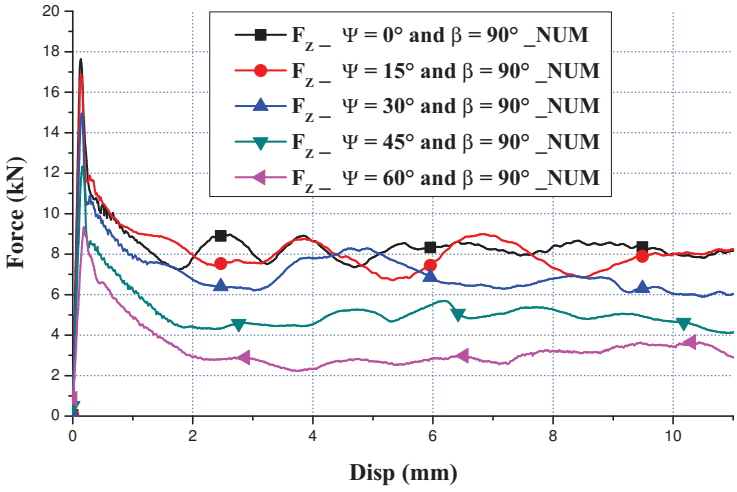

Figure B.9: *The loading angle ψ* ***numerical*** *effects under* ***dynamic*** *mixed shear-compression loading for $\beta = 90°$*

The in-plane orientation angle β effects on the F_Z force component

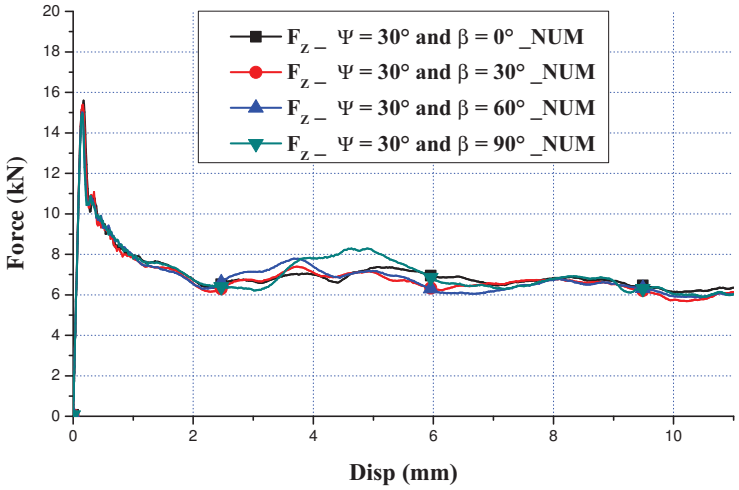

Figure B.10: *The in-plane orientation angle β* ***numerical*** *effects under* ***dynamic*** *mixed shear-compression loading for $\psi = 30°$*

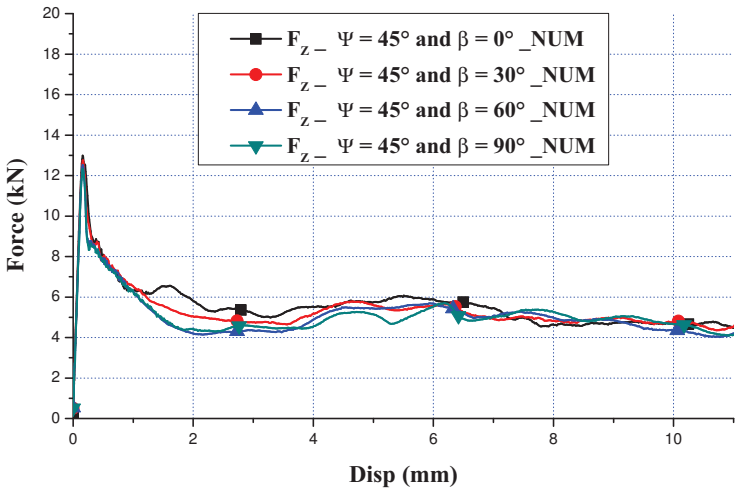

Figure B.11: *The in-plane orientation angle β* ***numerical*** *effects under* ***dynamic*** *mixed shear-compression loading for $\psi = 45°$*

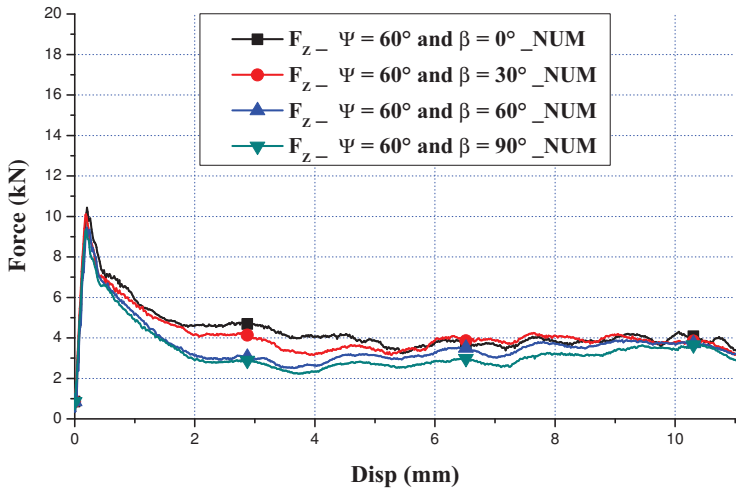

Figure B.12: *The in-plane orientation angle β* ***numerical*** *effects under* ***dynamic*** *mixed shear-compression loading for $\psi = 60°$*

Bibliography

[Abde 03] S. Abdennadher, H. Zhao, and R. Othman. "A study of cellular structures under impact loading". *Journal de Physique IV (Proceedings)*, Vol. 110, pp. 441–446, Sep. 2003. 10

[Akta 08] L. Aktay, A. F. Johnson, and B.-H. Kröplin. "Numerical modelling of honeycomb core crush behaviour". *Engineering Fracture Mechanics*, Vol. 75, No. 9, pp. 2616–2630, 2008. 11

[Ashb 00] M. Ashby, A. Evans, N. Fleck, L. Gibson, J. Hutchinson, and H. Wadley. "Metal foams: a design guide.". *Butterworth-Heinemann, Woburn, MA*, 2000. 15

[ASTM 00] ASTM. "Standard test method for shear properties of sandwich core materials.". *ASTM, Philadelphia, PA.*, 2000. 14

[Bake 98] W. Baker, T. Togami, and J. Weydert. "Static and dynamic properties of high-density metal honeycombs". *International Journal of Impact Engineering*, Vol. 21, No. 3, pp. 149–163, March 1998. 9, 64

[Bitz 97] T. Bitzer. "Honeycomb technology: materials, design, manufacturing, applications and testing.". *Chapman and Hall, New York, NY*, 1997. 15

[Chaw 03] A. Chawla, S. Mukherjee, D. Kumar, T. Nakatani, and M. Ueno. "Prediction of crushing behaviour of honeycomb structures". *International Journal of Crashworthiness*, Vol. 8, No. 3, 2003. 10

[Doyo 03] M. Doyoyo and D. Mohr. "Microstructural response of aluminum honeycomb to combined out-of-plane loading". *Mechanics of*

Materials, Vol. 35, No. 9, pp. 865–876, Sep. 2003. v, 12, 13, 23, 28

[Gold 92] W. Goldsmith and J. L. Sackman. "An experimental study of energy absorption in impact on sandwich plates". *International Journal of Impact Engineering*, Vol. 12, pp. 241–262, 1992. 9, 64

[Gold 95] W. Goldsmith and D. L. Louie. "Axial perforation of aluminum honeycombs by projectiles". *International Journal of Solids and Structures*, Vol. 32, No. 8–9, pp. 1017–1046, Apr. 1995. 9

[Harr 99] J. Harrigan, S. Reid, and C. Peng. "Inertia effects in impact energy absorbing materials and structures". *International Journal of Impact Engineering*, Vol. 22, No. 9–10, pp. 955–979, Oct. 1999. 28, 64

[Hill 50] Hill R . *The Mathematical Theory of Plasticity*. Vol. Oxford University Press, New York, NY, 1950. 27

[Hong 03] S. T. Hong, J. Pan, T. Tyan, and P. Prasad. "Crush Strength of Aluminum 5052-H38 Honeycomb Materials under Combined Compressive and Shear Loads". SAE Technical Paper 2003-01-0331, SAE International, Warrendale, PA, March 2003. 14

[Hong 04] S.-t. Hong, J. Pan, T. Tyan, and P. Prasad. "Dynamic Crush Behavior of Aluminum 5052-H38 Honeycomb Specimens Under Out-of-Plane Inclined Loads". *ASME 2004 International Mechanical Engineering Congress and Exposition, Anaheim, California, USA, November 13 – 19*, pp. 35–41, 2004. 14

[Hong 06a] S.-T. Hong, J. Pan, T. Tyan, and P. Prasad. "Quasi-static crush behavior of aluminum honeycomb specimens under compression dominant combined loads". *International Journal of Plasticity*, Vol. 22, No. 1, pp. 73–109, Jan. 2006. v, vi, 14, 15, 16, 17, 27, 30, 78, 118

[Hong 06b] S.-T. Hong, J. Pan, T. Tyan, and P. Prasad. "Quasi-static crush behavior of aluminum honeycomb specimens under non-proportional compression-dominant combined loads". *International Journal of Plasticity*, Vol. 22, No. 6, pp. 1062–1088, 2006. 14, 78

[Hong 08] S.-T. Hong, J. Pan, T. Tyan, and P. Prasad. "Dynamic crush behaviors of aluminum honeycomb specimens under compression dominant inclined loads". *International Journal of Plasticity*, Vol. 24, No. 1, pp. 89–117, Jan. 2008. v, vi, 17, 18, 19, 30, 73, 78, 118

[Hou 11] Hou Bing . *Comportement multiaxiale des nids d'abeilles sous sollicitations dynamiques*. Vol. Phd thesis, 2011. v, 19, 20, 21, 31, 66

[Hou 11a] B. Hou, A. Ono, S. Abdennadher, S. Pattofatto, Y. Li, and H. Zhao. "Impact behavior of honeycombs under combined shear-compression. Part I: Experiments". *International Journal of Solids and Structures*, Vol. 48, No. 5, pp. 687–697, March 2011. v, vi, 20, 21, 22, 31, 33, 36, 38, 39, 40, 41, 42, 78, 126

[Hou 11b] B. Hou, S. Pattofatto, Y. Li, and H. Zhao. "Impact behavior of honeycombs under combined shear-compression. Part II: Analysis". *International Journal of Solids and Structures*, Vol. 48, No. 5, pp. 698–705, March 2011. vi, 23, 25, 26, 31, 36, 39, 41, 42, 78, 118

[M Ar 78] A. V. M. Arcan, Z. Hashin. "A method to produce uniform plane-stress states with applications to fiber-reinforced materials". *Experimental Mechanics*, Vol. 18, pp. 141–146, 1978. 12

[Mark 98] E. Markiewicz, P. Ducrocq, and P. Drazetic. "An inverse approach to determine the constitutive model parameters from axial crushing of thin-walled square tubes". *International Journal of Impact Engineering*, Vol. 21, No. 6, pp. 433–449, 1998. 87

[Mohr 04a] D. Mohr and M. Doyoyo. "Deformation-induced folding systems in thin-walled monolithic hexagonal metallic honeycomb". *International Journal of Solids and Structures*, Vol. 41, No. 11–12, pp. 3353–3377, 2004. vi, 23, 24, 28, 29, 33, 78, 89, 103, 118, 126

[Mohr 04b] D. Mohr and M. Doyoyo. "Experimental investigation on the plasticity of hexagonal aluminum honeycomb under multiaxial

loading". *Journal of applied mechanics*, Vol. 71, No. 3, pp. 375–385, 2004. v, 12, 13, 28, 78

[Mohr 04c] D. Mohr and M. Doyoyo. "Large plastic deformation of metallic honeycomb: orthotropic rate-independent constitutive model". *International Journal of Solids and Structures*, Vol. 41, No. 16–17, pp. 4435–4456, 2004. 28, 78

[OCon 89] D. O'Connor. "A comparison of test methods for shear properties of the cores of sandwich constructions". *Journal of Testing and Evaluation*, Vol. 17, pp. 241–246, 1989. 14

[Sant 98] S. Santosa and T. Wierzbicki. "Crash behavior of box columns filled with aluminum honeycomb or foam". *Computers & Structures*, Vol. 68, No. 4, pp. 343–367, Aug. 1998. 10

[Toun 12] R. Tounsi, B. Zouari, F. Chaari, G. Haugou, E. Markiewicz, and F. Dammak. "Experimental study of aluminium honeycomb behaviour under dynamic multiaxial loading". *EPJ Web of Conferences*, Vol. 26, p. 01050, Aug. 2012. 46

[Toun 13] R. Tounsi, B. Zouari, F. Chaari, E. Markiewicz, G. Haugou, and F. Dammak. "Reduced numerical model to investigate the dynamic behaviour of honeycombs under mixed shear-compression loading". *International Journal of Thin-Walled Structures*, Vol. 73, pp. 290–301, 2013. 126

[Wier 83a] T. Wierzbicki and W. Abramowicz. "On the Crushing Mechanics of Thin-Walled Structures". *Journal of Applied Mechanics*, Vol. 50, No. 4a, p. 727, 1983. 9

[Wier 83b] T. Wierzbicki. "Crushing analysis of metal honeycombs". *International Journal of Impact Engineering*, Vol. 1, No. 2, pp. 157–174, 1983. 9

[Wilb 11] A. Wilbert, W.-Y. Jang, S. Kyriakides, and J. Floccari. "Buckling and progressive crushing of laterally loaded honeycomb". *International Journal of Solids and Structures*, Vol. 48, No. 5, pp. 803–816, March 2011. 129

[Wu 97] E. Wu and W.-S. Jiang. "Axial crush of metallic honeycombs". *International Journal of Impact Engineering*, Vol. 15, No. 5/6, 1997. 9, 64

[Yama 05] M. Yamashita and M. Gotoh. "Impact behavior of honeycomb structures with various cell specifications—numerical simulation and experiment". *International Journal of Impact Engineering*, Vol. 32, No. 1–4, pp. 618–630, 2005. 10, 22

[Zhan 92] J. Zhang and M. Ashby. "The out-of-plane properties of honeycombs". *International Journal of Mechanical Sciences*, Vol. 34, No. 6, pp. 475–489, June 1992. 28

[Zhao 04] H. Zhao and S. Abdennadher. "On the strength enhancement under impact loading of square tubes made from rate insensitive metals". *International Journal of Solids and Structures*, Vol. 41, No. 24–25, pp. 6677–6697, Dec. 2004. 69, 73

[Zhao 05] H. Zhao, I. Elnasri, and S. Abdennadher. "An experimental study on the behaviour under impact loading of metallic cellular materials". *International Journal of Mechanical Sciences*, Vol. 47, No. 4–5, pp. 757–774, 2005. 10, 64

[Zhao 98] H. Zhao and G. Gary. "Crushing behaviour of aluminium honeycombs under impact loading". *International Journal of Impact Engineering*, Vol. 21, No. 10, pp. 827–836, Nov. 1998. 9, 64

[Zhou 02] Q. Zhou and R. R. Mayer. "Characterization of Aluminum Honeycomb Material Failure in Large Deformation Compression, Shear, and Tearing". *Journal of Engineering Materials and Technology*, Vol. 124, No. 4, pp. 412–420, Sep. 2002. 64

[Zhou 12] Z. Zhou, Z. Wang, L. Zhao, and X. Shu. "Experimental investigation on the yield behavior of Nomex honeycombs under combined shear-compression". *Latin American Journal of Solids and Structures*, Vol. 9, No. 4, p. 515, June 2012. v, vi, 13, 14, 31, 32, 118

Abstract

Aluminium honeycombs combine lightweight with an efficient energy absorption capability (specific energy). They are widely used as crash energy absorbing and protective structures in a wide range of transport applications (automotive, aircraft ...) to reduce energy consumption and greenhouse gas emission. Reducing vehicle mass has however to be done while at least maintaining the same safety levels. In this thesis, the honeycomb behaviour is investigated under mixed shear-compression loadings taking into account the combined effect of the in-plane orientation angle and the impact velocity, which has not been deeply investigated in the literature. Experimental study based on an improvement of a mixed shear-compression loading device is realised. Experimental analysis focuses on the initial peak and average crushing forces as well as the deforming pattern modes. Comparing quasi-static and dynamic results, a dynamic enhancement depending of the loading angle ψ is observed under mixed shear-compression loading until a critical loading angle ($\psi_{critical}$). Beyond, a negative enhancement is observed. Thus, a numerical study is carried out. The negative enhancement phenomenon is attributed to the collapse mechanisms which are affected by the loading angle ψ. Numerical results also highlight that the in-plane orientation angle β has an effect on the collapse mechanisms and consequently on the mechanical response. This effect is more pronounced on the tangential force than the normal force. The combined effect of the in-plane orientation angle and the loading angle is analysed on the three identified deforming pattern modes. Combining numerical and experimental results, the average crushing normal and shear forces are dissociated. Therefore, the parameters of a macroscopic yield criterion for the mixed shear-compression honeycomb behaviour depending of the impact velocity, the loading angle and the in-plane orientation angle are identified. Finally, in order to optimise the cost in CPU-time of the numerical simulation, a reduced FE model based on the periodicity procedure taking into account the in-plane orientation angle is proposed and its validity range is evaluated.

Résumé

Les nids d'abeille d'aluminium combinent légèreté et grande capacité d'absorption d'énergie. Ils sont alors de plus en plus utilisés dans les secteurs du transport (automobile, aéronautique ...) pour contribuer conjointement à l'allègement structural et à la sécurité. Dans cette thèse, le comportement à l'écrasement des nids d'abeille est étudié en tenant compte de l'effet combiné de l'angle d'orientation dans le plan des cellules, de l'angle de chargement et de la vitesse de sollicitation, que la littérature ne relate pas. Un dispositif de chargement mixte compression/cisaillement est conçu pour mener l'étude expérimentale. L'analyse des résultats porte sur le pic initial d'effort, le plateau d'effort, ainsi que sur les modes de déformation. Les résultats montrent une augmentation de la résistance sous sollicitation dynamique dépendante de l'angle de chargement ψ. Elle devient moins significative quand l'angle de chargement augmente jusqu'à atteindre un angle critique. Pour $\psi > \psi_{critique}$, les réponses quasi-statiques sont même plus élevées que les réponses dynamiques. Une étude numérique est alors entreprise. Elle permet de comprendre ce phénomène qui est imputé aux mécanismes de déformation locaux des cellules. Les résultats numériques montrent également que l'effet de l'angle d'orientation β dans le plan est plus prononcé sur la force tangentielle que sur la force normale, que cela influence également les modes d'effondrement et donc la réponse mécanique. Ces simulations numériques, couplées aux résultats expérimentaux, permettent alors de dissocier les composantes normale et tangentielle de la réponse des nids d'abeille et d'identifier les paramètres d'un critère macroscopique de résistance exprimé en fonction de la vitesse d'impact, de l'angle de chargement et de l'angle d'orientation dans le plan. Finalement, dans le but de réduire le coût des simulations numériques, un modèle élément fini (EF) réduit basé sur un critère de périodicité tenant compte de l'angle d'orientation dans le plan est proposé et son domaine de validité est évalué.

Comportement des structures en nids d'abeilles sous sollicitations dynamiques mixtes compression/cisaillement et effet de l'orientation des cellules

Rami TOUNSI

Résumé : Les nids d'abeille d'aluminium combinent légèreté et grande capacité d'absorption d'énergie. Ils sont alors de plus en plus utilisés dans les secteurs du transport (automobile, aéronautique …) pour contribuer conjointement à l'allègement structural et à la sécurité. Dans cette thèse, le comportement à l'écrasement des nids d'abeille est étudié en tenant compte de l'effet combiné de l'angle d'orientation dans le plan des cellules, de l'angle de chargement et de la vitesse de sollicitation, que la littérature ne relate pas. Un dispositif de chargement mixte compression/cisaillement est conçu pour mener l'étude expérimentale. L'analyse des résultats porte sur le pic initial d'effort, le plateau d'effort, ainsi que sur les modes de déformation. Les résultats montrent une augmentation de la résistance sous sollicitation dynamique dépendante de l'angle de chargement Ψ. Elle devient moins significative quand l'angle de chargement augmente jusqu'à atteindre un angle critique. Pour $\Psi > \Psi_{critique}$, les réponses quasi-statiques sont même plus élevées que les réponses dynamiques. Une étude numérique est alors entreprise. Elle permet de comprendre ce phénomène qui est imputé aux mécanismes de déformation locaux des cellules. Les résultats numériques montrent également que l'effet de l'angle d'orientation dans le plan est plus prononcé sur la force tangentielle que sur la force normale, que cela influence également les modes d'effondrement et donc la réponse mécanique. Ces simulations numériques, couplées aux résultats expérimentaux, permettent alors de dissocier les composantes normale et tangentielle de la réponse des nids d'abeille et d'identifier les paramètres d'un critère macroscopique de résistance exprimé en fonction de la vitesse d'impact, de l'angle de chargement et de l'angle d'orientation dans le plan. Finalement, dans le but de réduire le coût des simulations numériques, un modèle élément fini (EF) réduit basé sur un critère de périodicité tenant compte de l'angle d'orientation dans le plan est proposé et son domaine de validité est évalué.

Mots clés: Nids d'abeille, chargement mixte, expérimental tests, numéral simulation, angle de chargement, vitesse d'impact, orientation des cellules, critère macroscopique de résistance.

Abstract: Aluminium honeycombs combine lightweight with an efficient energy absorption capability (specific energy). They are widely used as crash energy absorbing and protective structures in a wide range of transport applications (automotive, aircraft …) to reduce energy consumption and greenhouse gas emission. Reducing vehicle mass has however to be done while at least maintaining the same safety levels. In this thesis, the honeycomb behaviour is investigated under mixed shear-compression loadings taking into account the combined effect of the in-plane orientation angle and the impact velocity, which has not been deeply investigated in the literature. Experimental study based on an improvement of a mixed shear-compression loading device is realised. Experimental analysis focuses on the initial peak and average crushing forces as well as the deforming pattern modes. Comparing quasi-static and dynamic results, a dynamic enhancement depending of the loading angle Ψ is observed under mixed shear-compression loading until a critical loading angle ($\Psi_{critical}$). Beyond, a negative enhancement is observed. Thus, a numerical study is carried out. The negative enhancement phenomenon is attributed to the collapse mechanisms which are affected by the loading angle Ψ. Numerical results also highlight that the in-plane orientation angle has an effect on the collapse mechanisms and consequently on the mechanical response. This effect is more pronounced on the tangential force than the normal force. The combined effect of the in-plane orientation angle and the loading angle is analysed on the three identified deforming pattern modes. Combining numerical and experimental results, the average crushing normal and shear forces are dissociated. Therefore, the parameters of a macroscopic yield criterion for the mixed shear-compression honeycomb behaviour depending of the impact velocity, the loading angle and the in-plane orientation angle are identified. Finally, in order to optimise the cost in CPU-time of the numerical simulation, a reduced FE model based on the periodicity procedure taking into account the in-plane orientation angle is proposed and its validity range is evaluated.

Key-words: Honeycomb, mixed shear-compression loading, experiments, simulations, loading angle, impact velocity, in-plane orientation cells, macroscopic yield criterion.

Comportement des structures en nids d'abeilles sous sollicitations dynamiques mixtes compression/cisaillement et effet de l'orientation des cellules

Rami TOUNSI

Résumé :

Les nids d'abeille d'aluminium combinent légèreté et grande capacité d'absorption d'énergie. Ils sont alors de plus en plus utilisés dans les secteurs du transport (automobile, aéronautique …) pour contribuer conjointement à l'allègement structural et à la sécurité. Dans cette thèse, le comportement à l'écrasement des nids d'abeille est étudié en tenant compte de l'effet combiné de l'angle d'orientation dans le plan des cellules, de l'angle de chargement et de la vitesse de sollicitation, que la littérature ne relate pas. L'angle de chargement Ψ c'est l'angle entre la direction du chargement normal et la direction de l'axe de la cellule de nids d'abeille. L'angle d'orientation dans le plan de la cellule β c'est l'angle entre la direction de chargement de cisaillement et la direction des parois cellulaires double épaisseur (figure 1).

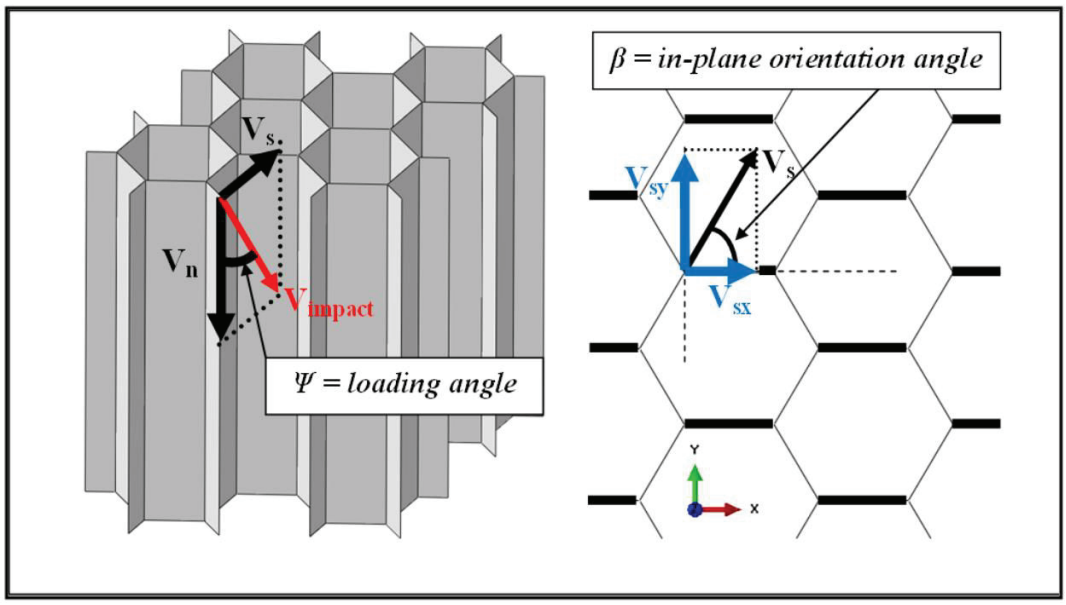

Figure1. *Angle de chargement Ψ et angle d'orientation dans le plan de la cellule β*

I- Etude bibliographique :

Dans le chapitre 1 : une étude bibliographique a été réalisée sur le comportement des nids d'abeilles en aluminium sous des chargements uni-axiaux dans un premier temps et sous des chargements mixtes compression/cisaillement. Le comportement uni-axial est largement étudié dans la littérature. Par contre le comportement sous des chargements mixtes compression/cisaillement est récemment étudié. L'étude a été présentée selon le dispositif utilisé pour réaliser des essais en chargement mixtes. Le premier dispositif est de type ARCAN où l'échantillon est sous forme d'un papillon afin de réaliser le chargement combiné. Il permet de réaliser uniquement des essais en quasi-statique pour un seul d'angle d'orientation dans le plan de la cellule (β). Un dispositif basé sur un montage de chargement mixte a été élaboré par Hong et al. Il permet de réaliser des essais en quasi-statique et en dynamique en tenant compte de (β) mais uniquement pour un seul angle de chargement Ψ = 15 °. Leurs résultats montrent que l'angle (β) a une influence sur la valeur du plateau représentant la contrainte d'écrasement. Ils ont élaboré un critère macroscopique de résistance à l'effondrement des nids d'abeille. Bing HOU a développé un nouveau montage pour le chargement combiné « Mixed shear-compression device ». Son montage permet de varier l'angle de chargement Ψ pour les deux conditions quasi-statique et dynamique. Elle a étudié l'influence de deux angles β (β =0° et 90°). Aucun effet de β n'a été rapporté par Bing HOU. Cependant il y des travaux très récents sur les nids d'abeille en Nomex présentés par Zhang qui a montré l'influence de l'angle β sur le critère macroscopique de résistance en quasi-statique.

Le tableau 1 résume les différents travaux dans la littérature.

Tableau 1. *Les travaux antérieurs sur le comportement des nids d'abeille sous chargement mixtes.*

	Le critère macroscopique de résistance			**Les mécanismes de déformation**	
	Ψ	**β**	**V_{imp}**	**Mode I**	**Mode II**
Mohr etal (02/04)	Oui	Non	Non	Oui	Non
Hong etal (06/08)	Non	Oui	Oui	Oui	Non
Hou etal (10/11)	Oui	Non	Oui	Oui	Oui
Zhang etal (12)	Oui	Oui	Non	Non	Non

La question qui se pose : est ce qu'il y a une influence de β en dynamique et en quasi-statique sur le comportement des nids d'abeille en Aluminium sous des chargements mixtes ?

II- Etude expérimentale

Le chapitre 2 présente les travaux expérimentaux effectués dans cette thèse. Un dispositif de chargement mixte compression/cisaillement est conçu pour mener l'étude expérimentale. Ce dispositif basé sur une amélioration du montage développé par Bing HOU incorporé dans le dispositif des barres de Hopkinson. Cette amélioration consiste à augmenter la rigidité du montage (bague de guidage) afin de garantir un bon alignement des deux bouts de barres du dispositif de chargement durant le test (figure 2).

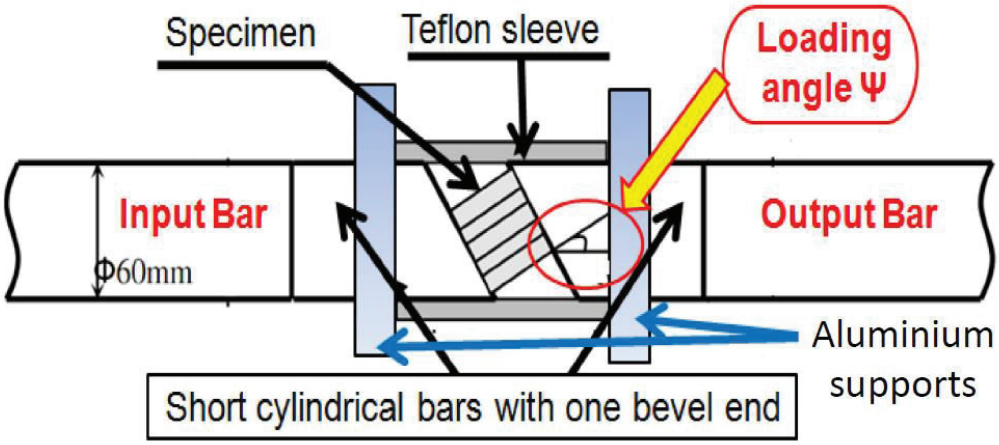

Figure 2. *Le dispositif des barres de Hopkinson avec le montage de chargement mixtes.*

Une étude numérique a été élaborée à ce niveau et montre qu'avec une couronne de Téflon d'épaisseur 5 mm entourée par une couronne en acier d'épaisseur 10 mm, on assure un bon alignement durant le test (figure3).

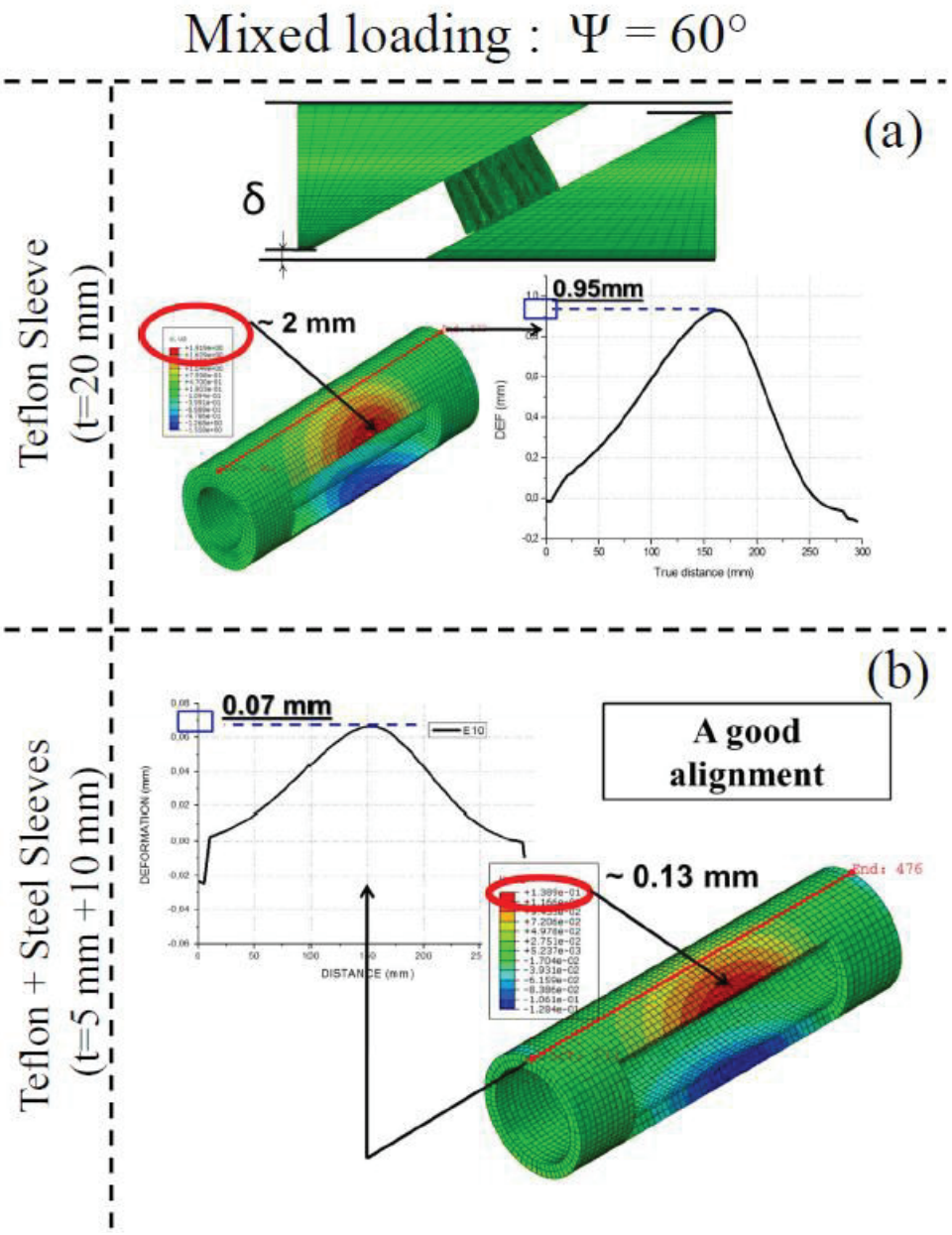

Figure 3. *L'amélioration du montage du chargement mixte.*

Au cours de cette étude numérique, un phénomène de séparation au niveau du montage avec le dispositif des barres de Hopkinson a été observé et l'effet de l'utilisation des manchons inclinés a été étudié (figure4). Cet effet montre une coupure au niveau de l'onde réfléchie qui met en cause la limitation du logiciel de traitement DAVID (logiciel de traitement des signaux d'onde récupérées sur les barres de Hopkinson). D'où l'idée d'utiliser un Extensomètre optique dans la campagne expérimentale afin de compléter la mesure de la force de sortie avec un grand déplacement d'écrasement de l'échantillon (figure 5).

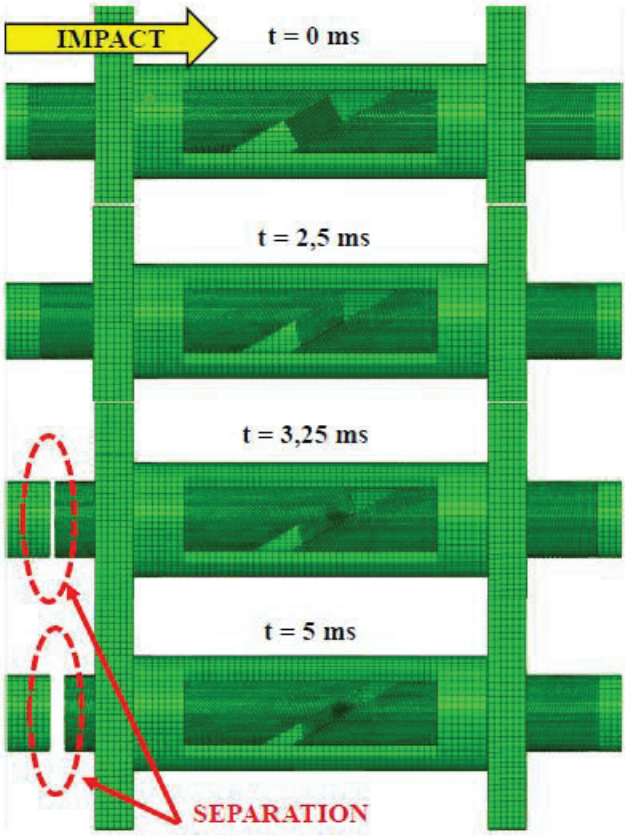

Figure 4. *Le phénomène de séparation sous un chargement mixte (Ψ = 60°)*

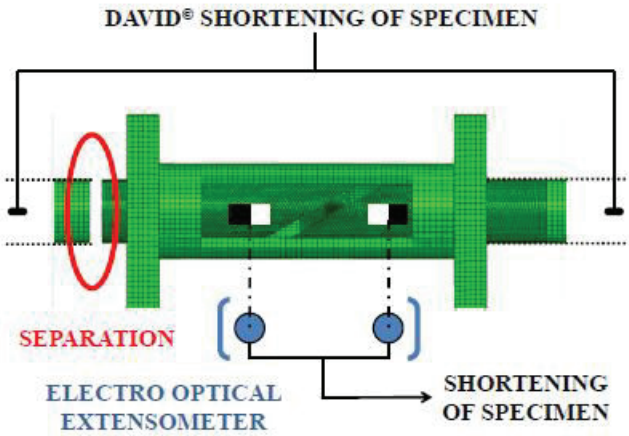

Figure 5. *L'amélioration de mesure de déplacement d'écrasement de l'échantillon à l'aide d'un extensomètre optique laser sous un chargement mixte.*

Finalement, le montage de chargement mixte amélioré est utilisé dans la campagne expérimentale en adaptant un extensomètre optique laser pour la mesure de la distance d'écrasement de l'échantillon sous des conditions en quasi-statique et en dynamique (figure 6).

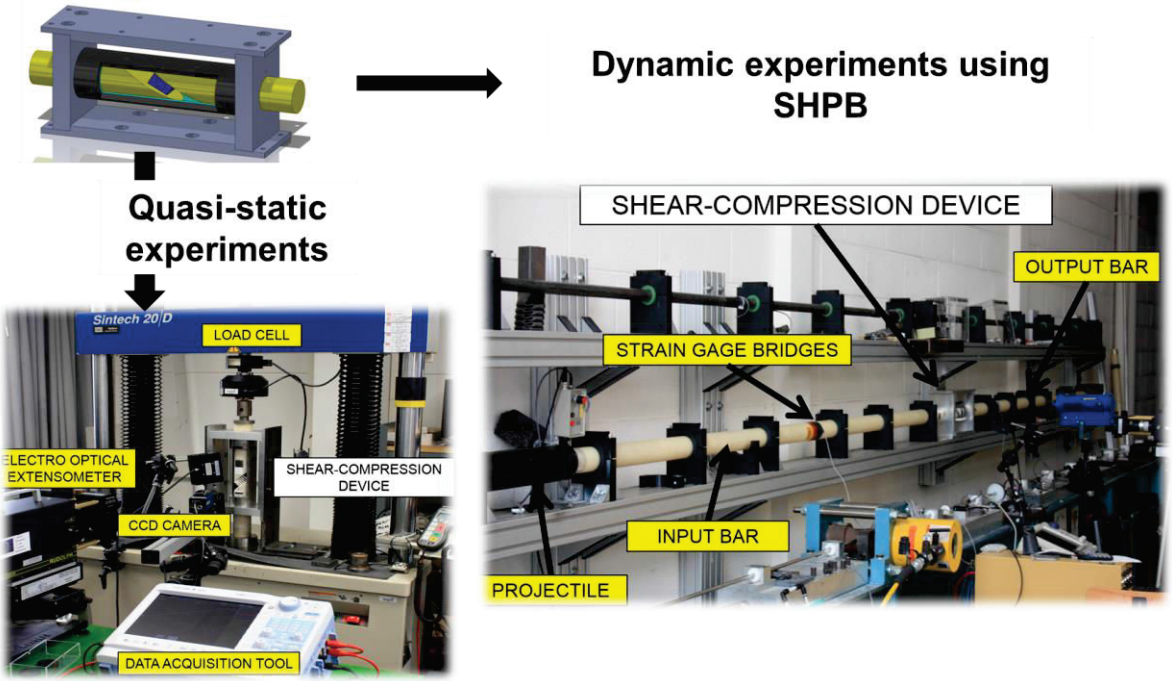

Figure 6. *Le montage de chargement amélioré introduit aux dispositifs en quasi-statique et en dynamique.*

L'analyse des résultats expérimentaux a été menée sur deux aspects : un pour les réponses d'écrasement (force-déplacement) et un pour les mécanismes de déformation. Pour l'analyse des résultats en termes de réponse, cette analyse porte sur le pic initial d'effort et le plateau d'effort (figure 7).

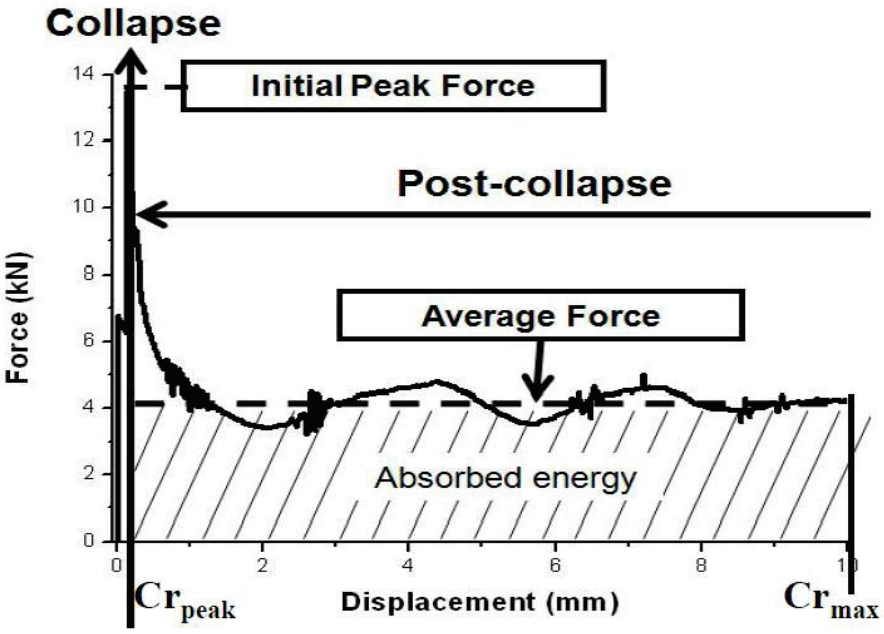

Figure 7. *La réponse d'écrasement d'une structure en nids d'abeille.*

Les résultats montrent un effet significatif de l'angle de chargement Ψ sur le pic et le plateau. Le niveau de force diminue avec l'augmentation de l'angle Ψ. Concernant l'influence de l'angle β, un effet négligeable a été observé et il devient plus important (significatif) quand l'angle de chargement Ψ augmente (figures 8-11).

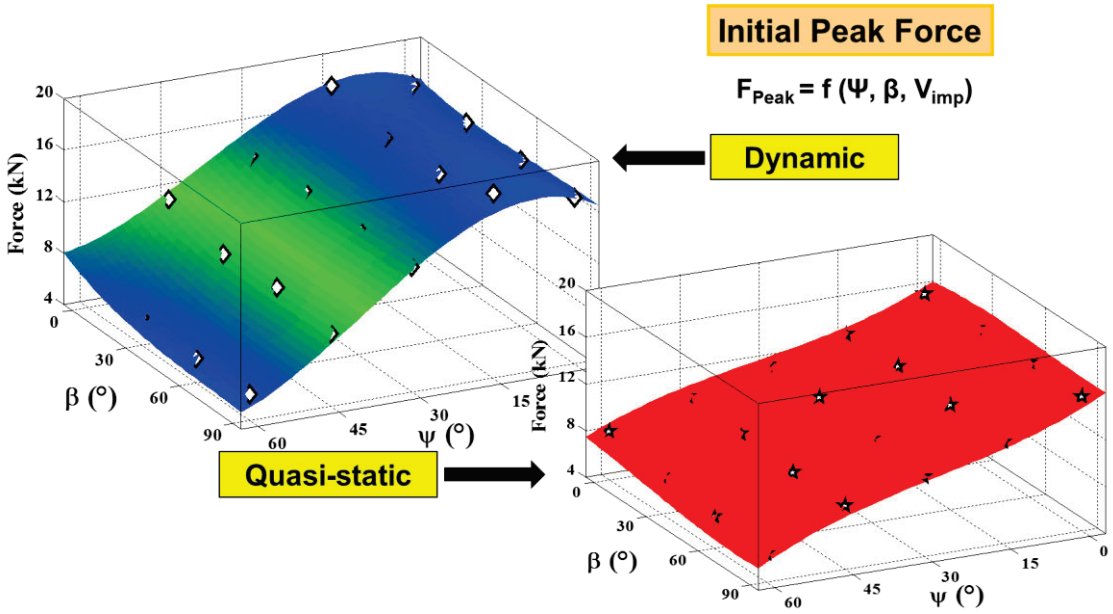

Figure 8. *L'effet combiné de l'angle de chargement Ψ et l'angle d'orientation dans le plan la cellule β sur le pic initial.*

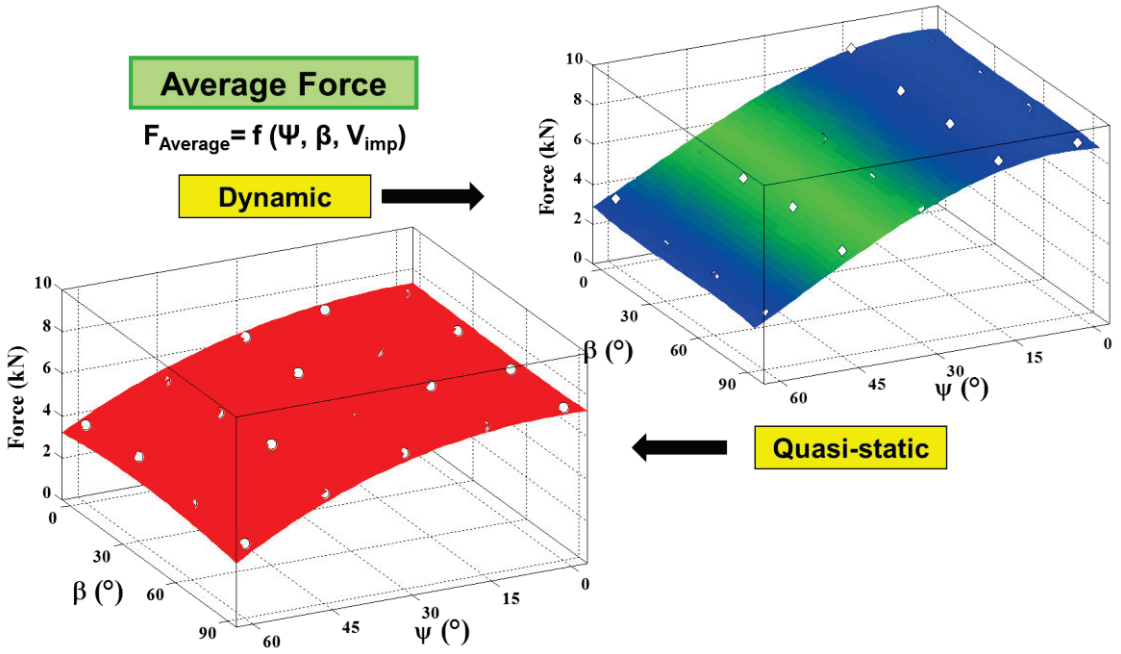

Figure 9. *L'effet combiné de l'angle de chargement Ψ et l'angle d'orientation dans le plan la cellule β sur le plateau.*

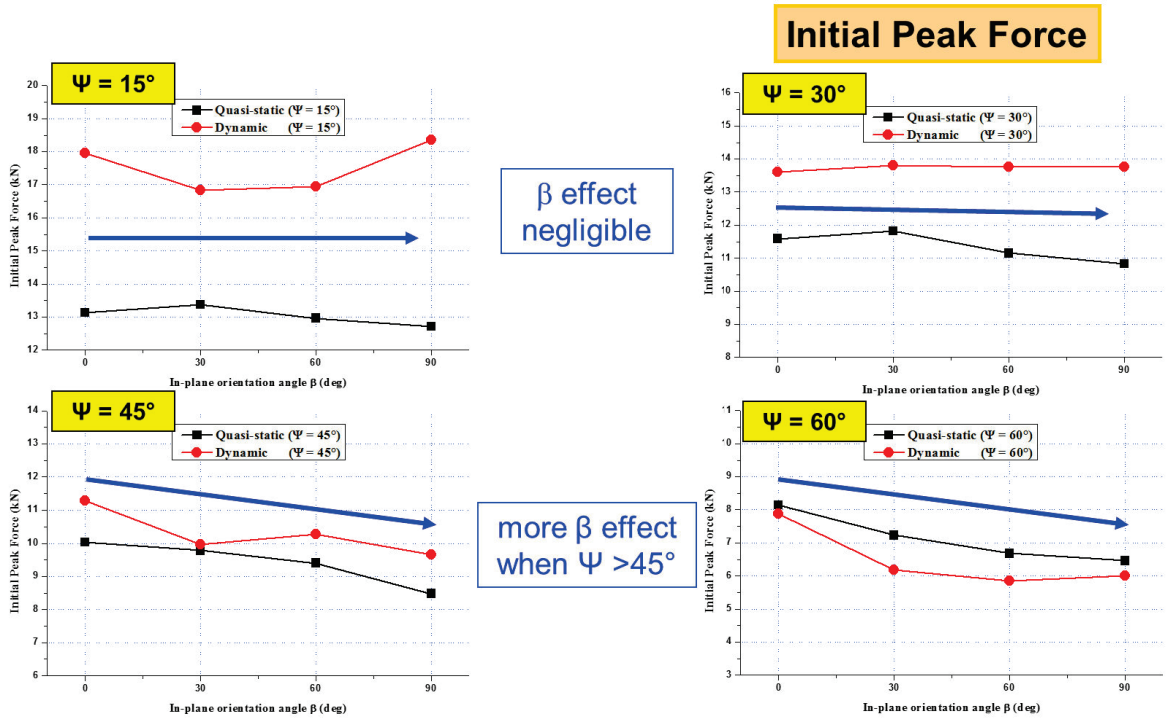

Figure 10. *L'influence de l'angle d'orientation dans le plan la cellule β sur le pic initial.*

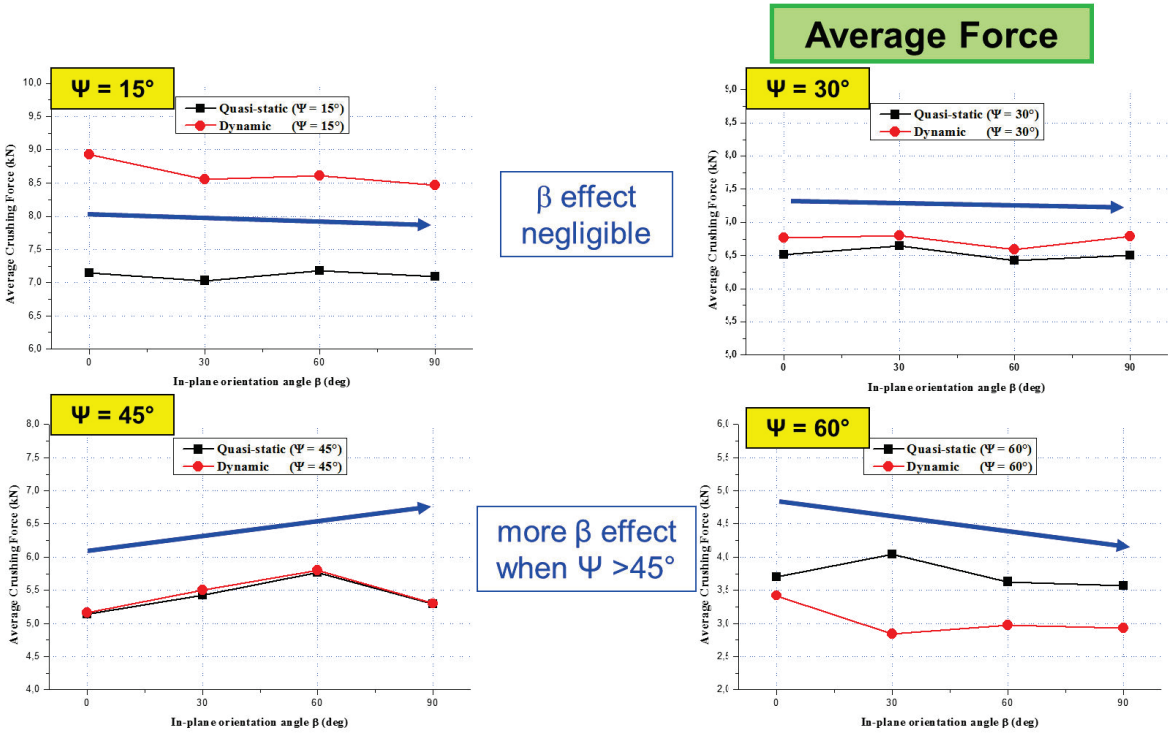

Figure 11. *L'influence de l'angle d'orientation dans le plan la cellule β sur le plateau.*

La comparaison entre les résultats quasi-statiques et dynamiques montre une augmentation de la résistance sous sollicitation dynamique dépendante de l'angle de chargement Ψ. Elle

devient moins significative quand l'angle de chargement augmente jusqu'à atteindre Ψ = 45°. Pour Ψ > 45°, les réponses quasi-statiques sont même plus élevées que les réponses dynamiques (figure 12 pour le pic initial et pour le plateau).

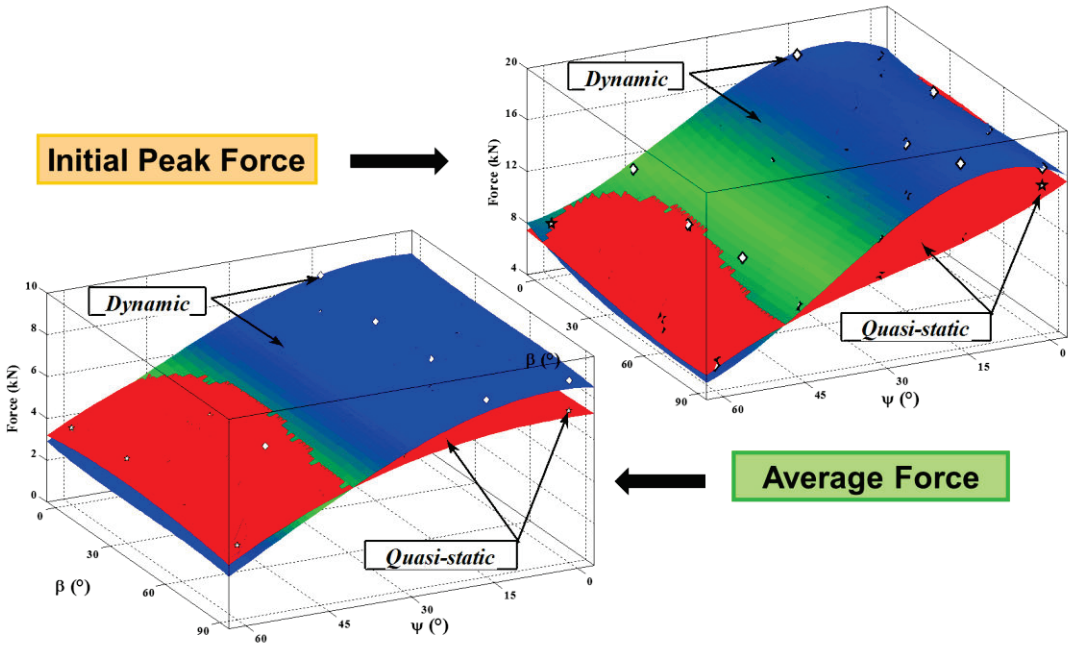

Figure 12. *L'effet dynamique sur le pic initial et sur le plateau.*

Au niveau des mécanismes de déformation, trois modes de déformations ont été observés expérimentalement. Le mode I consiste à un effondrement et formation progressive des lobes d'un seul côté de l'échantillon sans rotation de l'axe de la cellule. Ce mode I est observé par la plupart des travaux dans la littérature. Le mode II consiste en un effondrement et formation progressive des lobes localisée simultanément sur les deux côtés de l'échantillon dès le début d'écrasement. Ce ci provoque la rotation de l'axe de la cellule. Ce mode a été identifié par les travaux de Bing HOU. Un nouveau mode III a été observé dans nos expériences. Dans ce mode, la formation des lobes se localise en haut puis en bas de l'échantillon, ce qui provoque la rotation global de l'échantillon (figures 13 et 14).

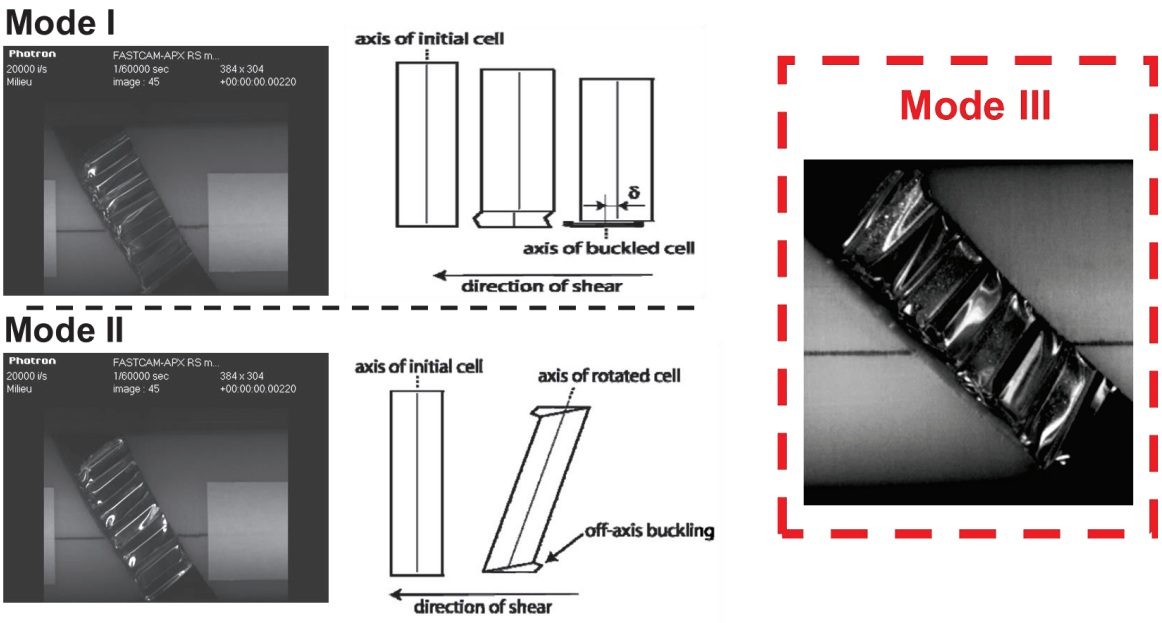

Figure 13. *Les modes de déformation observés expérimentalement.*

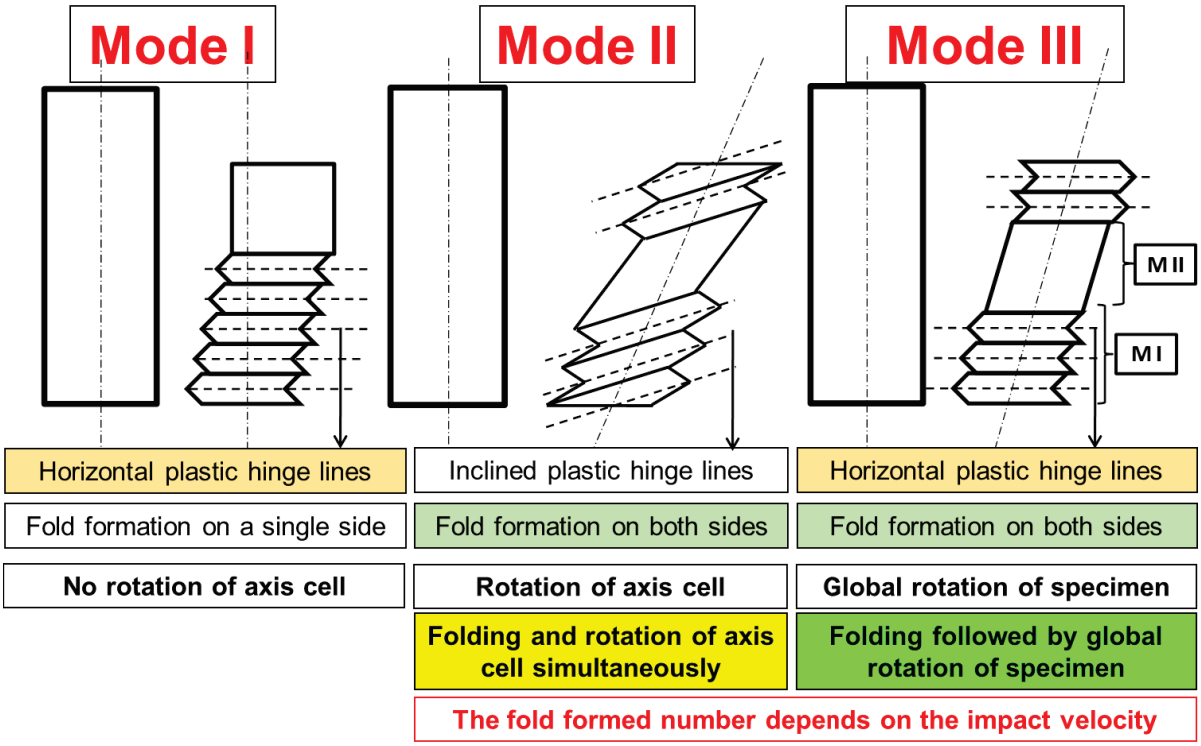

Figure 14. *Schéma des modes de déformation.*

La distribution de ces modes présentée par le tableau 2 est liée à l'effet combiné de l'angle de chargement Ø et l'angle d'orientation dans le plan de la cellule β (figure 15).

Tableau 2. *L'effet combiné de l'angle Ψ et l'angle β sur les modes de déformation*

	$\beta = 0°$	$\beta = 30°$	$\beta = 60°$	$\beta = 90°$
$\psi = 0°$		MI		
$\psi = 15°$		MI		
$\psi = 30°$	*MII*	MIII	MI	
$\psi = 45°$			MIII	MI
$\psi = 60°$				MIII/MI

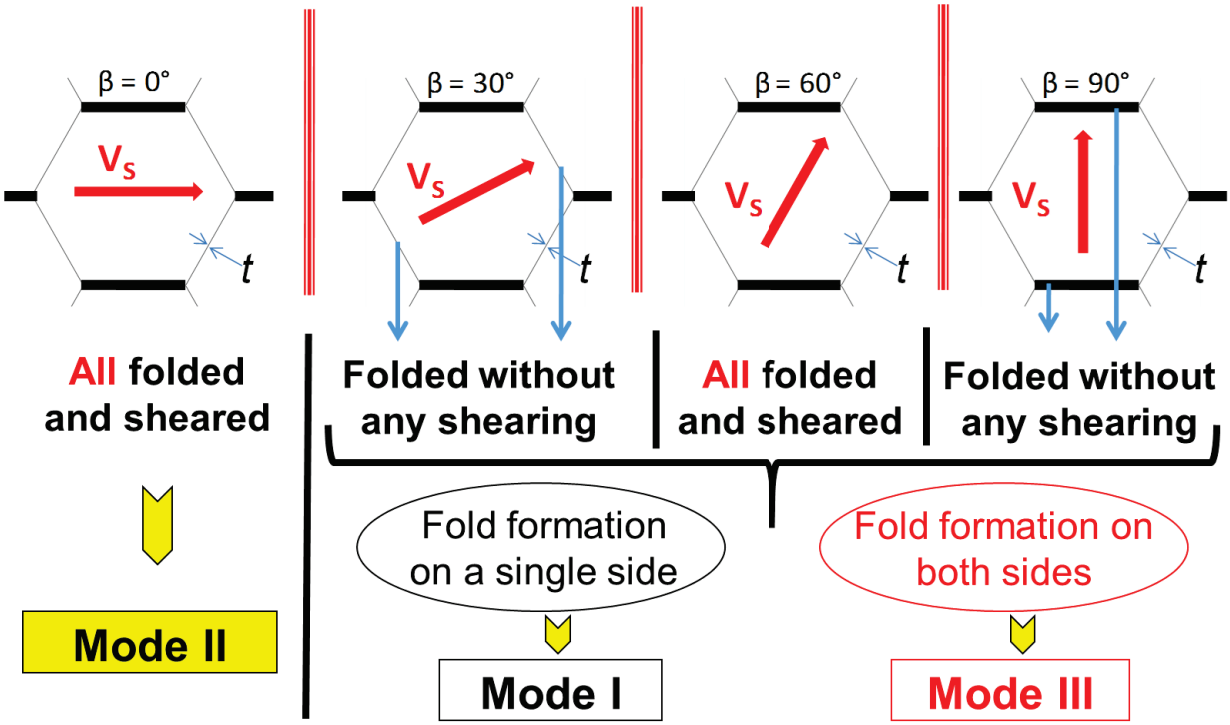

Figure 15. *L'effet de l'angle β sur les modes de déformation.*

L'analyse des mécanismes de déformation en quasi-statique et en dynamique permet de comprendre le phénomène inversé de l'effet dynamique sur les réponses d'écrasement quand l'angle Ψ augmente Ψ > 45° (figure 16).

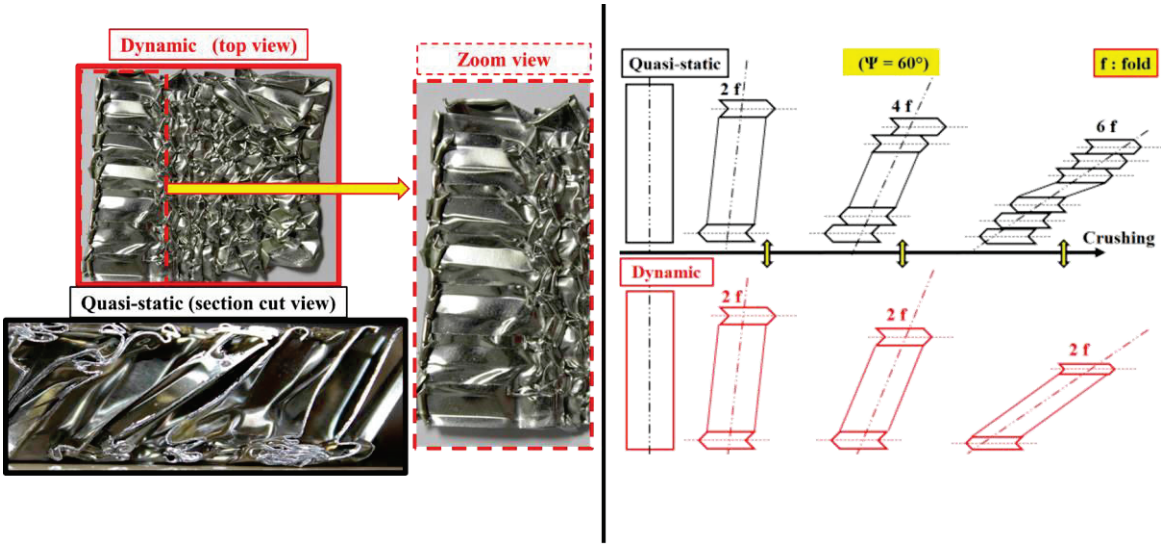

Figure 16. *L'effet de la vitesse sur les mécanismes de déformation.*

Due à la limitation des moyens de mesures pour les différentes composantes des forces (axiale et tangentielle), une étude numérique est alors nécessaire. Le but de cette étude est de mieux comprendre la distribution des modes de déformation, d'expliquer le phénomène de l'augmentation de la résistance sous sollicitation dynamique et sa relation avec l'angle Ψ.

III- Simulation numérique

Le chapitre 3 présente une étude numérique basée sur un modèle éléments finis. Elle permet de comprendre ce phénomène qui est imputé aux mécanismes de déformation locaux des cellules. Ce modèle permet aussi de calculer l'effort tangentiel et compléter les résultats de la campagne expérimentale (figure17). Cependant, l'effort normal et l'effort de cisaillement seront calculés.

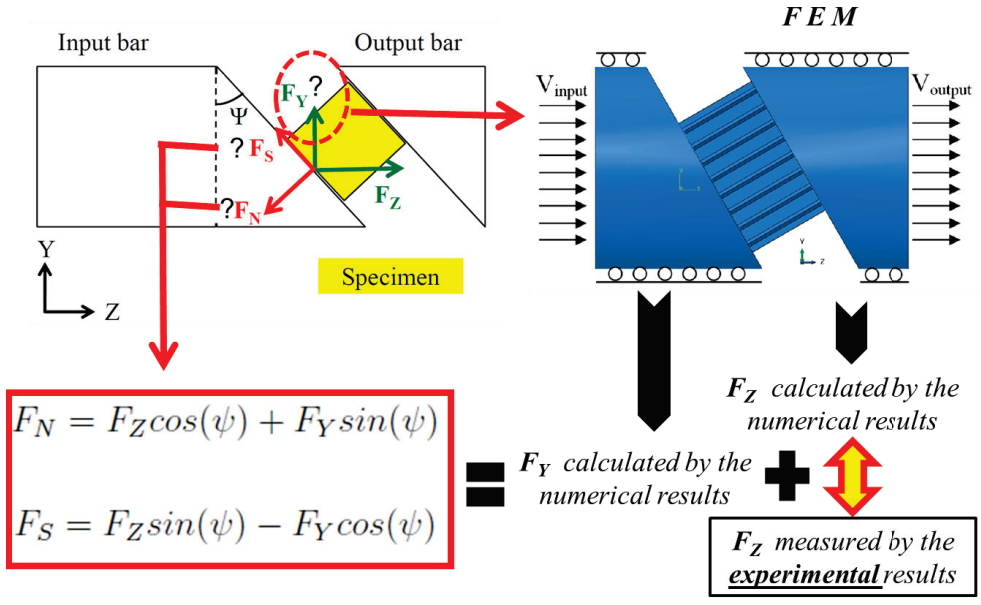

Figure 17. *Schéma des différentes composantes de la force et le modèle EF sous des chargements mixtes.*

Les résultats numériques montrent également que l'effet de l'angle d'orientation dans le plan de la cellule β est plus prononcé sur la force tangentielle que sur la force normale. Cela influence également les modes d'effondrement et donc la réponse mécanique.

Un bon accord est observé au niveau du pic et du plateau sous les deux conditions de chargement mixte en quasi-statique et en dynamique (la figure 18 montre un exemple de validation en quasi-statique pour un angle β = 30° et la figure 19 montre un exemple de validation en dynamique pour un angle β = 90°).

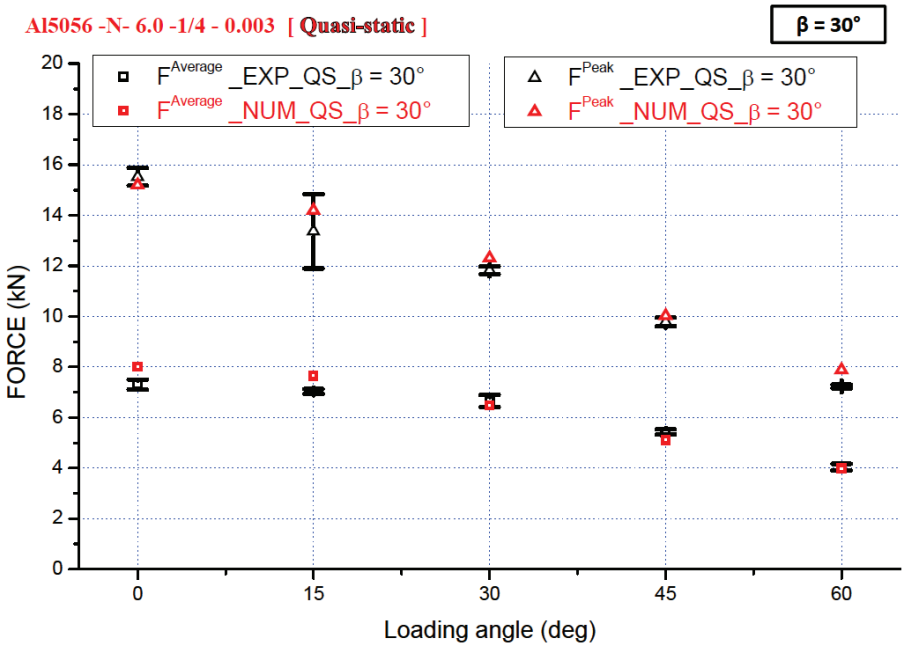

Figure 18. *Le pic initial et le plateau : comparaison numérique et expérimentale en quasi-statique.*

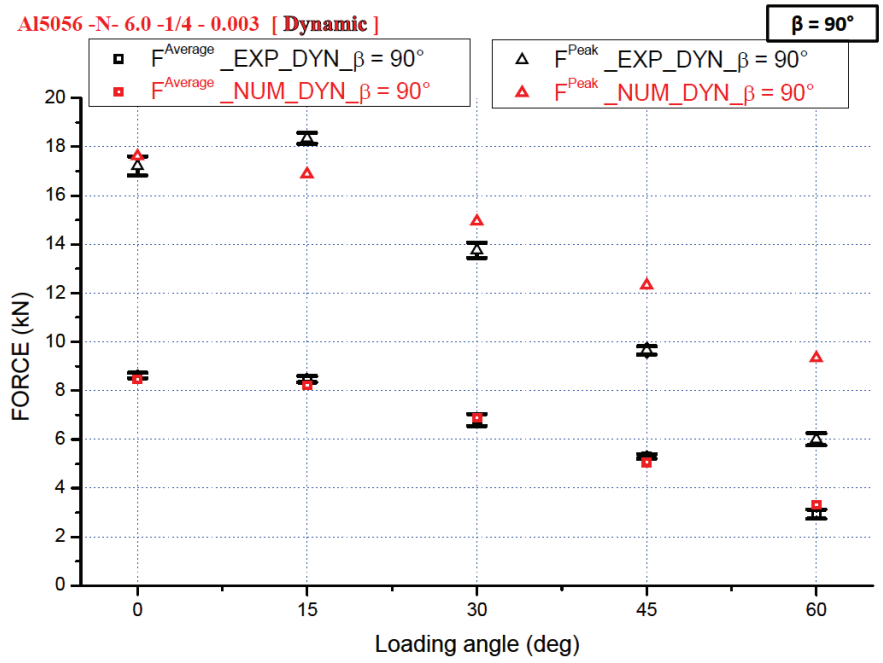

Figure 19. *Le pic initial et le plateau : comparaison numérique et expérimentale en dynamique.*

Les modes de déformation sont aussi vérifiés numériquement. Une comparaison entre les réponses numériques et expérimentales a été élaborée sous des conditions de chargement de compression/cisaillement mixtes (figure 20).

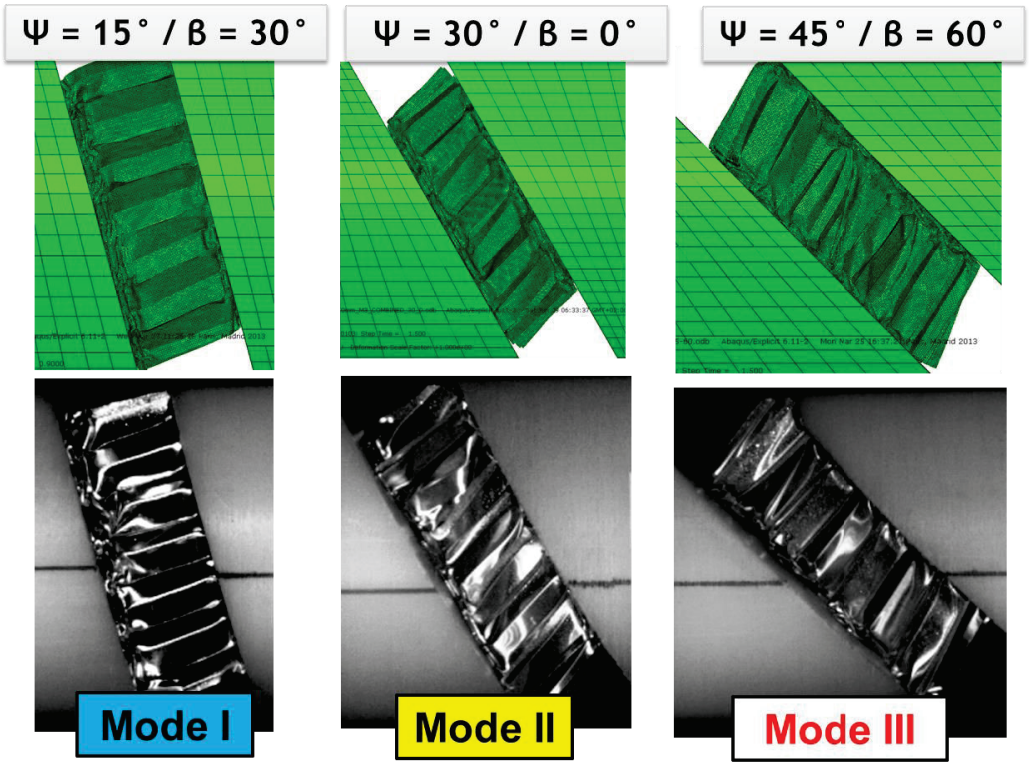

Figure 20. *Les modes de déformation : comparaison numérique et expérimentale.*

Un bon accord est observé et finalement le modèle numérique détaillé est validé de point de vue réponses d'écrasements et modes de déformation.

L'analyse des résultats numériques a concerné l'influence de l'angle de chargement Ψ et l'angle β sur les composantes axiale et tangentielle de la force. Les mêmes observations rapportées sur la composante axiale de la force mesurée expérimentalement sont prouvées par les résultats numériques. Un effet significatif de l'angle β est observé numériquement. En effet, la composante normale de la force et la composante tangentielle sont influencées par l'angle β (figure 21 montre l'influence de β sur la composante normale et la figure 22 montre l'influence de β sur la composante tangentielle).

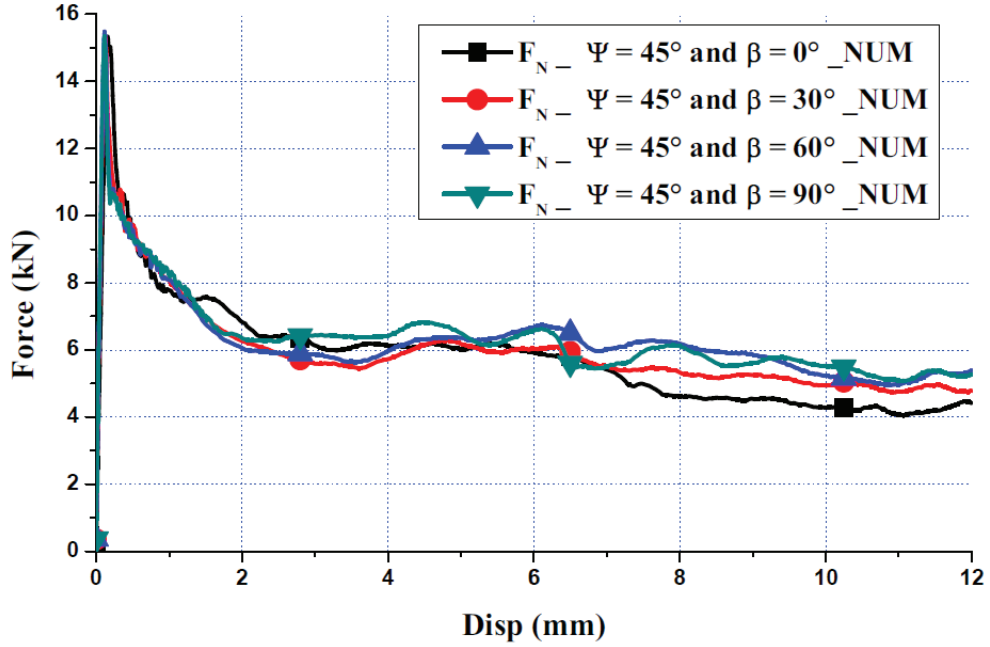

Figure 21. *L'influence de l'angle β sur la composante normale de la force Fn*

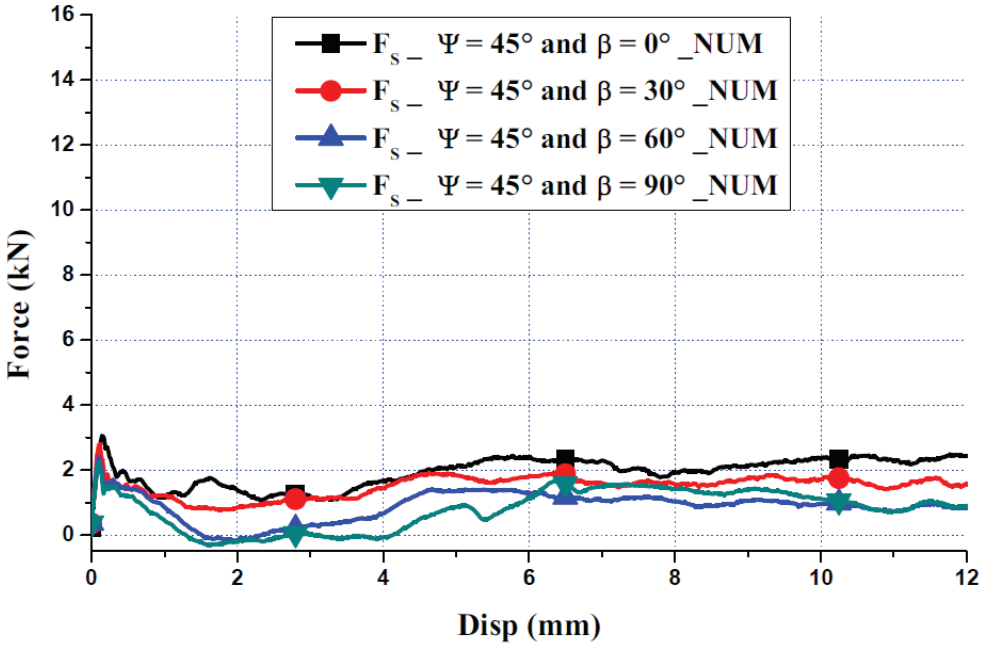

Figure 22. *L'influence de l'angle β sur la composante tangentielle de la force Fs.*

Ces simulations numériques, couplées aux résultats expérimentaux, permettent alors de dissocier les composantes normale et tangentielle de la réponse des nids d'abeille et d'identifier les paramètres d'un critère macroscopique de résistance exprimé en fonction de la vitesse d'impact, de l'angle de chargement et de l'angle d'orientation dans le plan. Le même effet de l'angle β sur l'augmentation de la résistance sous sollicitation dynamique est aussi prouvé par le critère macroscopique de résistance pour le comportement des nids d'abeille sous des chargements de compression/cisaillement mixtes. Cette augmentation est liée à l'angle de chargement Ψ. Un angle critique $\Psi_{critique}$ est exprimé en fonction de l'angle β et de la vitesse d'impact. Au-delà de cet angle le phénomène de rigidification dynamique n'est plus observé, il y a même une diminution de cette rigidité (figure 23).

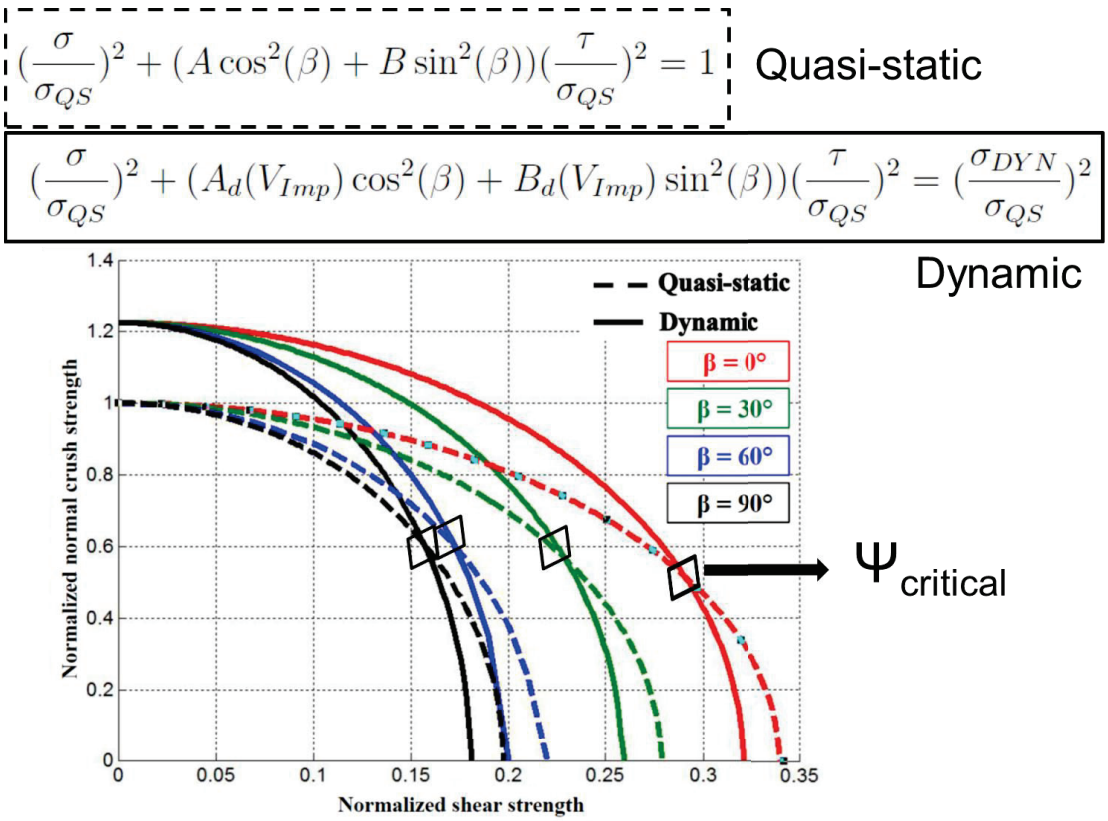

Figure 23. *L'influence combinée de l'angle Ψ, de l'angle β et de la vitesse d'impact sur le critère macroscopique de résistance pour le comportement des nids d'abeille sous des chargements de compression/cisaillement mixtes.*

IV- Modèle réduit

Finalement, dans le but de réduire le coût des simulations numériques, un modèle éléments finis (EF) réduit basé sur un critère de périodicité tenant compte de l'angle d'orientation dans le plan est proposé et son domaine de validité est évalué dans le chapitre 4 (figure 24).

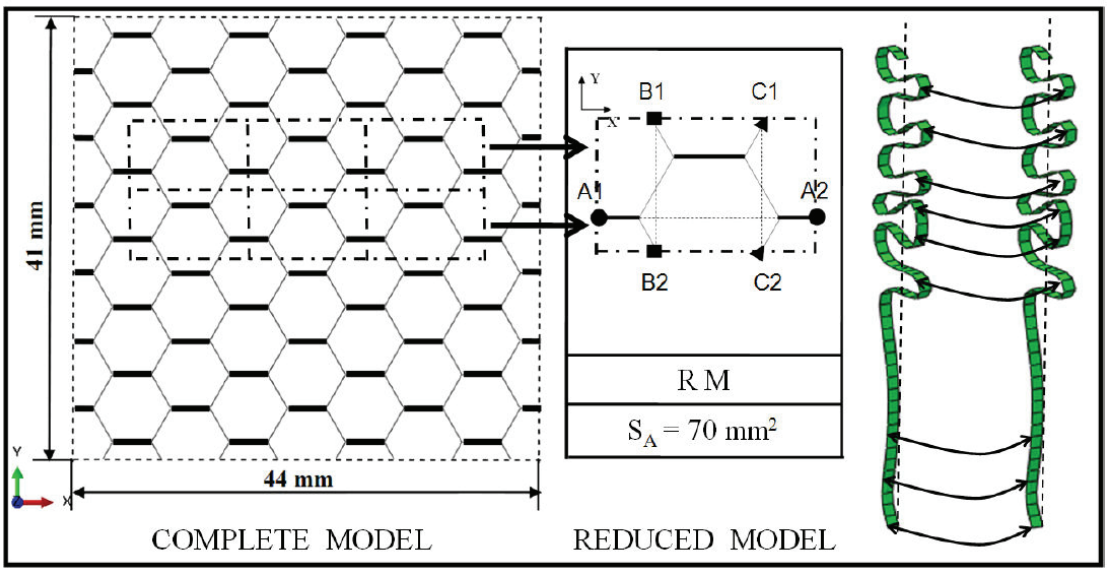

Figure 24. *la cellule élémentaire prise pour le modèle éléments finis (EF) réduit.*

Les résultats numériques montrent un bon accord entre le modèle réduit et le modèle détaillé d'un point de vue réponses d'écrasements et mécanismes de déformation (figure 25).

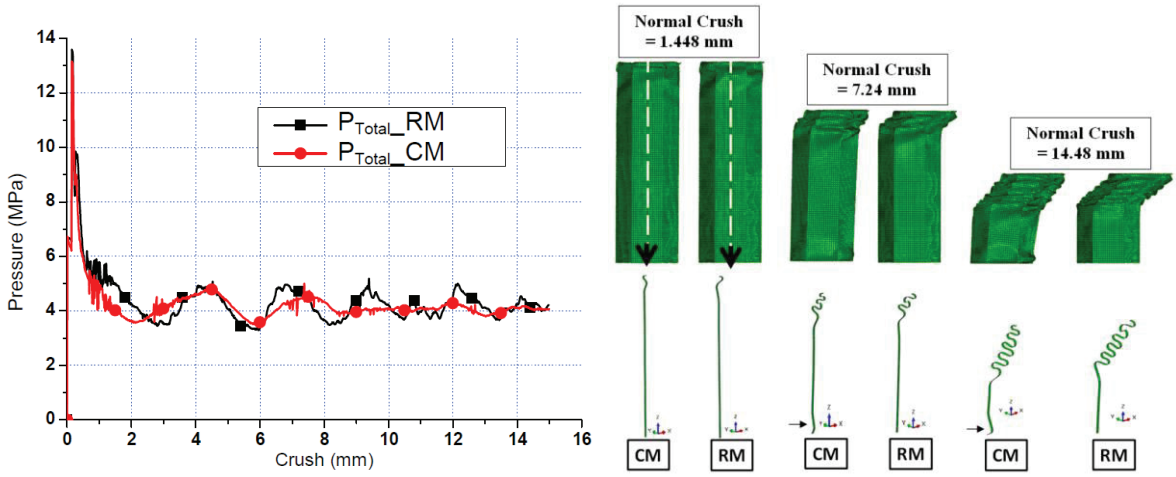

Figure 24. *Comparaison entre les réponses et les mécanismes de déformation du modèle éléments finis (EF) réduit et du modèle EF complet sous un chargement mixte.*

Ce modèle réduit permet d'assurer un gain de 97.17 % sur le temps de calcul. La comparaison entre le modèle global (avec 36 cellules) et le modèle réduit montre que ce dernier atteint sa limite de reproductibilité pour un angle de chargement Ψ_{limit} compris entre 30° et 45°. Cependant les nids d'abeille ne sont pas destinés pour être utilisés sous des chargements de cisaillement assez élevés. Ce modèle réduit peut être utilisé comme un moyen numérique

rapide pour réaliser des plans d'expériences tout en variant la taille de cellule, l'épaisseur de la paroi cellulaire, le matériau constitutif, etc… avec un faible coût de calcul.

V- Conclusion

Les nids d'abeille d'aluminium combinent légèreté et grande capacité d'absorption d'énergie. Ils sont alors de plus en plus utilisés dans les secteurs du transport (automobile, aéronautique …) pour contribuer conjointement à l'allègement structural et à la sécurité. Dans cette thèse, le comportement à l'écrasement des nids d'abeille est étudié en tenant compte de l'effet combiné de l'angle d'orientation dans le plan des cellules, de l'angle de chargement et de la vitesse de sollicitation, que la littérature ne relate pas. Un dispositif de chargement mixte compression/cisaillement est conçu pour mener l'étude expérimentale. L'analyse des résultats porte sur le pic initial d'effort, le plateau d'effort, ainsi que sur les modes de déformation. Les résultats montrent une augmentation de la résistance sous sollicitation dynamique dépendante de l'angle de chargement Ψ. Elle devient moins significative quand l'angle de chargement augmente jusqu'à atteindre un angle critique. Pour $\Psi > \Psi_{critique}$, les réponses quasi-statiques sont même plus élevées que les réponses dynamiques. Une étude numérique est alors entreprise. Elle permet de comprendre ce phénomène qui est imputé aux mécanismes de déformation locaux des cellules. Les résultats numériques montrent également que l'effet de l'angle d'orientation β dans le plan est plus prononcé sur la force tangentielle que sur la force normale, que cela influence également les modes d'effondrement et donc la réponse mécanique. Ces simulations numériques, couplées aux résultats expérimentaux, permettent alors de dissocier les composantes normale et tangentielle de la réponse des nids d'abeille et d'identifier les paramètres d'un critère macroscopique de résistance exprimé en fonction de la vitesse d'impact, de l'angle de chargement et de l'angle d'orientation dans le plan. Finalement, dans le but de réduire le coût des simulations numériques, un modèle éléments finis (EF) réduit basé sur un critère de périodicité tenant compte de l'angle d'orientation dans le plan est proposé et son domaine de validité est évalué.

Comme perspectives, les futures travaux peuvent porter sur l'extension du critère de résistance qui dépond des paramètres géométriques et matériaux, implémenter l'effet combiné de l'angle de chargement et l'angle d'orientation dans le plan de cellule dans des lois de comportement utilisables pour des éléments volumiques, de vérifier l'influence des paramètres (Ψ, β et V_{imp}) sur des panneaux sandwich formés par des nids d'abeille.